April 2021

# Cold-Formed Steel Stud Assemblies Bearing on Concrete Slabs

Abbas Joorabchian
*University of Massachusetts Amherst*

# Cold-Formed Steel Stud Assemblies Bearing on Concrete Slabs

A Dissertation Presented

by

**Abbas Joorabchian**

Submitted to the Graduate School of the

University of Massachusetts Amherst in partial fulfillment

of the requirements for the degree of

Doctor of Philosophy

February 2021

Civil and Environmental Engineering

**Cold-Formed Steel Stud Assemblies Bearing on Concrete Slabs**

A Dissertation Presented

By

**Abbas Joorabchian**

Approved as to style and content by:

_____
Kara D. Peterman, Chair

_____
Sergio Brena, Member

_____
Peggi Clouston, Member

_____
John E. Tobiason, Department Head
Civil and Environmental Engineering Department

This research project is funded by the American Iron and Steel Institute.

**To my family…**

# Acknowledgements

I would like to express my sincere gratitude to my doctoral advisor, Professor Kara Peterman, for her endless support and guidance during the course of my PhD studies. It has been great pleasure and honor to have the opportunity to work with her. Without her motivation, knowledge and valuable advice, this research would not have been successfully completed. In addition, my warn appreciation is extended to my doctoral committee members, Professor Sergio Brena and Professor Peggi Clouston for their time, guidance, and helpful suggestions.

I also gratefully thank Mark Gauthier, the University of Massachusetts Amherst lab technician for his great help during the experiments.

Last but not least, I wish to extend my utmost heartfelt appreciation to my family for their endless love, encouragement, and support.

February 2021

# Abstract


COLD-FORMED STEEL STUD ASSEMBLIES BEARING ON CONCRETE SLABS

FEBRUARY 2021

ABBAS JOORABCHIAN

B.Sc., AMIR KABIR UNIVERSITY OF TECHNOLOGY, IRAN

M.Sc., SHARIF UNIVERSITY OF TECHNOLOGY, IRAN

Ph.D., UNIVERSITY OF MASSACHUSETTS AMHERST

Directed by: Professor Kara D. Peterman

Cold-formed steel (CFS) bearing walls are frequently installed on concrete slabs, which do not provide perfectly rigid and uniform bearing conditions. Existing design guidance assumes bearing conditions have no impact on the axial capacity, though cold-formed steel compressive members are particularly susceptible to end conditions. Studs are typically installed at the edge of concrete slabs, which is prone to spalling and geometric irregularities. Moreover, they are occasionally installed inadvertently overhanging from concrete slabs. In this research project, the impact of non-uniform and partial bearing conditions on the axial strength of cold-formed steel wall assemblies is identified and characterized experimentally and numerically. The results are for a means of evaluating existing design guidelines presented in the North American Specification of the American Iron and Steel Institute (AISI S100-16). Twenty-seven tests were conducted on CFS wall assemblies. Studs of various cross-sections and bearing conditions were considered. Bearing conditions included: full bearing (edge distance ≥ 20.32 cm (8 inches)), close to

the edge, at the edge, and partially overhanging from the slab. In addition to the experiments, high-fidelity finite element modeling of all the systems was conducted to validate the experimental and elucidate the impact of parameters not captured during the tests.

Investigated cold-formed stud assemblies were fixed to 30.48 cm (12 inches) in height. However, variable height wall assemblies are utilized in typical construction. To better characterize the relationship between the bearing condition and axial strength, a computational modeling program at heights determined by buckling modes (local, distortional, and global) was conducted. In this program, 2376 high-fidelity 3D finite element analyses were performed. 66 variable stud cross-sections were investigated. The CFS assemblies were installed on concrete slabs in twelve different bearing conditions, from full-bearing condition with no edge effects to intermediate edge distances approaching the edge, to the edge itself, and finally overhanging from the edge.

The experimental and computational modeling results revealed that there is a potential need for improvement of current AISI specifications, where all bearing conditions are assumed rigid and uniform. The experimental-derived and analysis-based design recommendations for improving the current specification are discussed in this dissertation. Furthermore, it was concluded that by loading the end of specimens by the actual and non-uniform stress distribution which were generated by non-uniform bearing conditions, the axial strength could be captured precisely by direct strength method equations proposed in AISI S100-16.

# Table of Contents

# Table of figures

# Table of tables

# CHAPTER 1

# Introduction and Literature Review

## 1.1 Introduction

Generally, there are two types of structural steel used in building systems: hot-rolled and cold formed steel (CFS). Hot-rolled steel refers to not only heavier structural elements, but to construction method: post-and-beam. Cold-formed steel structural elements, by contrast, are thin and light, and repetitively-framed. Structural efficiency is enabled through complex cross-sections, folded to maximize stiffness and capacity. While both structural steels have advantages and disadvantages, cold-formed steel systems are particularly cost-effective and structurally efficient for low-to-midrise construction (1-10 stories). Furthermore, CFS members are recyclable, easy to ship (due to interlocking sections), rot- and moisture-resistant, and non-combustible. Panelization and modularization have transformed the industry, increasing construction speed and accuracy.

Cold-formed steel and hot-rolled steel are both steel, with nearly identical base material properties. But, there are also differences in how hot-rolled and cold-formed steels are manufactured, which lead to differences in residual stress distributions. In the hot-rolled steel making process, the steel is rolled at a temperature above its recrystallization temperature (~1000° F). When it is melted, it can be shaped and formed easily to any desirable cross section; then, the steel is cooled at room temperature. Cold-formed steel

structural sections begin as a coil of thin steel plate, formed via the same process as hot-rolled steel. This coil steel is then gradually folded into cross-sections via roll forming machines, in which the steel is passed through a series of dies. Roll forming occurs at room temperature. Because of this, CFS members have slightly higher elastic moduli than hot-rolled members, though the difference is small: 29500 ksi to 29000 ksi.

The most common cross-sections used in construction are lipped channels (sometimes referred to as “cees”), unlipped channels, decking, hats, and zees. CFS members can be used alone or connected back-to-back or front-to-front. The roll forming process enables great flexibility in cross-section shape and design, and sections can be customized for a given application. Figure 1 shows typical CFS members.

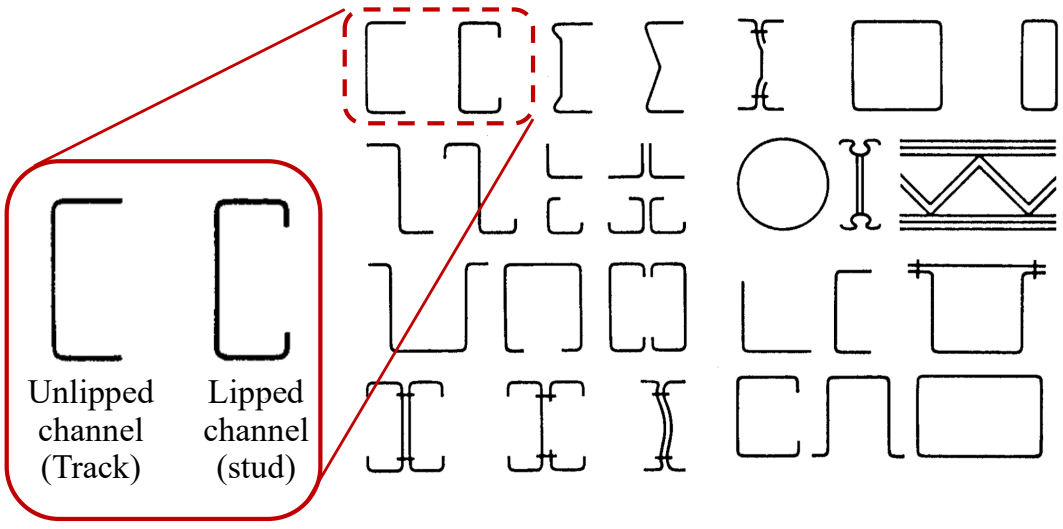


*Figure 1: Cold-formed steel members [1]*

Cold-formed steel studs and tracks form the vast majority of CFS structural members and are used as load-bearing members in repetitively-framed walls and floors. CFS framing members are typically spaced 30.5, 40.65, or 61 cm (12, 16, or 24 inches) apart. Walls are typically constructed of vertical lipped channels ("studs") capped in two horizontal unlipped channels ("tracks") (Figure 2) at the top and bottom.

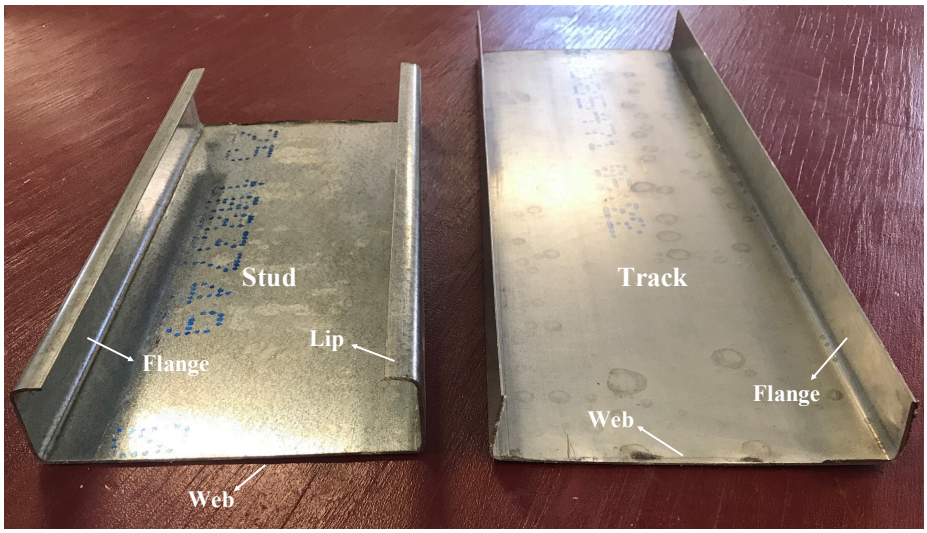


*Figure 2: Lipped and unlipped CFS channels (stud and track)*

The same configuration is utilized for floors and roofs, but the elements are placed horizontally for floors and either inclined or horizontally for roofs. A schematic of stud-track wall system is shown in Figure 3.

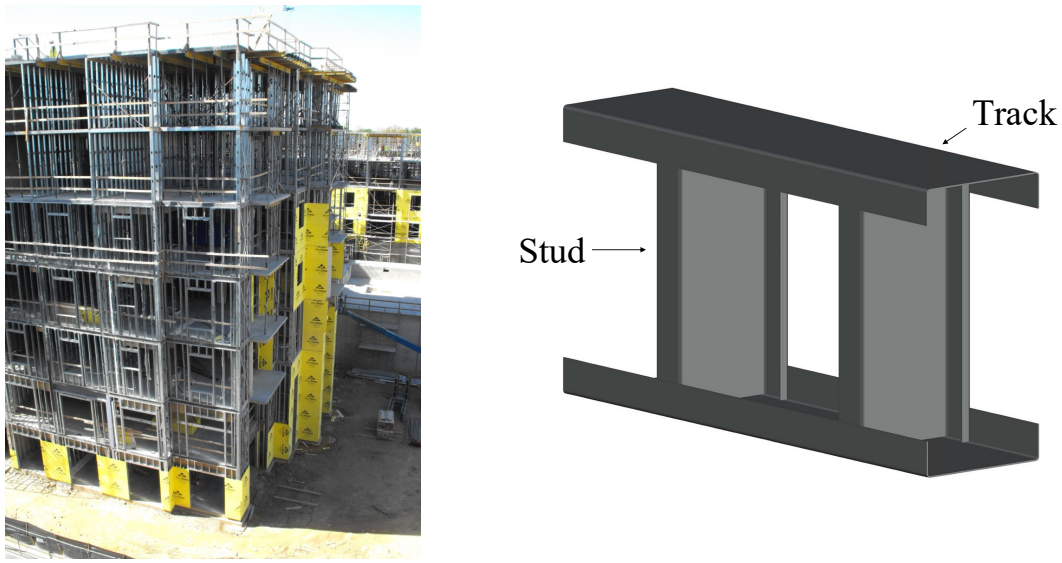


(a) (b)

*Figure 3: (a) CFS-framed apartment building with repetitively-framed walls (photo courtesy of Don Allen), (b) Schematic of stud-track wall assembly, demonstrating capping of studs within tracks.*

CFS structural walls are responsible for withstanding gravity loads, and lateral loads if they are part of the designated lateral force resisting system. This dissertation focuses on gravity framing, in which axial loads are the primary load imparted to the walls. The behavior of cold-formed steel axial members has been investigated comprehensively and implemented for North American design and construction in the American Iron and Steel Institute (AISI) specifications. Axial members are governed by the provisions of AISI S100-16 [2] and S240-15 [3]. In these provisions, axial members are assumed to have uniform stress distributions applied to the stud ends. However, this condition is not necessarily realistic. Load-bearing walls are typically placed on concrete slab floors. Furthermore, exterior walls may be installed at or near the slab edge, or may even overhang

slightly due to installation error (while overhanging walls should be avoided in construction, they do occur). These conditions may result in a non-uniform bearing condition and corresponding stress distribution on the stud end. Studs bearing under these situations will have reduced axial capacity, yet, current practice does not recognize a difference in the axial capacity or behavior due to partial end supports caused by edge distance, overhang, or non-uniform bearing surface. Complexities arise due to spalling or crushing of the slab edge which can induce eccentricity into the stud member.

## 1.2 Literature review

A wealth of data exists on the performance of axially-compressed cold-formed steel lipped and un-lipped channels. However, in previous works, the concrete slabs on which stud walls frequently bear are assumed to provide rigid uniform support resulting in a uniform stress distribution on the stud end and are eliminated from the test programs. Across available experiments, the stud-track assemblies were placed directly on fixed heavy steel platen supports or rigid laboratory floors. These works further do not capture the spalling or crushing of the concrete slab, which only intensifies the non-uniform condition at the stud end and may ultimately reduce contact. However, a few research programs did examine the interactions between stud assembly and concrete flooring.

In the experiments, the stud-track assemblies were placed on fixed steel beams providing a rigid bearing support for the systems. Miller and Pekoz [4] investigated the overall behavior of CFS wall assemblies under axial loading in 1993. They performed seven tests to estimate the loading eccentricity at the ends of studs with tracks bearing flat on a level surface. To achieve this, the wall assemblies were placed directly on concrete

floors as shown in Figure 4(a); however, the impact of the concrete floor was not considered on the behavior of the assemblies, and the concrete floors were assumed rigid. Telue and Mahendran [5] researched the axial behavior of wall assemblies using gypsum plasterboard, and in their experiments, the bottom track of the system was fixed to a steel beam, as shown in Figure 4(b). The acceptable tolerance of the gap between studs and tracks was examined by Laboube and Findlay [6]. They performed tests on wall assemblies with rigid bearing conditions to determine the impact of this gap on the overall response of the wall assembly. Wang and his colleagues in 2005 investigated the role of sheathing in the axial strength of load-bearing partition walls [7] (Figure 4(c)). The strength and stability of sheathed CFS wall assemblies under the compression were examined by Vieira et al. in 2011 as well [8], and the specimens were connected to the fixed beam of the rig Figure 4(d). In addition to the axial, the lateral behavior of a single sheathed stud in a CFS wall was researched by Peterman and Schafer [9], and the specimens were mounted on the rigid beam of a multi-degree of freedom wall testing rig Figure 4(e). Fratamico et al. [10] investigated experimentally the axial behavior of built-up cold-formed steel columns and similar to the other research projects, the wall assemblies were placed on fixed platen supports Figure 4(f). While all of these works formed the basis for the North American cold-formed steel specifications, none considered the impact of the bearing condition on the stud axial capacity. Works that included concrete bearing conditions involved laboratory “strong floors” which are designed to be perfectly rigid and flat (and do not spall or crush). Thus, while they are seminal works in cold-formed steel behavior, none discern the impact of realistic bearing conditions on gravity wall assemblies.

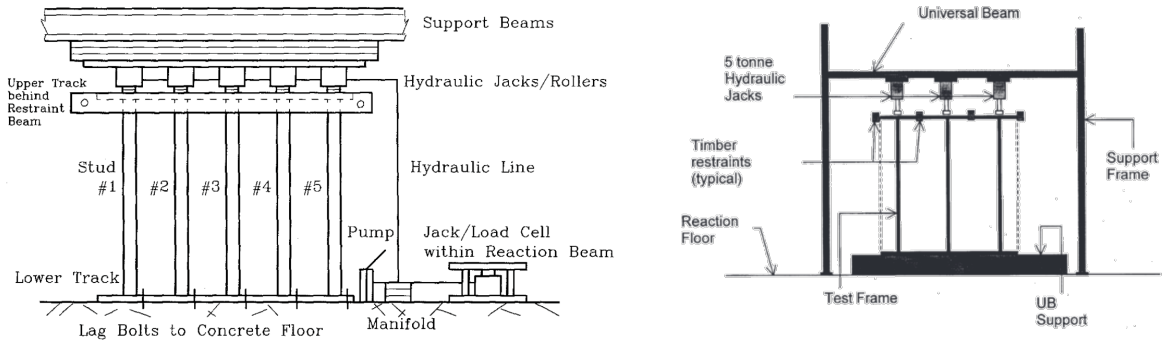


(a) (b)

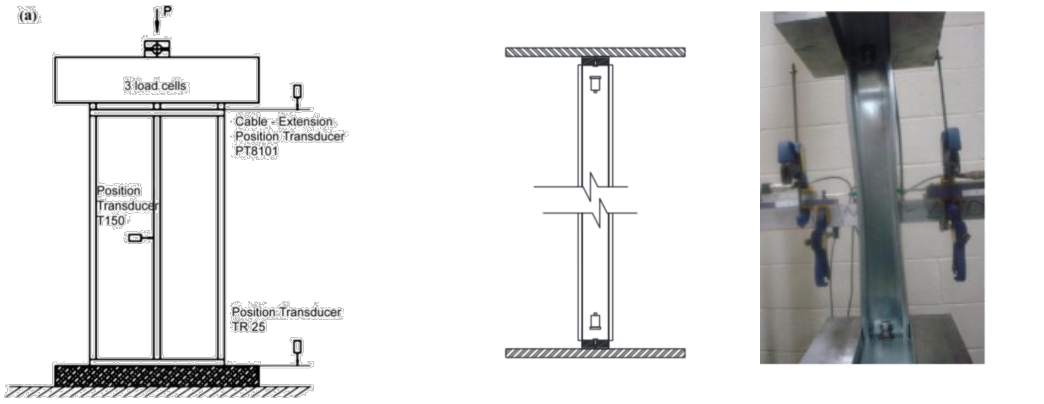


(c) (d)

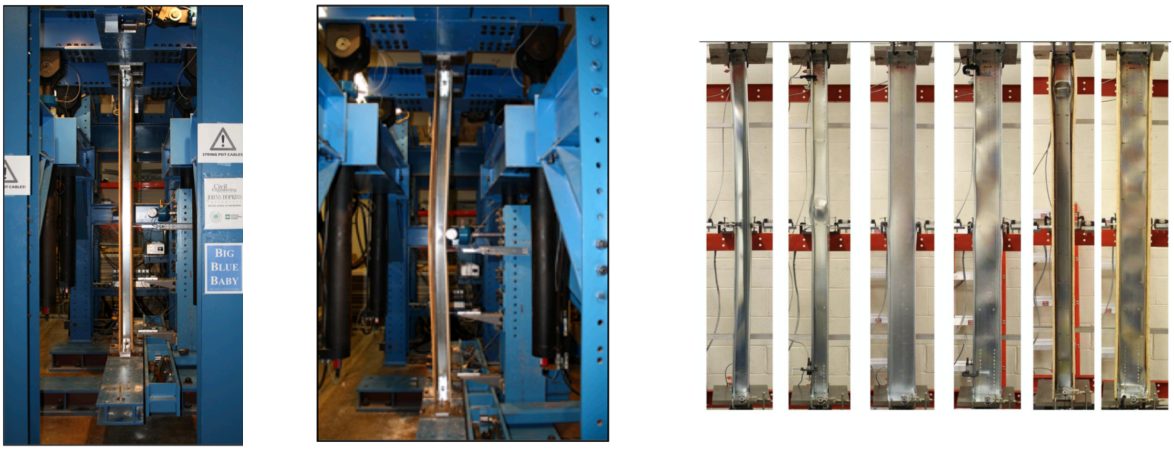


(e) (f)

*Figure 4: Experimental programs of cold-formed steel studs under axial load in which bearing conditions are not considered; (a) Miller and Pekoz [4], (b) Telue and*

*Mahendran [5], (c) Wang et al. [7], (d) Viera et al. [8], (e) Peterman and Schafer [9], (f) Fratamico et al [10].*

Two prior works examined the impact of stud bearing on concrete slabs. A research project was done at the University of Manitoba by Polyzois and Fox in 2001 [11], which focused on the stud capacities on concrete slabs. It supports a reduction in stud axial capacity due to the stud distance from slab edge. The experimental program undertaken by the authors included stud assemblies located 20.3 and 2.54 cm (8" and 1") from and at the concrete slab edge (Figure 5). The studs were sized such that they were permitted to buckle locally. This research indicated that assemblies locating at 8" from the slab edge were able to develop their local buckling capacity. However, in those installed at the edge, hindered by concrete spalling and cracking, axial compressive strength decreased by 15-25%. This decrease was due to the reduction in bearing area, and loss of a uniform stress distribution. Notably, this work only examined one stud-track assembly and did not consider intermediate edge distances.

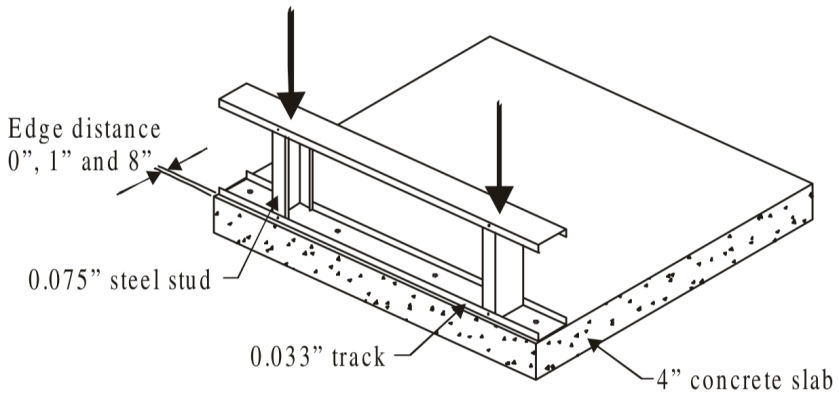


*Figure 5: Typical test configuration employed in [13] (image from [13]).*

Bae et al. [12] also examined the axial strength of stub stud walls bearing on concrete slabs. The research program was both experimental and numerical in nature, and primarily examined the effect of wall stud configurations on the performance of the system. Different configurations of the stud-track assembly were considered, such as: single stud columns, single stud walls, back-to-back stud columns, and back-to-back stud walls. These were tested on an 89 mm (3.5 in) concrete slab (intended to simulate typical residential floor systems), as shown in Figure 6. The studs were cut to 51 mm (2 in) in height to force failure into the slab, rather than buckling of the stud. Finite element analysis was conducted to determine the stress distribution in the concrete slab through the track section. The work demonstrated that edge distance did impact system bearing strength, and results were used to develop a method of determining bearing area for the stud-track assembly on concrete slabs, which accurately predicted experimental results (Figure 7). It also demonstrated the inadequacy and inapplicability of the bearing provisions in ACI 318-05 (Building Code Requirements for Reinforced Concrete) [13] for CFS wall systems. While this study expanded the state of knowledge for how stud assemblies interact with concrete foundations, it was limited in scope to one stud size and one stud height. And, the short stub column height did not permit buckling of the stud. The impact of stud thickness, cross-section, and stud length has been largely overlooked by previous work; this research study aims to fill these gaps. This work examines not only a range of overhang and edge distances but also various assembly configurations.

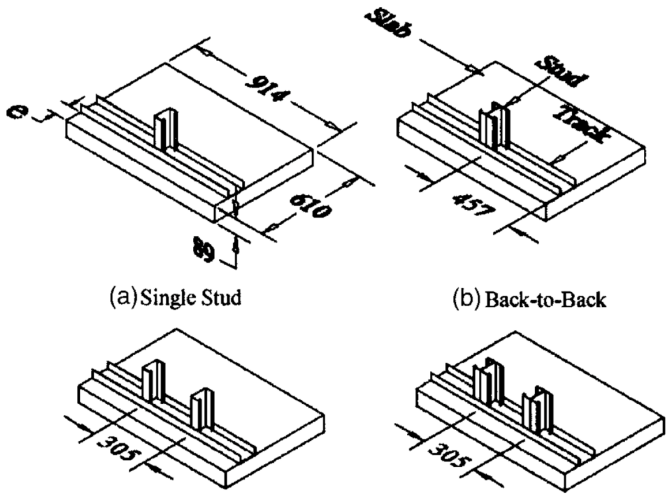


*Figure 6: Test specimen configurations (unit: mm) [12] (image from [12]).*

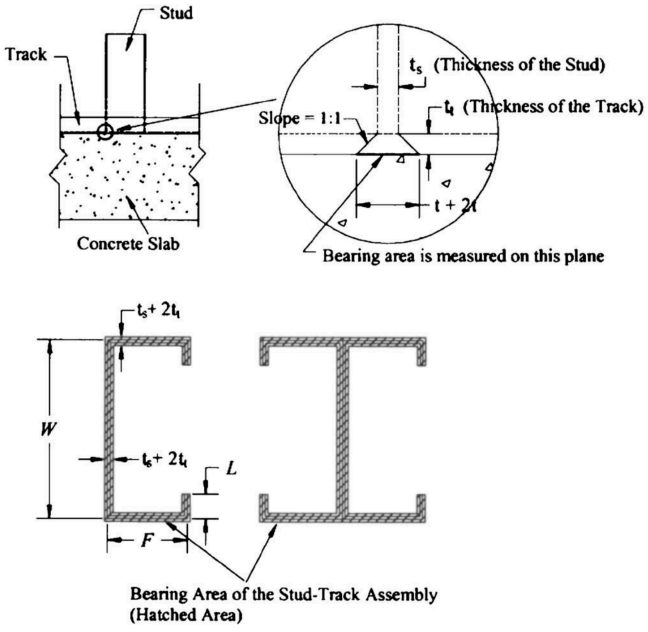


*Figure 7: Determining bearing area by using frustum concept [12] (image from [12]).*

A review of the literature highlighted that little has been done to discern the impact of concrete slabs on the axial behavior of cold formed steel wall assemblies; what has been done has significant applicability limitations. This work aims to characterize experimentally and computationally the effect of stud bearing on concrete slabs as a flexible or semi-rigid support, examining overhang distance, edge distance, and various assembly configurations. Through examining the impact of these variables, the true stress distribution of an axially-compressed stud and track assembly will be determined. Design recommendations to consider the impact of these variables on the assumed stress distributions will be developed. Design provisions developed will provide engineers a means to design the stud wall safely without making conservative assumptions to estimate the axial capacity or ignoring the condition, thus improve the competitiveness of CFS framing, especially in mid-rise projects.

## 1.3 Organization of the dissertation

27 tests were conducted at the Gunness structural laboratory of the University of Massachusetts, Amherst. These tests are discussed in Chapter 2 of this dissertation. Load applies to the built-up steel beam connected under the actuator to distribute the load from the actuator to the top track of the wall assembly. The assemblies were bear directly on 55.88×86.36×15.24 cm (22×34×6 in) concrete slab. The height of studs was fixed 30.48 cm (12 inches). The variables considered in the experiments included edge distance, overhang, and assembly configuration, in which several stud and track section combinations were explored. Once the experimental results were obtained, they were validated and expanded upon via computational modeling. Chapter 3 presents this work.

As a preliminary comparison, the sections were modeled in CUFSM tool [14,15] for elastic buckling analysis. Another means for comparing the experimental and numerical result were predictive methods provided in AISI S100-16.

All the configurations were modeled in ABAQUS [16] software. The nonlinear Finite Element Analysis (FEA) of the stud assemblies and concrete slabs as a system in ABAQUS [16] accurately predicted not only the response of the stud assembly but also the contact behavior with the concrete slab along with the potential edge cracking or crushing of concrete slab itself. The detailed nonlinear FEA modeling aligned with the experimental effort and the necessity of a more extensive parametric study.

In order to extend the utility of these results to variable-height walls and a range of cross-sections, high-fidelity 3D finite element analyses (FEA) of locally, distortionally, and globally-dominant (2.45 m (96 inches) members) stud assemblies bearing on reinforced concrete slabs were performed in Chapter 4. 66 different cross-sections, representing common wall stud members, were investigated in this computational modeling program. Position of the wall assemblies on the concrete slab was varied, from a full-bearing condition with no edge effects, to intermediate edge distances approaching the edge, to the slab edge itself, and overhanging from the edge. In total, 2376 high-fidelity finite element analyses were performed in this chapter.

This work aims to improve existing North American design provisions, which currently do not account for any reduction in axial capacity due to bearing conditions. The FEA study sheds light on the stress distributions imparted on the studs ends by the concrete slabs. The results reveal that there is a potential need for improvement of current AISI specifications,

where all bearing conditions are assumed rigid and uniform. Design recommendations based on the experiments and computational modeling program for improving the current specification are discussed in Chapter 5.

The height of specimen in the experiments was fixed. Therefore, experimentally, there are still knowledge gaps pertaining to the relation between bearing condition and assembly capacity. In Chapter 6, the experiments on the variable-height assemblies which is going to be conducted in the future is discussed. Eventually, in this chapter, conclusions of this comprehensive research project are discussed.

# CHAPTER 2

# Experimental Testing Program

The test program occurred at the Gunness structural laboratory at the University of Massachusetts Amherst. In total, 27 tests were conducted. The assemblies are loosely divided into two categories: with and without concrete slabs, in which tests without concrete slabs simulated idealized rigid bearing conditions. A typical wall assembly consists of two studs capped in two horizontal tracks at the top and bottom, fastened with self-drilling screws (Figure 8(a)). As shown in Table 1, studs of various cross-sections were explored. To investigate the role of section thickness and flange width on the impact of bearing condition, they differed in thickness and flange length. The thicknesses of studs were 0.84, 1.37, and 2.46 mm (33, 54, and 97 mils). Two flange lengths equal to 41.1 and 76.2 mm (1.62 and 3 inches) were utilized for 1.37 mm lipped channel sections. The track sections were sized to correspond with the stud sections; flange width was fixed all 31.7 mm (1.25 in) and thicknesses were matched. However, all of the sections had the same web height (152.4 mm or 6 in). Table 1 lists the stud and track sections by their AISI section designation as defined in AISI S220-15 [17]. Since direct metric equivalents of the section designations do not exist, the AISI section designations are maintained throughout this dissertation. To compare directly between assemblies, stud height was fixed to 30.48 cm (12 inches). Track length was set to 60.96 cm (24 inches).

Various bearing conditions were considered in this research program: rigid bearing condition in which the stud wall assemblies were installed on a rigid beam; full bearing where the stud assemblies were fastened to the center of concrete slabs (edge distance ≥ 20.32 cm (8 inches)), close to the edge, at the slab edge, and finally partially overhanging from the slab (Figure 8(b)). Schematic and definition of bearing conditions are illustrated in Figure 9.

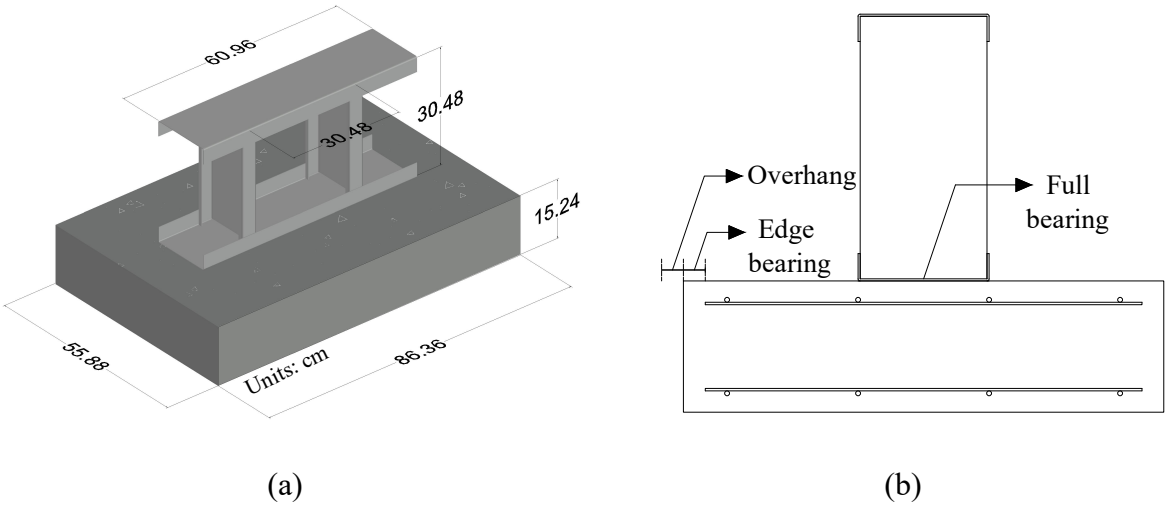


*Figure 8: (a) Schematic of stud-slab assemblies; (b) position of stud-track assembly on the concrete slab for various bearing conditions.*

*Table 1: Experimental test matrix (AISI S100-16 nomenclature for section designation maintained for clarity).*

| **Section** | | **Bearing Condition** | | | |
|---|---|---|---|---|---|
| ***Stud*** | ***Track*** | ***Rigid bearing*** | ***Full bearing*** | ***Close to the edge*** | ***Overhang*** |
| | | | *Distance from edge, mm (in)* | | |
| 600S162-33 | 600T125-33 | Rigid steel beam (No concrete slab) | 203.2 (8) | at the slab edge<br>25.4 (1)<br>12.7 (0.5)<br>3.175 (0.125) | 12.7 (0.5)<br>25.4 (1) |
| 600S162-54 | 600T125-54 | Rigid steel beam (No concrete slab) | 203.2 (8) | at the slab edge<br>25.4 (1)<br>12.7 (0.5)<br>3.175 (0.125) | 12.7 (0.5)<br>25.4 (1) |
| 600S162-97 | 600T125-97 | Rigid steel beam (No concrete slab) | 203.2 (8) | at the slab edge<br>25.4 (1)<br>12.7 (0.5)<br>3.175 (0.125) | 12.7 (0.5)<br>25.4 (1) |
| 600S300-54 | 600T125-54 | — | — | at the slab edge | 12.7 (0.5)<br>25.4 (1) |

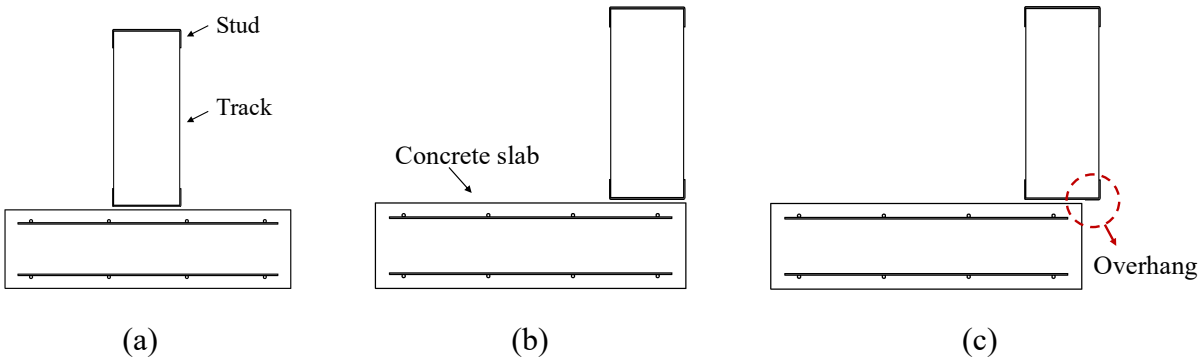


*Figure 9: Definition of bearing conditions; (a) full bearing condition, (b) edge bearing condition, and (c) overhang partial bearing condition.*

## 2.1 Test preparation

The experimental tests were performed on an existing self-reacting structural testing frame at the University of Massachusetts Amherst. The frame consisted of four built-up beams, modified to accommodate the stud assemblies for this work. Two beams were built up from two 33×2.54 0.64 cm (13×1 1/4 in) and one 55.88 1.9×1.9 cm (22 3/4×3/4 in) plates and the others were made from two 22.86×1.58 cm (9×5/8 in) and one 55.88 1.9×0.95 cm (22 3/4×3/8 in) plates (Figure 10). A 490 kN (110 kips) MTS actuator was utilized to apply the compressive force. To enable concentric loading, stud assemblies were concentric with the actuator centerline. Two built-up beams (consisting of two 20.32×2.54 cm (8×1 in) plates and one 10.16×2.54 cm (4×1 in) plate) were designed to support the stud assemblies. A bolted double angle connection was designed to connect the addition beams to the existing frame (Figure 11).

Figure 12 shows schematic of two types of experiments, where the tests without concrete slabs simulate idealized rigid bearing conditions. For the test simulating idealized rigid bearing condition, a rigid built-up beam (two 20.32×2.54 cm (8×1 in) plates and one 10.16×2.54 cm (4×1 in) plate) was designed in lieu of a concrete slab (Figure 17). To assess rigidity, the built-up beam was modeled in SAP2000 v17.1.1 and loaded with the full capacity of the actuator (490 kN [110 kips]). As Figure 13 demonstrates, the maximum deflection of the beam was 0.0076 mm (0.00033 in) which is considered negligible and the beam is thus adequate as a rigid support. This beam was placed on top of the other designed built-up beams and eight 15.87 mm (5/8") diameter A490 bolts were utilized to connect

them together. Figure 12 illustrates how these assemblies, with and without slabs, were placed on the test rig.

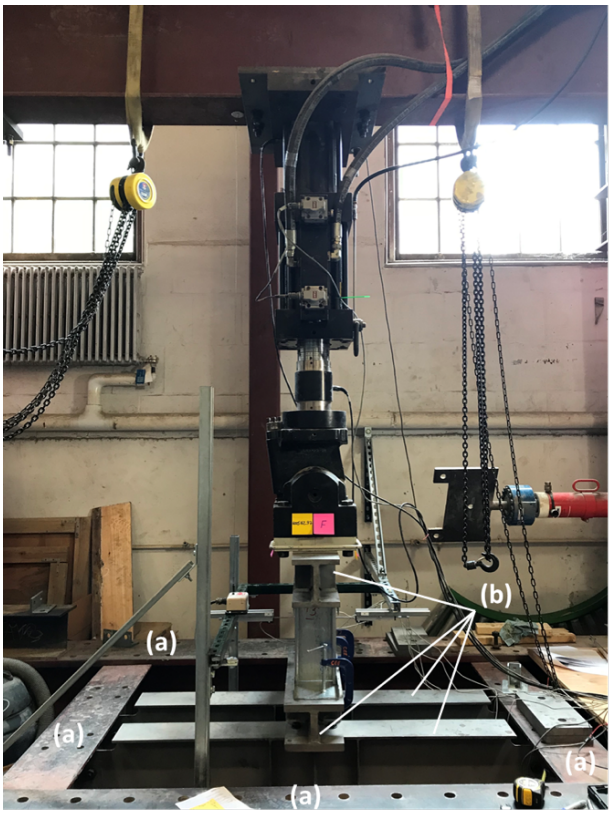


*Figure 10: Gunness structural laboratory testing frame: (a) existing beams; (b) additional beams designed for this test program.*

*Figure 11: Making holes in existing beams by magnet drill.*

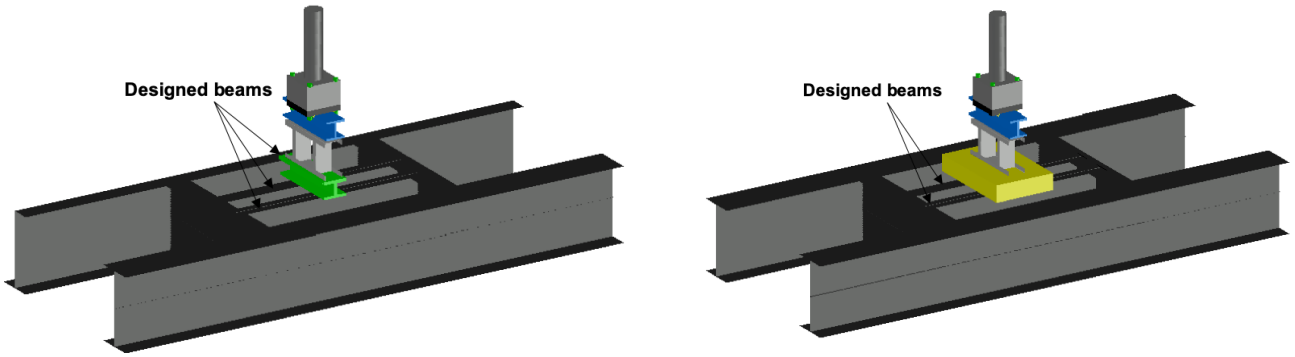


(a) (b)

*Figure 12:The schematic of the tests; (a) test with no slab, (b) test with slab.*

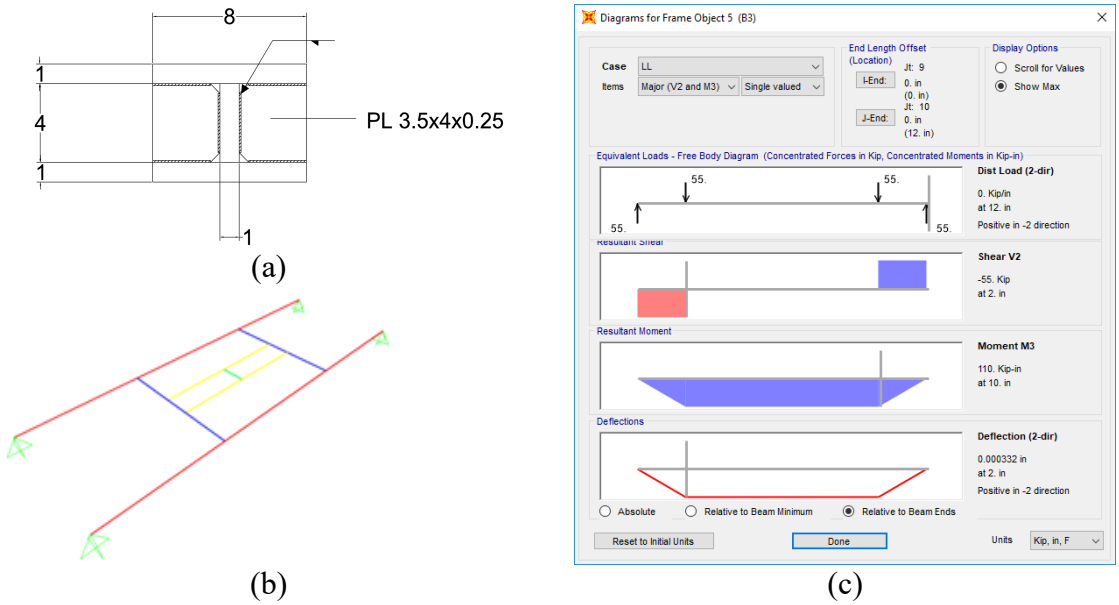


*Figure 13: Designed hot-rolled steel beam as a rigid bearing surface; (a) dimensions, (b) SAP2000 model, (c) diagrams for the rigid beam.*

To prevent any possible the uplift of the concrete slabs in the conditions in which the slabs were loaded eccentrically, an L 8×6×1 angle was designed (Figure 14) to resist uplift forces. The angle was connected to the test rig beams by two angles (L 8×6×1).

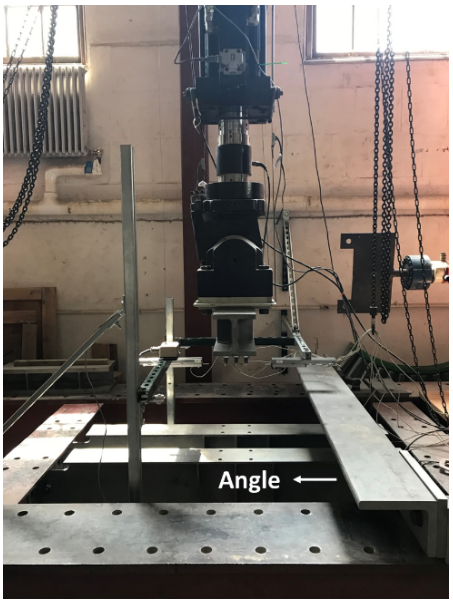


*Figure 14: Designed angle to prevent concrete slab uplift.*

## 2.2 Sensors and instrumentation

Load and displacements were measured via the crosshead load cell and a built-in LVDT. WinDaq software was used for data acquisition. Five transducers were installed on the stud cross-section, two for the flanges and three for the stud web, to capture deformation of each cross-section element and to provide quantitative measures of buckling modes. A rigid frame built-up from slotted strut channels was used to place the sensors at mid-height of the studs (Figure 15). Since the sensor frame was constructed from slotted strut channels, the sensors height was adjustable; hence, they were placed at the middle of a stud height regardless of whether the assembly was tested with or without a concrete slab. Two schematic views of sensor frame and the location of the transducers are presented in Figure 16.

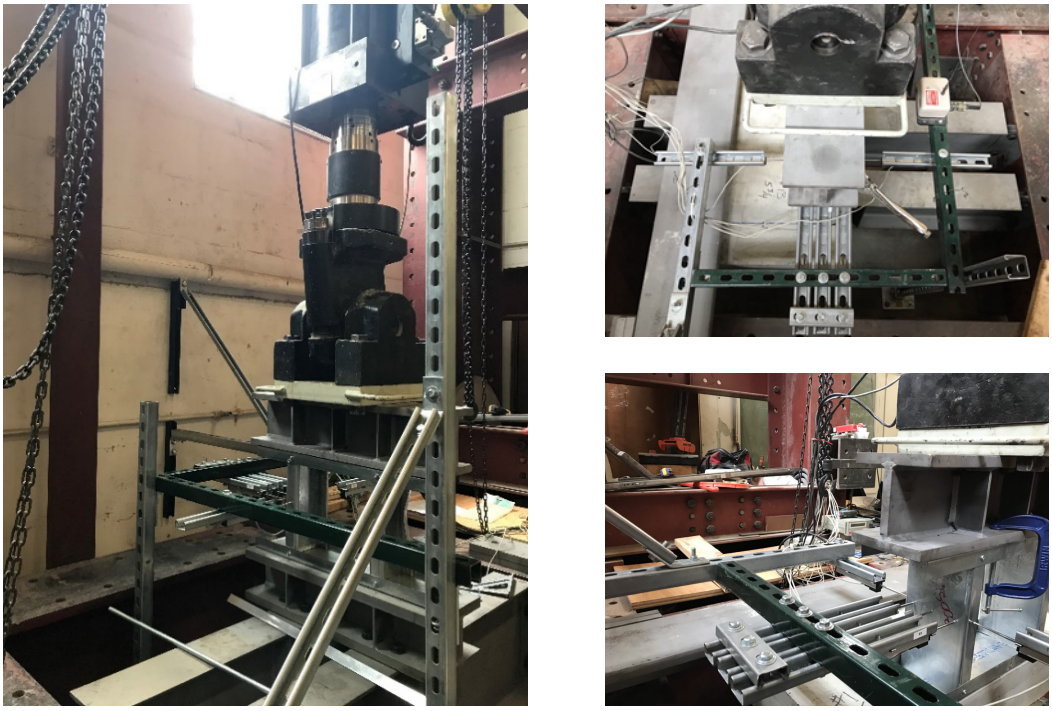

(a) (b)

*Figure 15: The frame built from slotted strut channels to hold the sensors, (b) transducers.*

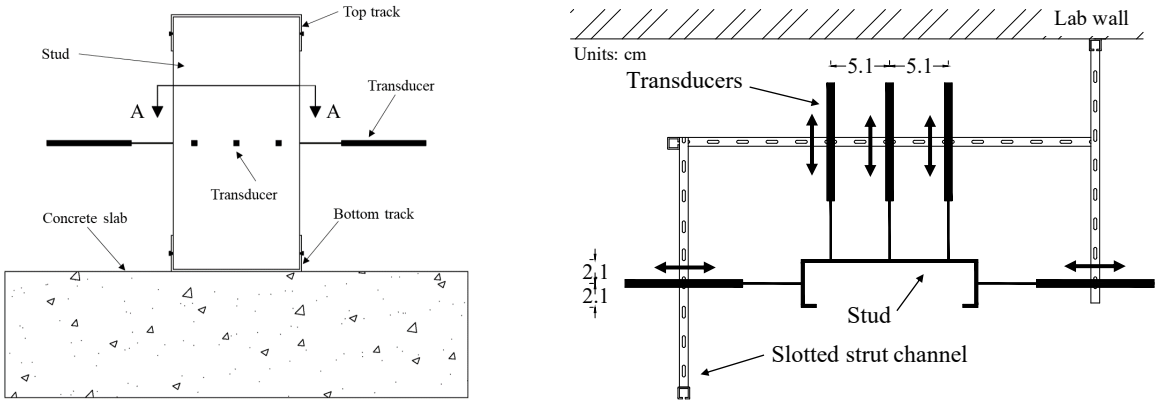


(a) (b)

*Figure 16: Sensor frame schematic view; (a) side view, (b) top view (section A-A).*

The test rig was also instrumented to account for rigidity, with a displacement transducer measuring crosshead displacement of the actuator and a displacement transducer which measured the deflection of the beams supporting the specimens (Figure 17). Before installing the transducers, their calibration factors were calculated through 50 kN (11.24 kips) Instron universal testing machine (Figure 18).

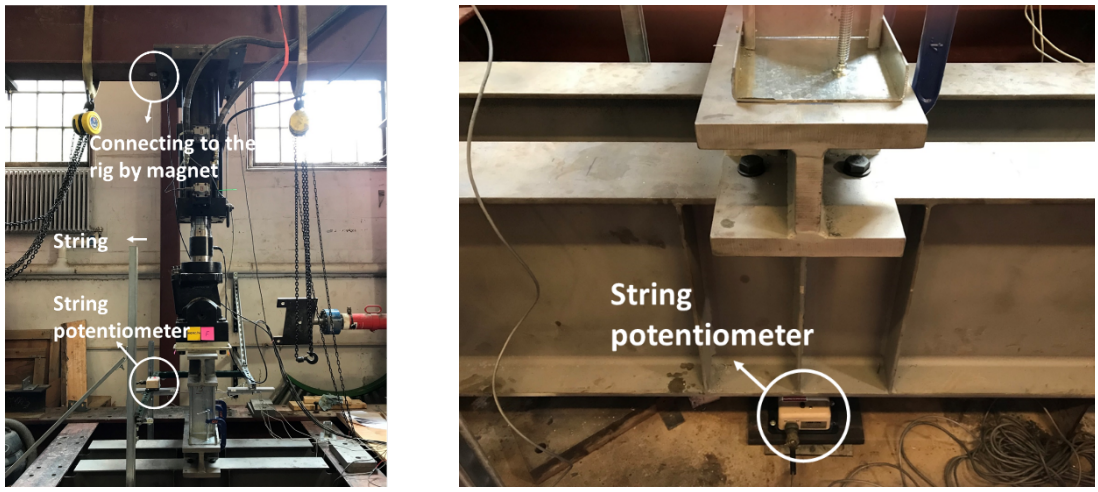


*(a)* *(b)*

*Figure 17: String potentiometers; (a) for the crosshead of the test rig, (b) for the beams supporting the specimens.*

*Figure 18: Finding calibration factors of transducers through through 50 kN (11.24 kips) Instron universal testing machine.*

An overall figure from the test setup including all component is illustrated in Figure 19.

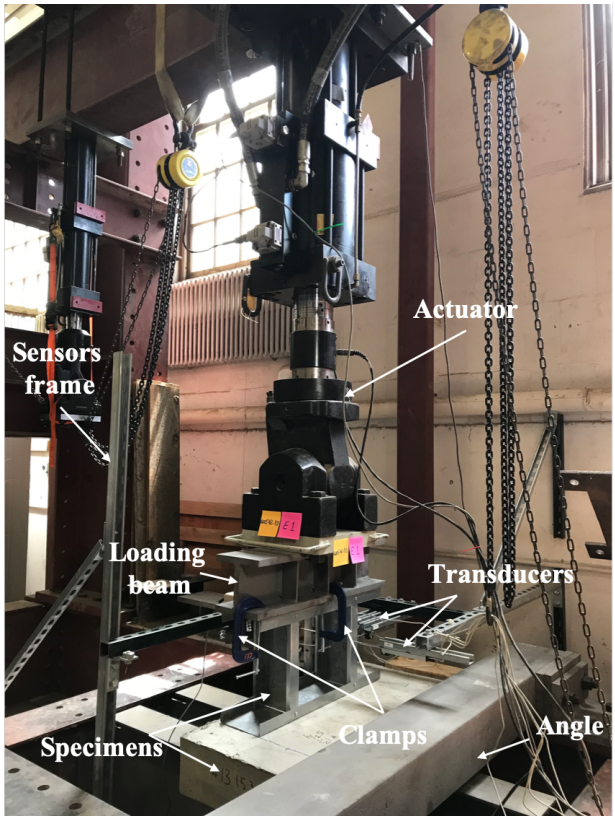


*Figure 19: Test setup of stud assembly-concrete slab experiments.*

## 2.3 Specimen preparation and fabrication

This section of the dissertation details the fabrication of the concrete slabs and stud-track systems. The concrete slabs were poured and the assemblies were fabricated at the Gunness Laboratory.

### 2.3.1 Concrete slabs

Prior to the concrete pour, wood forms were constructed. Treated lumber were used for the forms sides and plywood for their bottom. The size of ordered lumber was 5.08×20.32

cm × 3 m (2×8 in × 10 ft) and the size of plywood was 1.5×10.16 cm × 2.4 m (19/32 in ×4×8 ft). The dimension of the slabs was 55.88×86.36×15.24 cm (22×34×6 in) and the forms were fabricated to accommodate these internal dimensions. Figure 21 illustrates the formwork fabrication process, in which the sides were fastened together first, followed by the bottom.

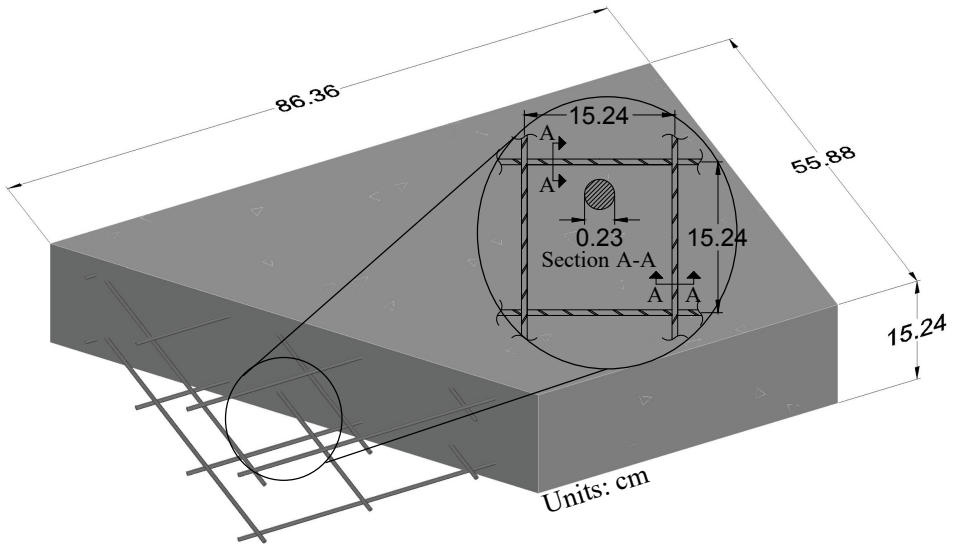


*Figure 20: Concrete slab and reinforcement mesh details.*

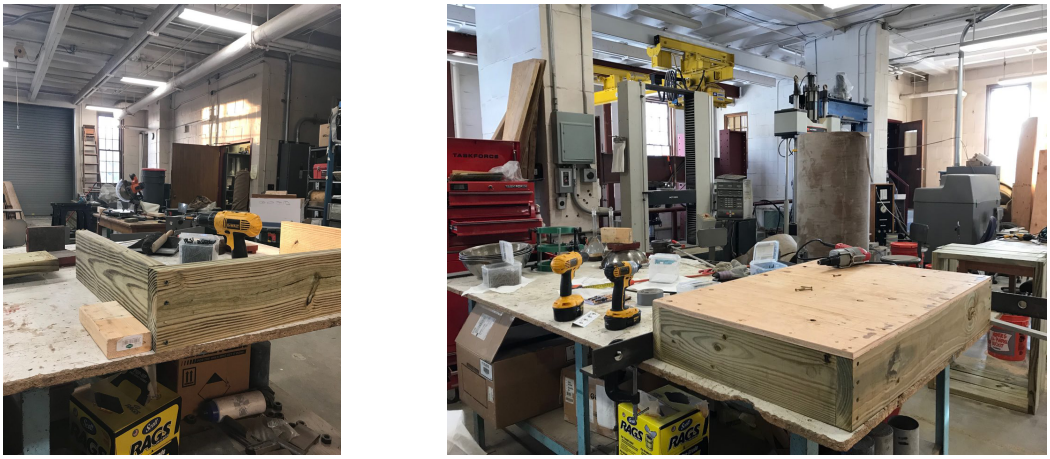

(a) (b)

*Figure 21: Building the concrete forms; (a) connecting the lumber, (b) connecting the plywood.*

After building the forms, wood sealant was utilized to seal the seams. In this project, two layers of mesh were used to reinforce the concrete. The mesh size was selected W4 15.24×15.24 cm (6×6 in) to meet ACI 318-14 [18] minimum requirements and they were shipped in sheets of 3×1.5 m (10×5 ft) in size, so they were cut to 50.8×81.3 cm (20×32 in) to ensure a 2.54 centimeter (1 inch) clear cover on each side (satisfying the minimum requirement of 1.9 cm (¾") specified in ACI 318-14 [18]). In order to provide the concrete clear cover at the top and bottom of the slabs, rebar spacers were ordered in two sizes: 9.5 and 1.9 cm (3-3/4 and 3/4 inch). The mesh and rebar spacers were tied together via rebar wires (Figure 22). Before placing the mesh inside the prepared forms, form release was applied twice (two weeks before pouring) to keep concrete from sticking to the form. Eighteen 15.24 by 30.48 cm (6 by 12 in) cylinder molds were filled with concrete as samples for measuring the tension and compression strength of the concrete.

(a)

(b)

*Figure 22: (a) Sealing the concrete forms, (b) Tying meshes and rebar spacers.*

Three cubic meters (Four cubic yards) of 27.6 MPa (4 ksi) winter concrete were ordered. Its mix design is summarized in Table 2. The slab forms were filled with concrete in two layers. They were consolidated by a concrete vibrator. Then, the top surface was finished by using magnesium floats to achieve a smooth surface (Figure 23).

*Table 2: Concrete mix design*

| **Sand** | **3/4" Trap** | **Cement type III** | **Slag** | **Water** | **Water reducer** | **Air 250** |
|---|---|---|---|---|---|---|
| *kg (Ib)* | *kg (Ib)* | *kg (Ib)* | *kg (Ib)* | *liter (gl)* | *oz* | *oz* |
| 2195 (4880) | 3438 (7580) | 886 (1955) | 297 (655) | 424 (112) | 86 | 14 |

* The amounts are for 3 cubic meters
** The sand and trap moisture were 4.5% and 0.5% respectively

The ACI 318-14 [18] water wet-curing method was used to cure the slabs. To achieve proper hydration at the concrete surface, the slabs were covered with soaked burlap. In order to prevent evaporation, the slabs were covered with plastic sheeting on top of the burlap for seven days. After 28 days, concrete forms were removed (Figure 23).


(a) (b)

*Figure 23: (a) Poured concrete slabs with finished surfaces, (b) A concrete slab after form removing.*

### 2.3.2 Specimen construction and attachment

The test specimens were built up stud-track assemblies with two studs, 30.48 cm (12 inches) long and 30.48 cm (12 inches) apart capped in horizontal tracks at the top and bottom (Figure 8(a)). In this research project, four cold-formed steel sections were examined, and tracks were selected such that their thickness matched the stud thickness (Table 3). Dimensions are show in Figure 8(a). Each stud specimen had a unique nomenclature illustrated in Figure 24. For the edge/overhang distances, the numbers “1”, “05”, and “0125” were used, which represents the distance to the edge of the slabs based on imperial measurements. For example, for a 1.27 cm (0.5 in) distance to the slab edge, “05” was appended to the nomenclature. Bearing condition designation in specimen nomenclature are tabulated in Figure 24.

*Table 3: Sections included in this study. Note that track sections are sized to correspond with the stud section*

| Stud | Track |
|---|---|
| 600S162-33 | 600T125-33 |
| 600S162-54 | 600T125-54 |
| 600S162-97 | 600T125-97 |
| 600S300-54 | 600T125-54 |

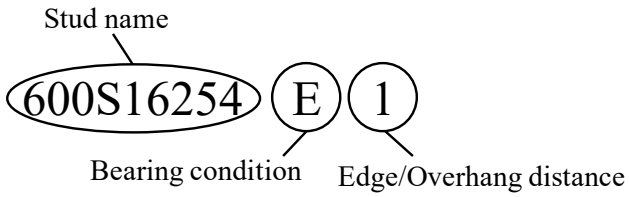


| Bearing Condition | Desination in nomenclature |
|---|---|
| Rigid | R |
| Full | F |
| Close to the edge | E |
| Overhang | O |

*Figure 24: Experimental nomenclature.*

Stud assemblies were fabricated on-site. As pictured in Figure 25, studs and tracks were cut to the desired length via circular saw. Stud and track sections were seated during fastening to ensure maximum possible gap closure between stud ends and track webs. The studs were connected to the track by eight screws, installed at the flange centerlines. Four at the top track and four at the bottom one. For 54 and 97-mil sections, self-drilling screw S-MD12-14×3/4 HWH3 (3/4 in. in length and 0.216 inch in diameter) was utilized, and for

33-mil sections Hilti drywall screw S-DD10-16×5/8 PPCH3 (5/8 in. in length and 0.19 inch in diameter) was utilized. First, the flanges of studs were fastened to the bottom track and then to the top track (Figure 26). A Hilti screw gun was utilized for screw fastening.

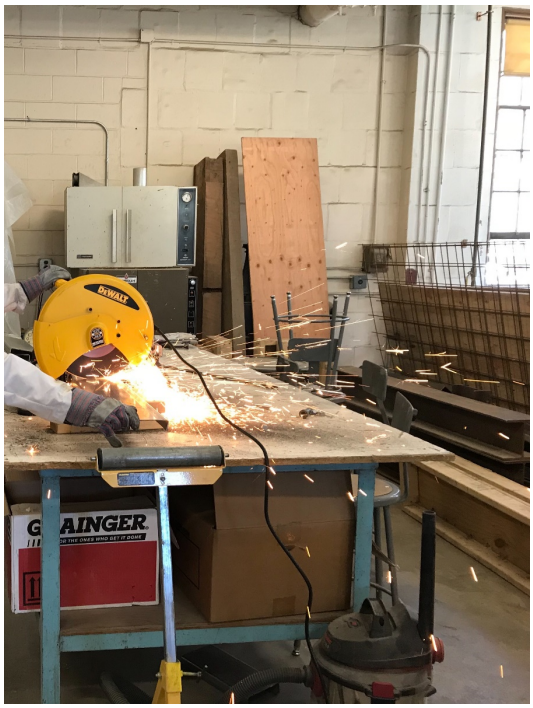


*Figure 25: Cutting the pieces by circle saw.*

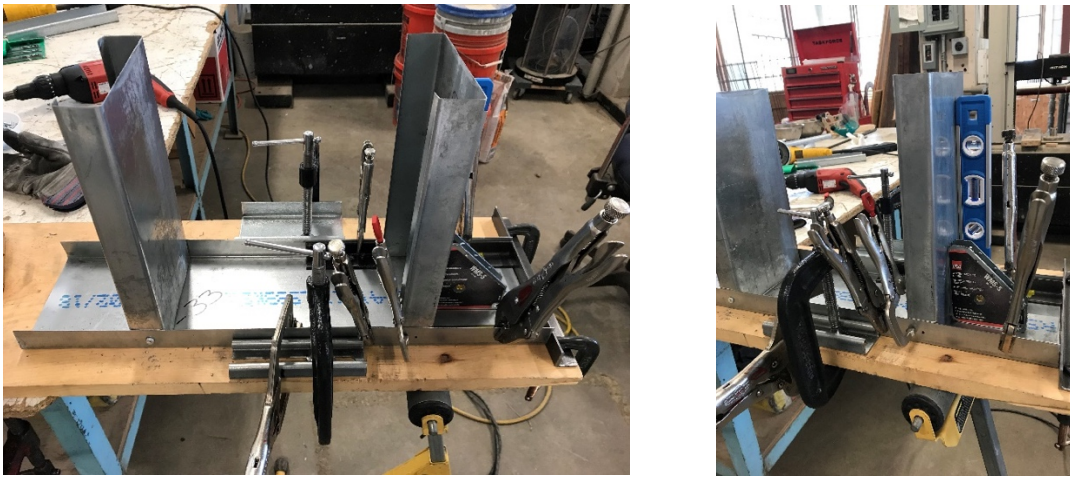

*Figure 26: Fabricating the stud-track assemblies.*

### 2.3.3 Attachment to concrete slabs

The stud-track systems were attached to concrete slabs by three single concrete powder-actuated fasteners (Hilti concrete nail X-P 27 P8 with 2.7 cm in length and 0.4 cm in diameter with plastic washers, which were installed 15.24 cm (6 in) apart. The flat surface of concrete slab was considered to be placed on the test rig, the cold-formed steel assembly was installed on the other side. A Hilti powder actuated tool was used for fastening single powder-actuated fasteners (Figure 27). The author and the lab technician were trained by Hilti representative to operate these tools and install the fasteners. Fasteners were installed by a team of three operators. First, according to the test conditions, the bottom track was placed precisely on its final location; then, it was fastened to the concrete slab via three fasteners. The remaining studs and track were then fastened once the slab-single track assembly was placed in the test rig (Figure 27). According to Hilti installation manuals [19], in order to prevent any breakout failure of the concrete slab, the

minimum edge distance of power-actuated fasteners is 7.6 cm (3 in). This minimum was provided by offsetting the fasteners from the centerline of tracks in overhang bearing conditions.

(a)

(b)

(c)

*Figure 27: Attaching cold-formed steel stud assemblies to concrete slabs; (a) fastening a bottom track to the concrete slab, (b) placing the concrete slab into the test rig with a three-ton crane, (c) fastening the stud assembly to the bottom track.*

## 2.4 Material characterization

In order to determine the tension and compression strength of the concrete, both tension and compression tests were performed. As, it is mentioned before, eighteen cylinder molds were filled with concrete as samples for the tests. The cylinders were sampled via the procedure outlined in ASTM C31M-18b [20]. In accordance to ASTM C31M-18b [20], the cylinder molds were filled in three equal layers, each layer was rodded 25 times with tamping rod. After 28 days, the cylinder molds were removed. Moreover, in accordance with ASTM C143M-15a [21], a slump test was done before each batch. The cylinders were loaded in a FX 500 Forney machine to failure with load rates 0.069 MPa/sec and 0.241 MPa/sec (10 psi/sec and 35 psi/sec) for tension and compression tests, respectively (Figure 28). The results of the tests are summarized in Table 4 and Table 5.

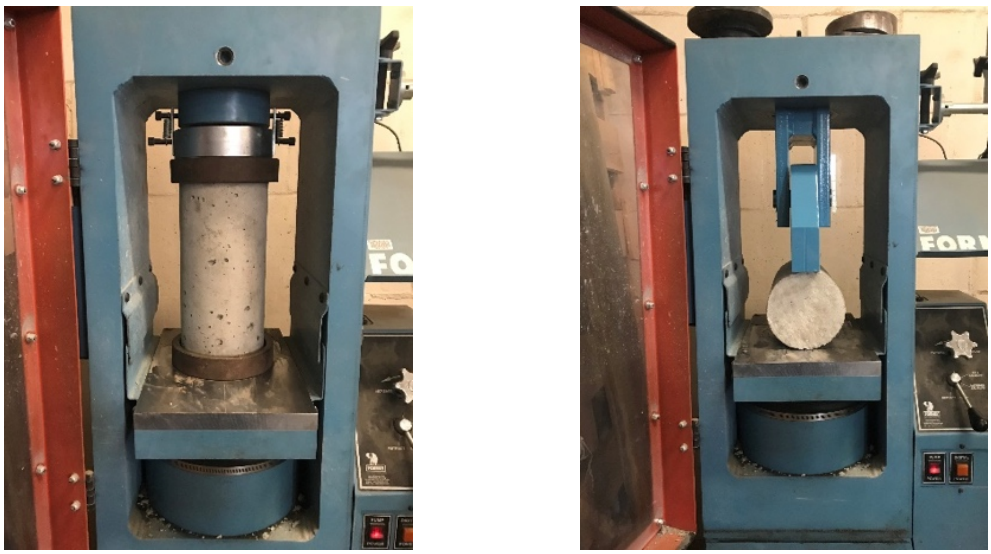

(a) (b)

*Figure 28: Concrete cylinder tests; (a) compression, (b) tension.*

*Table 4: Concrete cylinder compression test results.*

| | **Sample name** | **Failure load** *kN (kips)* | **Failure Stress** *MPa (ksi)* |
|---|---|---|---|
| Beginning of the batch (A) | 1A | 598.5 (134.6) | 32.8 (4.76) |
| | 4A | 599.1 (134.7) | 32.8 (4.76) |
| | 5A | 621.3 (139.7) | 34.1 (4.94) |
| Middle of the batch (B) | 9B | 622.2 (139.9) | 34.1 (4.95) |
| | 10B | 529.0 (118.9) | 29.0 (4.21) |
| | 12B | 610.5 (137.3) | 33.4 (4.85) |
| End of the batch (C) | 13C | 612.0 (137.6) | 33.6 (4.87) |
| | 15C | 634.6 (142.7) | 34.8 (5.05) |
| | 17C | 620.8 (139.6) | 34.1 (4.94) |
| | | **Mean** | 33.2 (4.81) |

*Table 5: Concrete cylinder tension test results.*

| | **Sample name** | **Failure load** *kN (kips)* | **Failure Stress** *MPa (ksi)* |
|---|---|---|---|
| Beginning of the batch (A) | 2A | 135.0 (30.4) | 1.8 (0.268) |
| | 3A | 155.1 (34.9) | 2.1 (0.308) |
| | 6A | 195.7 (44.0) | 2.7 (0.389) |
| Middle of the batch (B) | 7B | 199.2 (44.8) | 2.7 (0.396) |
| | 8B | 200.9 (45.2) | 2.8 (0.399) |
| | 11B | 155.8 (35.0) | 2.1 (0.310) |
| End of the batch (C) | 14C | 170.5 (38.3) | 2.3 (0.339) |
| | 16C | 151.2 (34.0) | 2.1 (0.300) |
| | 18C | 180.0 (40.5) | 2.5 (0.358) |
| | | **Mean** | 2.4 (0.341) |

To quantify the material properties of the CFS studs, tensile tests were performed for each steel thickness. The tensile coupons were cut from the webs and they were provided from the ends and the middle of specimens. The dimension of coupons shown in Figure 29 and the procedure of the tests were both in accordance with ASTM E8/E8M-16a [22]. The tests were conducted in a 50 kN (11.24 kip) capacity Instron universal testing machine

(Figure 30). The load and displacement were recorded by crosshead load cell and an extensometer with 5.08 cm (2 inch) gage length. In the beginning of the test, since the deflections were small, a load rate of 0.127 mm/min (0.005 in/min) was used; however, when the deflection of coupon specimens reached to 2.29 mm (0.09 inch), the load rate was increased to 1.27 mm/min (0.05 in/min). Then, yield stresses were determined via the 0.2% offset method. The tensile test results are summarized in Table 6. In the test names, A is the name of the stud member from that the coupons were cut, and M and E represent the location of the coupons (M=middle, E=end).

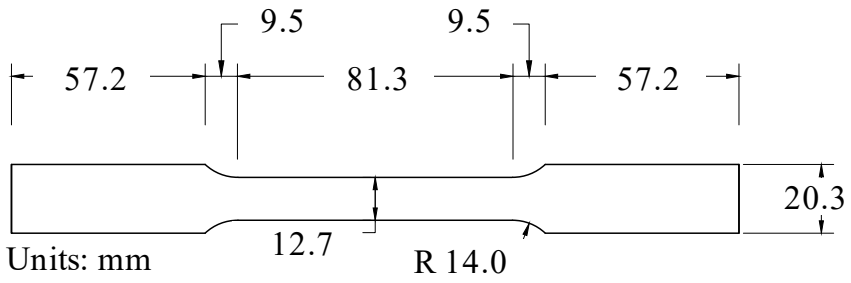


*Figure 29: ASTM E8/E8M-16a tensile coupon dimension (all the units are millimeters).*

*Figure 30: Tensile test rig setup and specimen orientation, with extensometer installed.*

*Table 6: Tensile coupon test results.*

| **Test name** | **Coupon specimen** | **Base metal thickness** $t$ *mm (in)* | **Yield stress** $F_y$ *MPa (ksi)* | **Ultimate strength** $F_u$ *MPa (ksi)* | **Strain at ultimate** $\varepsilon_u$ *mm/mm* |
|---|---|---|---|---|---|
| 33AM-1 | 600S162-33 | 0.91 (0.036) | 617.1 (89.5) | 669.5 (97.1) | 0.065 |
| 33AE1-1 | 600S162-33 | 0.93 (0.037) | 610.9 (88.6) | 661.2 (95.9) | 0.074 |
| 33AE2-1 | 600S162-33 | 0.90 (0.035) | 630.9 (91.5) | 686.7 (99.6) | 0.071 |
| 54AM-1 | 600S162-54 | 1.52 (0.060) | 318.5 (46.2) | 455.1 (66.0) | 0.174 |
| 54AE1-1 | 600S162-54 | 1.52 (0.060) | 315.8 (45.8) | 448.8 (65.1) | 0.177 |
| 54AE2-1 | 600S162-54 | 1.52 (0.060) | 326.8 (47.4) | 464.0 (67.3) | 0.174 |
| 97AM-1 | 600S162-97 | 0.101 (2.57) | 361.3 (52.4) | 493.0 (71.5) | 0.178 |
| 97AE1-1 | 600S162-97 | 0.101 (2.57) | 359.2 (52.1) | 490.2 (71.1) | 0.174 |
| 97AE2-1 | 600S162-97 | 0.101 (2.57) | 360.6 (52.3) | 493.7 (71.6) | 0.171 |

While the measured tensile strength of the 0.84 mm (33-mil) specimens is significantly higher than the nominal tensile strength, 10 repetitions on three different experimental setups at UMass Amherst were conducted to confirm this discrepancy. All repetitions

yielded the same, repeatable results. Furthermore, industry representatives were solicited for advice, and confirmed that these high tensile strength values in thinner steels can occur. The lower elongation is also notable in the 0.84 mm (33-mil) steel. The engineering stress-strain curves of three repetitions for each thickness is illustrated in Figure 31.The average of strength of all the materials used in this research project are summarized in Table 7. This table includes both nominal and measured strengths. More information can be found in Appendix A.

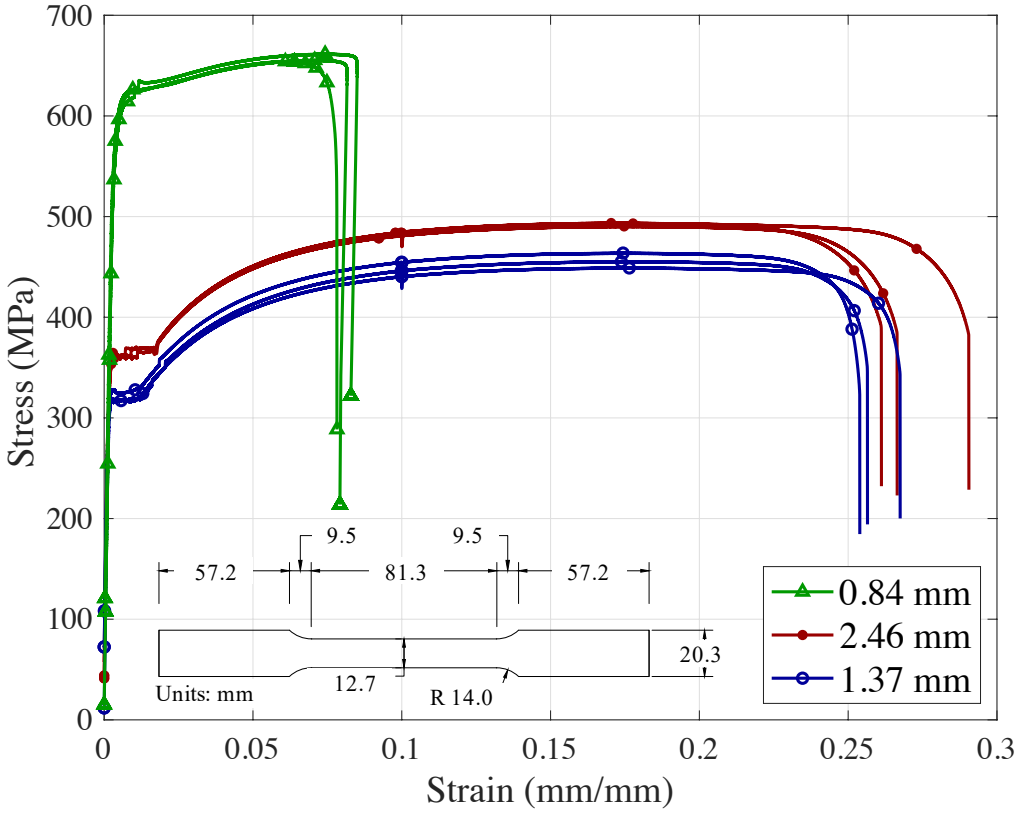


*Figure 31: Examples of stress vs. strain relations from tensile tests on coupon cut from different thickness.*

*Table 7: Summary of material properties, averaged across repetitions*

| | **Tensile strength** *MPa (ksi)* | | **Compressive strength** *MPa (ksi)* | | **Percentage elongation** *%* |
|---|---|---|---|---|---|
| | Nominal | Measured | Nominal | Measured | |
| CFS ($F_y$) | | | | | |
| 0.84 mm | 345 (50) | 619.6 (89.9) | — | — | 8.0 |
| 1.37 mm | 345 (50) | 320.4 (46.5) | — | — | 25.9 |
| 2.46 mm | 345 (50) | 360.4 (52.3) | — | — | 27.3 |
| Concrete | — | 2.3 (0.3) | 27.6 (4) | 33.2 (4.8) | — |
| Rebar mesh ($F_y$) | 275.8 (40) | — | — | — | — |

## 2.5 Placing the specimens and load application

The stud-track assemblies were clamped to the rigid beam (for without concrete slab tests) and to the built-up loading beam using C-clamps (Figure 32). These clamps were adequate for pure axial load case as the load was concentric, and no out of plane forces existed. After placing the specimens, load was monotonically applied via displacement control (0.254 mm/min [0.01in/min]) until failure and then continued to approximately 50% of the peak load.

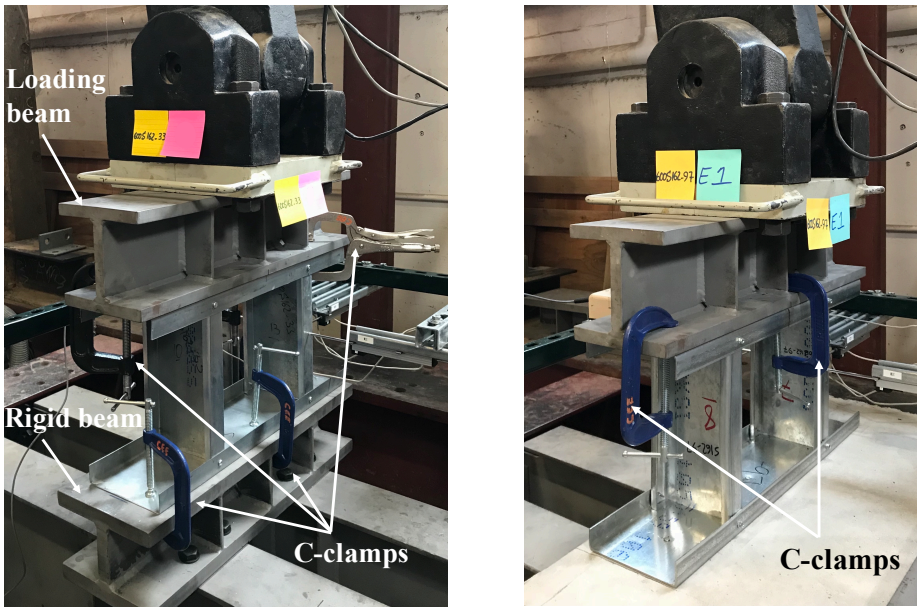


(a) (b)

*Figure 32: (a) Clamping the stud-track system to the rigid beam and the beam installed under the actuator; (b) clamping the stud assembly to the actuator beam.*

## 2.6 Experimental performance of stud assemblies

In total, 27 tests were performed; force and displacement were recorded, and the system stiffness was calculated for each test. Results are aggregated by stud thickness and section profile. The force-displacement curves of the 0.84 mm (33-mil) stud assembly tests are illustrated in Figure 33, which demonstrates the impact of bearing condition on the compressive strength and the stiffness of the stud assemblies. Peak loads ($P_{max}$), displacement ($\Delta$ at $P_{max}$), and the stiffness results ($k_i$) for stud wall assemblies are tabulated in Table 8. The displacement of the system was taken directly from the actuator. Flexibility in the test rig was not significant but was subtracted from the displacement results to isolate

the stiffness of the assembly. Stiffness was determined by finding the slope of the load-displacement curve between $0.4P_{max}$ and $0.6P_{max}$ to avoid seating loads.

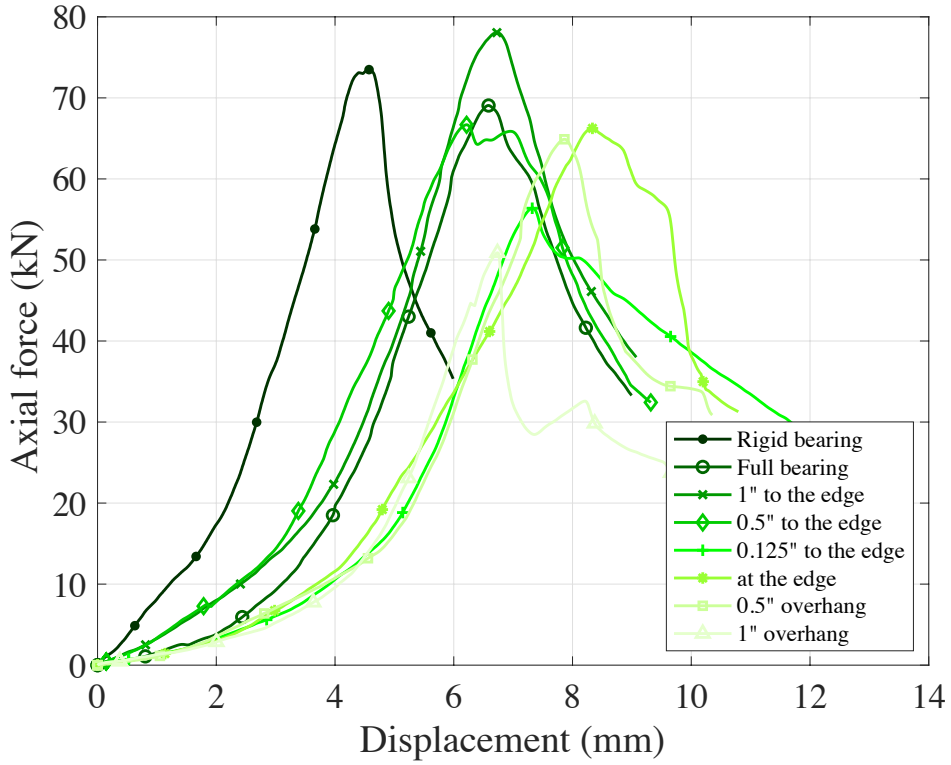


*Figure 33: Force-displacement curves for 0.84 mm (33-mil) stud assemblies.*

The axial capacities of the assemblies under both rigid and full (center of slab) bearing conditions were close, and the rigid bearing condition had the highest peak load. It indicates when the stud-track assembly was far from the concrete slab edge, in this case 20.32 cm (8 inches), the slab was near rigid and provided a uniform stress distribution for the studs. While there was a 6% difference between the two conditions, these results were variable, as further indicated by the high load (78.1 kN) attained by the 600S16233E1 specimen.

However, as the assembly was moved closer to the edge and even outside the edge, the impact of bearing condition was more significant, and the concrete slab acted as a flexible support causing a non-uniform stress distribution. This impact ranged between a 10% and 23% reduction for these specimens. Moreover, the non-uniform stress distribution was detrimental to the system stiffness as well. Overhanging specimens suffered significant capacity losses due to the combined effect of the reduced stud section (smaller bearing area) and the induced eccentricity resulting in bending moment on the stud.

Three sample images from different conditions under the peak load are shown in Figure 34. The studs buckled post-peak. Though the buckling mode was indistinct from visual observations alone, finite strip analyses, high-fidelity finite element analyses, and sensor data confirmed that the studs buckled in a combination of local and distortional buckling.


(a) (b) (c)

*Figure 34: Deformed 0.84 mm (33-mil) studs under the peak load; (a) rigid bearing, (b) 3.175 mm (0.125 inch) to the edge, (c) 12.7 mm (0.5 inch) overhang.*

The results of 1.37 mm (54-mil) tests are summarized in Table 8, and the load-displacement curves are plotted in Figure 35 and Figure 36 for the 4.11 cm (1.625 inches) flange specimens and the 7.62 cm (3 inches) flange specimens, respectively.

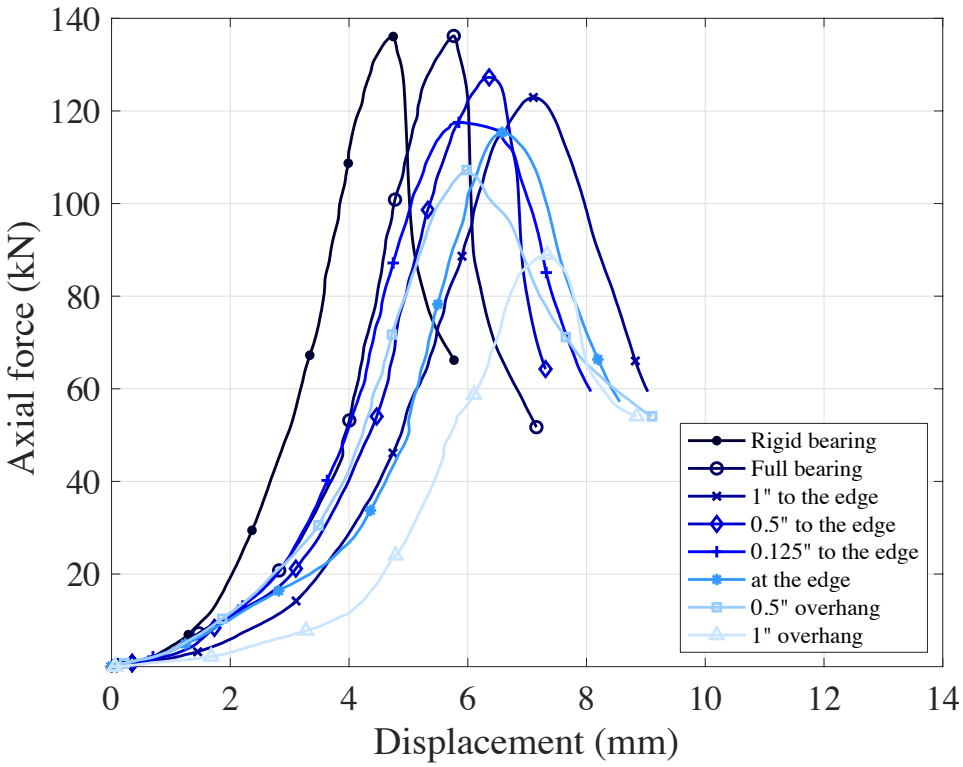


*Figure 35: Force-displacement curves for 1.37 mm (54-mil) stud assemblies.*

Similar to the 0.84 mm tests, the results demonstrate that the non-uniform stress distribution is detrimental to the system axial capacity and the stiffness. However, the impact of non-uniform stress distribution was more severe in 54-mil stud assemblies. For instance, in the 2.54 cm (1-inch) from the slab edge bearing condition, the axial capacity was reduced by 10%, but when the assembly was located at the edge, it was decreased 15%. In the overhang bearing conditions, for the 600S162-54 assemblies, in 2.54 cm (1-inch) overhang, it was reduced 35% in comparison with rigid end support. This phenomenon was further validated when the flange length was increased from 4.11 cm to

7.62 cm (1.62 inches to 3 inches). Photographs at peak loads for the 1.37 mm (54-mil) assembles are shown in Figure 37 below.

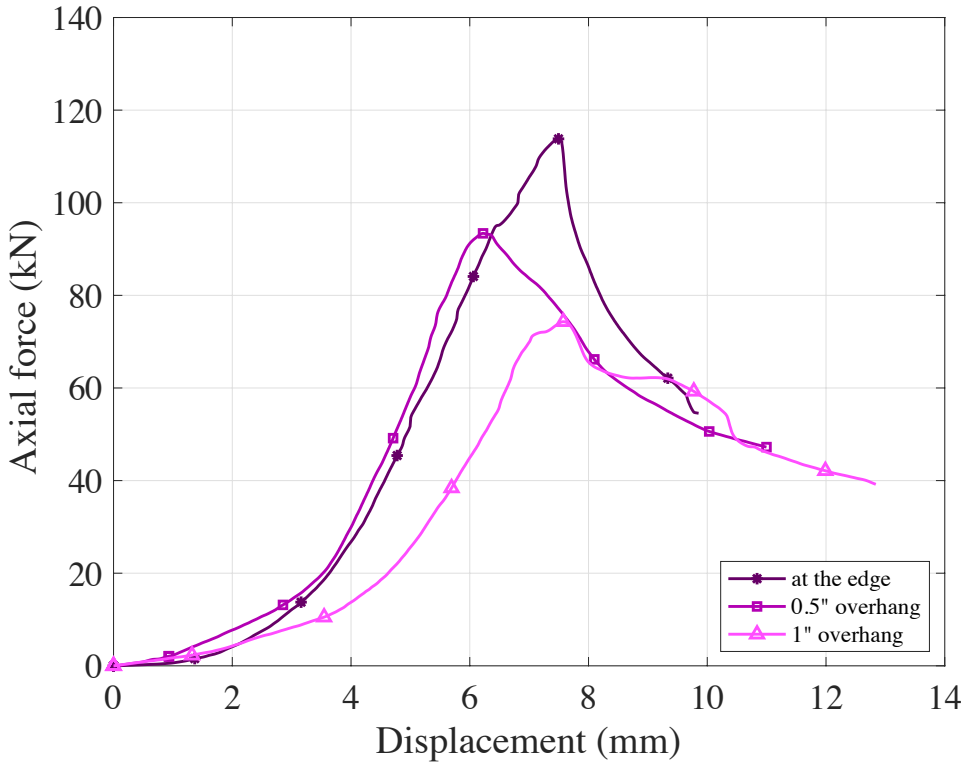


*Figure 36: Force-displacement curves for 1.37 mm (54-mil) stud assemblies with wide flange.*


(a) (b) (c)

*Figure 37: Deformed 1.37 mm (54-mil) studs under the peak load; (a) rigid bearing, (b) at the edge, (c) 25.4 mm (one inch) overhang.*

The results of the 2.46 mm (97-mil) specimen are summarized in Table 8 and Figure 38. In these experiments, the reduction in the axial capacity was more significant as the assemblies get closer to the edge. The peak load was decreased almost 15% when the assembly was located 25.4 mm (1 inch) to the edge of concrete slab, and it was reduced by 24% when it was located at the edge. In the thickest specimens, the reduction in axial capacity in overhang bearing conditions was as high as 40%. The behavior of these assemblies under the peak load is demonstrated in Figure 39. Furthermore, the results show that the non-uniform stress distribution was detrimental to the system stiffness as well, reductions up to 72% observed for 2.46 mm specimens. In 0.84 mm and 2.46 mm assemblies, axial capacity dramatically decreased from the rigid bearing condition

capacities when the assemblies were located near the edge of concrete slab, as shown in Figure 33 and Figure 38. While no phenomena were observed to cause these lower experimental strengths, the decreased capacity was attributed to end condition sensitivity of the studs to localized geometric variation in the concrete slabs.

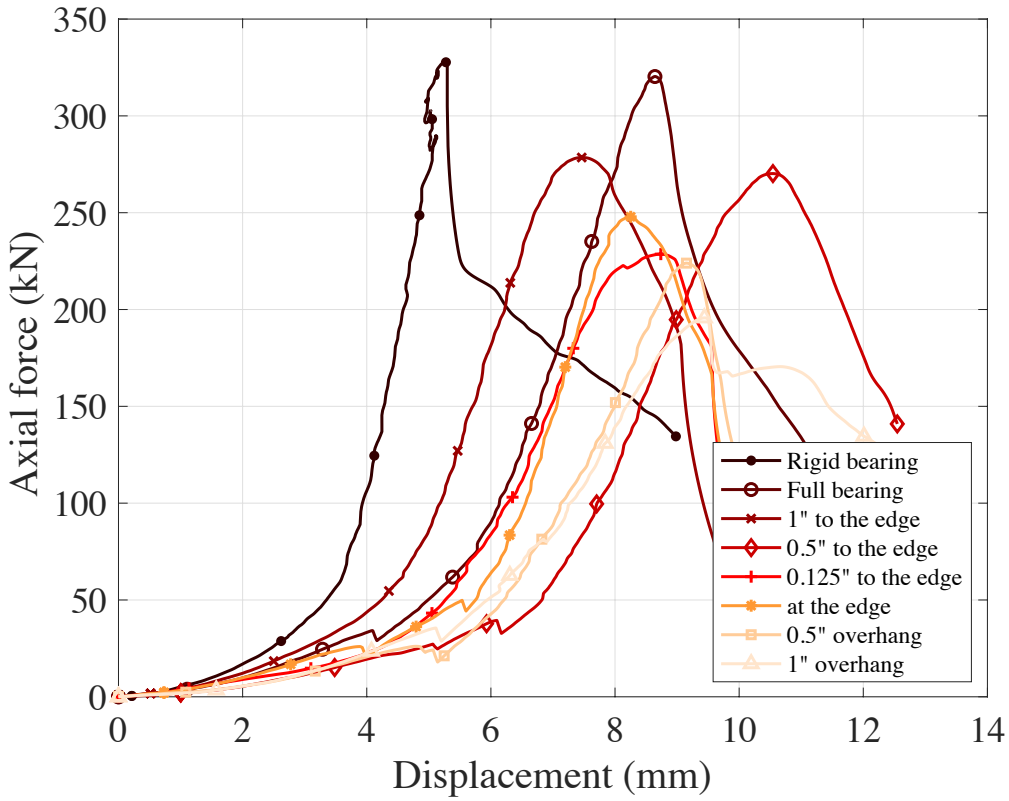


*Figure 38: Force-displacement curves for 2.46 mm (97-mil) stud assemblies.*

(a) (b) (c)

*Figure 39: Deformed 2.46 mm (97-mil) studs under the peak load; (a) rigid bearing, (b) at the edge, (c) 25.4 mm (one-inch overhang).*

Generally, as the stud assemblies approach the edge of the slab, they experience strength and stiffness erosion. Once they begin to overhang, this becomes significant. The force-displacement responses of the assemblies are characterized by two initial regimes (Figure 33, Figure 35, Figure 36, and Figure 38) leading to peak force, at which time the specimens buckled. Since there were small gaps (within allowable tolerances) between studs ends and tracks, the low initial stiffness was due to the stiffness of the screws until the gap was closed. The initial stiffnesses of the assemblies with rigid bearing condition were higher than the assemblies bearing on concrete slabs, because the slab roughness created additional gaps in the assembly. After these gaps were closed, the stiffnesses in the second regime were similar across specimens.

*Table 8: Summary of the results of experiments.*

| **Test Name** | **Experiment** | | | |
|---|---|---|---|---|
| | **$P_{max}$** | **$\triangle$ at $P_{max}$** | **$k_i$** | **$1-P_{max}/P_{max\_r}$** |
| | *kN* | *mm* | *kN/mm* | *%* |
| 600S16233R | 73.6 | 4.58 | 28 | - |
| 600S16233F | 69.2 | 6.56 | 23 | 6% |
| 600S16233E1 | 78.1 | 6.68 | 28 | -6% |
| 600S16233E05 | 66.8 | 6.20 | 20 | 9% |
| 600S16233E0125 | 56.5 | 7.32 | 20 | 23% |
| 600S16233E | 66.3 | 8.34 | 14 | 10% |
| 600S16233O05 | 65.0 | 7.86 | 21 | 12% |
| 600S16233O1 | 51.0 | 6.74 | 21 | 31% |
| 600S16254R | 136.3 | 4.72 | 72 | - |
| 600S16254F | 136.4 | 5.72 | 67 | - |
| 600S16254E1 | 123.1 | 7.06 | 44 | 10% |
| 600S16254E05 | 127.4 | 6.27 | 49 | 7% |
| 600S16254E0125 | 117.6 | 5.79 | 50 | 14% |
| 600S16254E | 115.5 | 6.53 | 51 | 15% |
| 600S16254O05 | 107.5 | 5.94 | 40 | 21% |
| 600S16254O1 | 89.1 | 7.29 | 34 | 35% |
| 600S30054E | 114.0 | 7.44 | 31 | - |
| 600S30054O05 | 93.6 | 6.25 | 35 | - |
| 600S30054O1 | 74.4 | 7.54 | 21 | - |
| 600S16297R | 327.8 | 4.92 | 225 | - |
| 600S16297F | 320.6 | 8.51 | 111 | 2% |
| 600S16297E1 | 278.6 | 7.34 | 104 | 15% |
| 600S16297E05 | 270.4 | 10.40 | 79 | 18% |
| 600S16297E0125 | 228.7 | 8.60 | 83 | 30% |
| 600S16297E | 248.1 | 8.12 | 119 | 24% |
| 600S16297O05 | 224.2 | 9.05 | 68 | 32% |
| 600S16297O1 | 195.8 | 9.35 | 62 | 40% |

A critical factor impacting the axial strength of 2.46 mm assemblies was failure of the screws. In the thinner specimens, i.e. 0.84 and 1.37 mm, the screws only tilted. However, in the 2.46 mm specimens, some of the screws failed before gap closure (which is common in thicker assemblies [6]), where the steel ply was sufficiently strong in bearing to force failure into the screw. In all of the 2.46 mm conditions except rigid and full bearing conditions, there were shear failures of the screws, notably in the screws nearest to the slab edge. The impact of screw failure on the load-displacement curves and peak load manifest itself in force drop around 6 mm of displacement in Figure 40.

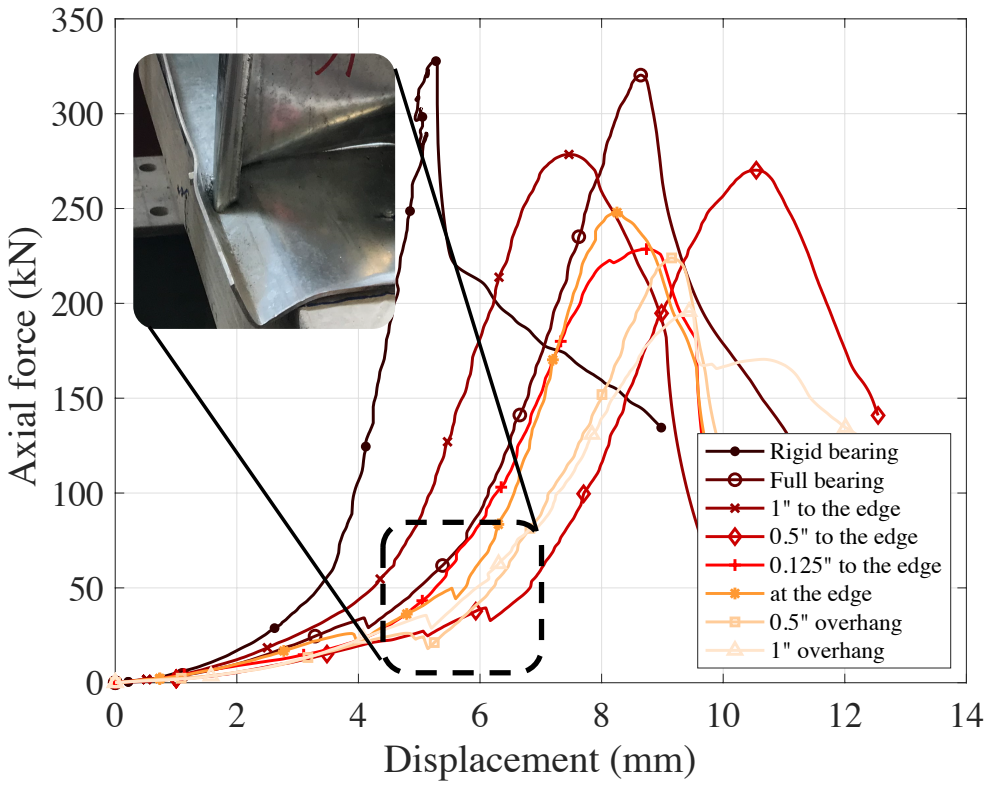


*Figure 40: Screw failure in 2.46 mm (97-mil) assemblies and its impact on the load-displacement curves.*

Figure 41 illustrates the percent reduction of the axial capacity compared to the rigid bearing condition. The results indicate when the stud-track assemblies were far from the concrete slab edge, in this case 20.3 cm (8 in), the slab was near rigid and provided a uniform stress distribution for the studs. However, as the assemblies were moved closer to the edge and even outside the edge, the impact of the bearing condition on the axial strength of the systems was more significant, and the concrete slab acted as a flexible support causing a non-uniform stress distribution. This impact ranged between 6% and 35% reduction in axial capacities for 0.84 mm (33-mil) and 1.37 mm (54-mil) specimens. This phenomenon was further observed when the flange length was increased from 4.11 to 7.62 cm in 1.37 mm (54-mil) stud-track assemblies. Finally, for the thickest members, the 2.46 mm (97-mil) specimens, the reduction ranged between 15% and 40%.

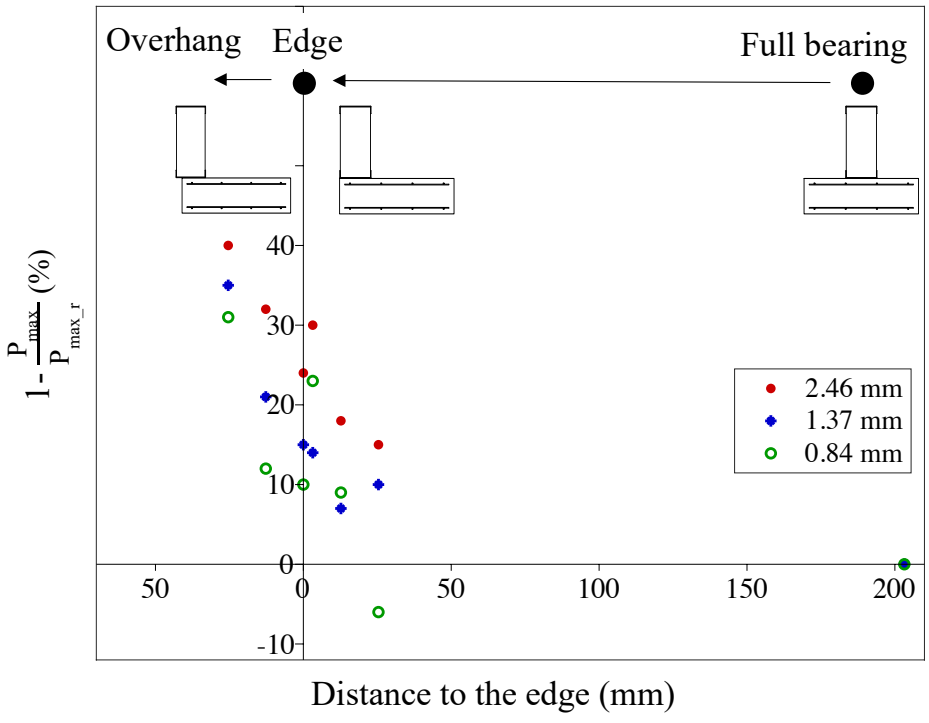


*Figure 41: Relationship between stud thickness and reduction in compressive strength.*

Three sample images for each cross-section and from different bearing conditions under the peak load are shown in Figure 42. The studs buckled post-peak; the buckling modes were indistinct from visual observations alone. Finite strip analysis ([14,15]) and sensor data were required to discern the buckling mode for each assembly. Displacement sensors installed on the web and flanges were used to characterize the cross-section deformed shapes, as shown in Figure 42. Sensor locations, as shown by markers, are used to estimate via interpolation the shape of the entire cross-section. In general, the studs buckled in combined local and distortional modes, though the participation of each mode was dependent on the stud geometry (Figure 42).

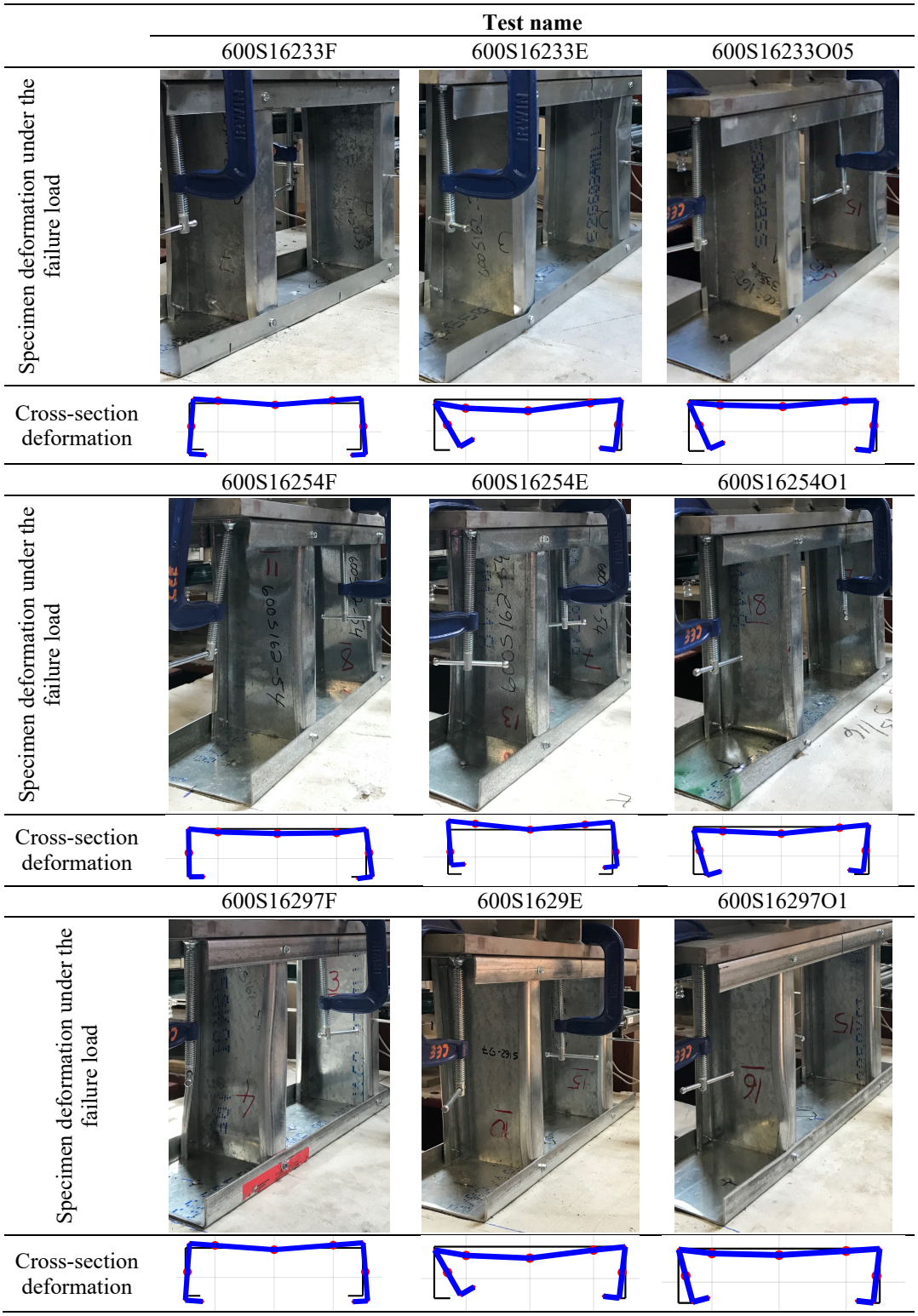


*Figure 42: Buckled shapes for representative test specimens, with cross-section deformations as measured by displacement sensors.*

Generally, the slabs did not exhibit spalling or cracking in a vast majority of the tests, excluding the tests 600S16233E, 600S16254E, 600S16297E, 600S16297O05, and 600S16297O1. The concrete cracked at all stud thicknesses when the assemblies were located at the edge of the slab. The 2.46 mm (97-mil) specimens overhanging from the slab also exhibited cracks emanating from the loaded corner of the slab. The higher buckling capacity of the 2.46 mm (97-mil) studs resulted in a direct load path to the slab before the failure. Damage to the slab is shown in Figure 43 below. Note that the photographs were taken well post peak when the applied load had dropped to 50% of the peak value. The author observed that the cracks in slabs first appeared at or around peak load. More detail regarding the experimental program can be found in the research report [23] published by the author.

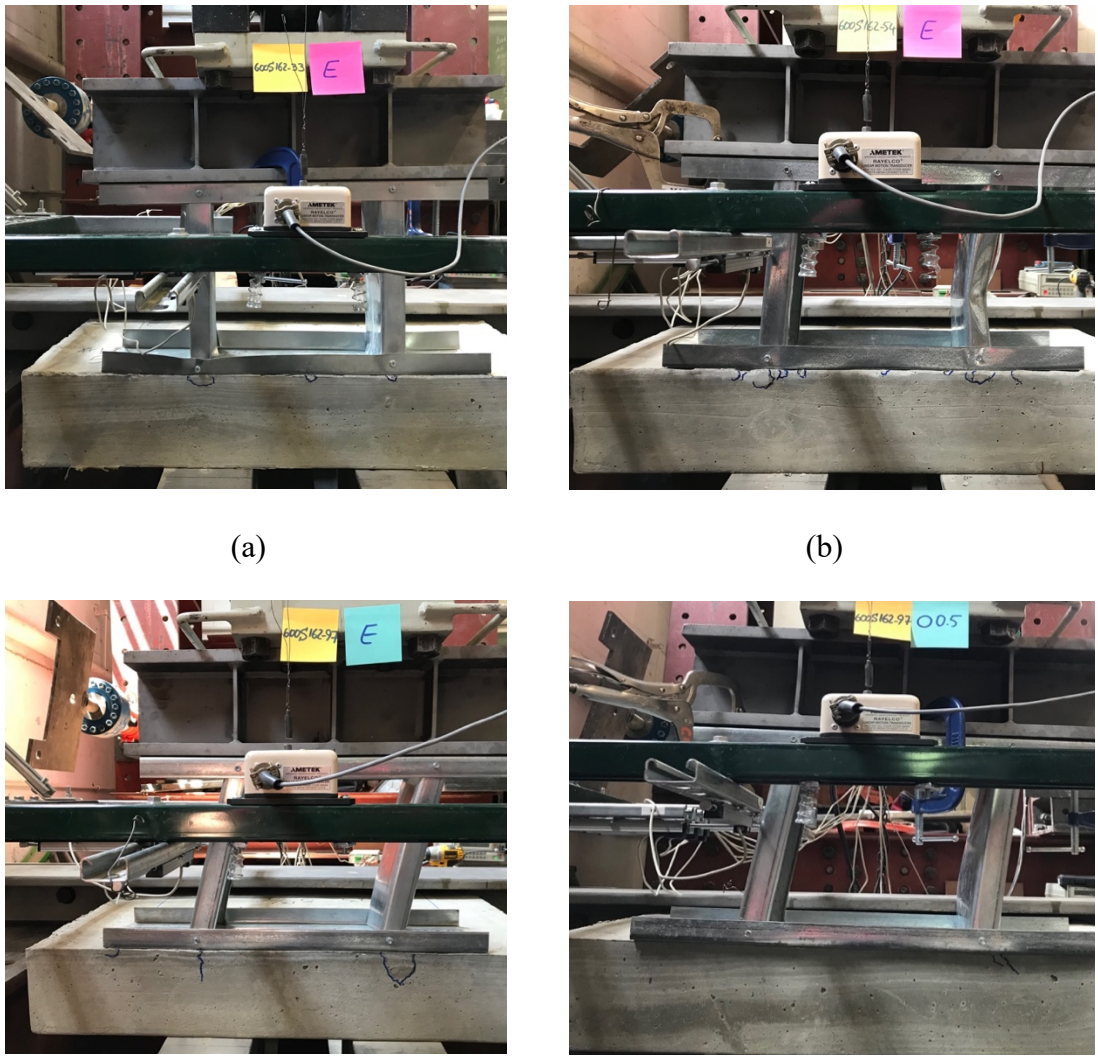


(a) (b)

(c) (d)

*Figure 43: Concrete slab spalling or cracking; (a) 600S16233E, (b) 600S16254E, (c) 600S16297E, (d) 600S16297O05.*

# CHAPTER 3

# Validation of Experimental Results and Development of High-Fidelity Finite Element Models

In this chapter, experimental results from Chapter 2 are validated via finite strip analysis, element Direct Strength Method (AISI S100-16), and high-fidelity finite element modeling. To fully-capture observed experimental behavior, it was necessary to create a high-fidelity finite element model to validate the experimental results and elucidate the impact of parameters not captured during the tests. Model development is described herein.

## 3.1 Finite strip analysis

As a preliminary comparison between the experimental and computational results, the tested cross-sections are modeled in CUFSM [14,15] to conduct an elastic buckling analysis via the finite strip method [14,15]. CUFSM provides a means of characterizing the buckling response of the stud assemblies and generates the signature curve for a given cross-section, which provides a "snapshot" of the elastic buckling strength and mode as they vary with member half-wavelength. Signature curves [24], as their name indicates, are unique for each cross section. Generating a signature curve involves first modeling the cross-section and discretizing it into nodes and elements. CFS members are not perfect and their dimensions and material properties can vary significantly from nominal properties and may impact the strength of members [25,26], so for modeling the sections, measured material and cross-section properties were used when available. For 0.84, 1.37, and 2.46

mm (33, 54, and 97-mil) members with 4.11 cm (1.625 in flanges), 37 nodes and 36 elements were used. And for the 7.62 cm (3 inches) flange cross-sections, 39 nodes and 38 elements were used. Simple-simple (pin-ended) supports were assumed for the boundary conditions, as required for an elastic buckling analysis. For all bearing conditions except the overhangs, it was assumed they all have the same hypothetical uniform stress distribution on the stud ends since they were placed on either a concrete slab or a rigid beam. This assumption implies that the entirety of the cross section is effective at carrying the axial load. While this was likely a poor assumption based on the experimental observations it was nonetheless a reflection of current design specifications [26,27]. However, the reduced sections (portion of cross section which directly bears on slab) were modeled for overhang conditions (Figure 44). Signature curves of modeled 600S162-54 in CUFSM software with full bearing, 1.27 cm (0.5 in) overhang, and 2.54 cm (1 in) overhang conditions are plotted in Figure 45. In this plot, the buckled shapes at the 30.5 cm (12 in) height for each case is illustrated as well.

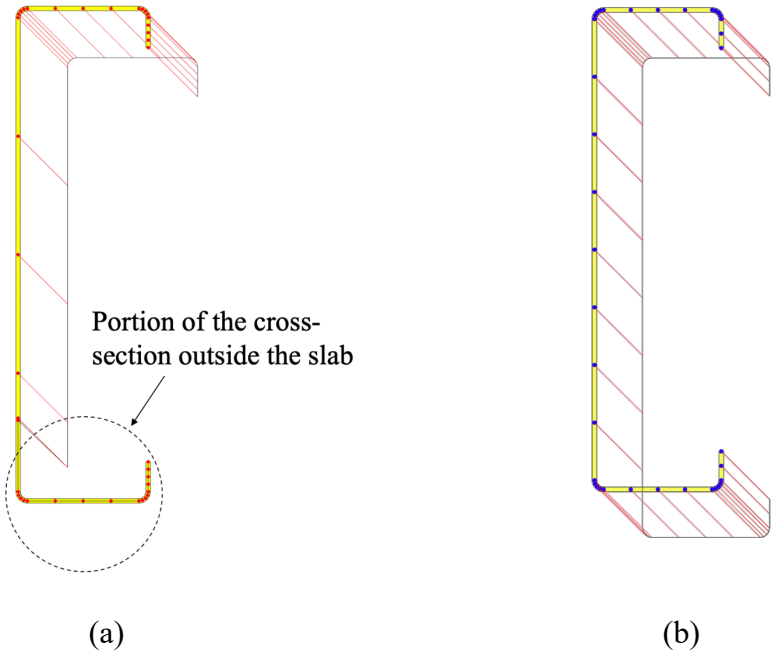


*Figure 44 : Modeled 600S162-54 section in CUFSM tool with (a) 2.54 cm (1 in) overhang, with non-uniformly applied stress shown on cross-section, (b) full bearing condition and uniform stress distribution.*

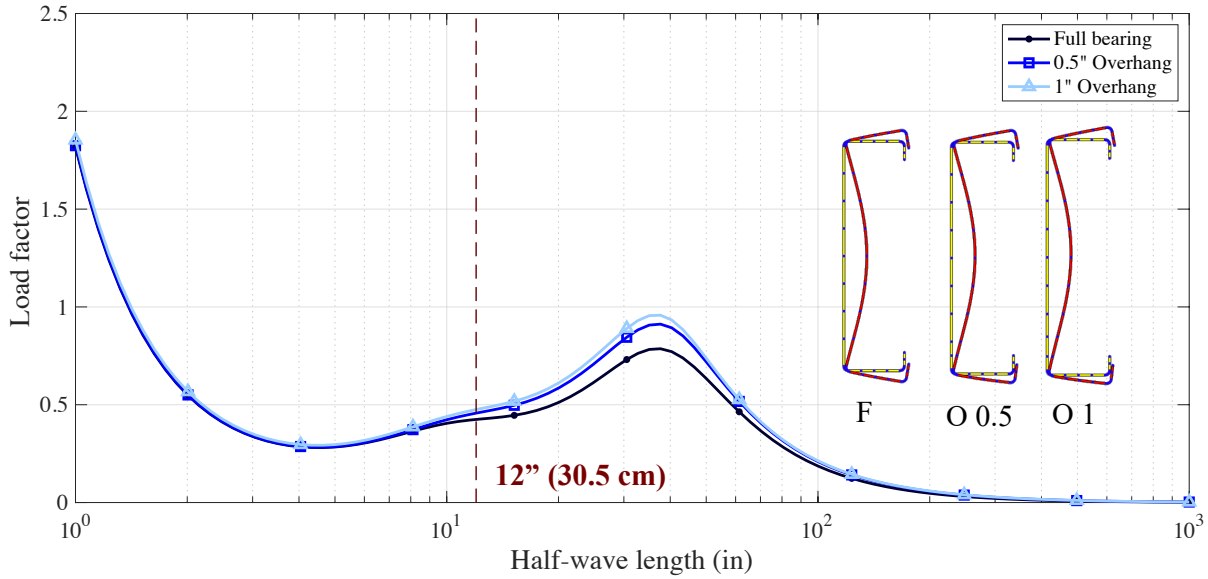


*Figure 45: Signature curves of modeled 600S162-54 with three different bearing conditions and their buckled shape at the 30.5 cm (12 in) height.*

Axial capacities calculated by finite strip analysis are tabulated and compared with experimental results in Table 9. In this table, participation of each buckling mode, determined from a finite strip analysis, is presented. The modal participation plot of 600S162-54 stud with uniform applied stress is illustrated in Figure 46. The buckling load for all of the conditions is a combination of local and distortional buckling though the dominance of distortional buckling is evident. These buckling strengths do not match the axial capacities of the wall assembly from the tests but serve as a useful performance indicator that can be used in design.

*Table 9: Comparing tests results with predicted axial strength by finite strip analysis.*

| **Test Name** | **Bearing Condition** | **$P_{max}$** | **CUFSM** | **Buckling mode** | |
|---|---|---|---|---|---|
| | | | | Local | Distortional |
| | | *kN (kips)* | *kN (kips)* | *%* | *%* |
| 600S16233F | Rigid | 73.6 (16.55) | 39.3 (8.83) | 26.9 | 71.3 |
| 600S16233C | Full bearing | 69.2 (15.55) | 39.3 (8.83) | 26.9 | 71.3 |
| 600S16233E1 | 1" to edge | 78.1 (17.56) | 39.3 (8.83) | 26.9 | 71.3 |
| 600S16233E05 | 0.5" to edge | 66.8 (15.01) | 39.3 (8.83) | 26.9 | 71.3 |
| 600S16233E0125 | 0.125" to edge | 56.5 (12.70) | 39.3 (8.83) | 26.9 | 71.3 |
| 600S16233E | at the edge | 66.3 (14.91) | 39.3 (8.83) | 26.9 | 71.3 |
| 600S16233O05 | 0.5" overhang | 65.0 (14.62) | 30.2 (6.79) | 28.1 | 70.0 |
| 600S16233O1 | 1" overhang | 51.0 (11.47) | 28.6 (6.44) | 30.0 | 68.3 |
| 600S16254F | Rigid | 136.3 (30.64) | 113.1 (25.43) | 13.7 | 83.4 |
| 600S16254C | Full bearing | 136.4 (30.66) | 113.1 (25.43) | 13.7 | 83.4 |
| 600S16254E1 | 1" to edge | 123.1 (27.67) | 113.1 (25.43) | 13.7 | 83.4 |
| 600S16254E05 | 0.5" to edge | 127.3 (28.63) | 113.1 (25.43) | 13.7 | 83.4 |
| 600S16254E0125 | 0.125" to edge | 117.6 (26.44) | 113.1 (25.43) | 13.7 | 83.4 |
| 600S16254E | at the edge | 115.5 (25.97) | 113.1 (25.43) | 13.7 | 83.4 |
| 600S16254O05 | 0.5" overhang | 107.5 (24.17) | 91.1 (20.48) | 15.3 | 81.7 |
| 600S16254O1 | 1" overhang | 89.1 (20.03) | 85.9 (19.31) | 16.5 | 80.6 |
| 600S30054E | at the edge | 113.9 (25.62) | 152.2 (34.21) | 23.3 | 75.3 |
| 600S30054O05 | 0.5" overhang | 93.7 (21.05) | 109.4 (24.59) | 25.7 | 73.2 |
| 600S30054O1 | 1" overhang | 74.4 (16.73) | 103.3 (23.23) | 27.5 | 71.5 |
| 600S16297F | Rigid | 327.8 (73.69) | 430.8 (96.84) | 6.0 | 88.2 |
| 600S16297C | Full bearing | 320.6 (72.07) | 430.8 (96.84) | 6.0 | 88.2 |
| 600S16297E1 | 1" to edge | 278.6 (62.63) | 430.8 (96.84) | 6.0 | 88.2 |
| 600S16297E05 | 0.5" to edge | 270.4 (60.79) | 430.8 (96.84) | 6.0 | 88.2 |
| 600S16297E0125 | 0.125" to edge | 228.7 (51.42) | 430.8 (96.84) | 6.0 | 88.2 |
| 600S16297E | at the edge | 248.1 (55.77) | 430.8 (96.84) | 6.0 | 88.2 |
| 600S16297O05 | 0.5" overhang | 224.2 (50.39) | 355.1 (79.83) | 6.0 | 86.7 |
| 600S16297O1 | 1" overhang | 195.8 (44.02) | 307.6 (69.16) | 7.7 | 86.3 |

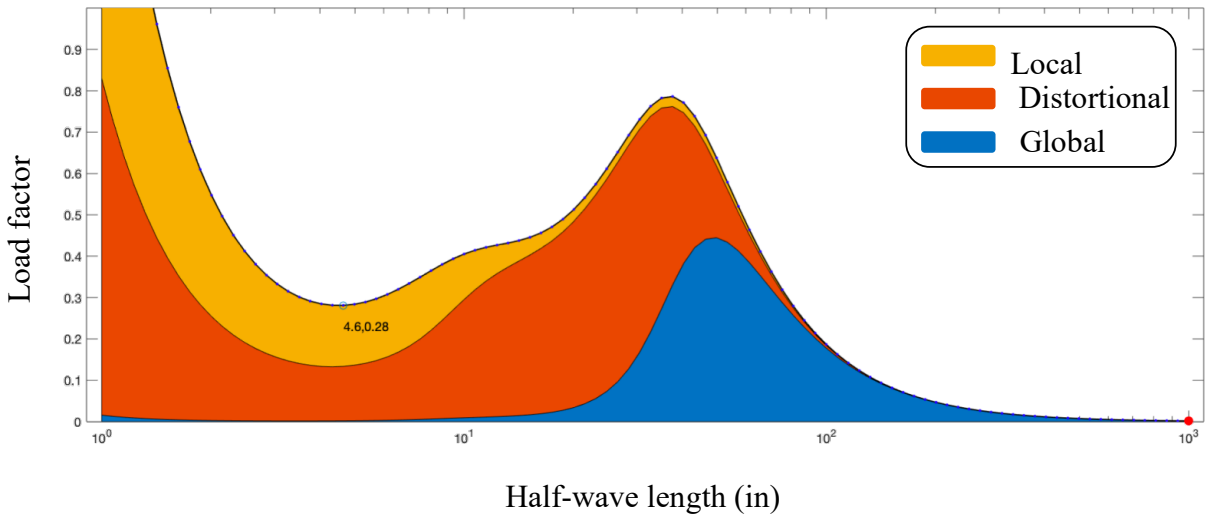


*Figure 46: Modal participation plot of 600S162-54 with uniform stress distribution on cross-section.*

## 3.2 Comparison with AISI S100-16 strength prediction

Calculating the compressive strength of members is enabled through the Direct Strength Method (DSM) equations for axial capacity calculations in the North American cold-formed steel specification (AISI S100-16, section E) [2]. Compressive strength, shown in Table 11, is calculated using nominal material properties ($P_n$) and as-measured material properties ($P_{nm}$). These material properties are provided in Table 2. As defined in AISI S100-16, member compressive strength is the minimum of the nominal axial strength for yielding and global buckling, local interacting with global buckling, and distortional buckling. In order to determine the critical elastic local and distortional column buckling loads, $P_{crl}$ and $P_{crd}$, respectively, the tested cross-sections were modeled in CUFSM ([14,15]) to determine the critical elastic local and distortional column buckling loads, $P_{crl}$ and $P_{crd}$, respectively; measured material and cross-section properties were used when

available [25]. Traditional signature curve analyses were performed as described in [14,15]. As discussed earlier, the stress distribution was presumed uniform in the models to provide characterization of current design assumptions.

The reduced section (the portion of the section which bears directly on the slab) was modeled for overhang bearing conditions (Figure 44). Overhanging systems were subjected to a combination of compression and flexure due to the induced eccentricity on the studs. The eccentricities are presented in Table 10, and the allowable axial strength was determined by Eq. 1, which is given in section H1.2 of AISI S100-16 [2].

$$\frac{\overline{P}}{\varphi_c P_n} + \frac{\overline{M_x}}{\varphi_b M_{nx}} \leq 1.0 \qquad (1)$$

where, $\overline{P}$ and $\overline{M_x}$ are required strengths, $M_{nx}$ is the nominal flexural strength which was calculated by ASIS S100-16 in Section F [2], and $\varphi_b$ (0.9 for LRFD) is the bending resistance factor. The DSM prediction equations were used to calculate the nominal strengths. The critical elastic local and distortional buckling for both axial load and moment were determined using the signature curves from finite strip analysis. The calculated axial strength of all the assemblies based on AISI S100-16 [2] and comparison are tabulated in Table 11. Test-to-predicted ratios are also determined.

*Table 10: Calculated eccentricities for overhang conditions.*

| Section | Eccentricity (mm) [in] | |
|---|---|---|
| | 12.7 mm (0.5 in) overhang | 25.4 mm (1 in) overhang |
| 600S162-33 | 0.70 [0.028] | 1.65 [0.065] |
| 600S162-54 | 0.75 [0.029] | 1.70 [0.067] |
| 600S300-54 | 0.78 [0.031] | 1.51 [0.059] |
| 600S162-97 | 0.83 [0.033] | 1.80 [0.071] |

*Table 11: Summary the results of the experiments and AISI S100-16 axial strength prediction.*

| **Test Name** | **Experiment** | | | | **AISI S100-16 capacity** | | |
|---|---|---|---|---|---|---|---|
| | **$P_{max}$** | **$\Delta$ at $P_{max}$** | **$k_i$** | **$1-P_{max}/P_{max\_r}$** | **$P_n$** | **$P_{nm}$** | **$P_{max}/P_n$** |
| | *kN* | *mm* | *kN/mm* | *%* | *kN* | *kN* | *kN/kN* |
| 600S16233R | 73.6 | 4.58 | 28 | - | 57.2 | 73.0 | 1.29 |
| 600S16233F | 69.2 | 6.56 | 23 | 6% | 57.2 | 73.0 | 1.21 |
| 600S16233E1 | 78.1 | 6.68 | 28 | -6% | 57.2 | 73.0 | 1.36 |
| 600S16233E05 | 66.8 | 6.20 | 20 | 9% | 57.2 | 73.0 | 1.17 |
| 600S16233E0125 | 56.5 | 7.32 | 20 | 23% | 57.2 | 73.0 | 0.99 |
| 600S16233E | 66.3 | 8.34 | 14 | 10% | 57.2 | 73.0 | 1.16 |
| 600S16233O05 | 65.0 | 7.86 | 21 | 12% | 55.5 | 70.2 | 1.17 |
| 600S16233O1 | 51.0 | 6.74 | 21 | 31% | 53.3 | 66.8 | 0.96 |
| 600S16254R | 136.3 | 4.72 | 72 | - | 141.3 | 135.1 | 0.96 |
| 600S16254F | 136.4 | 5.72 | 67 | - | 141.3 | 135.1 | 0.97 |
| 600S16254E1 | 123.1 | 7.06 | 44 | 10% | 141.3 | 135.1 | 0.87 |
| 600S16254E05 | 127.4 | 6.27 | 49 | 7% | 141.3 | 135.1 | 0.90 |
| 600S16254E0125 | 117.6 | 5.79 | 50 | 14% | 141.3 | 135.1 | 0.83 |
| 600S16254E | 115.5 | 6.53 | 51 | 15% | 141.3 | 135.1 | 0.82 |
| 600S16254O05 | 107.5 | 5.94 | 40 | 21% | 137.0 | 131.7 | 0.78 |
| 600S16254O1 | 89.1 | 7.29 | 34 | 35% | 131.7 | 127.5 | 0.68 |
| 600S30054E | 114.0 | 7.44 | 31 | - | 170.9 | 149.0 | 0.67 |
| 600S30054O05 | 93.6 | 6.25 | 35 | - | 168.9 | 147.4 | 0.55 |
| 600S30054O1 | 74.4 | 7.54 | 21 | - | 167.2 | 146.0 | 0.45 |
| 600S16297R | 327.8 | 4.92 | 225 | - | 322.7 | 331.2 | 1.02 |
| 600S16297F | 320.6 | 8.51 | 111 | 2% | 322.7 | 331.2 | 0.99 |
| 600S16297E1 | 278.6 | 7.34 | 104 | 15% | 322.7 | 331.2 | 0.86 |
| 600S16297E05 | 270.4 | 10.40 | 79 | 18% | 322.7 | 331.2 | 0.84 |
| 600S16297E0125 | 228.7 | 8.60 | 83 | 30% | 322.7 | 331.2 | 0.71 |
| 600S16297E | 248.1 | 8.12 | 119 | 24% | 322.7 | 331.2 | 0.77 |
| 600S16297O05 | 224.2 | 9.05 | 68 | 32% | 307.6 | 315.6 | 0.73 |
| 600S16297O1 | 195.8 | 9.35 | 62 | 40% | 291.9 | 299.1 | 0.67 |

Figure 12 presents test-to-predicted ratios for the configurations studied herein, where Figure 12(a) uses nominal material properties to predict axial capacity ($P_n$) and Figure 12(b) uses measured material properties ($P_{nm}$). As the material strength for the 0.84 mm thin specimens was significantly higher than nominal, these predictions performed particularly poorly, with test-to-predicted ratios larger than 1.0. When predicted strengths were calculated using measured properties, the DSM prediction matches experimental results for both rigid and full bearing conditions, across tested stud sections, with test-to-predicted ratios near one, as shown in Figure 47(b). However, as the system approached the edge, the prediction became worse, and the ratio could be as low as 0.5 in sections with 7.62 cm (3 inches) flanges. Although there is a trend in the behavior of test-to-predicted ratios across all the specimens, thinner assemblies are better-predicted than thicker assemblies. This may reflect the progression of failure in the assembly-slab system [26,28]. In 1.37 and 2.46 mm systems, since the cross-sections have higher capacities, the load was distributed to the concrete slab prior to stud instability, and slab played a more critical role in the system strength. As the slab is elastically deforming, additional flexibility was introduced into the assemblies, which impacted strength and load sharing between slab and studs.

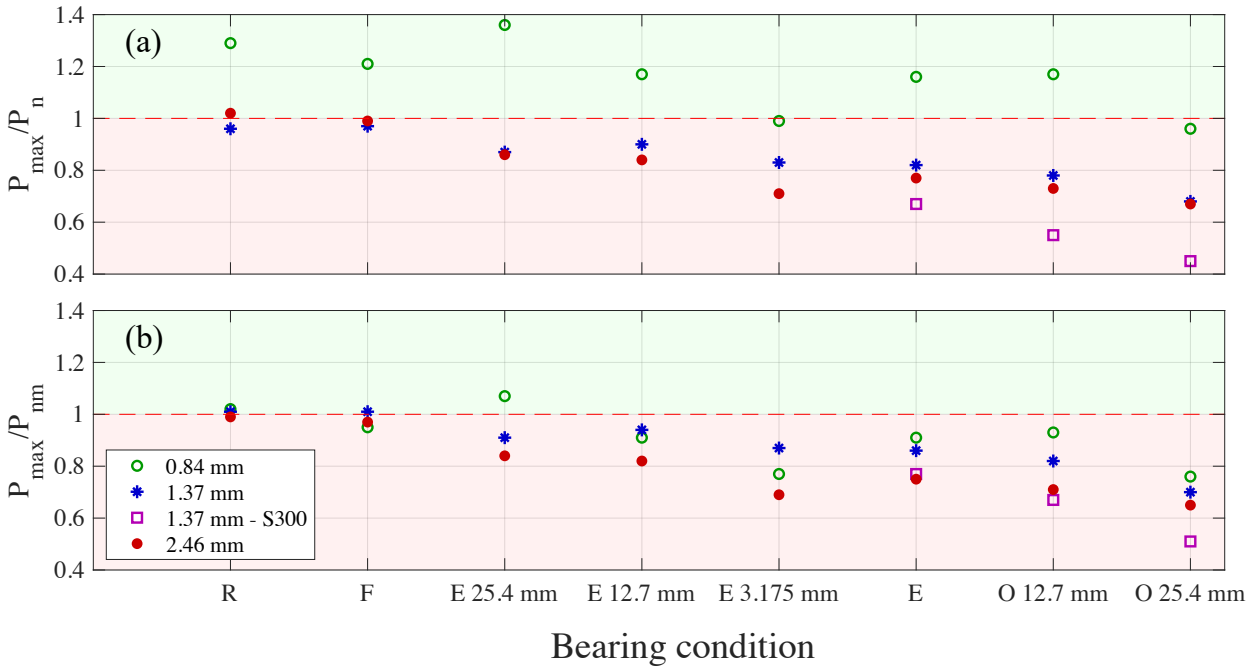


*Figure 47: Comparison of the test results vs. AISI S100-16 (Direct Strength Method) by considering (a) nominal properties; and (b) measured properties.*

## 3.3 High-fidelity finite element modeling

The commercial finite element package, ABAQUS [16], was utilized for high-fidelity non-linear finite element analysis (FEA). Studs, tracks, concrete slabs, rebar mesh, contact between studs and tracks, contact between the bottom track and concrete, and fasteners were modeled. Cold-formed steel members present strong nonlinearities, particularly through collapse. The model employed geometric and material nonlinearity analysis of the system. In this section, two types of model are simulated. In the first type, the assembly was assumed nominal, and only the impact of bearing condition on the axial capacity is discussed. Stiffness is ignored. However, in the second type, additional details such as fastener behavior definition, gap inclusion, and influence of the loading beam on the

assembly were included to capture stiffness and strength. Figure 48 shows the mesh discretization developed for 2.46 mm (97-mil) stud assembly with 3.175 mm (0.125 in) edge distance.

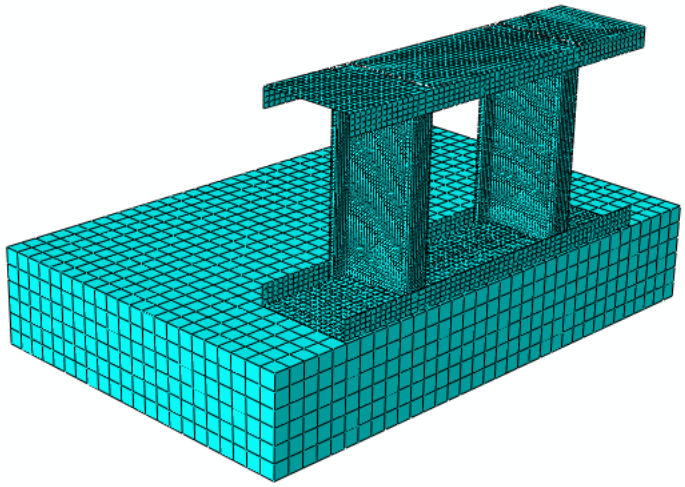

*Figure 48: Developed finite element model for the test 600S16297E0125.*

### 3.3.1 Geometry and material modeling

Nominal center-to-center dimensions were used for the cross-section geometry, except for the thickness in which measured properties were simulated. For concrete slabs and rebar mesh, nominal dimensions were employed as well (Figure 49). ABAQUS requires a true stress-strain curve ($\sigma_{true}$-$\varepsilon_{true}$), so engineering stress-strain curves obtained from the tensile tests were converted into the true curves using Eqs. (2) and (3), where the $\sigma_{eng}$ and $\varepsilon_{eng}$ are the engineering stress and strain, respectively. Then, the average of the converted curves

was defined as the cold-formed steel constitutive relationship. Poisson's ratio was defined as 0.3.

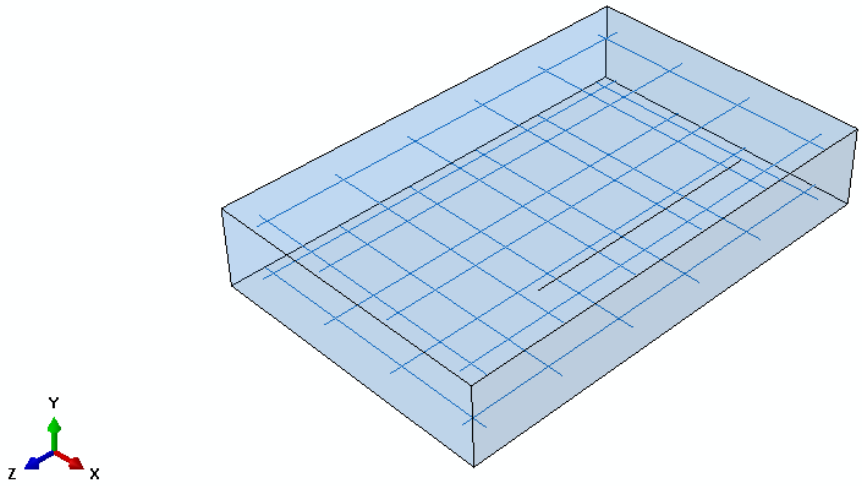


*Figure 49: Simulated rebar mesh embedded inside the concrete slabs.*

$$\sigma_{true} = \sigma_{eng}\,(1+\varepsilon_{eng}) \tag{2}$$

$$\varepsilon_{true} = ln\,(1+\varepsilon_{eng}) \tag{3}$$

For the concrete material, since only the compression and tensile strengths were available directly from test data, the complete stress-strain diagram was estimated and generated. Concrete compressive behavior was captured by the Hognestad parabola [26, 29, and 30], shown in Figure 50. As illustrated in Figure 50, the estimated compressive stress-strain curve ($\sigma_c$-$\varepsilon_c$) has three components. The first one is the linear-elastic behavior

with the modulus of elasticity equal to $E_o$=5500$\sqrt{f_c'}$ , where $f_c'$ is the compressive strength of the concrete. This linear region continues until $\sigma_{co}$=0.4$f_c'$. Then, the second region is characterized by the Hognestad parabola. The corresponding strain to $f_c'$ is defined as $\varepsilon_o$=2$f_c'$/$E_{sec}$, where $E_{sec}$=5000$\sqrt{f_c'}$ is the secant modulus of elasticity. After $f_c'$ is attained, the stress-strain curve continues until $\varepsilon_u$, the ultimate compressive strain. Poisson's ratio for concrete was defined as 0.18. For the concrete damage plasticity model, the dilation angle was defined as 30°. The shape factor, K=0.667, the stress ratio fb0/fc0 = 1.16, the eccentricity 0.1, and the viscosity parameter equal to 0 were modelled per the recommendations in [30].

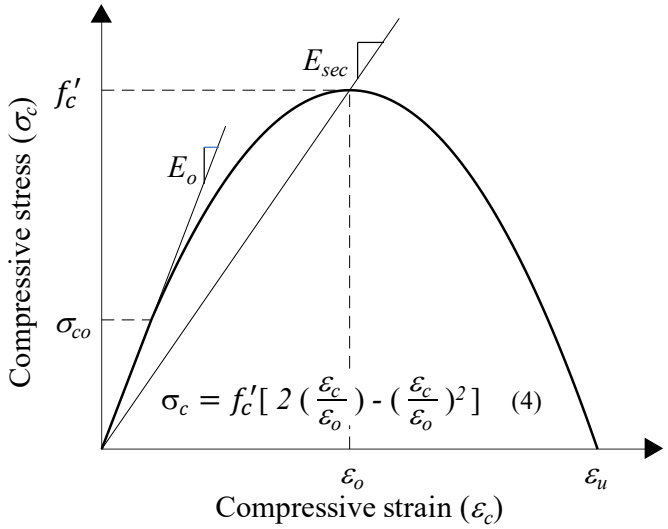


*Figure 50: Uniaxial compressive stress-strain curve of concrete (adapted from [30]).*

The uniaxial tensile stress-strain behavior of concrete likewise consists of three parts. First, there is the linear elastic response with the modulus of elasticity equal to $E_o$=5500$\sqrt{f_c'}$ until the experimental tensile strength, reported in Table 7 presented in Chapter 2. After cracking, tensile behavior until ultimate strain (εu) can be characterized by one of three relationships: linear, bilinear, or exponential softening. In this project, the bilinear relation shown in Figure 51(b) was utilized. These behaviors representing the brittle behavior of concrete in tension are defined by stress-crack width relation. Figure 51(a) represents the tensile stress-crack width relation, where $f_t'$ is the concrete tensile stress and Gf is the concrete fracture energy. The fracture energy is related to the concrete properties and aggregate size, and is defined as the area under the tensile stress-crack width plot [26,30]. This parameter can be calculated by Eq. (5) given in CEB-FIP model Code 90 [31], and is the energy required to propagate a unit area tensile crack [31]. To obtain the stress-strain relation, the strain is calculated by dividing the crack width (w) by element length ($l_c$), i.e. the size of concrete slab elements in ABAQUS.

$$G_f = G_{f0} \, (f_{cm} / 10) \;\; (N/mm) \tag{5}$$

where $G_{f0}$ is the base value of the fracture energy. $G_{f0}$ was determined based on the maximum aggregate size from [31]. $G_{f0}$ = 0.035 N/mm was utilized. $f_{cm}$ is the mean compressive strength of concrete.

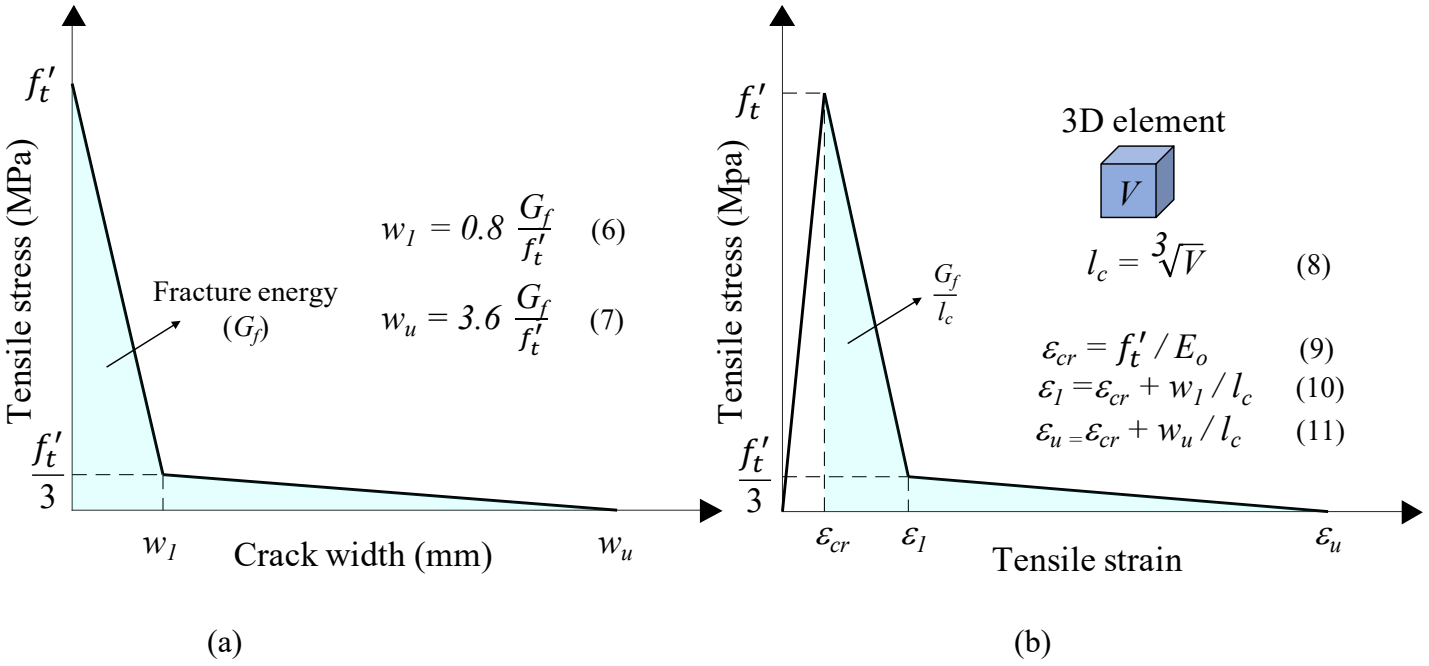


*Figure 51: (a) The relation between the uniaxial stress and crack width for concrete; (b) Uniaxial tensile stress-strain curve of concrete (adapted from [30]).*

For the tensile behavior of the reinforcing mesh, an elastic-perfectly plastic behavior with tensile strength 275.8 MPa (40 ksi) and modulus of elasticity and Poisson's ratio equal 200,000 MPa and 0.3 respectively was adopted.

### 3.3.2 Element type and mesh size

The cold-formed steel members (i.e., studs and tracks) were modeled using a 4-node shell element with reduced integration, termed S4R in the ABAQUS element library. For the concrete slab, 8-node hexahedral elements with reduced integration (C3D8R) were employed [26,28]. Two-node three-dimensional truss elements were utilized for modeling the reinforcement. The element sizes were 5 mm, 10 mm, 20 mm, and 13 mm for lipped-

channels (studs), channels (tracks), concrete slabs, and reinforcement, respectively (Figure 48).

### 3.3.3 Boundary conditions and loading applications

Three types of contact were simulated between the surfaces modeled herein. Surface-to-surface contacts were employed to simulate the contact between studs and tracks flange (Figure 52), and between the web of the bottom track and the top surface of the concrete slab (Figure 53). Node-to-surface contacts were utilized between studs ends and tracks webs Figure 54.

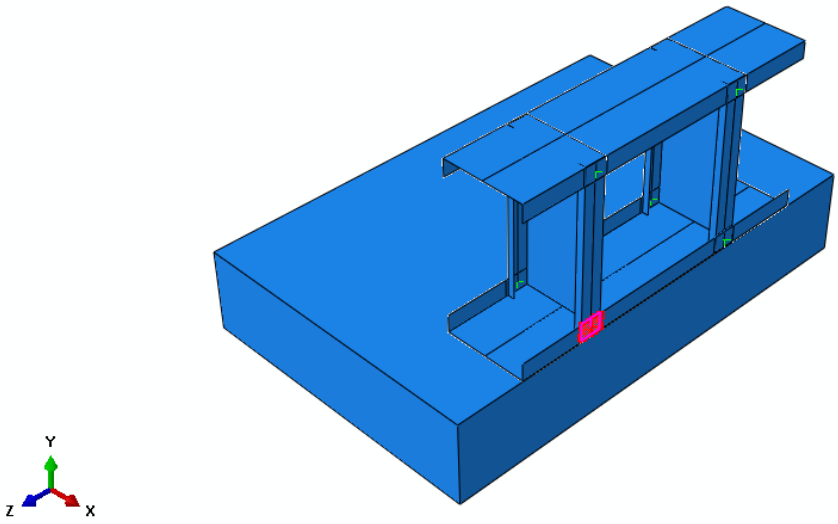


*Figure 52: Example of surface-to-surface contact between studs and tracks flanges.*

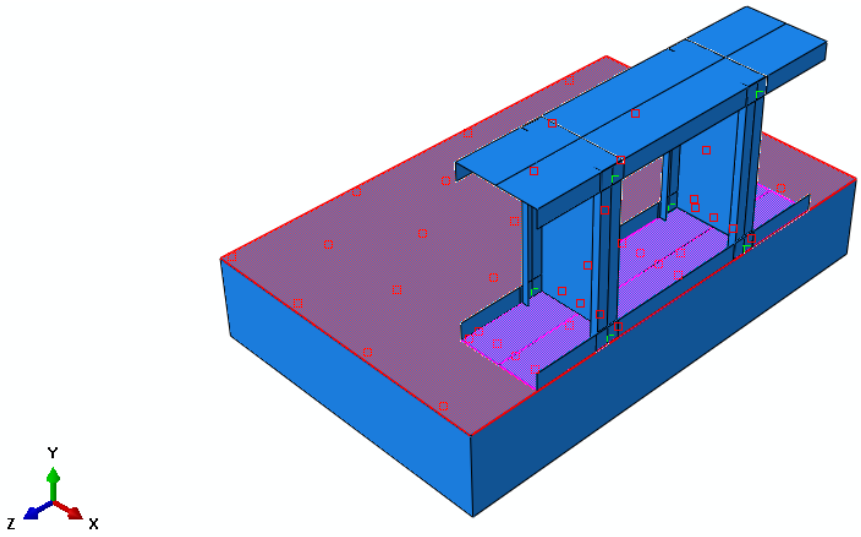


*Figure 53: The surface-to-surface contact between the track web and concrete slab.*

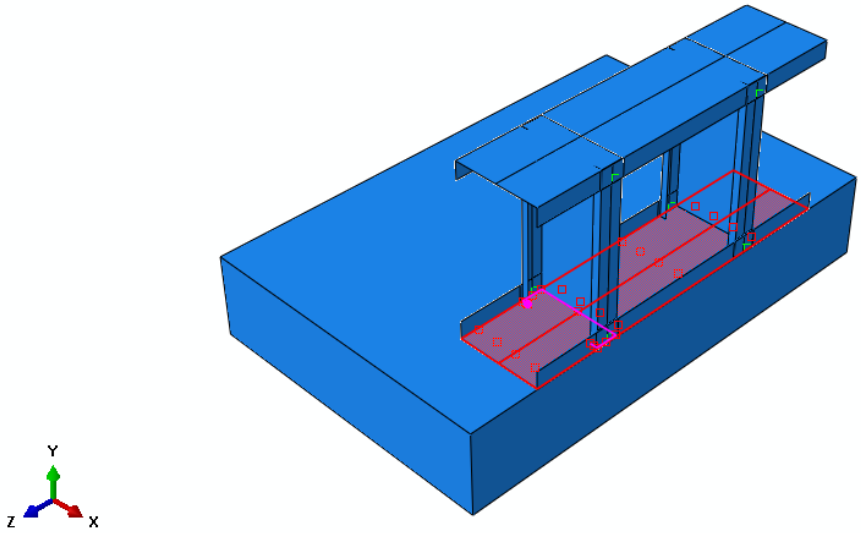


*Figure 54: Example of node-to-surface contact between studs ends and tracks webs.*

Since the CFS members were modeled with shell elements, and contact at the stud ends occurred at shell edges, “small sliding” formulation was utilized so ABAQUS could

consider the thickness of shell elements. For the rest of the contact definitions, “finite sliding” was used. “Hard contact” for normal behavior and “frictionless” formulation for tangential behavior of was defined for all contact definitions. In the ideal FEMs, the screws and powder-actuated fasteners were simulated by multi-point constraints (MPC pin) (Figure 55 and Figure 56). Idealized simple support of the system was simulated by restraining the translational degree of freedoms for all the nodes of the underneath surface of the concrete slab.

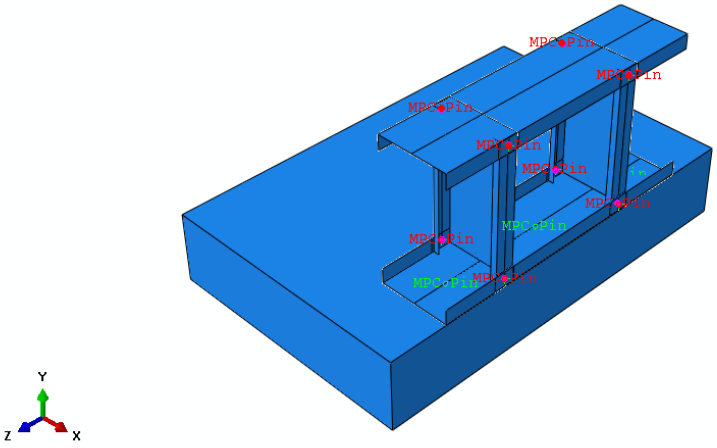


*Figure 55: Idealized steel-to-steel screws with MPC pin.*

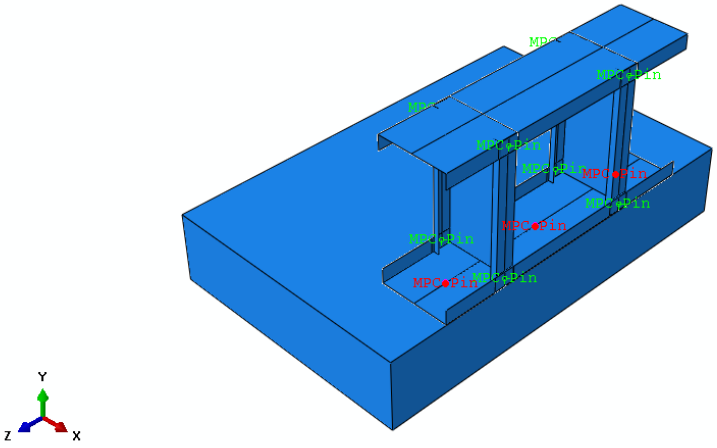


*Figure 56: Simulated powder-actuated fasteners with MPC pin.*

In order to apply the load, one general static step with ABAQUS default dissipated energy factor was created. Except for the longitudinal translational degree of freedom, transverse degrees of freedoms of the nodes at the top track web were fixed. A downward uniform displacement was applied to the top track web and the simulated specimens were pushed down (Figure 57).

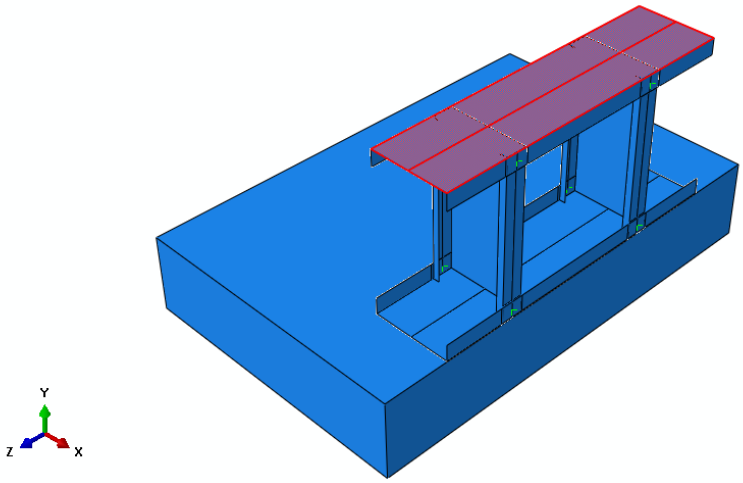


*Figure 57: Applying a uniform displacement in order to simulate the load.*

### 3.3.4 Initial geometric imperfection

In this research project, the initial geometric imperfections of the CFS members were not measured directly. Hence, the imperfection magnitude was based on measurements done by Schafer and Pekoz [32]. These were implemented in ABAQUS by applying the magnitude of the imperfection in shape of the first two buckling modes of the studs (Figure 58). The magnitudes were scaled to the 50% probability of exceedance [32] (0.34t for the local and 0.94t for the distortional geometric imperfection). The buckling mode of the studs

dictated whether the shape of the imperfections followed local or distortional modes (Figure 59). 0.34t was utilized for 0.84 mm (33-mil) assemblies and 0.94t for 1.37 mm and 2.46 (54- and 97-mil) assemblies.

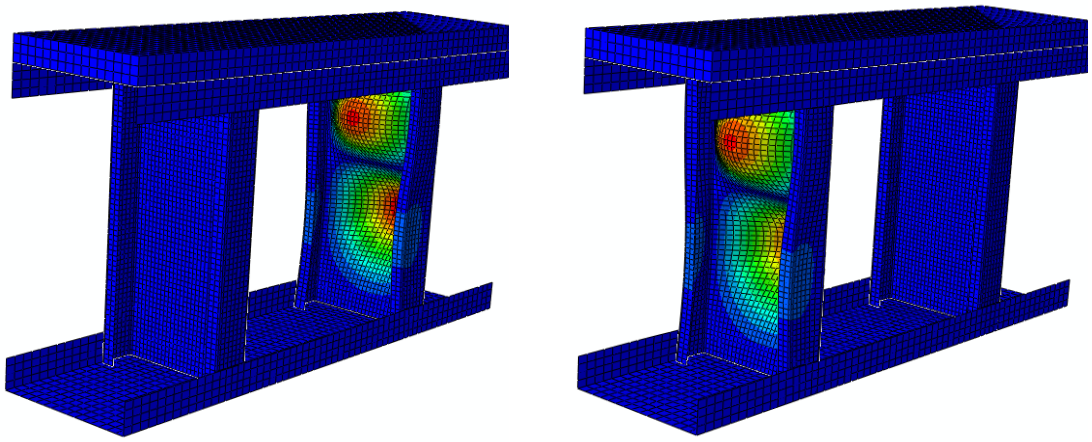

(a) (b)

*Figure 58: Buckling mode shapes of 1.37 mm (54-mil) stud-track assembly; (a) first mode, (b) second mode.*

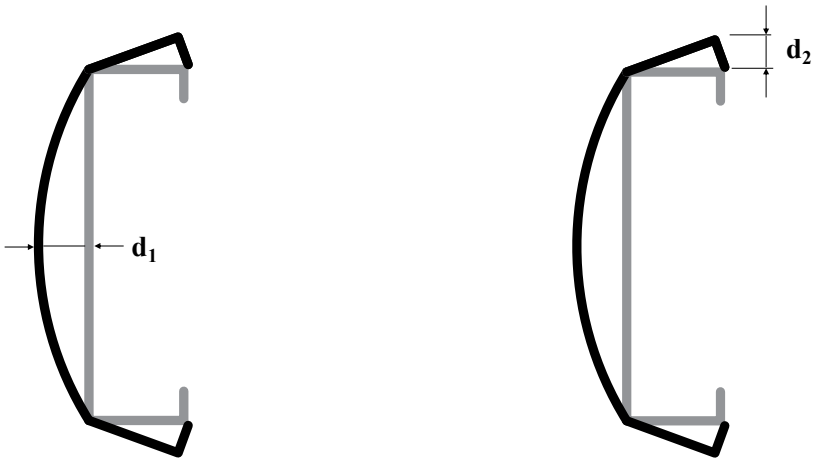


*Figure 59: Definition of the local and distortional geometric imperfections; (a) local, (b) distortional.*

### 3.3.5 Finite element results and comparison with experimental results

As shown in Table 12, the peak loads of the finite element analysis and the experimental results are in good agreement, within 0.1%-8.7%. Figure 60 highlights results for the 1.37 mm (54-mil) assemblies. To enable direct comparison, the initial part of the experimental plot is removed, and the plot is shifted to the left. While axial strength is well-captured by the finite element models, stiffness is not. This is discussed in detail later in this dissertation. It is notable that design provisions do not consider assembly stiffness. For 2.46 mm (97-mil) assemblies, two types of finite element models were simulated: with and without failed screws. Table 12 includes results for both no screw failure and screw failure.

*Table 12: Experimental results, AISI S100-16 predictions, and FEMs results.*

| Test Name | Experiment | AISI S100-16 capacity | | FEM | | |
|---|---|---|---|---|---|---|
| | $P_{max}$ *kN* | $P_n$ *kN* | $P_m$ *kN* | $P_{FEM}$ *kN* | | $P_{FEM}/P_{max}$ |
| | | | | *No screw failure* | *Screw failure* | |
| 600S16233R | 73.6 | 57.2 | 73 | 76.1 | — | 1.03 |
| 600S16233F | 69.2 | 57.2 | 73 | 73 | — | 1.06 |
| 600S16233E1 | 78.1 | 57.2 | 73 | 71.5 | — | 0.92 |
| 600S16233E05 | 66.8 | 57.2 | 73 | 67.1 | — | 1.01 |
| 600S16233E0125 | 56.5 | 57.2 | 73 | 66.7 | — | 1.18 |
| 600S16233E | 66.3 | 57.2 | 73 | 66.4 | — | 1 |
| 600S16233O05 | 65 | 55.5 | 70.2 | 63.9 | — | 0.98 |
| 600S16233O1 | 51 | 53.3 | 66.8 | 48.6 | — | 0.95 |
| 600S16254R | 136.3 | 141.3 | 135.1 | 140.7 | — | 1.03 |
| 600S16254F | 136.4 | 141.3 | 135.1 | 134.4 | — | 0.99 |
| 600S16254E1 | 123.1 | 141.3 | 135.1 | 133.3 | — | 1.08 |
| 600S16254E05 | 127.4 | 141.3 | 135.1 | 128.3 | — | 1.01 |
| 600S16254E0125 | 117.6 | 141.3 | 135.1 | 127.9 | — | 1.09 |
| 600S16254E | 115.5 | 141.3 | 135.1 | 120.5 | — | 1.04 |
| 600S16254O05 | 107.5 | 137 | 131.7 | 103.1 | — | 0.96 |
| 600S16254O1 | 89.1 | 131.7 | 127.5 | 90.1 | — | 1.01 |
| 600S30054E | 114 | 170.9 | 149 | 117 | — | 1.03 |
| 600S30054O05 | 93.6 | 168.9 | 147.4 | 99.4 | — | 1.06 |
| 600S30054O1 | 74.4 | 167.2 | 146 | 78 | — | 1.05 |
| 600S16297R | 327.8 | 322.7 | 331.2 | 312.4 | — | 0.95 |
| 600S16297F | 320.6 | 322.7 | 331.2 | 294.6 | — | 0.92 |
| 600S16297E1 | 278.6 | 322.7 | 331.2 | 293.8 | 285 | 1.02 |
| 600S16297E05 | 270.4 | 322.7 | 331.2 | 292.6 | 275.8 | 1.02 |
| 600S16297E0125 | 228.7 | 322.7 | 331.2 | 289 | 235.8 | 1.03 |
| 600S16297E | 248.1 | 322.7 | 331.2 | 279.3 | 253.6 | 1.02 |
| 600S16297O05 | 224.2 | 307.6 | 315.6 | 240 | 229.1 | 1.02 |
| 600S16297O1 | 195.8 | 291.9 | 299.1 | 207.5 | 199.3 | 1.02 |
| | | | | Mean | | 1.02 |
| | | | | Standard deviation | | 0.05 |

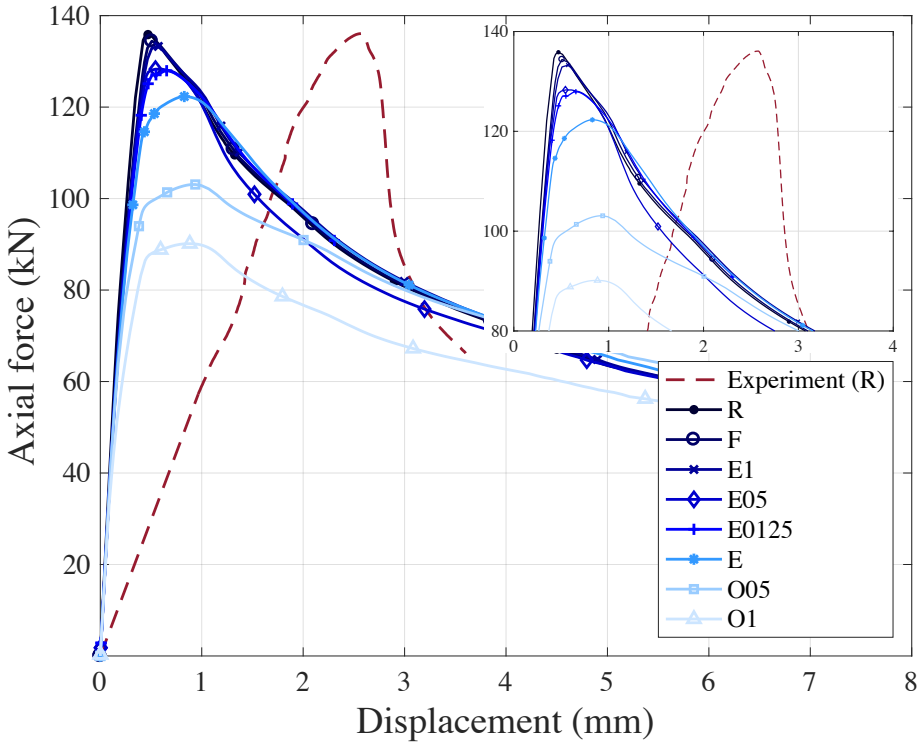


*Figure 60: FEM results and experimental result of rigid bearing condition for 1.37 mm (54-mil) assemblies.*

Figure 61 illustrates the slab cross-sections at peak load directly under the stud which buckled first, for 2.46 mm (97-mil) specimens. The letters in the Figure 61 represent the bearing conditions according to Figure 15 of Chapter 2. The Von Mises stress distributions in the tracks as the studs moved towards the edge and eventually overhang are also presented. Figure 61 demonstrates that when the assembly was placed at the middle of the concrete slab, the stress was distributed uniformly into the concrete slab. The stress distribution on the stud end can be assumed uniform. As the assembly moved closer to the edge, the concrete slab provided a non-uniform stress distribution. In the overhang bearing

condition, since the stud bearing section was reduced, the stress concentrated under the stud flange bearing on the concrete slab.

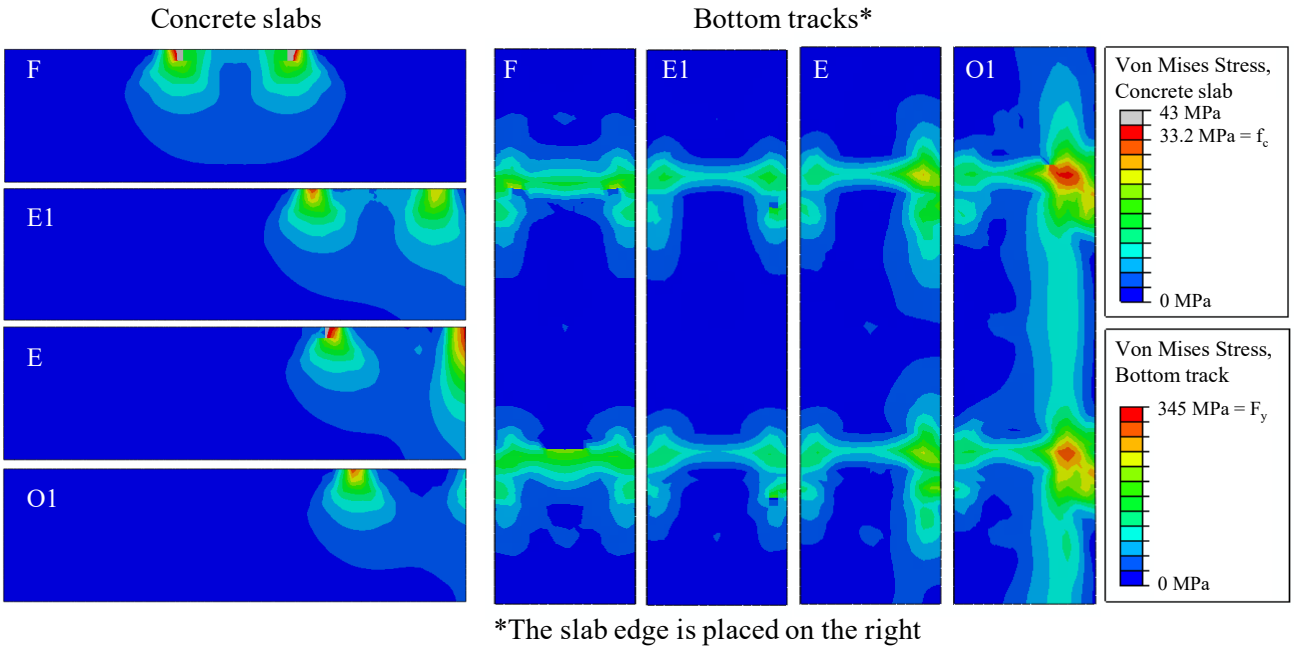


*Figure 61: Von Mises stress distribution of the slab section and the bottom track of 2.46 mm assemblies under the peak load.*

## 3.4 Capturing experimental stiffness through consideration of manufacturing and construction details

As it is seen in Figure 60, although the peak loads of FEMs are in good agreement with experimental results, the FEM results are significant stiffer. This variation is common in stub column specimens and especially those in which the studs are capped in horizontal tracks, as noted in Liao et. al [33]. Gaps between stud and track also played a role. While they were minimized by clamping the assemblies during installation, they were still present and vary across the stud-to-track contact area. Surface roughness of the concrete slabs,

while minimized in fabrication, also created gaps in the assemblies. Flatness of stud ends also contributed to response, as noted in [34]. Moen and Schafer [34] concluded that for short and intermediate length columns with the domination of local or distortional buckling, the end condition of the cold-formed steel columns plays a key role in the behavior of assemblies and the ends should milled flat and the platens level and parallel. However, cutting the studs via circular saw (standard in the CFS construction industry) created stud ends that were not perfectly straight, despite care taken during fabrication.

To confirm the source of the stiffness discrepancy between experiments and FEM, more complex FEMs were simulated for the assemblies with rigid bearing conditions. Since these FEMs were computationally expensive, and other parameters impacting the stiffness of assemblies including concrete slabs, for instance gaps between track web and slab surface, could not be measured, only models with rigid bearing condition were simulated. The gap distances were measured at three points: the left and right corners and the middle by feeler gauge (Figure 62 and Figure 63). The maximum gap tabulated in Table 13, at each end was considered. Hence, the top track was inclined.

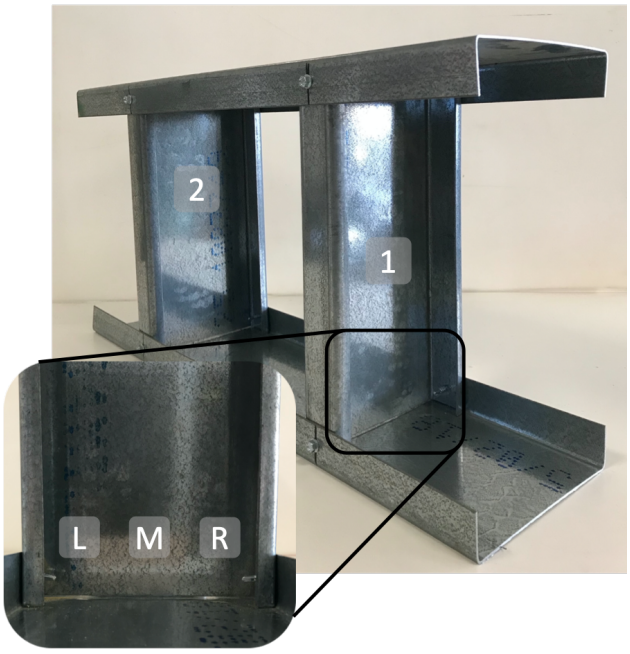


*Figure 62: 1.37 mm (54-mil) assembly and its variable gap distances across the stud-to-track contact area.*

*Figure 63: Measuring the gap distances by feeler gauge.*

*Table 13: Measured gaps at the ends of the studs (symbols are described in Figure 62)*

| **Stud** | **Gap distance** (*mm*) | | | | | |
|---|---|---|---|---|---|---|
| | Top | | | Bottom | | |
| | L | M | R | L | M | R |
| 1 | 1.09 | 1.65 | 1.37 | 0.64 | 1.30 | 1.22 |
| 2 | 1.40 | 1.04 | 1.32 | 0.86 | 1.55 | 1.22 |

In order to simulate the gap closure accurately, a steel rigid plate was simulated at the top of the top track as the actuator beam. 8-node hexahedral elements with reduced integration (C3D8R) were employed for modeling the rigid beam; the element size was 10 mm. A surface-to-surface contact was defined between the top track and the rigid plate. “Hard contact” and “frictionless” formulation were defined for the normal and tangential behaviors, respectively. The displacement-controlled load was applied at the central node of the rigid plate. The transverse degrees of freedoms of this node, except the longitudinal translational one, were fixed. The top track and the rigid plate could rotate to simulate the behavior of the actuator swivel (Figure 64), leading to gap closure (Figure 65).

*Figure 64: Rotational degree of freedom of actuator swivel which is simulated in the detailed FEM.*

Since there were gaps, detailed behavior of the screws was also defined. The screws were modeled utilizing mesh-independent capabilities available in ABAQUS. Connector elements with CARTESIAN sections were deployed to simulate the behavior of the screws (Figure 65). In the FEMs discussed herein, the screws were assumed linear elastic, and the behavior of screws was simulated with elastic spring stiffness of 7 kN/mm (40 kips/in) in the transitional degrees of freedoms [35]. Figure 66, Figure 67, and Figure 68 show how the behavior of the screws and gap distances affect the initial and secondary stiffnesses. There is still discrepancy in Figure 66 to Figure 68 between FEM results and experiments; however, only the screw behavior and gaps between stud ends and tracks were considered.

Furthermore, the behavior of the screws was assumed linear, and the gap distances were considered uniform at each end.

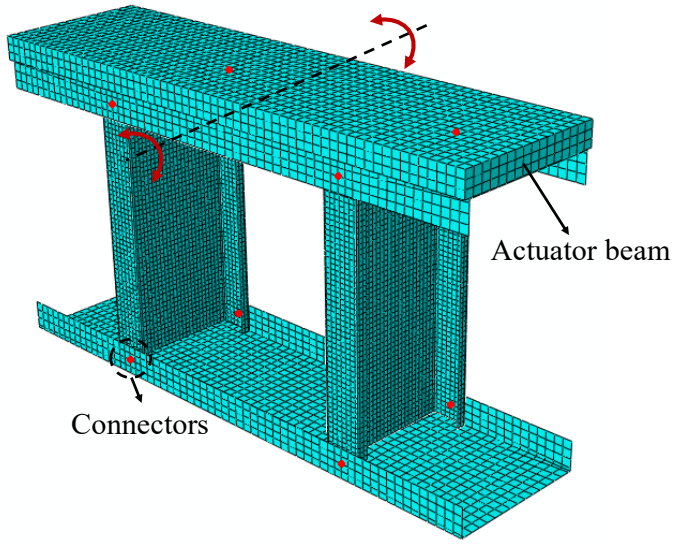


*Figure 65: Detailed and high-fidelity finite element model with rigid bearing condition.*

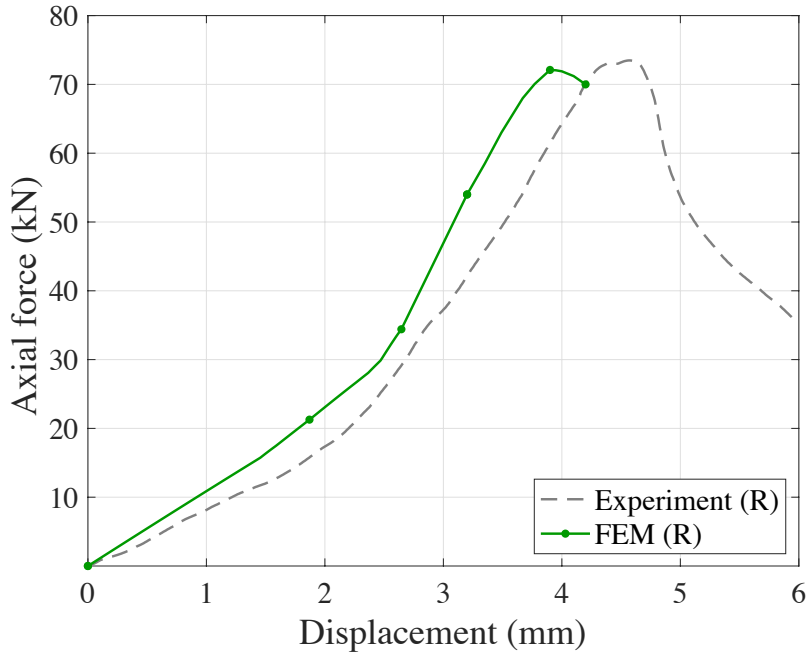


*Figure 66: The behavior of the complex FEM of 0.84 mm (33-mil) stud assembly in comparison with the experimental result.*

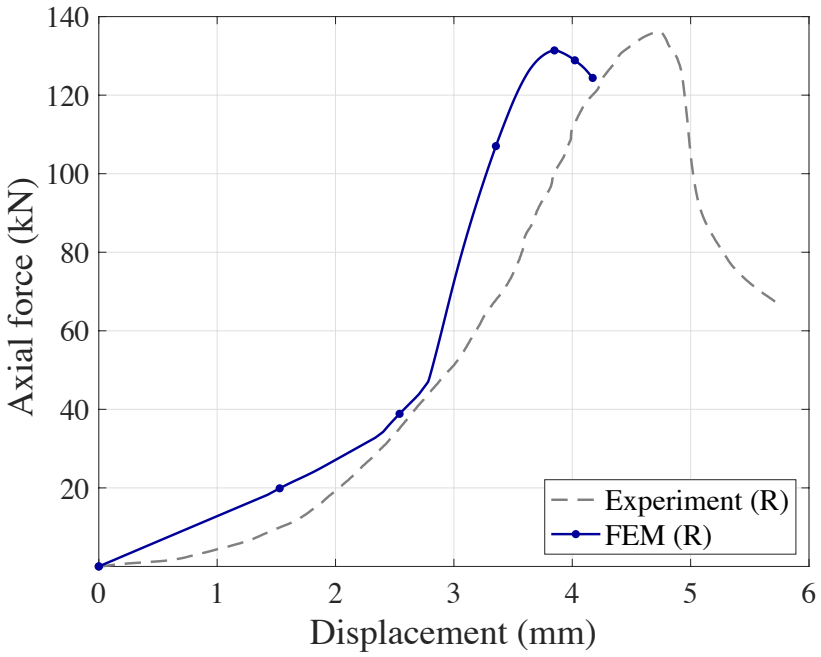


*Figure 67: The behavior of the complex FEM of 1.37 mm (54-mil) stud assembly in comparison with the experimental result.*

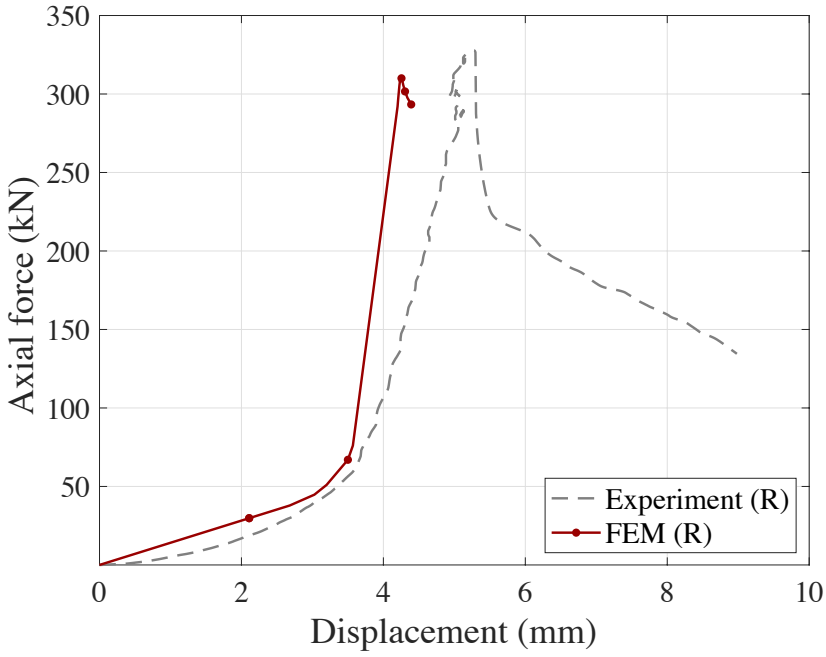


*Figure 68: The behavior of the complex FEM of 2.46 mm (97-mil) stud assembly in comparison with the experimental result.*

Figure 66, Figure 67, and Figure 68 demonstrate that peak strengths remain consistent between modeling approaches, indicating that gaps in the assembly affect only stiffness, and not peak strength. In design, stiffness is not considered in column design, so the reduced-order modeling approach is appropriate for characterizing these assemblies.

# CHAPTER 4

# Extending Experimental Results Using Parametric Variation Via a High-Fidelity Computational Modeling Program

27 experiments discussed in Chapter 2 explored studs of various cross-sections, all fixed to 30.48 cm (12 inches) in height. While maintaining identical assembly height enabled direct comparison between assemblies, the 30.48 cm (12 inches) height resulted in buckling failure modes on the local-distortional cusp for the sections examined. The participation of local and distortional modes changed with cross-section. To better identify the relationship between the bearing condition and axial capacity, a parametric study and finite element analysis at heights determined by buckling mode (local, distortional, and global) was conducted. Stud heights were determined via elastic buckling analyses to identify the stud lengths which correspond to local, distortional, and global buckling modes. Globally-dominant configurations are of particular interest as these assemblies most reflect common use in load-bearing walls. In the tests, only four different cross-sections were explored. To extend the utility of these results to variable-height walls and a range of cross-sections, high-fidelity 3D finite element analyses (FEA) of variable-height stud assemblies bearing on reinforced concrete slabs were performed in ABAQUS software. 66 different cross-sections, representing common wall stud members, were investigated. The position of the wall assemblies on the concrete slab was varied, from a full-bearing condition with no edge effects to intermediate edge distances approaching the

edge, to the slab edge itself, and overhanging from the edge. Hence, in this parametric study, the variables were: cross-section, stud height, and bearing condition.

## 4.1 Computational modeling matrix

In total, 2376 finite element analyses (Figure 69) were performed. 66 different stud cross-sections were explored. Similar to the experiments, tracks were sized to correspond with the stud sections; webs and thicknesses were matched (Table 14) and flange widths of tracks were fixed to 31.7 mm (1.25 in). The track length was fixed and set to 60.96 cm (24 inches). For each stud cross-section, three different heights were considered, which forced them to buckle either locally, distortionally, or globally. In the experiments, eight different bearing conditions were explored. However, in this computational modeling program twelve variable bearing conditions were investigated. Various bearing conditions were considered in this research program: full bearing where the stud assemblies were fastened to the center of concrete slabs, far from the edge (edge distance ≥ 5.08 cm (2 inches)), close to the edge (edge distance ≤ 2.54 cm (1 inch)), at the slab edge, and finally partially overhanging from the slab (Table 14).


*Figure 69: 2376 possible finite element models.*

*Table 14: Computational models matrix.*

| Section | | Stud height | Bearing condition | | | |
|---|---|---|---|---|---|---|
| **Stud** | **Track** | | **Full bearing** | **Far from the edge** | **Close to the edge** | **Overhang** |
| | | | *Distance from edge, mm (in)* | | | |
| (XXX) S (YYY) - ZZ | (XXX) T 125 - ZZ | Local | Center of concrete slab | 127.0 (5) | 19.05 (0.75) | 6.35 (0.25) |
| 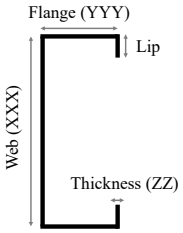 | | Distortional | | 50.8 (2) | 12.70 (0.5) | 12.70 (0.5) |
| | | 2.45 m (8 ft) | | 25.4 (1) | 6.35 (0.25) | 25.40 (1) |
| | | | | | 3.17 (0.125) | |
| | | | | | at the slab edge | |



In Table 14, XXX, YYY, and ZZ represent web height, flange length, and thickness of studs and tracks respectively in 1/100 inches for web and flange and in 1/1000 inches for thickness, described in Table 15. As tabulated in Table 15, the depth of members ranged between 91.9 mm (3.62 in) to 203.2 mm (8.00 in). The range of flange width was 34.9 mm (1.37 in) to 63.5 mm (2.50 in). The studs investigated herein had five different thicknesses. Also, it should be mentioned that in this parametric study, the corner radius of cross-sections was not modeled [33,34]. The dimensionless parameters, such as depth-to-width ratio and flange-to-lip ratio, of selected cross-sections are illustrated in Figure 70 based on the height of sections. The cross-sections were selected based on their application in cold-formed steel gravity walls. In this project, very small cross-sections, web depth less than 3.62 in (9.2 cm), and very large cross-sections, web depth greater than 8 in (20.3 cm) were ignored. Furthermore, members with flange width larger than 2.5 in (6.4 cm) were ignored as well.

*Table 15: Dimension of 66 common stud members investigated in the computational modeling program.*

| | AISI S100-16 nomenclature | Length, mm (in) |
|---|---|---|
| Web (XXX) | 362 | 91.9 (3.62) |
| | 400 | 101.6 (4.00) |
| | 550 | 139.7 (5.50) |
| | 600 | 152.4 (6.00) |
| | 800 | 203.2 (8.00) |
| Flange (YYY) | 137 | 34.9 (1.375) |
| | 162 | 41.3 (1.625) |
| | 200 | 50.8 (2.000) |
| | 250 | 63.5 (2.500) |
| Thickness (ZZ) | 33 | 0.88 (0.0346) |
| | 43 | 1.15 (0.0451) |
| | 54 | 1.44 (0.0566) |
| | 68 | 1.81 (0.0713) |
| | 97 | 2.58 (0.1017) |
| Lip | — | 9.5 (0.375) |
| | — | 12.7 (0.500) |
| | — | 15.9 (0.625) |

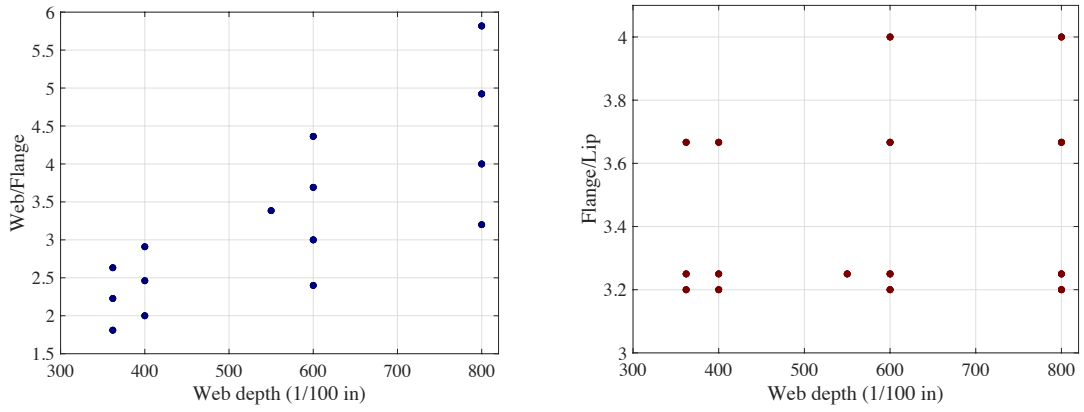


(a) (b)

*Figure 70: Dimension parameters of selected cross-sections; (a) web-to-flange ratio, (b) flange-to-lip ratio.*

## 4.2 Calculating stud height

Stud heights were determined through conducting elastic buckling analysis via finite strip method software CUFSM [14,15]. Figure 71 illustrates the signature curve of 362S162-68 as an example. The load factors are $P_{cr}/P_y$, where $P_y$ is the member axial yield strength. The half-wave length is the length of specimen. The lengths at which the local and distortional buckling occur are the corresponding half-wave lengths of first and second minima, respectively. For global buckling, the length equal to 2.45 m (8 ft) was considered for all the sections. Figure 72 shows the lengths (half-wave lengths) corresponding to the local, distortional, and global buckling.

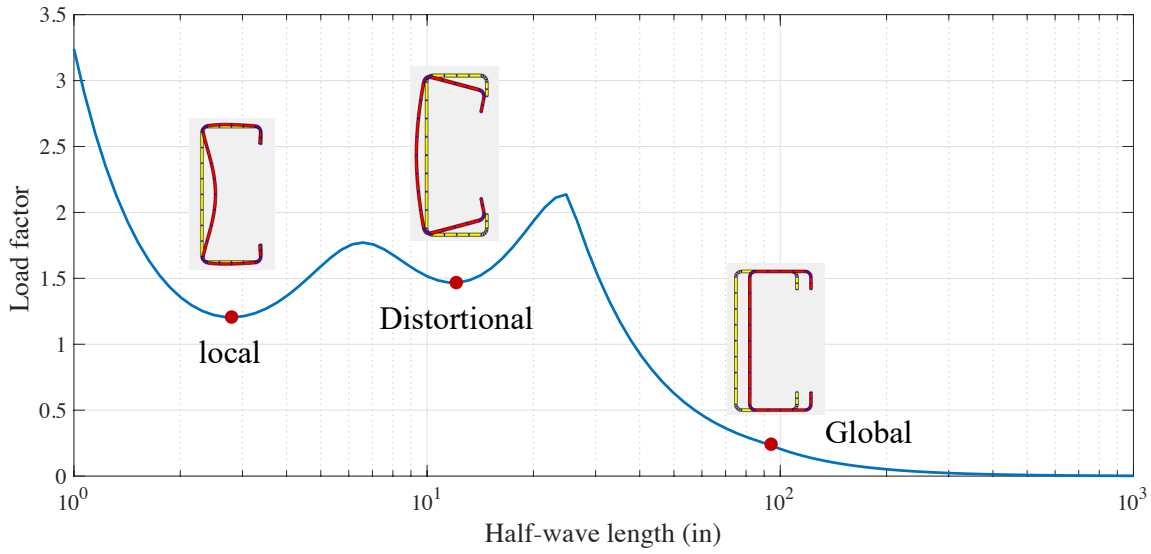


*Figure 71: Signature curve of 362S162-68 for determining stud height.*

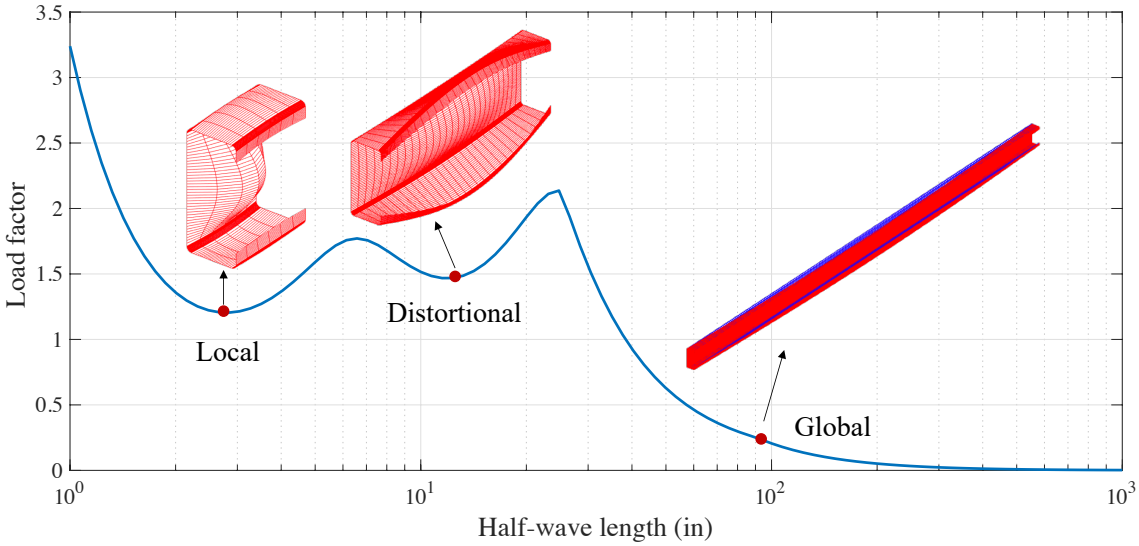


*Figure 72: Signature curve of 362S162-68 and corresponding half-wave length to each buckling mode.*

The heights of studs were calculated and summarized in Table 16 and Figure 73. Figure 73 depicts stud height against their cross-sectional area. Studs buckling locally are stub column specimens; their height ranged between 6.9 cm to 18.3 cm (2.7 to 7.2 inches). For the distortional buckling mode, the studs have generally longer lengths, 15.9 cm to 74.9 cm (6.26 to 29.5 inches). Finally, for the global buckling mode, all the heights were fixed 245 cm (96 in). The range of heights is shown schematically in Figure 74.

*Table 16: Variable height of cold-formed steel stud assemblies.*

| **Section** | **Stud height** | | |
|---|---|---|---|
| | **Buckling mode** | | |
| | Local | Distortional | Global |
| | *cm (in)* | | |
| 362S137-33 | 6.9 (2.7) | 32.1 (12.7) | 243.8 (96) |
| 362S137-43 | 6.9 (2.7) | 27.9 (11.0) | 243.8 (96) |
| 362S137-54 | 6.9 (2.7) | 24.3 (9.6) | 243.8 (96) |
| 362S137-68 | 6.9 (2.7) | 21.1 (8.3) | 243.8 (96) |
| 362S162-33 | 6.9 (2.7) | 20.3 (8.0) | 243.8 (96) |
| 362S162-43 | 6.9 (2.7) | 42.2 (16.6) | 243.8 (96) |
| 362S162-54 | 6.9 (2.7) | 37.1 (14.6) | 243.8 (96) |
| 362S162-68 | 6.9 (2.7) | 32.1 (12.7) | 243.8 (96) |
| 362S200-33 | 7.6 (3.0) | 65.0 (25.6) | 243.8 (96) |
| 362S200-43 | 6.9 (2.7) | 65.5 (22.3) | 243.8 (96) |
| 362S200-54 | 6.9 (2.7) | 49.0 (19.3) | 243.8 (96) |
| 362S200-68 | 6.9 (2.7) | 42.7 (16.8) | 243.8 (96) |
| 400S137-33 | 7.9 (3.1) | 32.1 (12.7) | 243.8 (96) |
| 400S137-43 | 7.9 (3.1) | 27.9 (11.0) | 243.8 (96) |
| 400S137-54 | 7.9 (3.1) | 24.3 (9.6) | 243.8 (96) |
| 400S137-68 | 7.9 (3.1) | 21.1 (8.3) | 243.8 (96) |
| 400S162-33 | 7.9 (3.1) | 49.0 (19.3) | 243.8 (96) |
| 400S162-43 | 7.9 (3.1) | 42.5 (16.8) | 243.8 (96) |
| 400S162-54 | 7.9 (3.1) | 56.4 (22.2) | 243.8 (96) |
| 400S162-68 | 7.9 (3.1) | 32.1 (12.7) | 243.8 (96) |
| 400S200-33 | 7.9 (3.1) | 65.0 (25.6) | 243.8 (96) |
| 400S200-43 | 7.9 (3.1) | 56.5 (22.3) | 243.8 (96) |
| 400S200-54 | 7.9 (3.1) | 49.0 (19.3) | 243.8 (96) |
| 400S200-68 | 7.9 (3.1) | 42.7 (16.8) | 243.8 (96) |
| 550S162-33 | 10.4 (4.1) | 56.5 (22.3) | 243.8 (96) |
| 550S162-43 | 10.4 (4.1) | 49.0 (19.3) | 243.8 (96) |
| 550S162-54 | 10.4 (4.1) | 42.5 (16.8) | 243.8 (96) |
| 550S162-68 | 10.4 (4.1) | 42.5 (16.8) | 243.8 (96) |
| 600S137-33 | 11.9 (4.7) | 42.5 (16.8) | 243.8 (96) |
| 600S137-43 | 11.9 (4.7) | 37.1 (14.6) | 243.8 (96) |
| 600S137-54 | 11.9 (4.7) | 32.1 (12.7) | 243.8 (96) |
| 600S137-68 | 13.8 (5.4) | 27.9 (11.0) | 243.8 (96) |

| | | | |
|---|---|---|---|
| 600S137-97 | 10.4 (4.1) | 15.9 (6.3) | 243.8 (96) |
| 600S162-33 | 11.9 (4.7) | 56.5 (22.2) | 243.8 (96) |
| 600S162-43 | 11.9 (4.7) | 49.0 (19.3) | 243.8 (96) |
| 600S162-54 | 11.9 (4.7) | 42.5 (16.8) | 243.8 (96) |
| 600S162-68 | 11.9 (4.7) | 37.1 (14.6) | 243.8 (96) |
| 600S162-97 | 11.9 (4.7) | 27.9 (11.0) | 243.8 (96) |
| 600S200-33 | 11.9 (4.7) | 65.0 (25.6) | 243.8 (96) |
| 600S200-43 | 11.9 (4.7) | 56.5 (22.3) | 243.8 (96) |
| 600S200-54 | 11.9 (4.7) | 49.0 (19.3) | 243.8 (96) |
| 600S200-68 | 11.9 (4.7) | 42.5 (16.8) | 243.8 (96) |
| 600S200-97 | 11.9 (4.7) | 42.5 (16.8) | 243.8 (96) |
| 600S250-43 | 11.9 (4.7) | 65.0 (25.6) | 243.8 (96) |
| 600S250-54 | 11.9 (4.7) | 56.5 (22.3) | 243.8 (96) |
| 600S250-68 | 11.9 (4.7) | 49.0 (19.3) | 243.8 (96) |
| 600S250-97 | 11.9 (4.7) | 42.5 (16.8) | 243.8 (96) |
| 800S137-33 | 15.9 (6.3) | 42.5 (16.8) | 243.8 (96) |
| 800S137-43 | 15.9 (6.3) | 37.1 (14.6) | 243.8 (96) |
| 800S137-54 | 18.3 (7.2) | 32.1 (12.7) | 243.8 (96) |
| 800S137-68 | 13.8 (5.5) | 21.1 (8.3) | 243.8 (96) |
| 800S137-97 | 13.8 (5.5) | 21.1 (8.3) | 243.8 (96) |
| 800S162-33 | 15.9 (6.3) | 56.5 (22.3) | 243.8 (96) |
| 800S162-43 | 15.9 (6.3) | 49.0 (19.3) | 243.8 (96) |
| 800S162-54 | 15.9 (6.3) | 42.5 (16.8) | 243.8 (96) |
| 800S162-68 | 15.9 (6.3) | 37.1 (14.6) | 243.8 (96) |
| 800S162-97 | 13.7 (5.4) | 32.1 (12.7) | 243.8 (96) |
| 800S200-33 | 15.9 (6.3) | 74.9 (29.5) | 243.8 (96) |
| 800S200-43 | 15.9 (6.3) | 65.0 (25.6) | 243.8 (96) |
| 800S200-54 | 15.9 (6.3) | 56.5 (22.3) | 243.8 (96) |
| 800S200-68 | 15.9 (6.3) | 49.0 (19.3) | 243.8 (96) |
| 800S200-97 | 15.9 (6.3) | 42.5 (16.8) | 243.8 (96) |
| 800S250-43 | 15.9 (6.3) | 74.9 (29.5) | 243.8 (96) |
| 800S250-54 | 15.9 (6.3) | 65.0 (25.6) | 243.8 (96) |
| 800S250-68 | 15.9 (6.3) | 56.5 (22.3) | 243.8 (96) |
| 800S250-97 | 15.9 (6.3) | 49.0 (19.3) | 243.8 (96) |

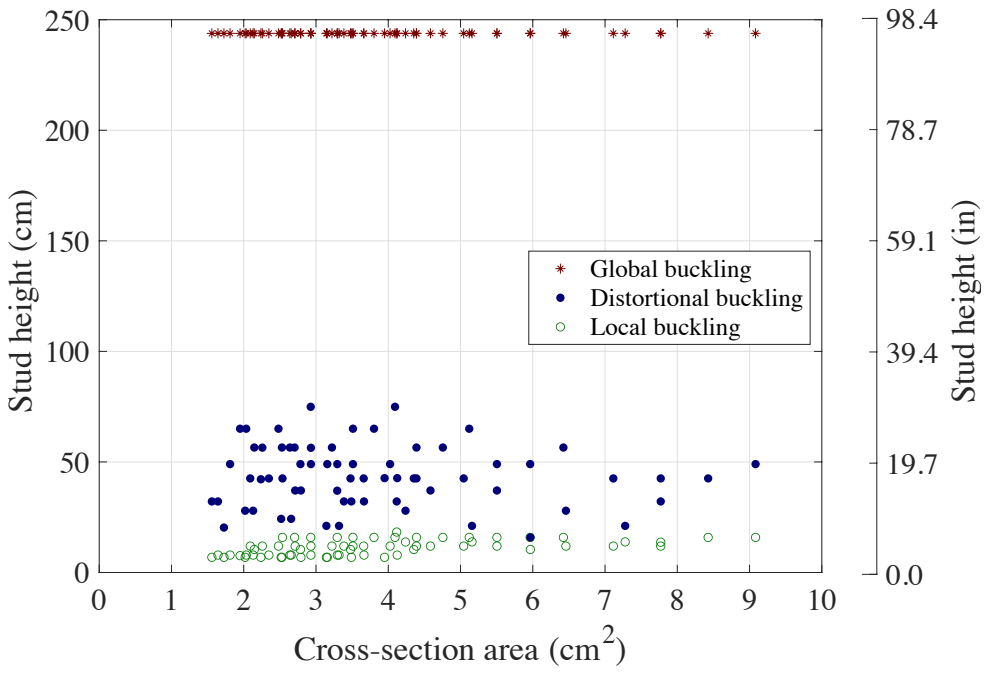


*Figure 73:Height of investigated CFS wall assemblies.*

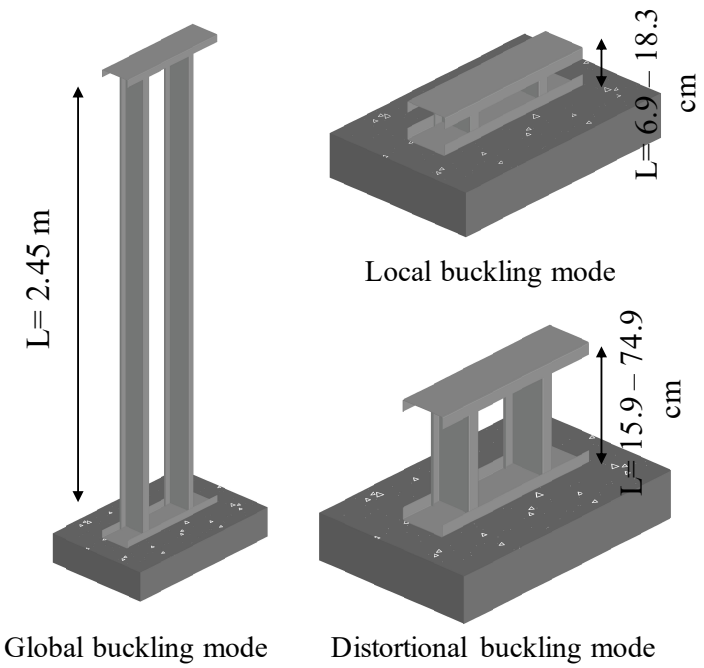


*Figure 74: Schematic of the assemblies and their range of heights.*

## 4.3 Geometry and material modeling

Like high-fidelity finite element models in Chapter 3, nominal center-to-center dimensions were employed for the cross-section geometry, including the thickness. However, simulating the corner radii of CFS specimens was ignored in this computational modeling program to reduce the number of nodes and elements and decrease computation time. Nominal dimensions were used for concrete slabs (55.88×86.36×15.24 cm) and rebar mesh.

In parametric study projects such as this one, with thousands of models, the CPU time becomes a critical issue. Consequently, in order to save CPU time, an elastic-perfectly-

plastic material was defined for CFS members. Two nominal yield strength of 228 MPa (33 ksi ) and 345 MPa (50 ksi) were used corresponding to the nominal strength of products in the industry [38]. For 0.84 and 1.09 mm (33- and 43-mil) members, 228 MPa, and for the rest of specimens, 345 MPa was used. The Young's modulus of elasticity and Poisson's ratio were $2.03\times10^5$ MPa (29500 ksi) and 0.3, respectively. Von Mises yield criterion and corresponding flow were considered for plastic behavior [38]. For the material of concrete slabs and rebar mesh, the same assumptions made in Chapter 3 were used.

## 4.4 Element type and mesh size

In order to model cold-formed steel members, 4-nodal shell elements with reduced integration, S4R in the ABAQUS element library, were employed. Concrete slabs were simulated by 8-node hexahedral elements with reduced integration (C3D8R), and reinforcement was modeled by utilizing a two-node linear 3D truss element (T3D2).

The element size of components impacted significantly the CPU time. Hence, selecting the optimum element size was necessary. In order to select the optimum mesh size for the members, two parametric studies were conducted. In the first one, the variable parameters were stud, track, and concrete slab element sizes. In this parametric study, three cross-sections with three various dimensions were investigated. The cross-sections represented the range of stud sections: small (362S137-33), intermediate (600S250-54), and large (800S162-97). They were selected in such a way that they had variable depth, flange width, and thickness. In Chapter 3, the element sizes utilized in high-fidelity FEMs were 5 mm (0.2 in), 10 mm (0.4 in), 25.4 mm (1 in), and 13 mm (0.5 in) for lipped channels (studs),

channels (tracks), concrete slabs, and reinforcement, respectively. Since the peak loads of the finite element analysis and the experimental results were in good agreement in Chapter 3, the element sizes employed therein were considered as the reference. The results of new FEMs, which are called efficient finite element models, in this parametric study were compared to the results of reference models. For studs, element sizes 5, 7.6, and 10 mm (0.2, 0.3, and 0.4 in) were investigated. For the tracks, they were 10, 13, and 15.2 mm (0.4, 0.5, and 0.6). Finally, element sizes equal to 25.4, 28, 30.5, and 38 mm (1, 1.1, 1.2, and 1.5 in) were investigated for concrete slabs. The results are tabulated in Table 17. Furthermore, in addition to the Table 17, Figure 75, demonstrates well the response of FEMs to element size of various components. In Figure 75, only sensitivity of models with full bearing condition is illustrated.

Although the parametric study done herein was not comprehensive and did not cover a wide range of element sizes Table 17 and Figure 75 show clearly how sensitive were modeled to element sizes. In Table 17 and Figure 75, the axial capacities of efficient FEMs, were compared to their corresponding prediction of AISI S100-16 specification, since it was concluded in Chapter 3 that in full bearing condition, the predictions of AISI S100-16 match well to the results of high-fidelity finite element models.

The responses of cross-sections were different. Increasing element size of concrete slabs by 20% could reduce CPU time ~20-60% while it could change axial strengths of efficient FEMs 1-7%. By increasing the element size of studs up to 50%, 9-60% CPU time could be saved; however, axial capacities changed 2-9%. Finally, increasing the element

size of tracks reduced CPU time of efficient FEMs by 22-55%, while the axial strengths were 2-18% off.

Figure 75 is only based on the assemblies with full bearing condition, since prediction of AISI S100-16 was considered as the means for evaluating the behavior of efficient FEMs. However, it was concluded in Chapter 3 that wall assemblies with edge bearing conditions have reduced axial capacity and their strength does not match the predicted strengths by AISI S100-16. Hence, Table 18, was produced. In Table 18, the element sizes of various components were changed for two cross-sections (600S250-54 and 800S162-97) and two different bearing conditions: full and edge. In this table, the axial capacities of efficient FEMs with edge bearing condition were compared to their corresponding full bearing condition, where $P_F$ is axial capacity of full bearing condition and $P_E$ is the peak load of edge bearing condition. Then, these reductions were compared to the reduction of high-fidelity finite element models (FEMs with 5 mm stud element size, 10 mm track element size, and 25.4 mm slab element size). Table 18 illustrates that increasing the element size of the concrete slab by 10% did not impact the amount of reductions in axial capacities for 600S250-54 and 800162-97 cross-sections and $P_E/P_F$ was kept 0.87 and 0.98, respectively. However, changing the element size of 600S250-54 stud from 5 mm (0.2 in) to 7.6 mm (0.3 in) and 10 mm (0.4), changed the reduction of axial capacity from 13% to 11%, and 17% respectively. In other words, in the high-fidelity finite element model, by moving the stud-track assembly from the center to the edge, the axial capacity was reduced 13%. However, this reduction was 11% and 17% in efficient FEMs. The impact of track element size was more significant such that employing 13 mm (0.5 in) track element size could change the reduction in axial capacity from 13% in high fidelity FEM with 10 mm

(0.4 in) track element size to 28% (efficient FEM) in 600S250-54 stud assembly. For 800S162-97 system, increasing the track element size from 10 mm (0.4 in) to 13 mm (0.5 in) changed the impact of edge bearing condition from 2% (reduction in high-fidelity FEM) to 5% (reduction in efficient FEM). This phenomenon illustrates the impact of track element size on the results of FEMs and in turn the role of the track in CFS wall assemblies. The goal of this research project was investigating the impact of edge distances on the axial capacities of stud assemblies and proposing design recommendations. Hence, by comparing the amount of reduction in axial capacities of efficient FEMs (reductions due to moving the assemblies to the edge) with their corresponding high-fidelity ones, it was concluded that the element size of component (i.e. stud, track, and concrete slab) in finite element models could change the result of this research and design recommendations subsequently. Accordingly, like Chapter 3, mesh sizes equal to 5 mm (0.2 in), 10 mm (0.4 in), 25.4 mm (1 in), and 13 mm (0.5 in) for studs, tracks, concrete slabs, and reinforcement were utilized, respectively.

*Table 17: Mesh sensitivity of FEMs with full and at the edge bearing conditions to element size of studs, tracks, and concrete slabs.*

| Section | Bearing condition | Stud length | Stud element size | Track element size | Slab element size | CPU time | AISI S100-16 prediction ($P_{n)}$ | FEM $P_{FEM}$ | $P_{FEM}/P_n$ | Reduction in CPU time |
|---|---|---|---|---|---|---|---|---|---|---|
| | | *cm (in)* | *mm (in)* | *mm (in)* | *mm (in)* | *(Sec.)* | *kN (kips)* | *kN (kips)* | | *%* |
| 362S137-33 | F | 30.5 (12) | 5 (0.2) | 10 (0.4) | 25.4 (1) | 1200 | 44.7 (10.4) | 46.3 (10.4) | 1.03 | — |
| | F | 30.5 (12) | 5 (0.2) | 10 (0.4) | 28 (1.1) | 854 | 44.7 (10.4) | 43.5 (9.8) | 0.97 | 28.8 |
| | F | 30.5 (12) | 5 (0.2) | 10 (0.4) | 38 (1.5) | 690 | 44.7 (10.4) | 42.6 (9.6) | 0.95 | 42.5 |
| | F | 30.5 (12) | 7.6 (0.3) | 10 (0.4) | 25.4 (1) | 1097 | 44.7 (10.4) | 48.8 (11.0) | 1.09 | 8.6 |
| | F | 30.5 (12) | 10 (0.4) | 10 (0.4) | 25.4 (1) | 864 | 44.7 (10.4) | 47.4 (10.7) | 1.06 | 28.0 |
| | F | 30.5 (12) | 5 (0.2) | 13 (0.5) | 25.4 (1) | 954 | 44.7 (10.4) | 45.8 (10.3) | 1.02 | 20.5 |
| | F | 30.5 (12) | 5 (0.2) | 15.2 (0.6) | 25.4 (1) | 892 | 44.7 (10.4) | 43.9 (9.9) | 0.98 | 25.7 |
| | F | 30.5 (12) | 10 (0.4) | 15.2 (0.6) | 38 (1.5) | 362 | 44.7 (10.4) | 47.6 (10.7) | 1.06 | 69.8 |
| 600S250-54 | F | 38.1 (15) | 5 (0.2) | 10 (0.4) | 25.4 (1) | 3652 | 160.8 (156.5) | 156.5 (35.2) | 0.97 | — |
| | F | 38.1 (15) | 5 (0.2) | 10 (0.4) | 28 (1.1) | 1516 | 160.8 (156.5) | 154.2 (34.7) | 0.96 | 58.5 |
| | F | 38.1 (15) | 5 (0.2) | 10 (0.4) | 30.5 (1.2) | 1514 | 160.8 (156.5) | 149.7 (33.7) | 0.93 | 58.5 |
| | F | 38.1 (15) | 5 (0.2) | 10 (0.4) | 38 (1.5) | 1387 | 160.8 (156.5) | 152.7 (34.3) | 0.95 | 62.0 |
| | F | 38.1 (15) | 7.6 (0.3) | 10 (0.4) | 25.4 (1) | 1528 | 160.8 (156.5) | 158.4 (35.6) | 0.98 | 58.2 |
| | F | 38.1 (15) | 10 (0.4) | 10 (0.4) | 25.4 (1) | 1300 | 160.8 (156.5) | 173.6 (39.0) | 1.08 | 64.4 |
| | F | 38.1 (15) | 5 (0.2) | 13 (0.5) | 25.4 (1) | 1658 | 160.8 (156.5) | 190.4 (42.8) | 1.18 | 54.6 |
| | F | 38.1 (15) | 5 (0.2) | 15.2 (0.6) | 25.4 (1) | 1560 | 160.8 (156.5) | 175.3 (39.4) | 1.09 | 57.3 |
| | F | 38.1 (15) | 10 (0.4) | 15.2 (0.6) | 38 (1.5) | 592 | 160.8 (156.5) | 178.7 (40.2) | 1.11 | 83.8 |
| | E | 38.1 (15) | 5 (0.2) | 10 (0.4) | 25.4 (1) | 3839 | 160.8 (156.5) | 135.4 (30.4) | 0.84 | — |
| | E | 38.1 (15) | 5 (0.2) | 10 (0.4) | 28 (1.1) | 2350 | 160.8 (156.5) | 133.9 (30.1) | 0.83 | 38.8 |
| | E | 38.1 (15) | 5 (0.2) | 10 (0.4) | 30.5 (1.2) | 1611 | 160.8 (156.5) | 145.4 (32.7) | 0.90 | 58.0 |
| | E | 38.1 (15) | 5 (0.2) | 10 (0.4) | 38 (1.5) | 1365 | 160.8 (156.5) | 134.6 (30.3) | 0.84 | 64.4 |
| | E | 38.1 (15) | 7.6 (0.3) | 10 (0.4) | 25.4 (1) | 2704 | 160.8 (156.5) | 141.7 (31.9) | 0.88 | 29.6 |
| | E | 38.1 (15) | 10 (0.4) | 10 (0.4) | 25.4 (1) | 2782 | 160.8 (156.5) | 144.3 (32.5) | 0.90 | 27.5 |
| | E | 38.1 (15) | 5 (0.2) | 13 (0.5) | 25.4 (1) | 2074 | 160.8 (156.5) | 136.7 (30.7) | 0.85 | 46.0 |
| | E | 38.1 (15) | 5 (0.2) | 15.2 (0.6) | 25.4 (1) | 1861 | 160.8 (156.5) | 143.0 (32.1) | 0.89 | 51.5 |
| | E | 38.1 (15) | 10 (0.4) | 15.2 (0.6) | 38 (1.5) | 796 | 160.8 (156.5) | 144.1 (32.4) | 0.90 | 79.3 |
| 800S162-97 | F | 61 (24) | 5 (0.2) | 10 (0.4) | 25.4 (1) | 2109 | 296.0 (66.5) | 296.3 (66.6) | 1.00 | — |
| | F | 61 (24) | 5 (0.2) | 13 (0.5) | 25.4 (1) | 1637 | 296.0 (66.5) | 297.1 (66.8) | 1.00 | 22.4 |
| | F | 61 (24) | 5 (0.2) | 15.2 (0.6) | 25.4 (1) | 1432 | 296.0 (66.5) | 299.5 (67.3) | 1.01 | 32.1 |
| | F | 61 (24) | 5 (0.2) | 10 (0.4) | 28 (1.1) | 1764 | 296.0 (66.5) | 330.1 (74.2) | 1.11 | 16.4 |
| | F | 61 (24) | 5 (0.2) | 10 (0.4) | 30.5 (1.2) | 1557 | 296.0 (66.5) | 297.8 (67.0) | 1.01 | 26.2 |
| | E | 61 (24) | 5 (0.2) | 10 (0.4) | 25.4 (1) | 2301 | 296.0 (66.5) | 319.8 (65.3) | 0.98 | — |
| | E | 61 (24) | 5 (0.2) | 13 (0.5) | 25.4 (1) | 1966 | 296.0 (66.5) | 282.0 (63.4) | 0.95 | 14.6 |
| | E | 61 (24) | 5 (0.2) | 15.2 (0.6) | 25.4 (1) | 1743 | 296.0 (66.5) | 283.4 (63.71) | 0.96 | 24.3 |
| | E | 61 (24) | 5 (0.2) | 10 (0.4) | 28 (1.1) | 1970 | 296.0 (66.5) | 319.6 (71.84) | 1.08 | 14.4 |
| | E | 61 (24) | 5 (0.2) | 10 (0.4) | 30.5 (1.2) | 1832 | 296.0 (66.5) | 287.8 (64.69) | 0.97 | 20.4 |

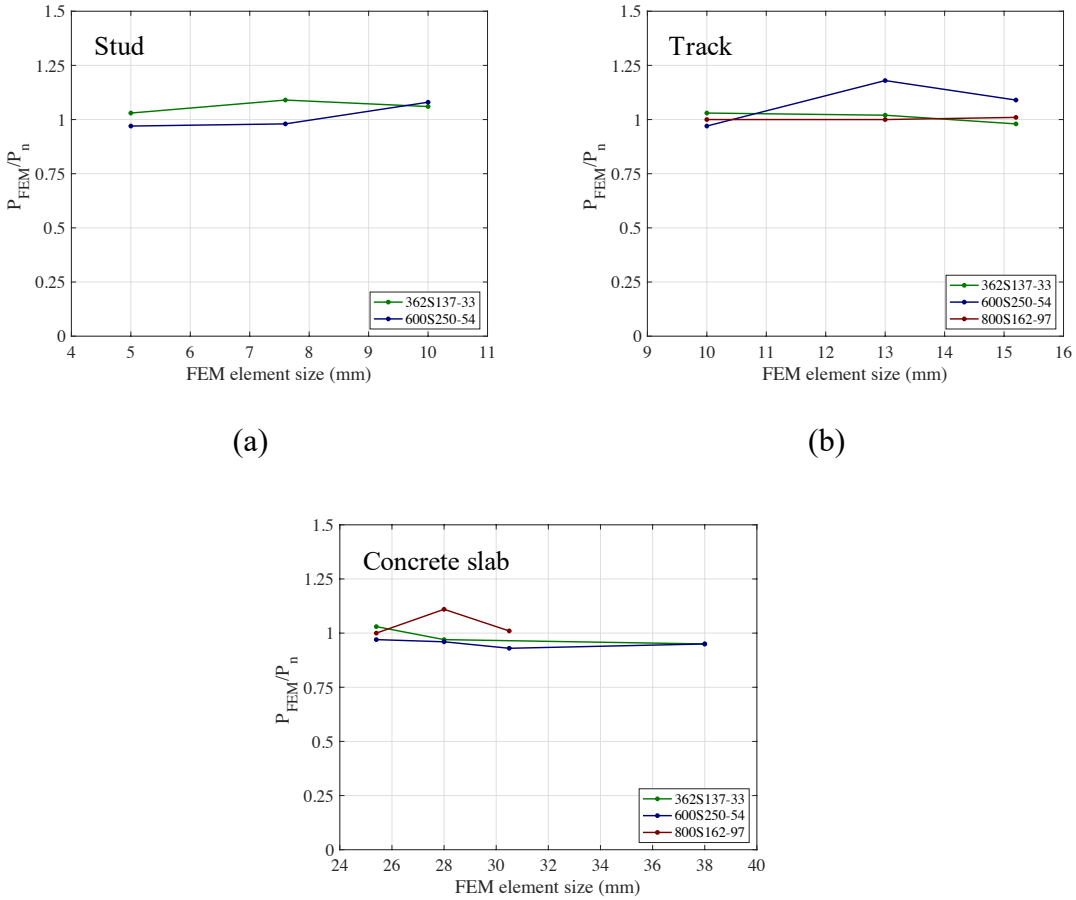


*Figure 75: Parametric study on element sizes of different components of FEMs with full bearing condition; (a) stud, (b) track, and (c) concrete slab.*

*Table 18: Impact of element sizes on the reduction in axial strength of wall assemblies placed at the edge.*

| Section | Bearing condition | Stud length | Stud element size | Track element size | Slab element size | CPU time | FEM $P_{FEM}$ | $P_E/P_F$ |
|---|---|---|---|---|---|---|---|---|
| | | *cm (in)* | *mm (in)* | *mm (in)* | *mm (in)* | *(Sec.)* | *kN (kips)* | |
| 600S250-54 | F | 38.1 (15) | 5 (0.2) | 10 (0.4) | 25.4 (1) | 3652 | 156.5 (35.2) | — |
| | F | 38.1 (15) | 5 (0.2) | 10 (0.4) | 28 (1.1) | 1516 | 154.2 (34.7) | — |
| | F | 38.1 (15) | 5 (0.2) | 10 (0.4) | 30.5 (1.2) | 1514 | 149.7 (33.7) | — |
| | F | 38.1 (15) | 5 (0.2) | 10 (0.4) | 38 (1.5) | 1387 | 152.7 (34.3) | — |
| | F | 38.1 (15) | 7.6 (0.3) | 10 (0.4) | 25.4 (1) | 1528 | 158.4 (35.6) | — |
| | F | 38.1 (15) | 10 (0.4) | 10 (0.4) | 25.4 (1) | 1300 | 173.6 (39.0) | — |
| | F | 38.1 (15) | 5 (0.2) | 13 (0.5) | 25.4 (1) | 1658 | 190.4 (42.8) | — |
| | F | 38.1 (15) | 5 (0.2) | 15.2 (0.6) | 25.4 (1) | 1560 | 175.3 (39.4) | — |
| | F | 38.1 (15) | 10 (0.4) | 15.2 (0.6) | 38 (1.5) | 592 | 178.7 (40.2) | — |
| | E | 38.1 (15) | 5 (0.2) | 10 (0.4) | 25.4 (1) | 3839 | 135.4 (30.4) | 0.87 |
| | E | 38.1 (15) | 5 (0.2) | 10 (0.4) | 28 (1.1) | 2350 | 133.9 (30.1) | 0.87 |
| | E | 38.1 (15) | 5 (0.2) | 10 (0.4) | 30.5 (1.2) | 1611 | 145.4 (32.7) | 0.97 |
| | E | 38.1 (15) | 5 (0.2) | 10 (0.4) | 38 (1.5) | 1365 | 134.6 (30.3) | 0.88 |
| | E | 38.1 (15) | 7.6 (0.3) | 10 (0.4) | 25.4 (1) | 2704 | 141.7 (31.9) | 0.89 |
| | E | 38.1 (15) | 10 (0.4) | 10 (0.4) | 25.4 (1) | 2782 | 144.3 (32.5) | 0.83 |
| | E | 38.1 (15) | 5 (0.2) | 13 (0.5) | 25.4 (1) | 2074 | 136.7 (30.7) | 0.72 |
| | E | 38.1 (15) | 5 (0.2) | 15.2 (0.6) | 25.4 (1) | 1861 | 143.0 (32.1) | 0.82 |
| | E | 38.1 (15) | 10 (0.4) | 15.2 (0.6) | 38 (1.5) | 796 | 144.1 (32.4) | 0.81 |
| 800S162-97 | F | 61 (24) | 5 (0.2) | 10 (0.4) | 25.4 (1) | 2109 | 296.3 (66.6) | — |
| | F | 61 (24) | 5 (0.2) | 13 (0.5) | 25.4 (1) | 1637 | 297.1 (66.8) | — |
| | F | 61 (24) | 5 (0.2) | 15.2 (0.6) | 25.4 (1) | 1432 | 299.5 (67.3) | — |
| | F | 61 (24) | 5 (0.2) | 10 (0.4) | 28 (1.1) | 1764 | 330.1 (74.2) | — |
| | F | 61 (24) | 5 (0.2) | 10 (0.4) | 30.5 (1.2) | 1557 | 297.8 (67.0) | — |
| | E | 61 (24) | 5 (0.2) | 10 (0.4) | 25.4 (1) | 2301 | 319.8 (65.3) | 0.98 |
| | E | 61 (24) | 5 (0.2) | 13 (0.5) | 25.4 (1) | 1966 | 282.0 (63.4) | 0.95 |
| | E | 61 (24) | 5 (0.2) | 15.2 (0.6) | 25.4 (1) | 1743 | 283.4 (63.71) | 0.95 |
| | E | 61 (24) | 5 (0.2) | 10 (0.4) | 28 (1.1) | 1970 | 319.6 (71.84) | 0.97 |
| | E | 61 (24) | 5 (0.2) | 10 (0.4) | 30.5 (1.2) | 1832 | 287.8 (64.69) | 0.97 |

After starting this computational modeling program with aforementioned element sizes, it was observed that in some bearing conditions close to the edge, there was a sudden increase or reduction in the axial strength of assemblies. Figure 76 illustrates these results for assemblies including 362S137-68 studs, where the height of studs was 21 cm (8.3 in). Hence, a second parametric study on the slab element size and different bearing conditions was conducted. Smaller increments close to the edge were investigated. For instance, for a concrete slab with 25.4 mm (1 in) element size, 19 bearing conditions were investigated (Figure 76).

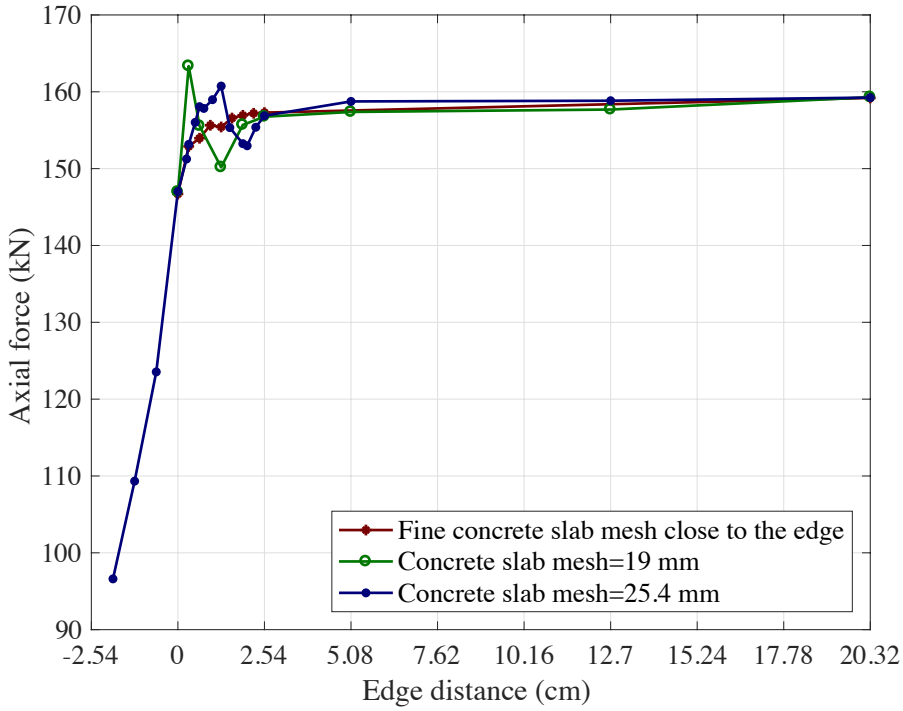


*Figure 76: Parametric study on concrete slab element size and various bearing conditions.*

The element size of concrete slabs was reduced to 19 mm (0.75 in), which increased CPU time but did not improve the result of FEMs, and as it can be observed in Figure 76, there was force rise in 3.17 mm (0.125 in) edge distance. Finally, in 50.8 mm (2 in) to the edge, at the top and bottom of elements, the dimension was reduced to 12.7 mm (0.5 in). Along the slab depth, the dimension equal to 19 mm (0.75 in) was employed (Figure 77). Figure 76 demonstrates that by utilizing finer mesh size close to the edge for concrete slabs, the anomalous behavior near the edge disappeared and the axial reduction aligned with the experiments in Chapter 2. As this element size increased the CPU time significantly, the element sizes presented in Figure 77 were only employed in the assemblies with 19.05 mm (0.75 in), 12.7 mm (0.5 in), 6.35 mm (0.25 in), and 3.17 mm (0.125 in) edge distances.

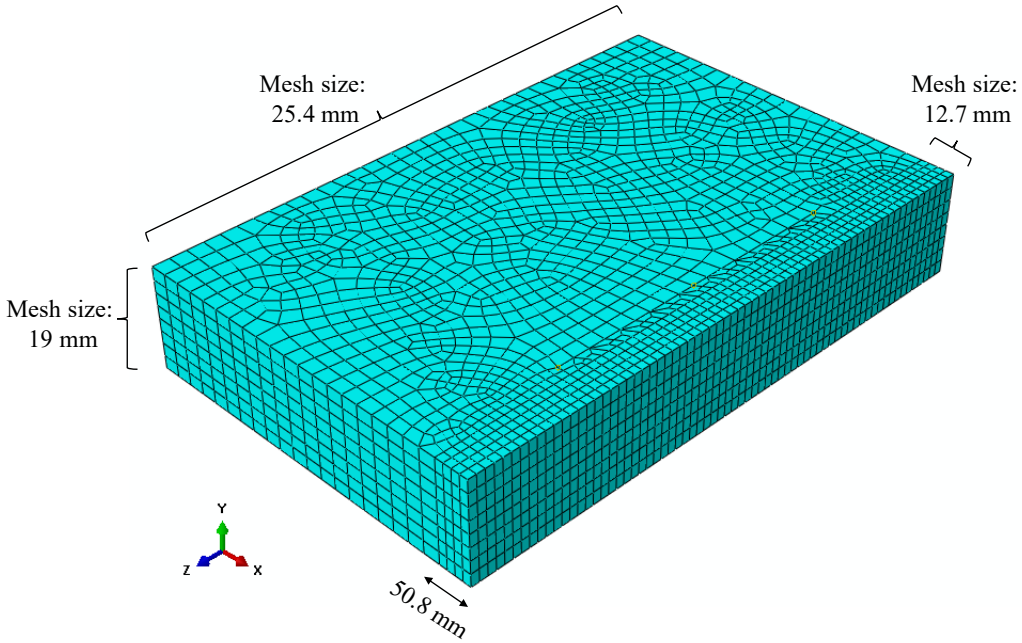


*Figure 77: Fine concrete slab mesh size.*

## 4.5 Boundary conditions, loading application, and initial imperfections

Surface-to-surface and node-to-surface contacts were defined, as described in Chapter 3, to simulate the contact between studs and track flanges, and between the web of the bottom track and the top surface of the concrete slab. The only change in modeling an efficient FEM was removing the node-to-surface contact between studs ends at the top and replacing it with Tie constraints (Figure 78). Generally, contact definitions require more calculation and accordingly add more CPU time to the analyses. Furthermore, it was observed that replacing the top track contact with Tie constraint did not impact the results, since the bearing condition occurred at the bottom ends of the studs, and the tops were less sensitive to small changes in modelling approach.

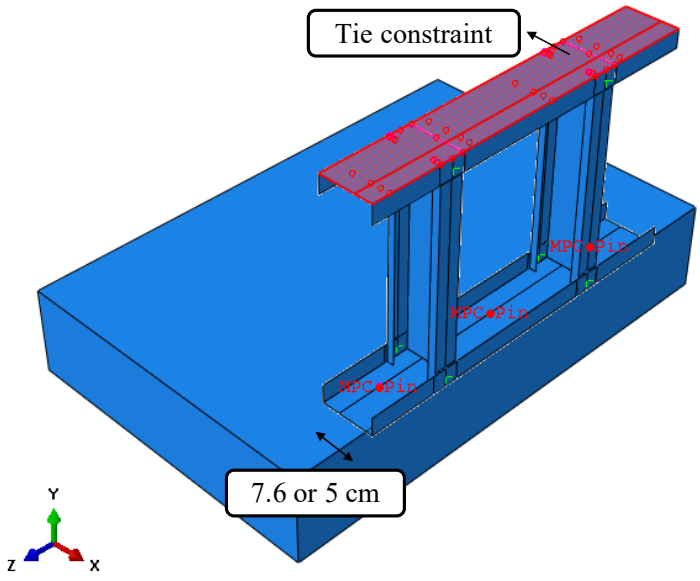


*Figure 78: Tie constraint at the top studs ends and minimum edge distance of MPC pins connecting the bottom track to concrete slab.*

Steel-to-steel fasteners and steel-to-concrete powder-actuated ones were simulated by multi-point constraints (MPC pin). As discussed in Chapter 2, according to Hilti installation manuals [19], in order to prevent any breakout failure of the concrete slab, the minimum edge distance of powder-actuated fasteners is 7.6 cm (3 in). This minimum was provided by offsetting the fasteners from the centerline of tracks in overhang bearing conditions in the experiments. However, in computational modeling program, the web height of cross-sections was variable, and enforcing this minimum was impractical for the smaller cross-sections, such as 362S137-33. Thus, either 7.6 cm or 5 cm (3 in or 2 in) was utilized for edge distance of MPC pins (Figure 78). depending on the web height of the track.

Load application was identical to that described in Chapter 3. Furthermore, since the impact of geometric imperfections was not significant [28], all the components were assumed perfect to save CPU time.

## 4.6 Finite element results

A Python script was developed to automate simulation and analyzing 2376 finite element models in ABAQUS. This Python code can be found in Appendix B. The results of the 2376 finite element analysis are illustrated in Figure 79. The results also are tabulated in Appendix B. Figure 79 consists of six smaller figures and each figure consists of 66 plots illustrating the results of various cross-sections (66 cross-sections were investigated). In the first row, the results of CFS wall assemblies buckling locally is shown by green plots. The blue plots at the second rows illustrates the results of specimen which buckle

distortionally, and finally, the result of full-height specimens buckling globally are displayed in the last row and red plots. In the left column figures, the axial strengths of all the assemblies are plotted against their bearing condition. Each plot illustrates the axial force of each assembly in different bearing condition when it was moved to the edge. The x-axis represents the edge distance. There are negative edge distances which shows the overhang bearing conditions. In order to see better the reduction in axial capacities, right column figures were produced. They consist of normalized plots and in each bearing condition, the axial forces were divided by their corresponding axial strength of full bearing condition. Figure 79 demonstrates clearly that there is a trend in the response of wall assemblies of various heights and cross-sections to their bearing condition. As the assemblies were moved from the slab center (20.32 cm) to the edge (0 cm) and finally overhang (negative values in x-axis), the axial strength decreased. The axial capacity of stud-track assemblies with various bearing conditions was compared with the strength of the corresponding assembly with the full bearing condition and plotted separately in Figure 80. The symbols shown in each plot represent the bearing condition according to Figure 24 (chapter2).

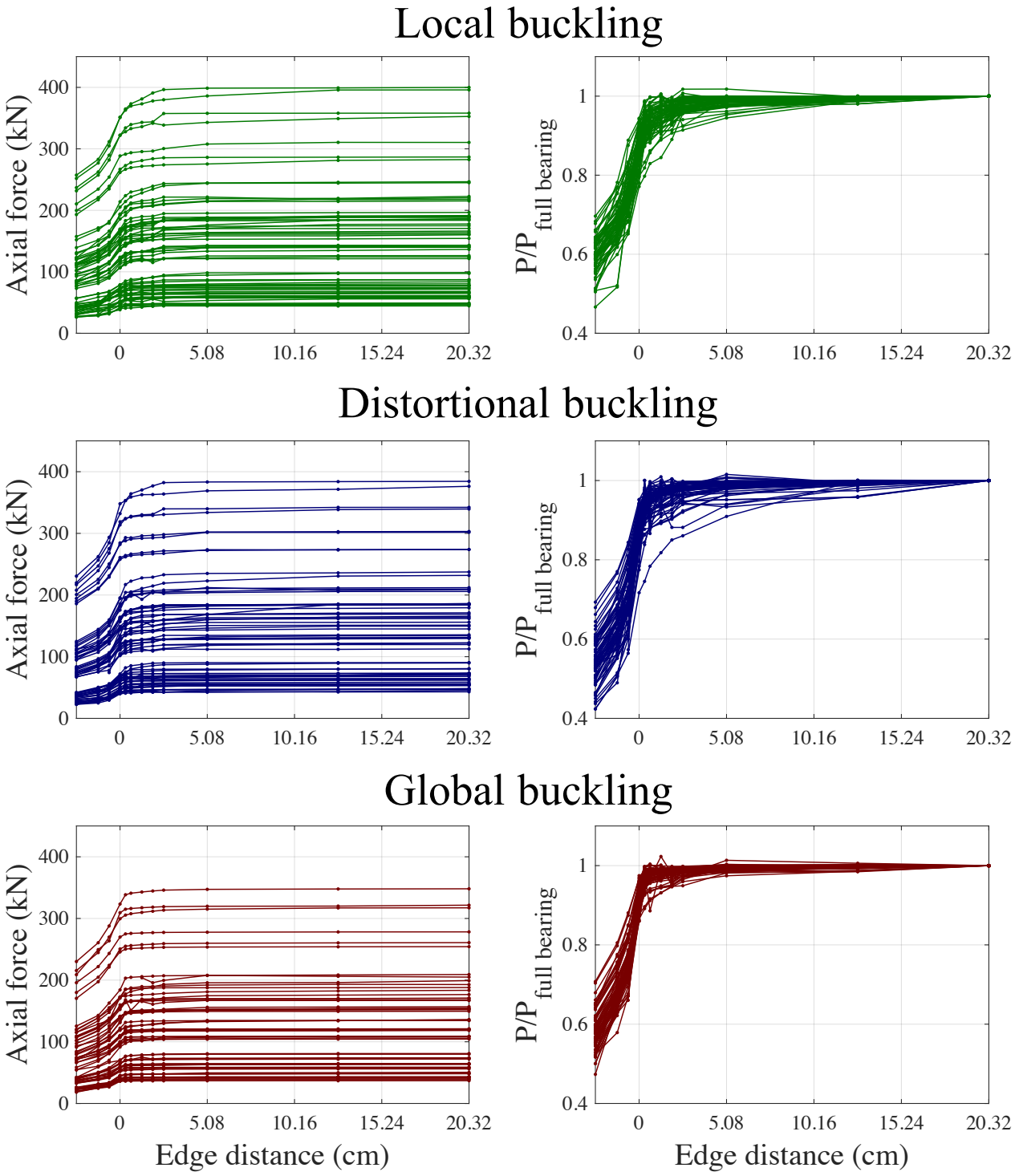


*Figure 79: force-edge distance plots of 2376 finite element models.*

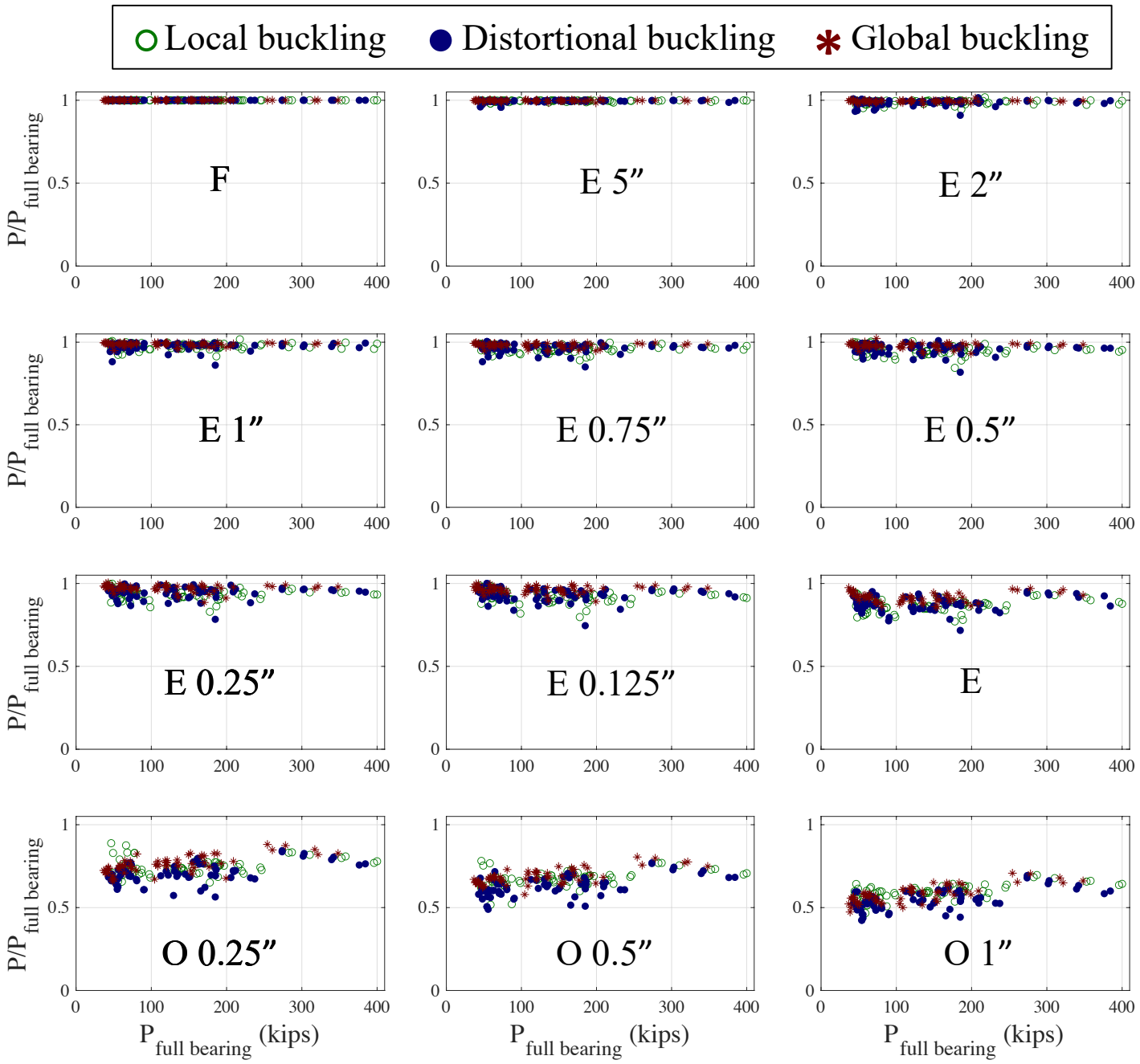


*Figure 80: Normalized plots of finite element analysis for each bearing conditions.*

Figure 80 shows the reduction in each bearing condition and edge distance is almost constant regardless of cross-section and height. When the assemblies were placed far from the edge, the $P/P_{full\ bearing}$ ratios were almost one, indicating there was no reduction in axial strength. However, by moving them closer to the edge, for instance 3.17 mm (0.125 in) to the edge and at the edge, the reduction was considerable and should be considered in designs and calculations. Although the response of different assemblies can be considered constant, as the assembles became close to the edge and finally overhang, the data and responses became more variable. Furthermore, it can be observed that the spread of the results of global buckling specimens is less variable rather than local and distortional cold-formed steel stud assemblies. Finally, as observed in experiments, the reduction in axial strength of wall assemblies overhanging from the edge was significant.

## 4.7 Stress distribution at studs ends

To determine a mechanics-based description of the underlying stress imparted to the studs, the Von Mises stress distribution at the end of studs under the peak load was exported from ABAQUS software. Stud-track assemblies consisting of 600S162-54 were selected with two heights: 30.5 cm (12 in), on which the experiments were conducted, and full-height (2.4 m). Furthermore, four different bearing conditions were investigated: full bearing, 25.4 mm (1 in) to the edge, at the edge, and 3.17 mm overhanging from the edge.

By default, ABAQUS uses five section points through the thickness of a S4R shell element. In order to get the stress distribution, the Von Mises stress of middle section point, i.e. the third point (SP3), of each element at the end of studs was outputted. In Figure 81,

Figure 82, and Figure 83, the stress distribution of 30.5 cm (12 in) 600S162-54 assembly with three different bearing condition is compared to the result of the assembly with full bearing condition. The edge of the concrete slab is placed at the right hand of cross-section. While the assemblies consisted of two studs only the stress distribution of the stud first to buckle is plotted.

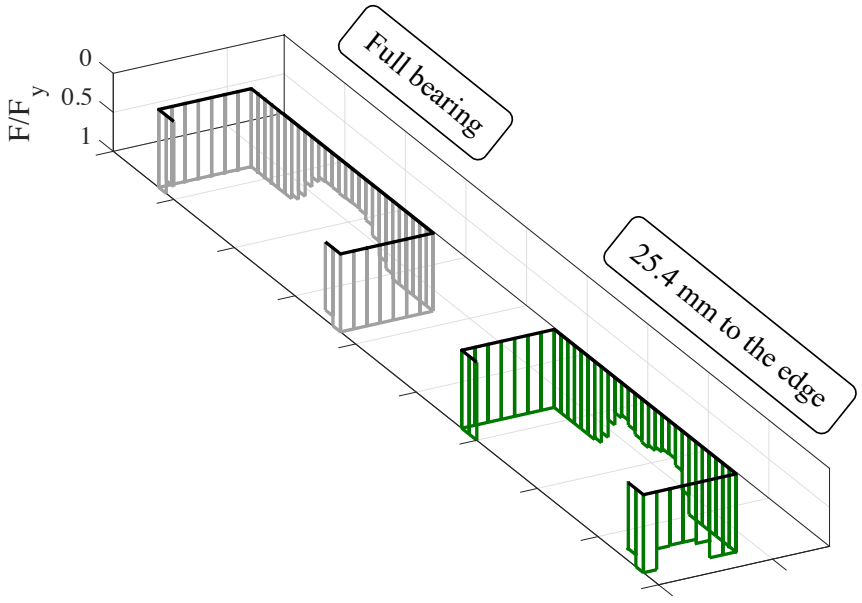


*Figure 81: Comparing the Von Mises stress distribution of 30.5 cm assembly (600S162-54) with 25.4 mm edge distance with the corresponding assembly with full bearing condition.*

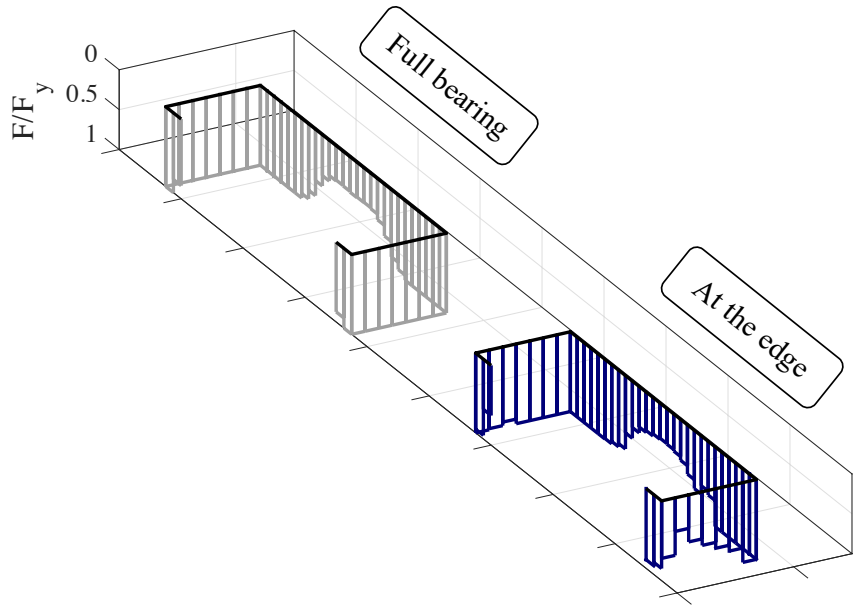


*Figure 82: Comparing the Von Mises stress distribution of 30.5 cm assembly (600S162-54) with at the edge bearing condition with the corresponding assembly with full bearing condition.*

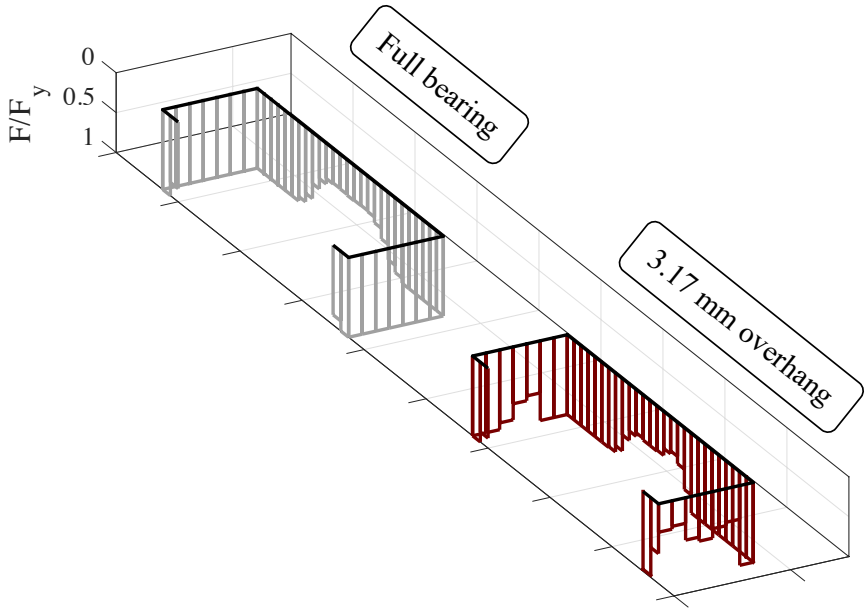


*Figure 83: Comparing the Von Mises stress distribution of 30.5 cm assembly (600S162-54) overhanging 3.17 mm from edge with the corresponding assembly with full bearing condition.*

Figure 84 to Figure 86 illustrate the stress distribution of full-height assemblies. Figures show that the stress distribution was uniform when the assemblies were placed at the center of concrete slabs. As the system became closer to the edge, the stress distribution became more non-uniform, which impacted the axial strength of assemblies. However, in each bearing condition, this non-uniformity was different according to the height of studs. For instance, by comparing Figure 82 with Figure 85, the stress at the end of 30.5 cm stud (at the edge bearing condition) and the flange close to the edge was more non-uniform than in the full-height assembly. Correspondingly, the reduction in axial capacity was 15% for 30.5 cm (12 in) 600S162-54 stud assembly when it was installed at the edge and this reduction was 9% for 2.45 m (96 in) 600S162-54 system installed at the edge. To better understand the distribution of Von Mises stress at the end of studs, Figure 87, obtained from ABAQUS, shows these distributions for full-height assemblies.

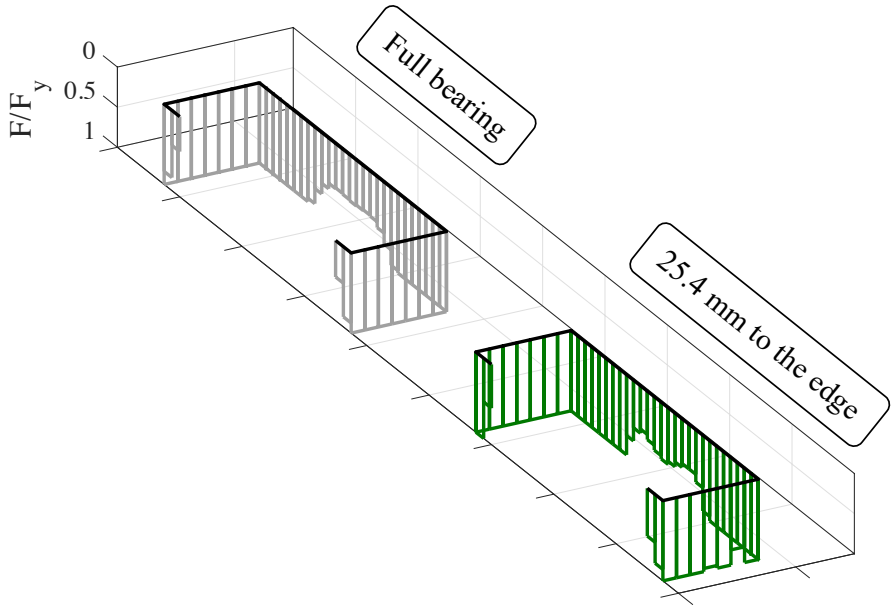


*Figure 84: Comparing the Von Mises stress distribution of full-height assembly (600S162-54) with 25.4 mm edge distance with the corresponding assembly with full bearing condition.*

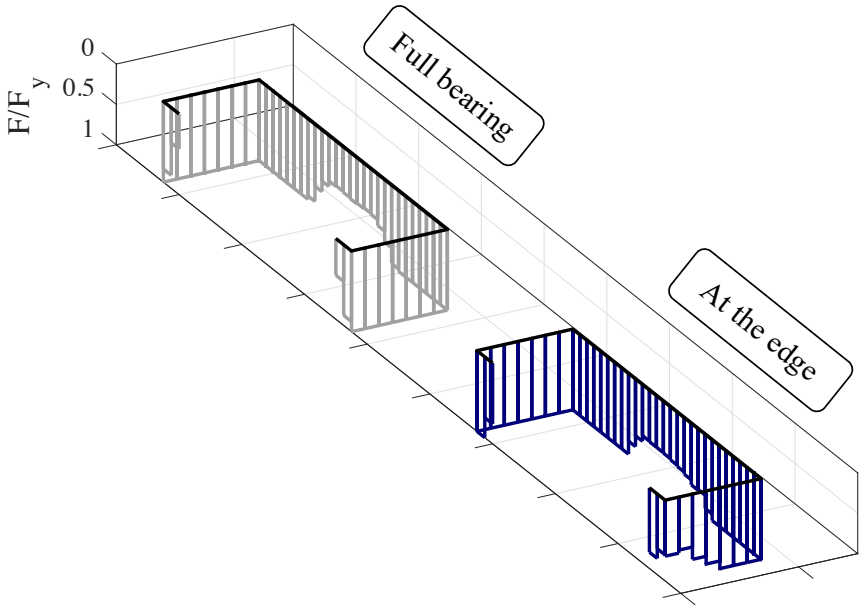


*Figure 85: Comparing the Von Mises stress distribution of full-height assembly (600S162-54) with edge bearing condition with the corresponding assembly with full bearing condition.*

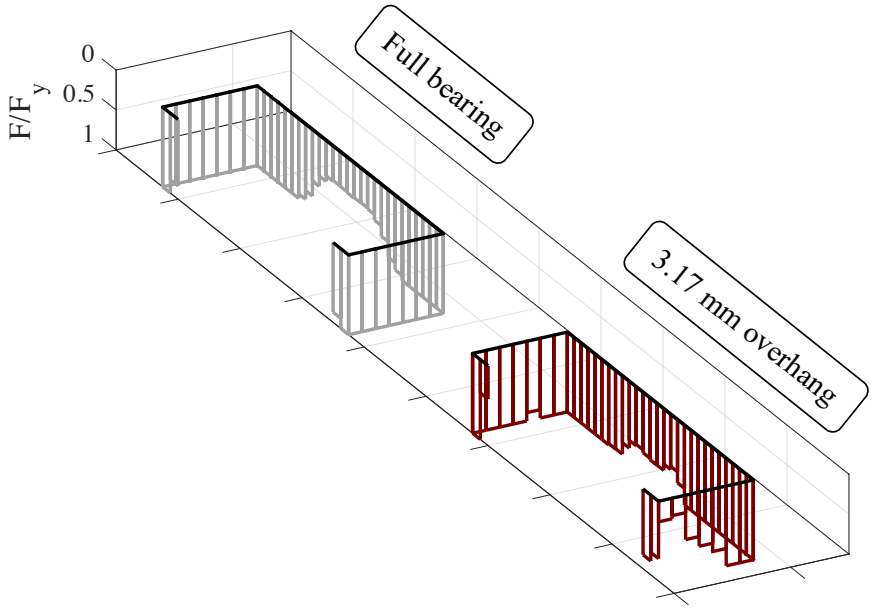


*Figure 86: Comparing the Von Mises stress distribution of full-height assembly (600S162-54) overhanging 3.17 mm from edge with the corresponding assembly with full bearing condition.*

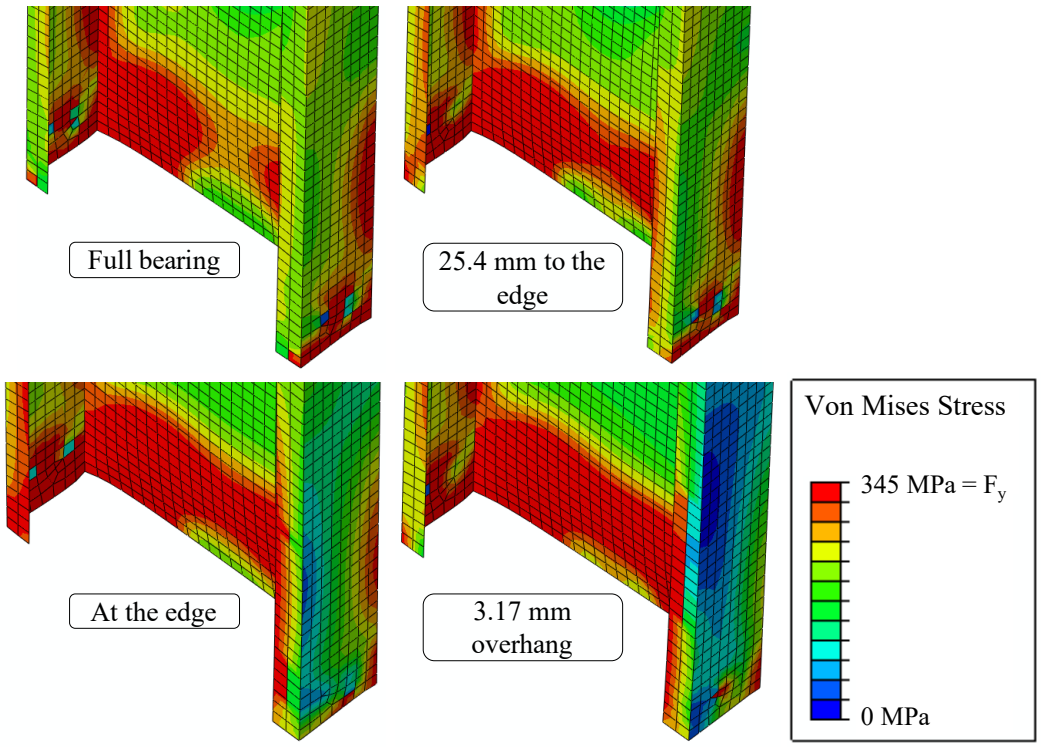


*Figure 87: The Von Mises stress distribution at the end of full- height stud assemblies (600S162-54) under the peak load.*

# CHAPTER 5

# Implementing Slab Edge Effects into Design Codes

Experimental and finite element analysis results confirm that placing the cold-formed steel wall assemblies near the edge impacts the axial strength of these systems. Comparing experimental results with the compressive strengths predicted by AISI S100-16 ($P_{nm}$) in Figure 47 demonstrates that available predictive methods do not accurately capture axial capacity at these column heights. The final thrust of this dissertation is to provide recommendations for the designer that capture the observed reduction in axial capacity. In this chapter, two types of design recommendations are formulated: empirical reduction factors derived from the experimental and computational programs, and new stress distributions that mimic slab edge effects on the studs. The intent in providing two methods of accounting for strength reduction is to enable both back-of-the-envelope calculations and analysis-based design.

## 5.1 Experimental-derived reduction factors

Comparing the experimental results (Chapter 2) with the axial strength of assemblies calculated by AISI S100-16, three different reduction factors are suggested, dependent on the distance to the slab edge. As illustrated in Figure 88, when the stud assembly was placed sufficiently far from the edge, at distances larger than 25.4 mm (1 in), there is no need for reduction factor. However, for the assemblies placed between 25.4 mm (1 in) and 12.7 mm

(0.5 in) to the edge, a reduction factor (RF) of RF= 0.9 is recommended. For cases in which the edge distance is between 3.175 mm (0.125 in) to the edge, also for those assemblies overhanging less than 12.7 mm (0.5 in) from the edge, the reduction factor RF=0.8 is proposed. However, due to the significant reduction in the axial capacity of assemblies overhanging more than 12.7 mm (0.5 in) from the edge and a considerable difference between the experimental results and $P_{nm}$ (Figure 88), it is recommended that these assemblies should be removed and reinstalled. The proposed reduction factors almost match the average of $P_{max}/P_{nm}$ in each bearing condition, as tabulated in Table 19.

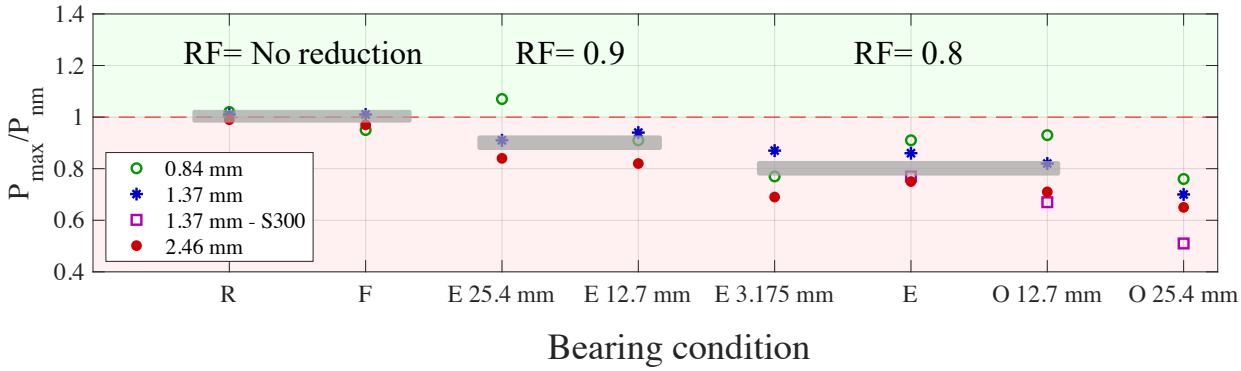


*Figure 88: The proposed reduction factors based on the comparison between experimental results and predicted compression strengths by AISI S100-16.*

The reduction factors proposed herein were based on experiments, where only four edge distance close to the edge were investigated. Conducted finite element simulations in chapter 4 and considering smaller increment closer to the edge could improve the design recommendations, which is discussed follow.

## 5.2 Recommendations for analysis-based design

In Chapter 4, results from 2376 finite element models of variable-height assemblies were described. The compressive strengths of all the assemblies were calculated through direct strength method (DSM) equations presented in the North American cold-formed steel specification (AISI S100-16, section E). Furthermore, for overhang bearing conditions, the allowable strength of members was calculated by equations proposed in section H1.2 of AISI S100-16, as described in Chapter 3. To determine the critical elastic local and distortional column buckling loads, $P_{crl}$ and $P_{crd}$, respectively, all the 66 cross-sections were simulated in CUFSM software. The traditional signature curves of all the cross-sections were conducted. Figure 89 which is the signature curve of 800S62-68 illustrates that finding the local and distortional buckling loads and corresponding half-wave lengths cannot always be identified from the first and second minima of signature curve, which may have indistinct minima [2]. For those sections with indistinct minima, the constrained finite strip method (*c*FSM), which can determine both local and distortional buckling half-wave lengths in all cases [36], were conducted and the corresponding local and distortional buckling loads were identified from signature curves.

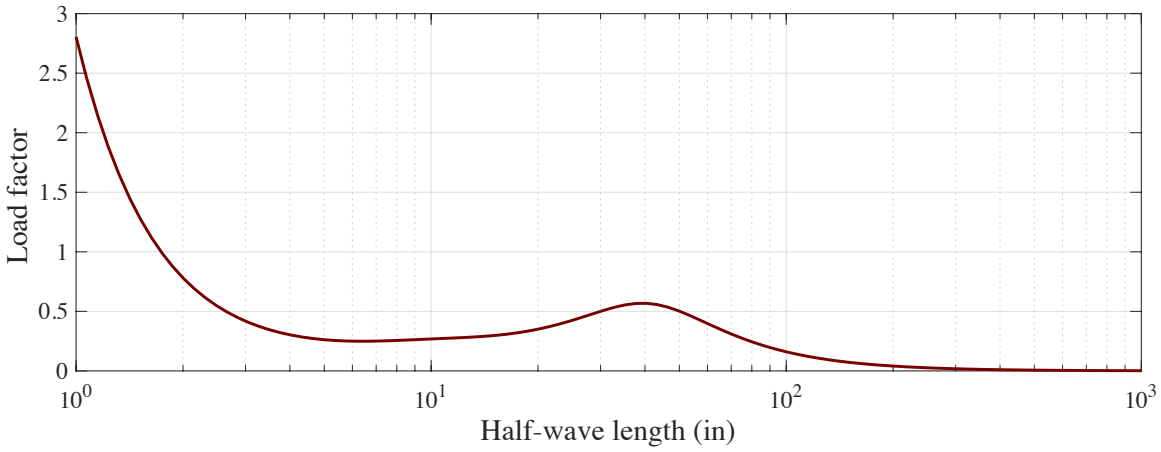


*Figure 89: Signature curve of member 800S162-68 with indistinct distortional buckling load.*

Figure 90 represents FEM-to-predicted ratios for all the assemblies studied herein. Figure 90(a) illustrates the result of short specimens buckling locally. The results of specimens buckling distortionally are illustrated in Figure 90(b). And the ratios of full-height specimens are shown in Figure 90(c).

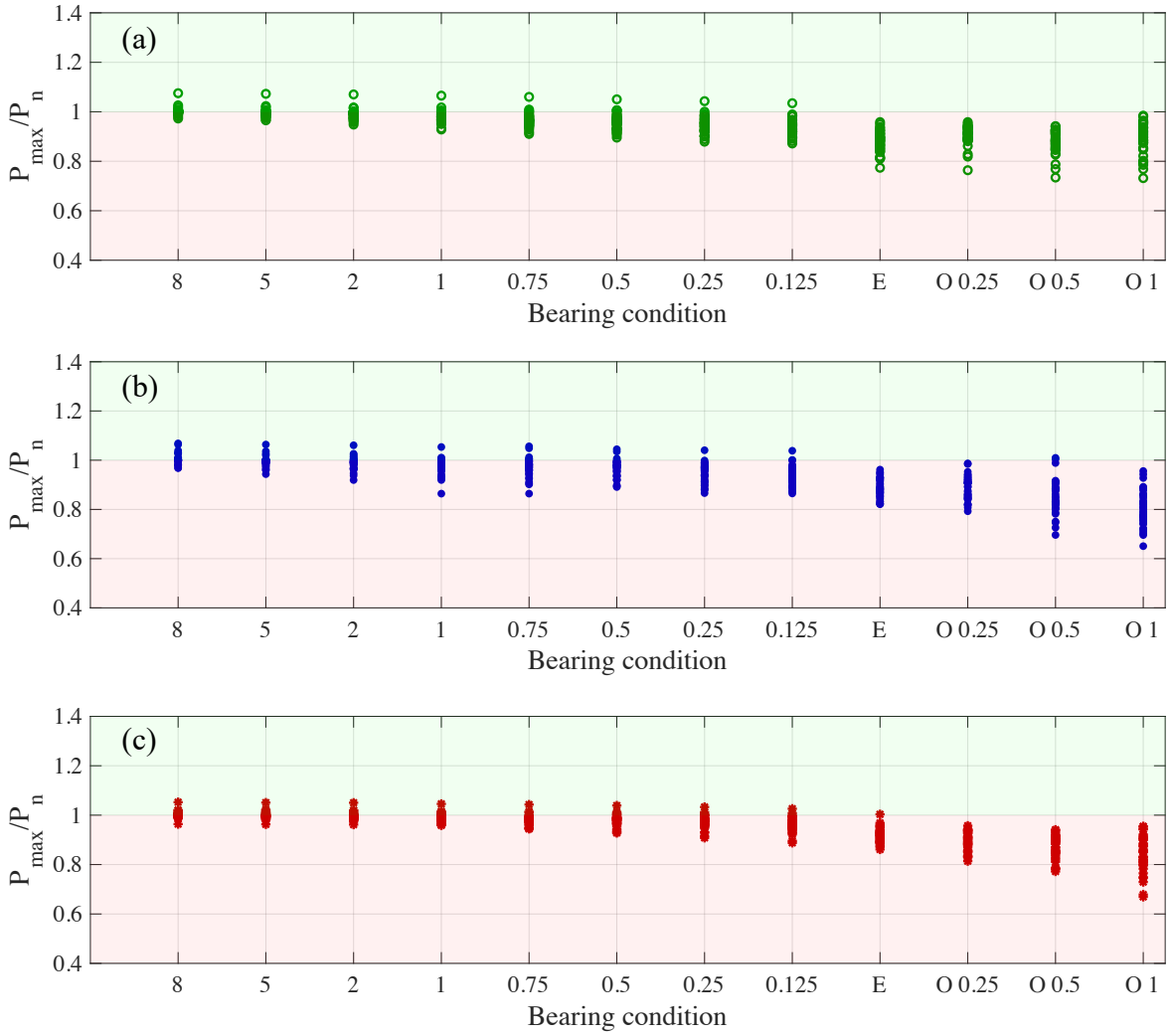


*Figure 90: FEM-to-predicted ratios by Direct Strength Method; (a) assemblies buckling locally, (b) assemblies buckling distortionally, and (c) assemblies buckling globally.*

Figure 90 clarifies well that in the assembles with enough edge distance (edge distance > 2.54 cm), the DSM predictions match FEM results, with FEM-to-predicted ratios near or even more than one. However, by moving the systems close to the edge, the prediction became worse. There is a trend in the FEM-to-predicted ratios across all the various-height

specimens. Hence, generalized reduction factors, regardless of cross-section and stud height, can be proposed. The averages and standard deviations (σ) of all $P_{max}/P_n$ are tabulated in Table 19, which can be used for proposing reduction factors. In this table, for each bearing condition, first the averages and standard deviations were calculated for variable-height specimens, i.e. local, distortional, and global buckling specimens, separately. Then they were calculated regardless of wall assemblies height. Reduction factors are proposed in Figure 91. The proposed reduction factors are close to the averages of $P_{max}/P_n$, although they are more conservative.

*Table 19: The averages and standard deviations of $P_{max}/P_n$*

| **Bearing Condition** | **Computational Modeling Program** | | | | | | | | **Experiments** | |
|---|---|---|---|---|---|---|---|---|---|---|
| Distance from edge | Specimens Height | | | | | | | | | |
| | Local | | Distortional | | Global | | All FEMs | | | |
| mm (in) | mean | σ | mean | σ | mean | σ | mean | σ | mean | σ |
| Full | 1.00 | 0.015 | 1.00 | 0.021 | 1.00 | 0.013 | 1.00 | 0.017 | 0.98 | 0.031 |
| 127.0 (5) | 1.00 | 0.017 | 0.99 | 0.021 | 1.00 | 0.014 | 1.00 | 0.017 | — | — |
| 50.8 (2) | 0.99 | 0.020 | 0.99 | 0.026 | 1.00 | 0.015 | 0.99 | 0.021 | — | — |
| 25.4 (1) | 0.98 | 0.024 | 0.98 | 0.032 | 0.99 | 0.017 | 0.98 | 0.026 | 0.94 | 0.118 |
| 19.1 (0.75) | 0.96 | 0.027 | 0.97 | 0.038 | 0.98 | 0.020 | 0.97 | 0.030 | — | — |
| 12.7 (0.5) | 0.96 | 0.032 | 0.97 | 0.035 | 0.98 | 0.022 | 0.97 | 0.031 | 0.89 | 0.062 |
| 6.4 (0.25) | 0.94 | 0.034 | 0.95 | 0.040 | 0.97 | 0.025 | 0.96 | 0.036 | — | — |
| 3.2 (0.125) | 0.94 | 0.034 | 0.94 | 0.039 | 0.96 | 0.029 | 0.95 | 0.036 | 0.78 | 0.090 |
| Edge | 0.88 | 0.042 | 0.89 | 0.039 | 0.92 | 0.030 | 0.89 | 0.041 | 0.84 | 0.082 |
| O 6.4 (0.25) | 0.90 | 0.039 | 0.88 | 0.051 | 0.89 | 0.038 | 0.89 | 0.044 | — | — |
| O 12.7 (0.5) | 0.92 | 0.051 | 0.85 | 0.071 | 0.87 | 0.046 | 0.88 | 0.064 | 0.82 | 0.110 |
| O 25.4 (1) | 0.89 | 0.065 | 0.80 | 0.073 | 0.84 | 0.072 | 0.84 | 0.078 | 0.70 | 0.055 |

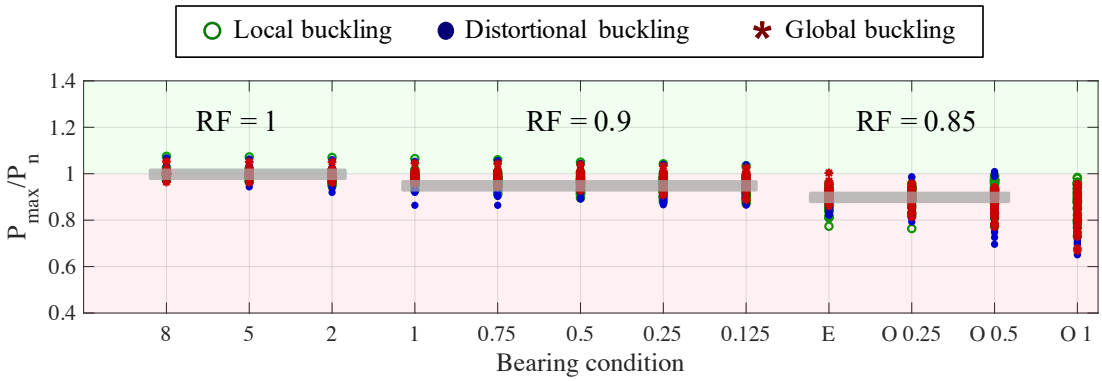


*Figure 91: The proposed reduction factors based on the high-fidelity computational modeling program and predicted compression strengths by AISI S100-16.*

Figure 91 shows that for all of the assemblies, regardless of their height, 2.54 cm (1 in) is a point where the stress distribution at the ends of studs start to become nonuniform. This phenomenon can be observed in the Von Mises stress at end of 30.5 cm (12 in) and 244 cm (96 in) assemblies, shown in Figure 92. Furthermore, for the edge distances less than 2.54 cm (1 in), reduction factors are required.

For the assemblies that their edge distance is greater than 25.4 mm (1 in), there is no need for applying a reduction factor. For the edge distances between 25.4 mm (1 in) and 3.17 mm (0.125 in) to the edge, the proposed reduction was 0.9. For the assemblies placed at the edge or overhanging from the edge and the overhang distance is less than 12.7 mm (0.5 in), the reduction factor RF= 0.85 was recommended. Finally, as discussed before, it is highly recommended that the assemblies with overhang edge distance greater than 12.7 mm (0.5 in) should be removed and reinstalled.

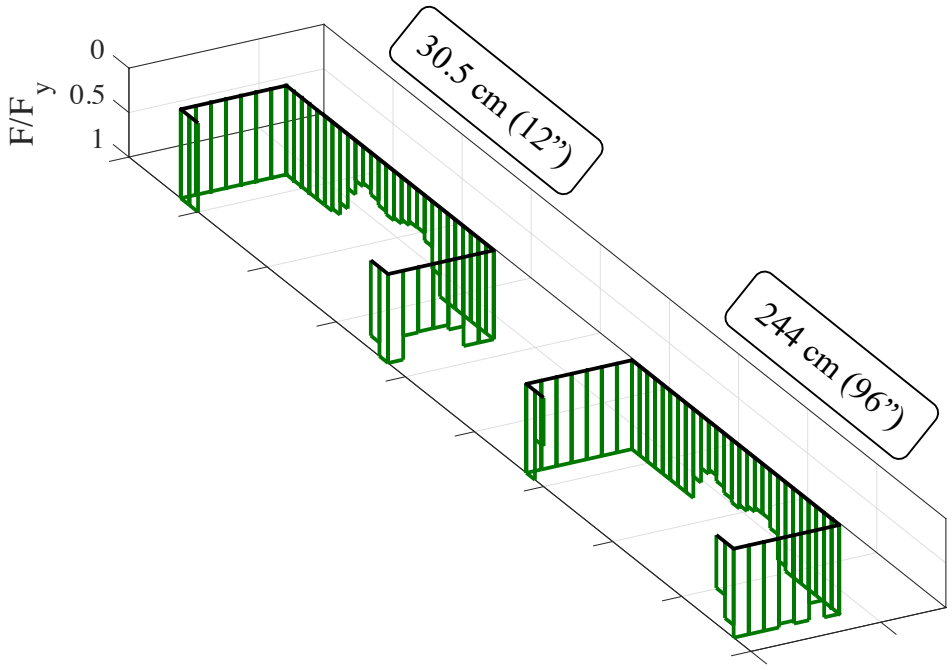


*Figure 92: Von Mises stress distribution of 30.5 cm (12 in) and full-height 600S162-54 stud assemblies when they were installed 25.4 mm (1 in) to the edge.*

The proposed reduction factors based on the high-fidelity computational modeling program on 2376 finite element models were less-conservative than the reduction factors based on the experiment results. $P_{max}/P_n$ ratios of computational modeling program and experiments are combined in Figure 93. As illustrated in Figure 93, the experimental $P_{max}/P_n$ ratios follow the trend in the FEM-to-predicted ratios, although it approves more-conservative reduction factors were required in some bearing conditions based on the experiments. Both of the experiments and the computational modeling program showed that for edge distance greater than 25.4 mm (1 in), no reduction factor is required. According to the experiments, for 3.17 mm (0.125 in) edge distance, the proposed reduction factor is 0.8 (Figure 88), which is 11% more conservative than the proposed

reduction factor proposed in Figure 91. Furthermore, for the edge and overhang bearing conditions, the reduction factor was 0.8 based on the experiment. However, for the mentioned bearing conditions, 0.85 was suggested based on the computational modeling program (Figure 91). Hence, for these bearing conditions, the reduction factor based on the experiments was 6% more conservative. It can be due to the screw failure which happened during the experiments in 2.46 mm (97-mil) assemblies. And due to this phenomenon, a smaller reduction factor was proposed for the assemblies placed at the slab edge or overhanging from it.

Although by employing the proposed reduction factors, the compressive strength of the cold-formed steel wall assemblies can be calculated through direct strength equations of AISI S100-16, it is recommended conservatively that the wall assemblies should be kept 2.54 cm (1 in) far from the edge to prevent any impact of the non-uniform bearing condition on the axial strength.

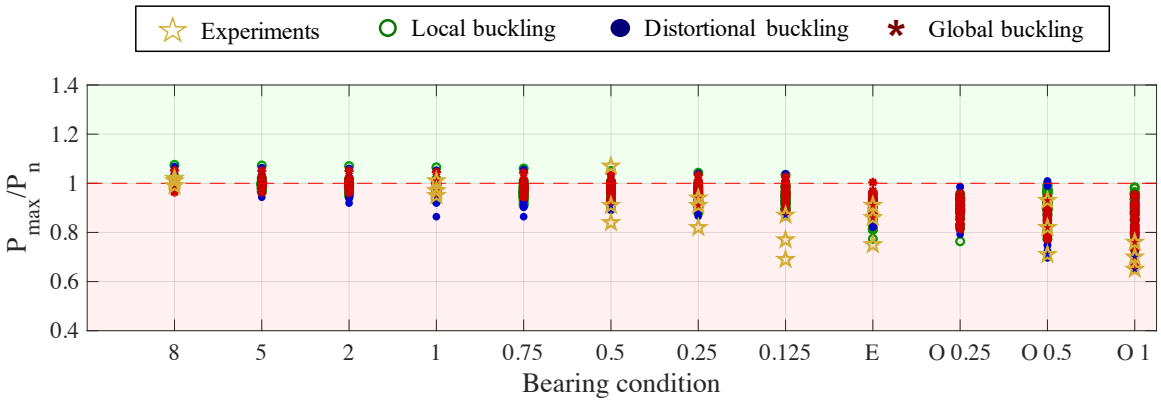


*Figure 93: FEM-to-predicted and experiment-to-predicted ratios.*

## 5.3 AISI S100-16 strength prediction by utilizing non-uniform stress distribution

As mentioned before, the stress distribution is assumed uniform in Direct Strength Method which is employed for calculating the compressive strength of members in AISI S100-16. However, according to the finite element results, it was concluded that the stress distribution at the end of studs became non-uniform as the wall assembly get closer to the edge. This is the source of the erosion of axial capacity as the studs approached the slab edge. In previous sections and chapters, in order to compare the results of experiments and finite element analyses with the predicted strengths by AISI S100-16, uniform stress distributions at the end of studs are assumed for calculating the critical elastic local and distortional buckling loads of studs, $P_{crl}$ and $P_{crd}$, respectively. However, in this chapter, $P_{crl}$ and $P_{crd}$ of the sections with non-uniform stress distribution are determined to be utilized in DSM equations.

Ten variable stud assemblies with different cross-sections, height, and bearing condition were considered (Table 20). The studs were simulated in CUFSM software. The length of the elements was considered the same as the element size of simulated studs in ABAQUS software in Chapter 3 and 4. The actual Von Mises stress distributions of specimens, output from the computation modeling program in Chapter 4, were used for loading. These stress distributions are illustrated in Figure 94. The simulated 600S162-54 stud (at the edge bearing condition) in CUFSM tool with non-uniform stress distribution at its end is illustrated in Figure 95(a), and its corresponding non-uniform Von Mises stress distribution acquired from ABAQUS software is illustrated in Figure 95(b) as an example.

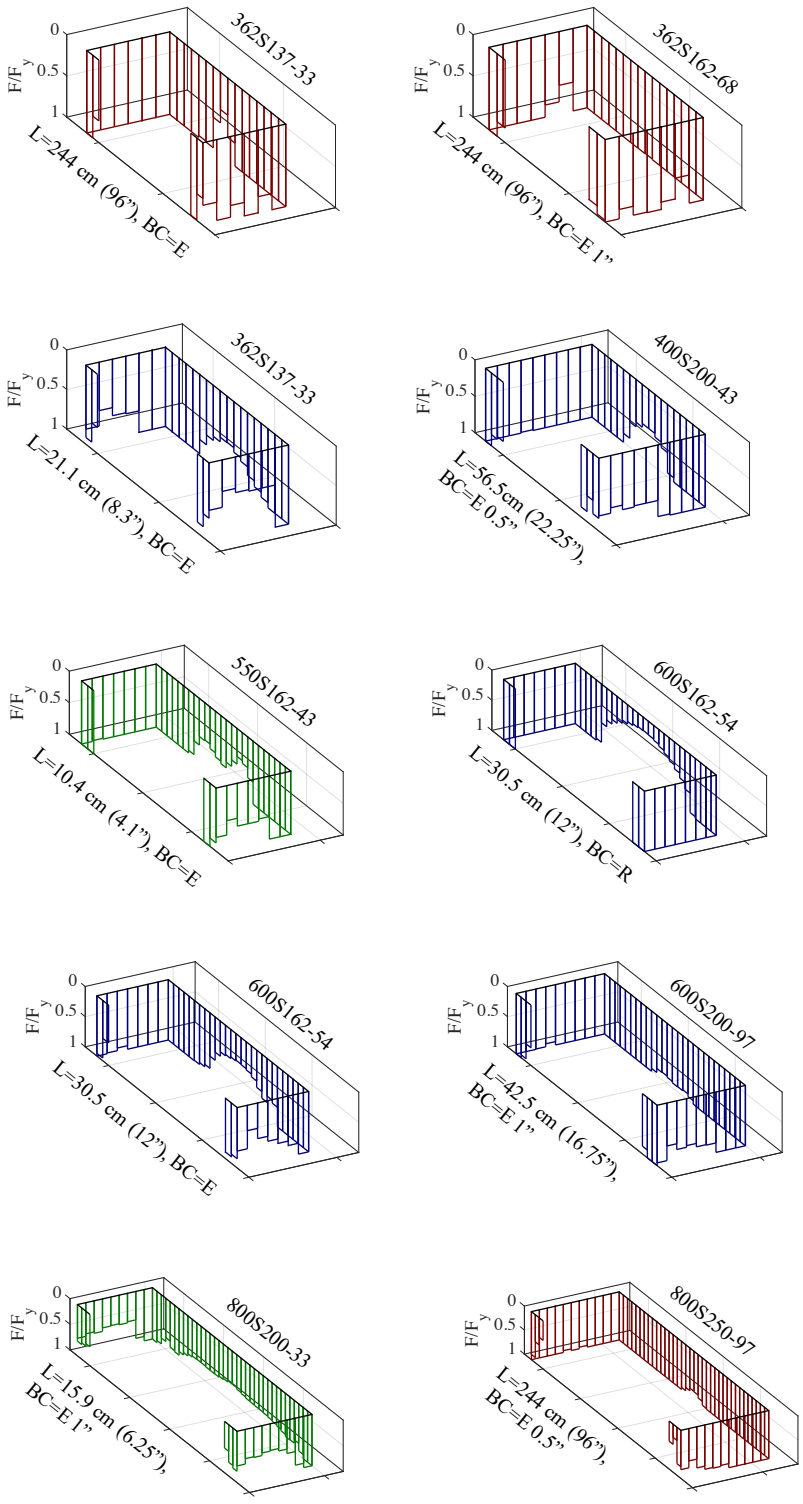


*Figure 94: Non-uniform stress distribution of different assemblies obtained from ABAQUS.*

*Table 20: Variable modeled assemblies in CUFSM software with actual Von Mises stress distribution.*

| Section | Length *cm (in)* | Buckling Mode | Bearing Condition |
|---|---|---|---|
| 362S137-33 | 244 (96) | G | E |
| 362S162-68 | 244 (96) | G | E 1" (2.54 cm) |
| 400S137-68 | 21.1 (8.3) | D | E |
| 400S200-43 | 56.5 (22.25) | D | E 0.5" (1.27 cm) |
| 550S162-43 | 10.4 (4.1) | L | E |
| 600S162-54 | 30.5 (12) | D/L | R |
| 600S162-54 | 30.5 (12) | D/L | E |
| 600S200-97 | 42.5 (16.75) | D | E |
| 800S200-33 | 15.9 (6.25) | L | E 1" (2.54 cm) |
| 800S250-97 | 244 (96) | G | E 0.5" (1.27 cm) |

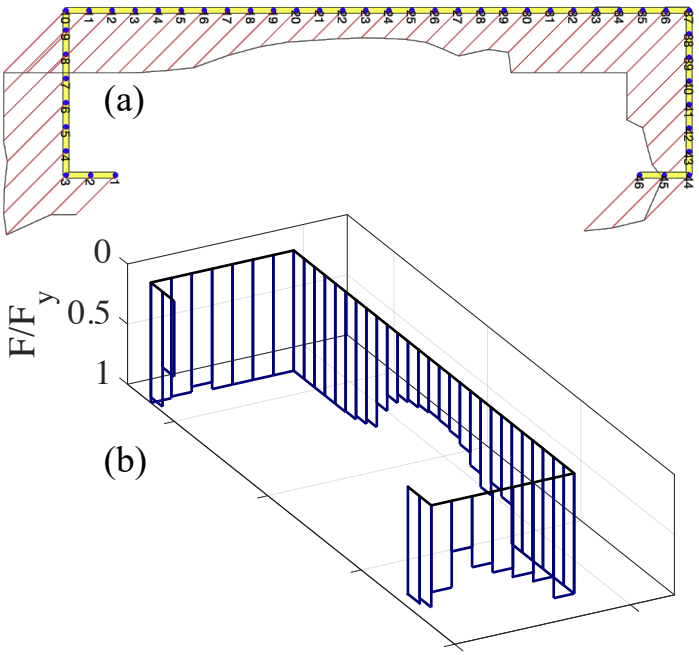


*Figure 95: (a) Modeled 600S162-54 cross-section with edge bearing condition in CUFSM with non-uniform stress distribution; (b) Von Mises stress distribution output from ABAQUS.*

Traditional signature curve analyses were performed for all the assemblies described in Table 20. These results for 600S162-54 stud assembly with edge bearing condition are compared to the same section with a uniform stress distribution. Their signature curves are shown in Figure 96.

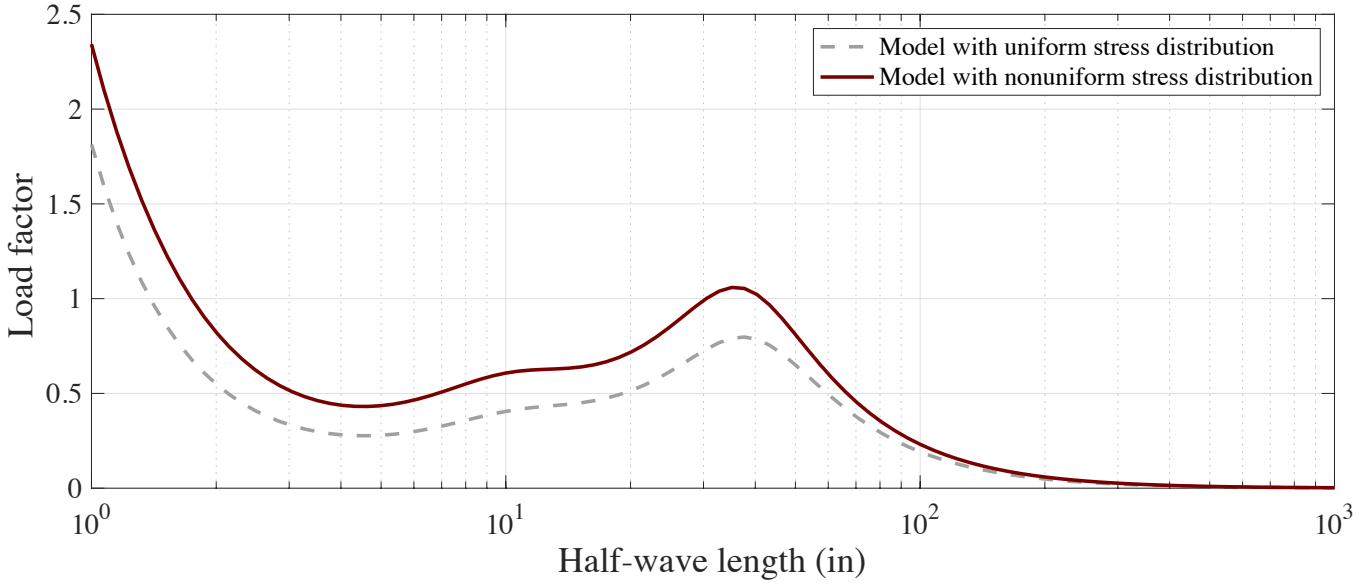


*Figure 96: Signature curves of 30.5 cm (12 in) 600S162-54 cross-section with uniform and nonuniform stress distribution.*

It should be noted, in the signature curves plotted in Figure 96, although the load factor of the section with nonuniform stress distribution is higher than the cross-section with uniform stress distribution, the member axial yield strength, $P_y$, is lower and cannot be calculated by Eq (12). The member axial yield strength was calculated by multiplying the area of each element by the distributed stress in the element. For instance, for 600S162-54 cross-sections which their signature curves are illustrated in Figure 96, $P_y$ for rigid bearing

condition was 126.2 kN (28.36 kips) and for the edge bearing condition with a non-uniform stress distribution was 101.6 kN (22.83 kips). The critical elastic local and distortional column buckling loads were determined by load factors and calculated member axial yield strength. The predicted strengths by AISI S100-16, $P_n$, are compared to the finite element results ($P_{FEM}$) in Table 21.

$$P_y = A_g F_y \tag{12}$$

*Table 21: Predicted compressive strength by AISI S100-16 specification when nonuniform stress distributions were applied at the end of members.*

| **Section** | **Length** *cm (in)* | **Bearing condition** | **$P_{FEM}$** *kN (kips)* | **AISI S100-16 ($P_n$)** *kN (kips)* | **1-$P_{FEM}/P_n$** *%* |
|---|---|---|---|---|---|
| 362S137-33 | 244 (96) | E | 36.7 (8.24) | 38.0 (8.54) | 3.6 |
| 362S162-68 | 244 (96) | E 1" (2.54 cm) | 171.3 (38.5) | 174.9 (39.32) | 2.1 |
| 400S137-68 | 21.1 (8.3) | E | 144.7 (32.54) | 148.7 (33.44) | 2.8 |
| 400S200-43 | 56.5 (22.25) | E 0.5" (1.27 cm) | 77.6 (17.44) | 81.0 (18.22) | 4.5 |
| 550S162-43 | 10.4 (4.1) | E | 66.4 (14.93) | 68.9 (15.48) | 3.7 |
| 600S162-54 | 30.5 (12) | R | 144.7 (32.53) | 143.2 (32.19) | -1.0 |
| 600S162-54 | 30.5 (12) | E | 123.4 (27.75) | 127.4 (28.63) | 3.2 |
| 600S200-97 | 42.5 (16.75) | E | 322.3 (72.46) | 337.5 (75.87) | 4.7 |
| 800S200-33 | 15.9 (6.25) | E 1" (2.54 cm) | 56.7 (12.75) | 54.6 (12.27) | -3.8 |
| 800S250-97 | 244 (96) | E 0.5" (1.27 cm) | 342.6 (77.01) | 358.2 (80.52) | 4.6 |

It is shown in Table 21 that when the actual stress distributions were applied at the end of studs in CUFSM tool, the range of difference between finite element analysis and predicted strength is only 1%-4.6%. Hence, by defining the actual stress at the end of specimens, $P_{crl}$ and $P_{crd}$ can be captured correctly from the finite-strip analysis in CUFSM,

and therefore, the axial strength can be predicted precisely by direct strength method equations in AISI S100-16 design specification. This comparison confirms the hypothesis that by moving the wall assemblies to the edge, the concrete slab cannot maintain a uniform stress distribution on the stud ends.

# CHAPTER 6

# Future Work and Conclusions

## 6.1 Future work

Experimentally, there are still knowledge gaps pertaining to the relationship between the bearing condition and assembly axial capacity. Chapters 2 and 3 explored studs of various cross-sections, all fixed to 30.5 cm (12 in) in height. Maintaining identical assembly height resulted in buckling failure modes on the local-distortional cusp for the sections examined. The degree of participation of local and distortional modes changed with cross-section. In Chapter 4, finite element analyses of variable-height stud assemblies were conducted. The stud heights were selected so that they buckled either locally, distortionally, or globally. The finite element analyses necessarily preceded the experimental tests described in this Chapter due to COVID-19 laboratory disruptions, during which the UMass Amherst structural testing labs were closed for four months (and re-opened at 25% capacity).

To better identify the relationship between the bearing condition and axial capacity, tests at each buckling mode (local, distortional, and global) will be conducted. Except for the stud height, dimensions will be maintained from the fixed-height experimental program, as shown in Figure 97. Furthermore, stud assemblies installed on concrete slabs are generally full-height (2.45 meters (8 ft) or higher) and thus globally-dominant. This

was absent in the original experimental program as at project-outset, it was hypothesized that global-height studs would not experience loss of axial capacity due to bearing on the slab. However, Chapter 4 finite element modeling suggests that this is not true. Thus, these full-height tests are critical for creating realistic design provisions.

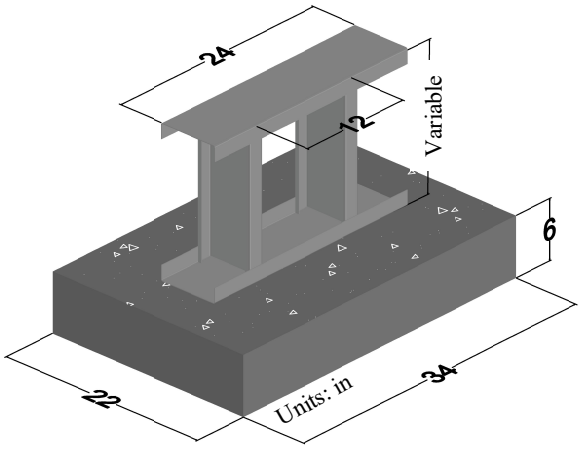


*Figure 97: Schematic of specimens and dimensions.*

To fulfill this aim, the specific lengths are determined via finite strip analyses, as described in Chapter 4. Schematics of the proposed stud assembly configurations for future experiments are illustrated in Figure 98.

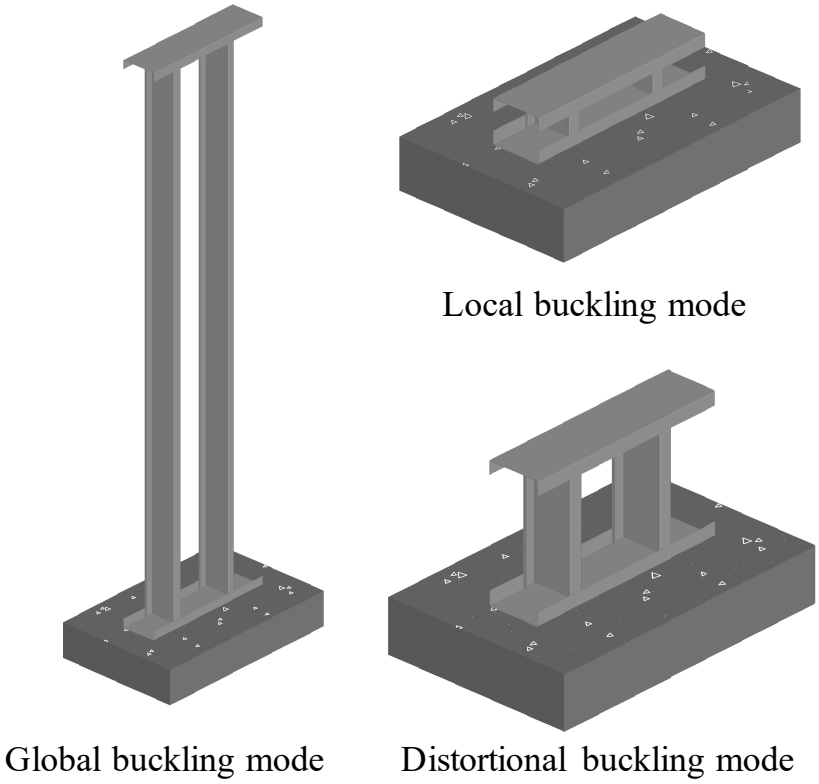


*Figure 98: Schematic of the assemblies for the future experiments.*

The proposed test matrix is shown in Table 22 below. In total, 38 experiments will be conducted. Stud height has been determined through finite strip modeling. Calculated heights are shown in Table 23. As an example, constructing a short stub column assembly for local buckling test is shown in Figure 99. Bearing conditions will be selected to align with Chapters 2 and 3. 362S162-68 cross-section will be added to the cross-sections of Chapters 2 and 3. This section will be tested only in full-height experiments to determine the impact of web height and add a new thickness to the test program.

*Table 22: Experimental test matrix of the future experiments.*

| Stud | Track | Stud Height | Bearing Condition |
|---|---|---|---|
| 600S162-33 [50 ksi] | 33 mil | Local | Full bearing, At Edge, Overhang |
| | 33 mil | Distortional | Full bearing, At Edge, Overhang |
| | 33 mil | 96" | Full bearing, Near Edge, At Edge, Overhang |
| | 54 mil* | 12" | Near Edge, At Edge |
| 600S162-54 [50 ksi] | 54 mil | Local | Full bearing, At Edge, Overhang |
| | 54 mil | Distortional | Full bearing, At Edge, Overhang |
| | 54 mil | 96" | Full bearing, Near Edge, At Edge, Overhang |
| | 97 mil* | 12" | Near Edge, At Edge |
| 362S162-68 [50 ksi] | 68 mil | 96" | Full bearing, Near Edge, At Edge, Overhang |
| 600S162-97 [50 ksi] | 97 mil | Local | Full bearing, At Edge, Overhang |
| | 97 mil | Distortional | Full bearing, At Edge, Overhang |
| | 97 mil | 96" | Full bearing, Near Edge, At Edge, Overhang |

*Upsized two thicknesses from stud thickness

It was concluded in Chapter 3, 4, and 5 that the non-uniform stress distribution caused by various bearing conditions was the main reason for decreasing the compressive strength of assemblies. It is hypothesized that by increasing the thickness of tracks, tracks might help maintain a uniform stress distribution at the end of studs. In order to see the impact of track thickness, two series of experiments are added to the experimental test matrix and are marked with * in Table 22. In these experiments, tracks will be upsized two thicknesses from their corresponding stud thickness. Typically, studs and tracks are specified with matching thicknesses.

*Table 23: The height of specimens in the future experiments.*

| **Section** | **Stud height** | | |
|---|---|---|---|
| | Buckling mode | | |
| | Local | Distortional | Global |
| | *cm (in)* | | |
| 600S162-33 | 11.4 (4.5) | 50.8 (20) | 243.8 (96) |
| 600S162-54 | 11.7 (4.6) | 38.1 (15) | 243.8 (96) |
| 362S162-68 | — | — | 243.8 (96) |
| 600S162-97 | 12.7 (5.0) | 27.9 (11) | 243.8 (96) |

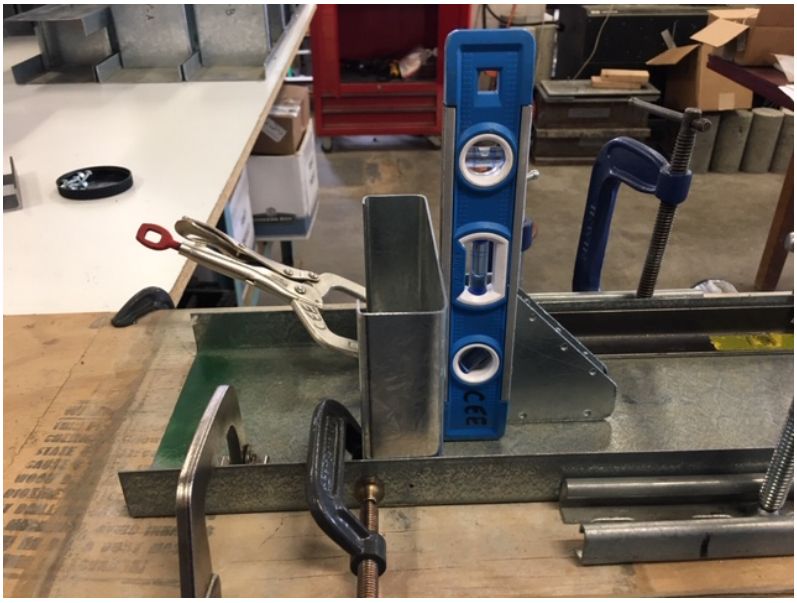

*Figure 99: Constructing local-height specimen for local buckling experiments.*

The procedure of the tests will be the same as Chapter 2. In Chapter 3, the impact of gap distances between studs and tracks were investigated numerically. It was concluded that the gap distances can impact the stiffness of cold-formed steel wall assemblies, especially short ones. Hence, since in the future experiments the height of studs will be

variable and the range of heights will be between short to full-height, the gap distances will be measured and recorded precisely.

The experiments including short and intermediate studs will be conducted in the Gunness structural laboratory. However, for the global tests, another actuator and test rig would be required, due to the fact that the current actuator at the Gunness structural laboratory is unable to move up sufficiently to provide sufficient height. Figure 100 demonstrates the test rig and its 650 kN (146-kips) actuator in the Brack structural testing laboratory of the University of Massachusetts Amherst which are going to be utilized for the full-scale stud assembly experiments, illustrated in Figure 100. The drawings of the test rig in the Brack structural lab are available in Appendix B.

In Chapter 5, the experimental-derived and analysis-based design recommendations and reduction factors were proposed. Furthermore, it was concluded that by loading the end of specimens by the actual and non-uniform stress distributions which were generated by non-uniform bearing conditions, the axial strength could be estimated precisely by direct strength method equations proposed in AISI S100-16. However, obtaining the true stress distribution requires finite element analysis and FEM software. Therefore, general stress distributions for each bearing condition will be proposed to be fit to the non-uniform stress distribution extracted from ABAQUS in section 5.3. These general stress distributions can be utilized in direct strength method analyses efficiently.

(a) (b)

*Figure 100: The test rig and 650-kN actuator in the Brack structural testing laboratory of the University of Massachusetts, Amherst.*

## 6.2 Conclusions

Placing wall assemblies near to the edge of concrete slabs or even placing a part of them outside of the slabs (overhang) is common in construction. In this research study, the impact of bearing conditions on the axial behavior of stud assemblies-concrete slabs was explored experimentally and computationally. In total, 27 experiments and nearly 2400

finite element models were conducted across a range of stud shapes and thicknesses and bearing conditions, selected to represent typical construction practice.

In the experimental program, the height of assemblies was fixed 30.5 cm (12 in) to enable comparisons across stud thicknesses and cross-sections. Detailed nonlinear finite element analysis of the tests was employed in the ABAQUS software environment to explore the impact of edge distance on the members strength numerically. Two fidelities of finite element model were developed: a high-fidelity model which captured strength and stiffness of the assemblies and a high-throughput model which captured strength only. The high-fidelity models were used to validate the efficacy of the experimental program and design of the test rig. The high-throughput models were used to run a large parametric modeling suite to populate the design space. Both the experimental and computational programs demonstrated that when the system was placed at the middle of a concrete slab, or when there was adequate distance to the slab edge, the slab provided a uniform stress distribution. However, as the assembly approached the edge or even overhung from the slab, the impact of non-uniform bearing condition on the axial strength and the stiffness was magnified. With increasing section thickness, the observed reduction in axial capacity and stiffness became more severe. In overhang bearing conditions, in addition to the impact of non-uniform bearing conditions, reduction in stud section and the created moment by eccentricity made the strength and stiffness reduction more significant. The data demonstrate for any short stud column bearing sufficiently far from the slab edge, the prediction methods presented in AISI-S100-16 are accurate, and there is no need for a

reduction in axial capacity. However, for studs bearing close to an edge or overhang, the AISI-S100-16 methods become less accurate.

In order to extend the experimental results, parametric variation via a high-fidelity computational modeling program was conducted. High-fidelity 3D finite element analysis of variable-height stud assemblies were conducted in ABAQUS software. 66 lipped-channels utilized commonly in cold-formed steel gravity walls were selected. Furthermore, twelve different bearing conditions were considered. The stud lengths correspond to local, distortional, and global buckling loads were considered as the heights of studs. It was concluded that there was a trend in the behavior of the variable-height specimens, and as the assemblies were moved to edge, the impact of bearing condition was more significant. Furthermore, it was concluded experimentally and numerically that for the edge distance greater than 2.54 cm (1 in), the impact of edge distance can be ignored. However, in order to calculate the axial strength of systems via Direct Strength Method (DSM) equations, presented in AISI S100-16, using the proposed reduction factors is recommended. Based on the experiments, for the assemblies in which the edge distance is between 25.4 mm (1 in) and 12.7 mm (0.5 in) to the edge, a reduction factor of RF=0.9 was proposed. For the cases placed between 3.175 mm (0.125 in) to the edge, also for those assemblies overhanging less than 12.7 mm (0.5 in) from the edge, the reduction factor RF=0.8 was recommended. Based on the results of the computational modeling program, the suggested reduction factors were the same as the experimentally-derived reduction factors except for 3.17 mm (0.125 in) to the edge, at the edge, and overhang bearing conditions. The proposed reduction factor was 0.9 instead of 0.8 for 3.17 mm (0.125 in) edge bearing condition, and

it was 0.85 instead of 0.8 for the edge and overhang bearing conditions. The source of this difference could be screw failure which occurred during the tests on 2.46 mm (97-mil) assemblies. Since, screw failures are inevitable during the construction, especially in thick members, it is recommended that more conservative reduction factors derived by experiments be used in axial design of cold-formed steel members. Furthermore, according to the experimental and computational results, it is highly recommended to remove and reinstall the assemblies overhanging from the concrete slab edge.

The stress distribution at the end of studs could not be measured directly during the experiments. They were obtained through finite element analyses performed in ABAQUS. It was confirmed that by installing the assemblies close to the edge, the stress distribution became non-uniform, which was the source of reduction in compressive strength. It was concluded that by defining the actual stress distribution at the end of studs in CUFSM tool, the actual elastic local and distortional buckling loads of studs could be obtained. DSM equations were then able to predict precisely (within 4.6%) the strength of CFS wall assemblies by true local and distortional loads.

Finally, it is recommended that concrete slabs should be considered in axial design of cold-formed steel members. And, in research projects investigating the axial behavior of members, the edge bearing conditions and the impact of concrete slab should be included in the study.

# Appendix A

Notes:

1. Structural steel rolled shapes, plates, and angles shall conform to the following ASTM designations:

- ASTM A992, Grade 50, unless noted otherwise.

2. All steel surfaces shall be Class A surfaces (unpainted clean mill scale steel surfaces or surfaces with Class A coating on blast-cleaned steel or hot-dipped galvanized and roughened surfaces).

3. All welds used in this project are field and 3/8 inches in size, unless noted otherwise.

4. All shop and field welds shall be made by certified welders, and shall conform to "Structural Welding Code - Steel" (AWS D 1.8 2009) and "AISC 341" section A3.4a and A3.4b.

5. Electrodes for all field and shop welding shall conform to AWS E-70 Series.

6. For specimen steel, all steel shapes of the same size and all steel plates of the same thickness shall be from the same heat.

7. Material specification documentation is requested for all supplied materials.

| | | |
|---|---|---|
| University of Massachusetts, Amherst | | |
| Project : | AISI stud bearing | Sheet No. 1/8 |
| Abbas Joorabchian, Kara Peterman | | |

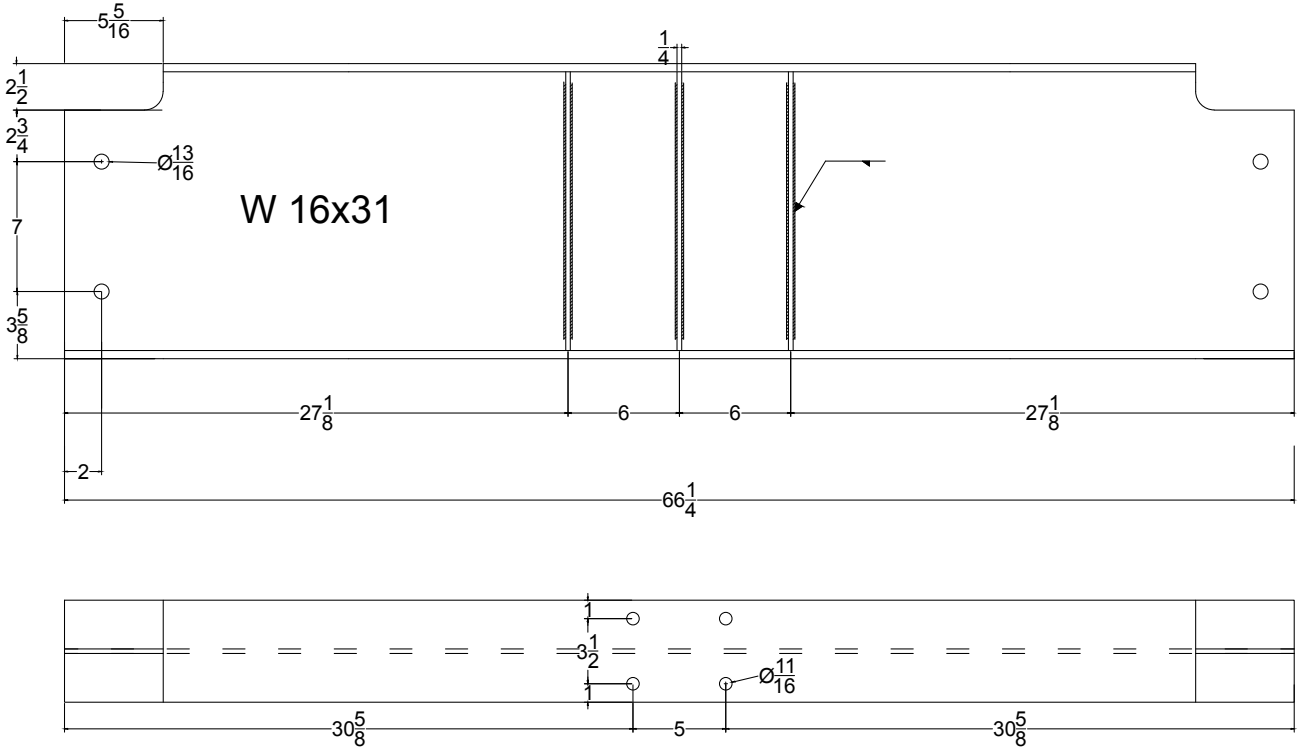


| section | Quantity | Length (in.) |
|---|---|---|
| W 16x31 | 2 | 66-1/4 |
| PL2.5x15x0.25 | 12 | |

University of Massachusetts, Amherst

Project : AISI stud bearing

Sheet No. 2/8

Abbas Joorabchian, Kara Peterman

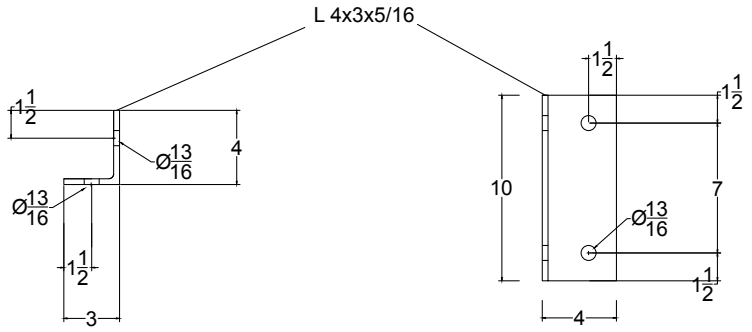


L-1

| section | Quantity | Length (in.) |
|---|---|---|
| L 4x3x5/16 | 8 | 10 |

| | | |
|---|---|---|
| University of Massachusetts, Amherst | | |
| Project : | AISI stud bearing | Sheet No. 3/8 |
| Abbas Joorabchian, Kara Peterman | | |

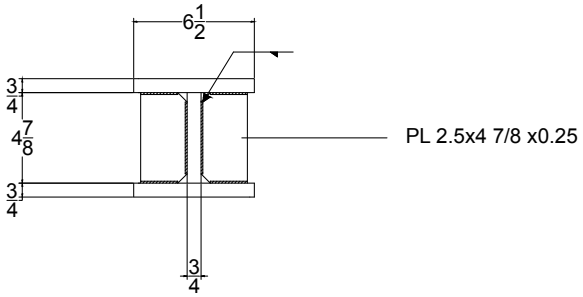


B - 1

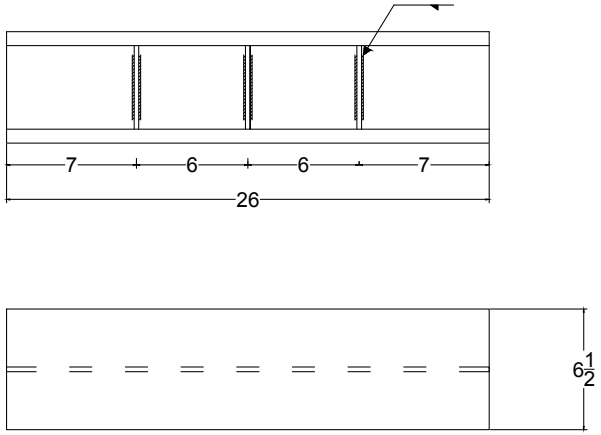


Top view

| section | Quantity | Length (in.) |
|---|---|---|
| B - 1 | 1 | 26 |
| PL2.5x4 7/8x0.25 | 6 | |

| | | |
|---|---|---|
| University of Massachusetts, Amherst | | |
| Project : | AISI stud bearing | Sheet No. 4/8 |
| Abbas Joorabchian, Kara Peterman | | |

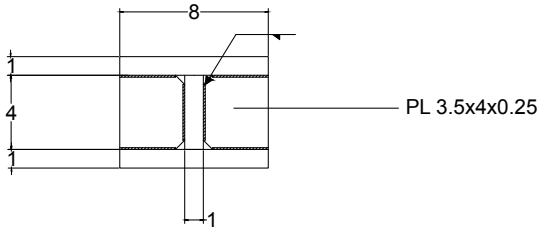


B - 2

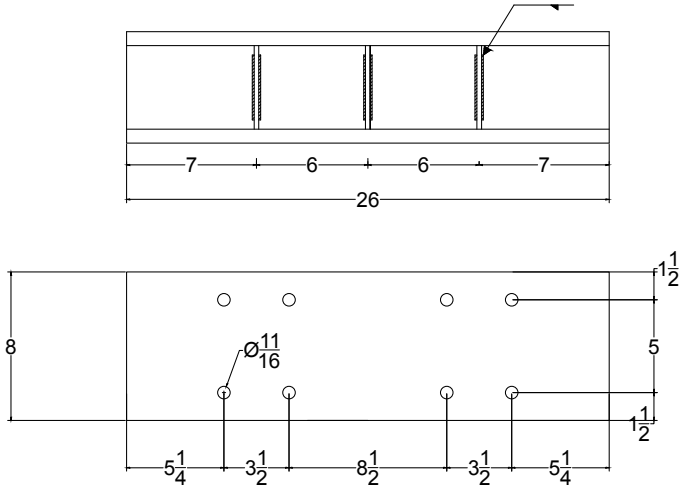


Bottom Flange

| section | Quantity | Length (in.) |
|---|---|---|
| B - 2 | 1 | 26 |
| PL3.5x4x0.25 | 6 | |

| | | |
|---|---|---|
| University of Massachusetts, Amherst | | |
| Project : | AISI stud bearing | Sheet No. 5/8 |
| Abbas Joorabchian, Kara Peterman | | |

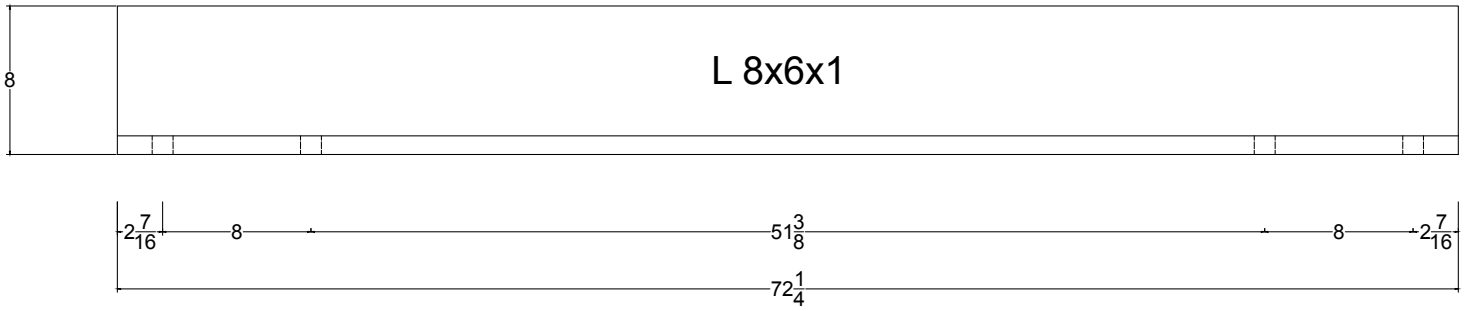


L-2 View 1

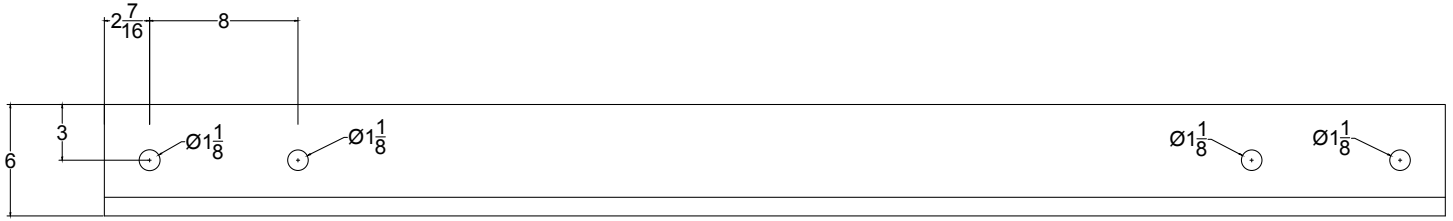


L-2 View 2

| section | Quantity | Length (in.) |
|---|---|---|
| L 8x6x1 (L-2) | 1 | 72-1/4 |

| | | |
|---|---|---|
| University of Massachusetts, Amherst | | |
| Project : | AISI stud bearing | Sheet No. 6/8 |
| Abbas Joorabchian, Kara Peterman | | |

# L 8x6x1

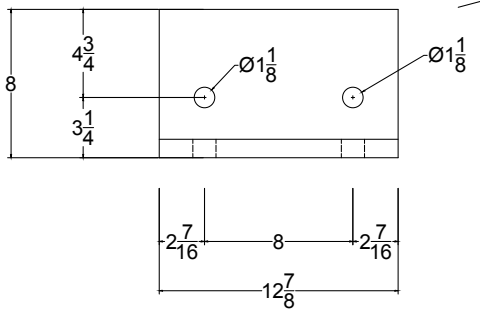


L-3 View 1

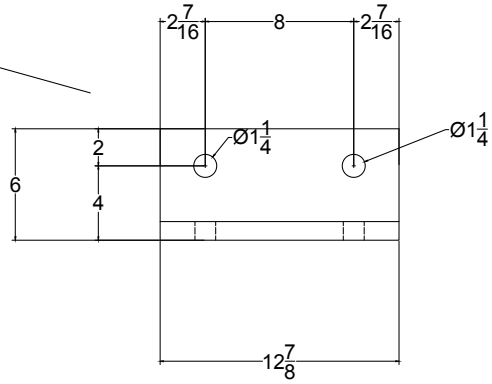


L-3 View 2

| section | Quantity | Length (in.) |
|---|---|---|
| L 8x6x1 (L-3) | 2 | 12-7/8 |

| | | |
|---|---|---|
| University of Massachusetts, Amherst | | |
| Project : | AISI stud bearing | Sheet No. 7/8 |
| Abbas Joorabchian, Kara Peterman | | |

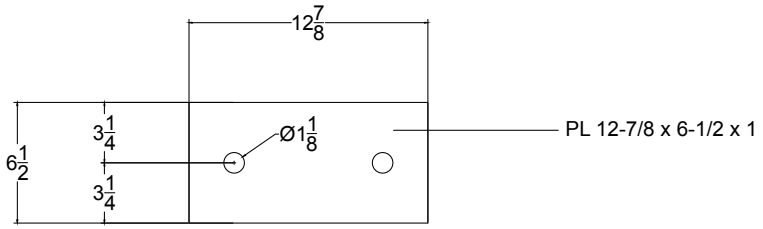


Shim plate

| section | Quantity | Length (in.) |
|---|---|---|
| Shim plate | 8 | 12-7/8 |

| | | |
|---|---|---|
| University of Massachusetts, Amherst | | |
| Project : | AISI stud bearing | Sheet No. 8/8 |
| Abbas Joorabchian, Kara Peterman | | |

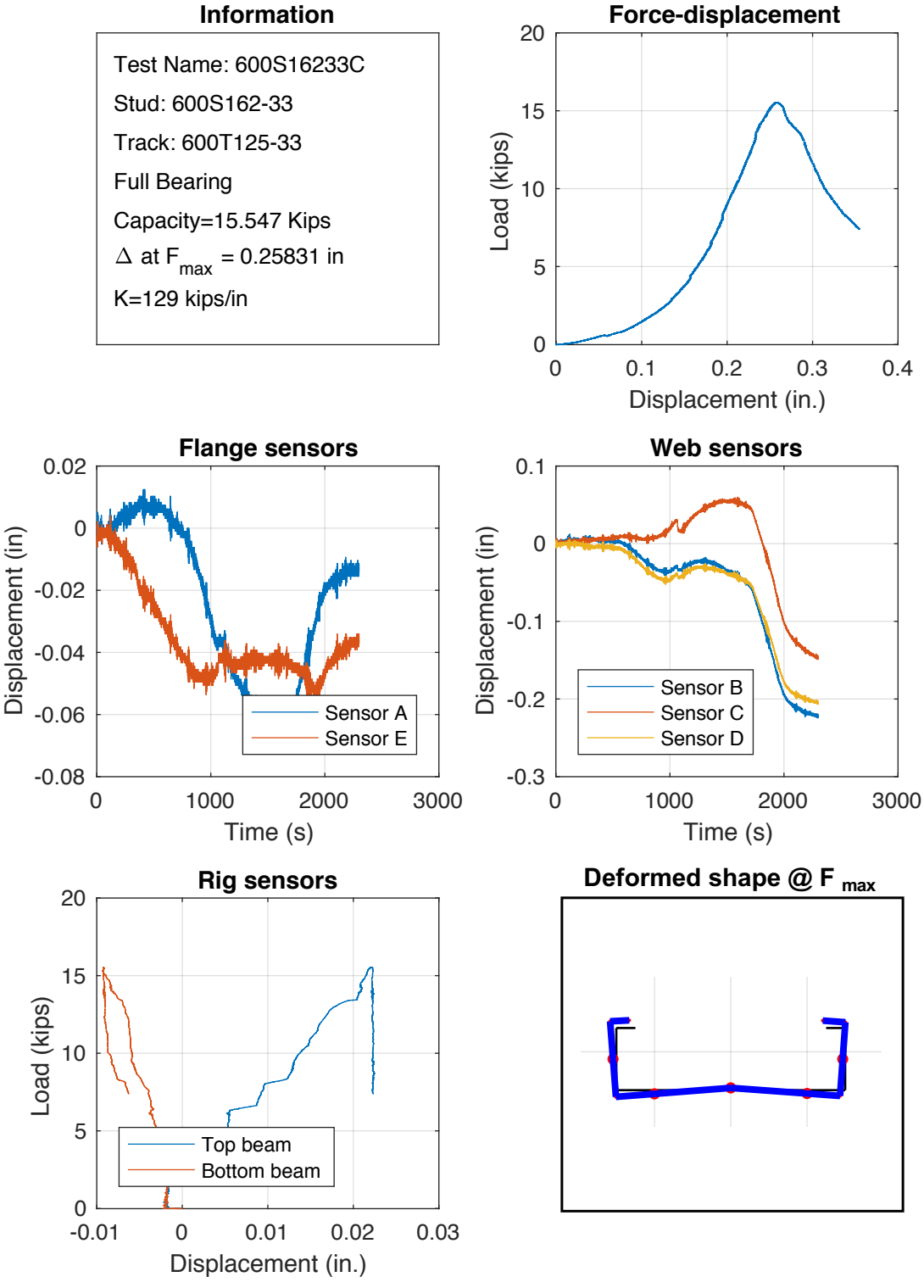
Information
Test Name: 600S16233C
Stud: 600S162-33
Track: 600T125-33
Full Bearing
Capacity=15.547 Kips
Δ at F max = 0.25831 in
K=129 kips/in
Force-displacement
Load (kips)
Displacement (in.)
Flange sensors
Displacement (in)
Time (s)
Sensor A
Sensor E
Web sensors
Displacement (in)
Time (s)
Sensor B
Sensor C
Sensor D
Rig sensors
Load (kips)
Displacement (in.)
Top beam
Bottom beam
Deformed shape @ F max

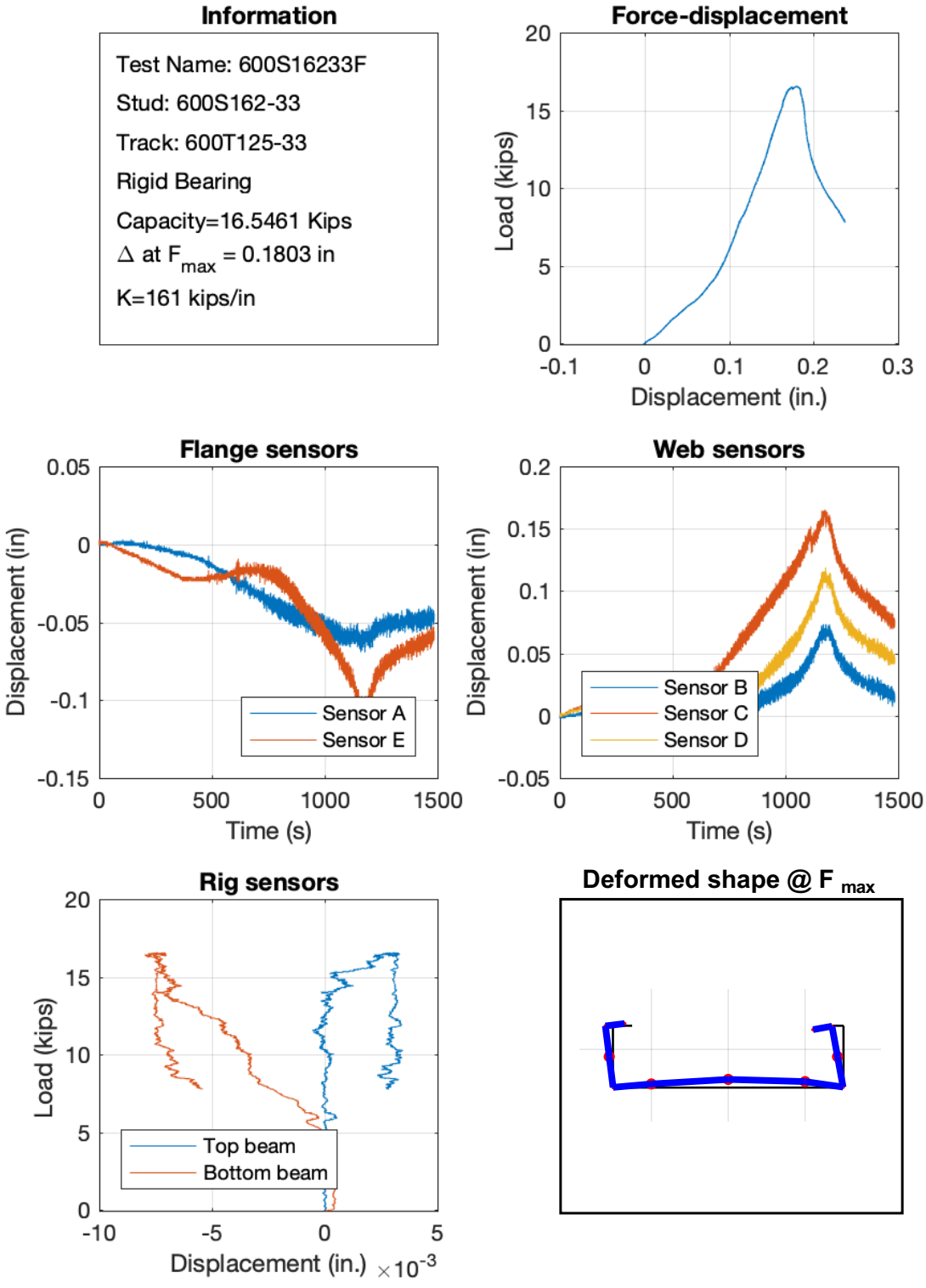
Information
Test Name: 600S16233F
Stud: 600S162-33
Track: 600T125-33
Rigid Bearing
Capacity=16.5461 Kips
Δ at F max = 0.1803 in
K=161 kips/in
Force-displacement
Load (kips)
Displacement (in.)
Flange sensors
Displacement (in)
Time (s)
Sensor A
Sensor E
Web sensors
Displacement (in)
Time (s)
Sensor B
Sensor C
Sensor D
Rig sensors
Load (kips)
Displacement (in.) ×10-3
Top beam
Bottom beam
Deformed shape @ F max

**Information**

Test Name: 600S16233E1

Stud: 600S162-33

Track: 600T125-33

1" to the edge

Capacity=17.5585 Kips

$\Delta$ at $F_{max}$ = 0.26289 in

K=158 kips/in

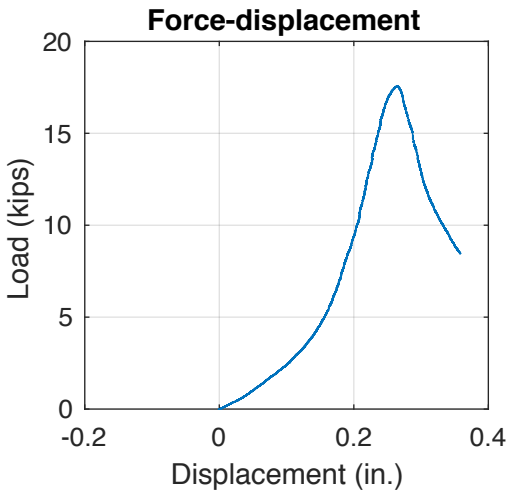


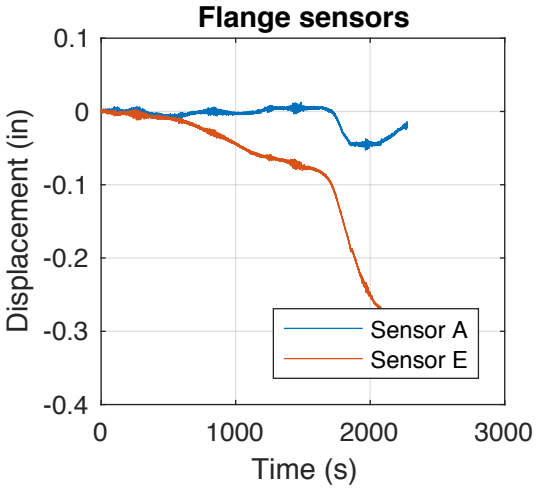


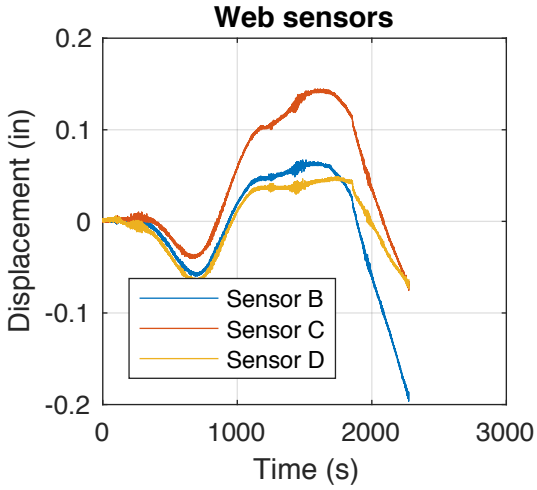


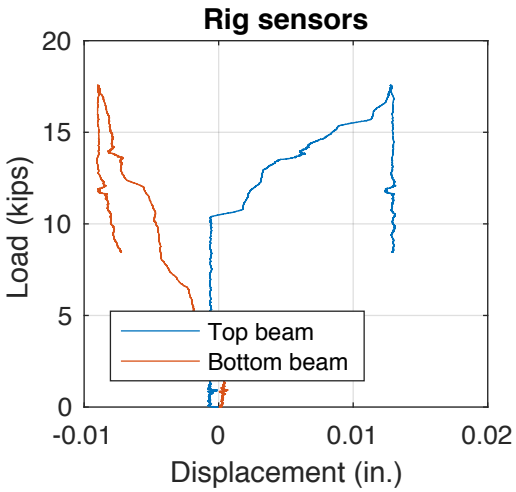


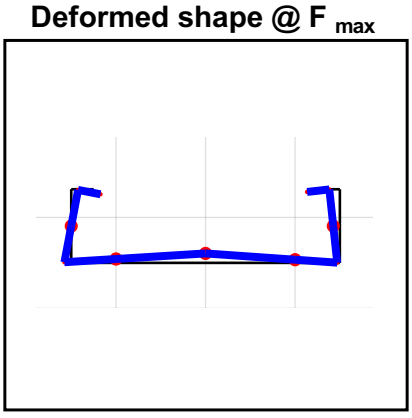

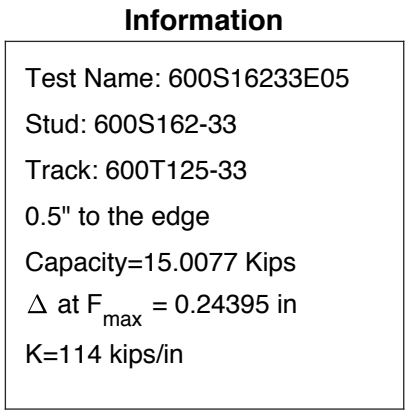
Information
Test Name: 600S16233E05
Stud: 600S162-33
Track: 600T125-33
0.5" to the edge
Capacity=15.0077 Kips
Δ at F max = 0.24395 in
K=114 kips/in

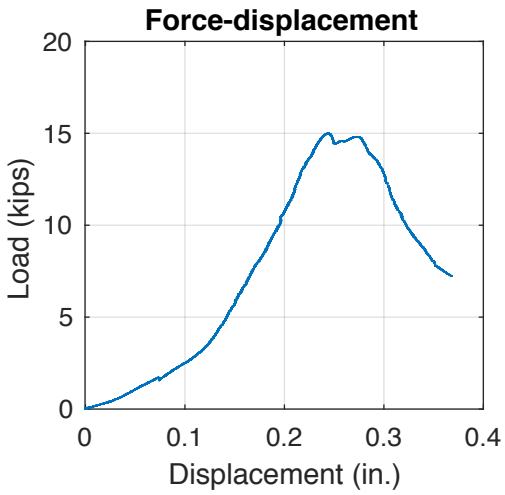
Force-displacement
Load (kips)
Displacement (in.)
0
5
10
15
20
0
0.1
0.2
0.3
0.4

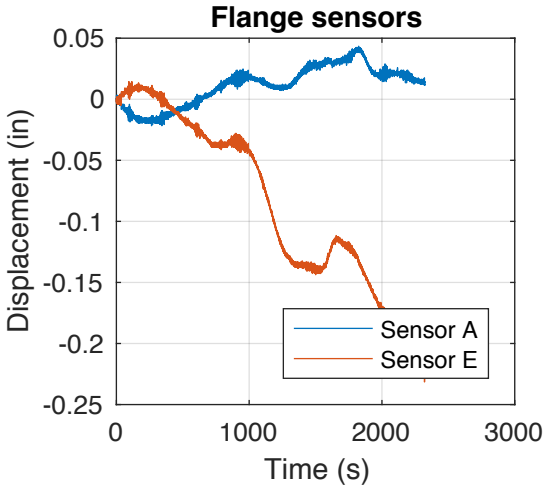
Flange sensors
Displacement (in)
Time (s)
Sensor A
Sensor E
0.05
0
-0.05
-0.1
-0.15
-0.2
-0.25
0
1000
2000
3000

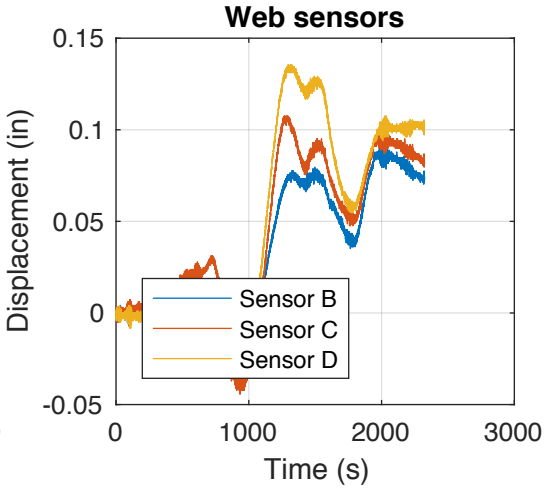
Web sensors
Displacement (in)
Time (s)
Sensor B
Sensor C
Sensor D
0.15
0.1
0.05
0
-0.05
0
1000
2000
3000

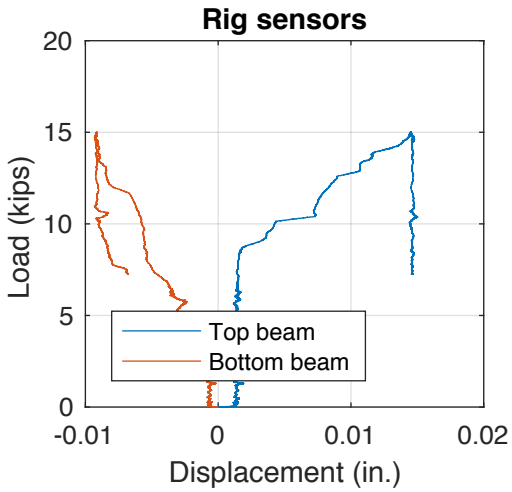
Rig sensors
Load (kips)
Displacement (in.)
Top beam
Bottom beam
20
15
10
5
0
-0.01
0
0.01
0.02

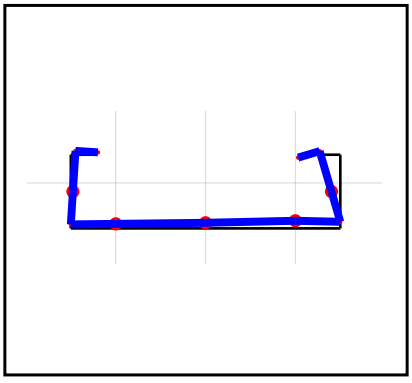
Deformed shape @ F max

**Information**

Test Name: 600S16233E0125

Stud: 600S162-33

Track: 600T125-33

0.125" to the edge

Capacity=12.6998 Kips

$\Delta$ at $F_{max}$ = 0.28816 in

K=117 kips/in

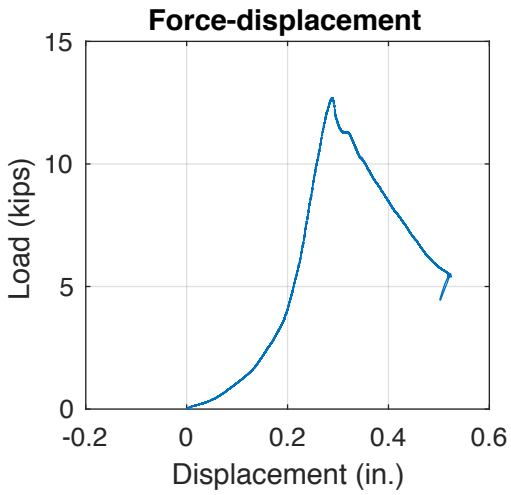


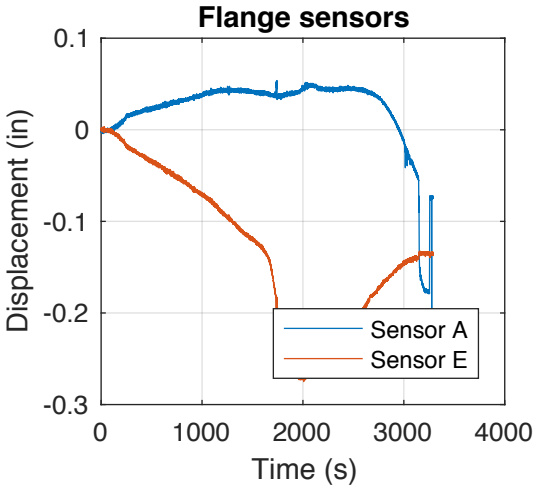


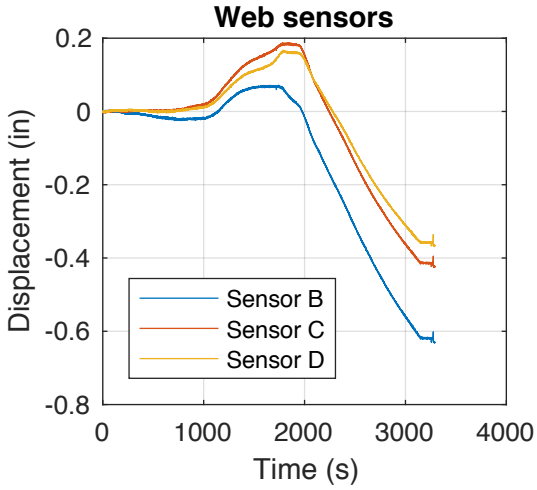


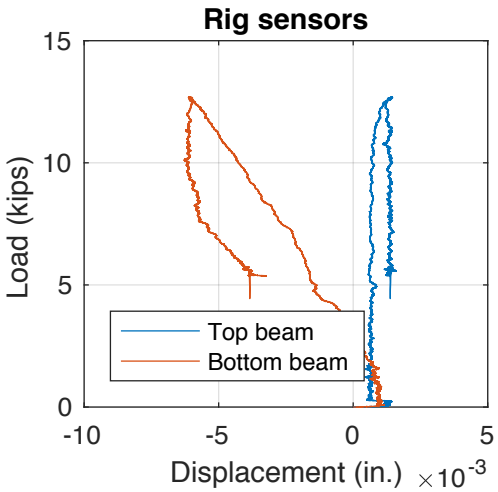


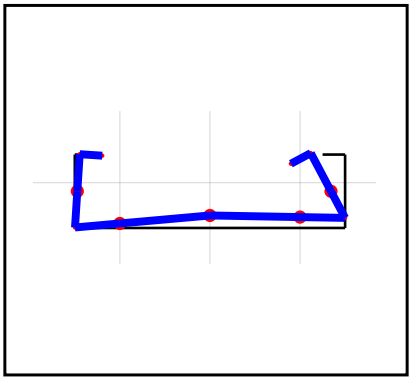

**Information**

Test Name: 600S16233E

Stud: 600S162-33

Track: 600T125-33

At the edge

Capacity=14.9131 Kips

$\Delta$ at $F_{max}$ = 0.3284 in

K=82 kips/in

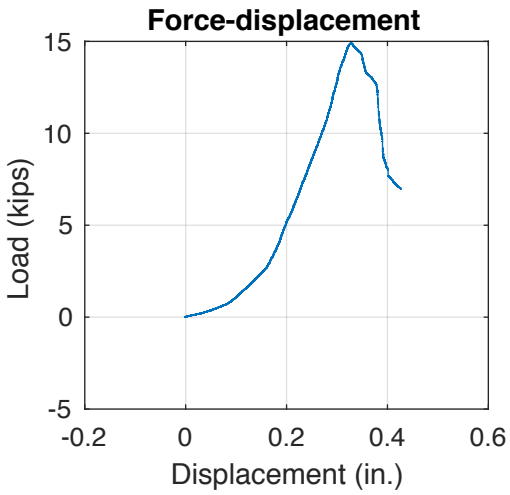


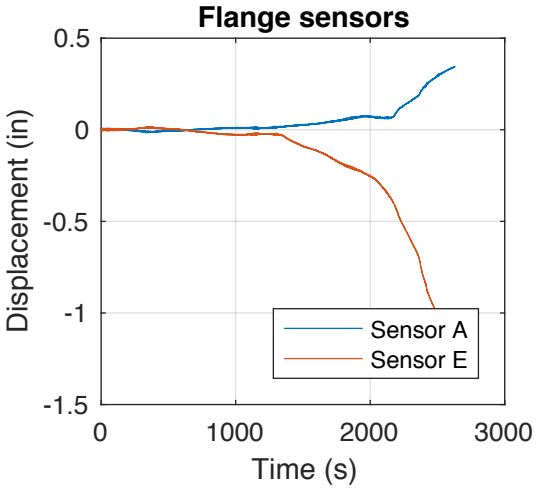


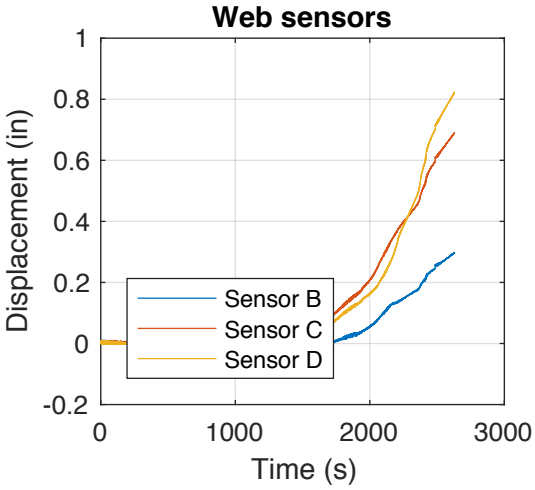


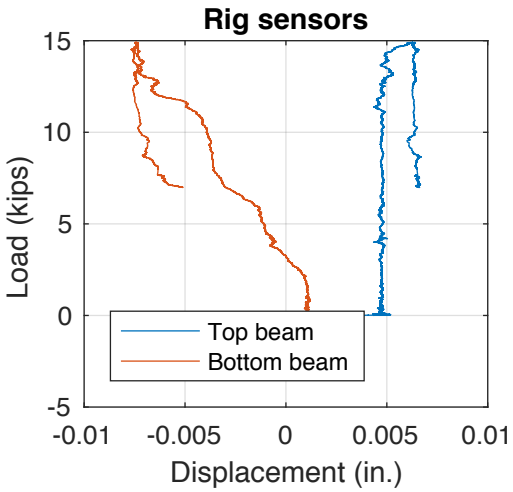


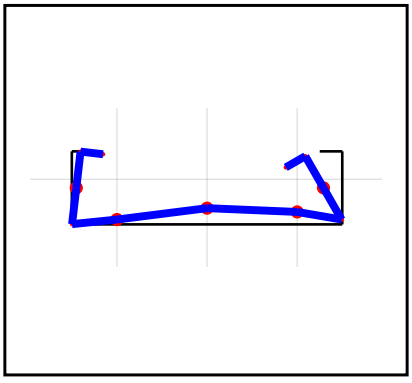

**Information**

Test Name: 600S16233O05

Stud: 600S162-33

Track: 600T125-33

0.5" Overhang

Capacity=14.6161 Kips

$\Delta$ at $F_{max}$ = 0.30944 in

K=122 kips/in

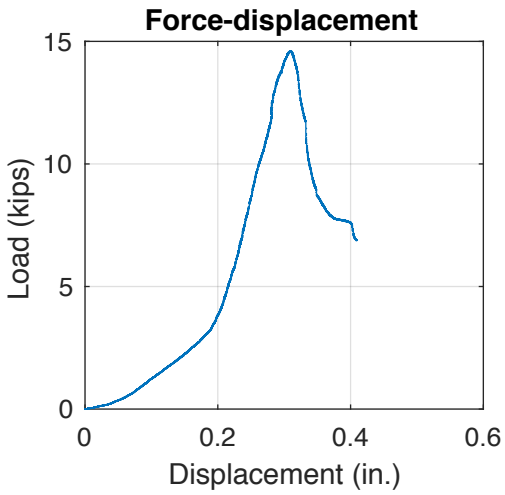


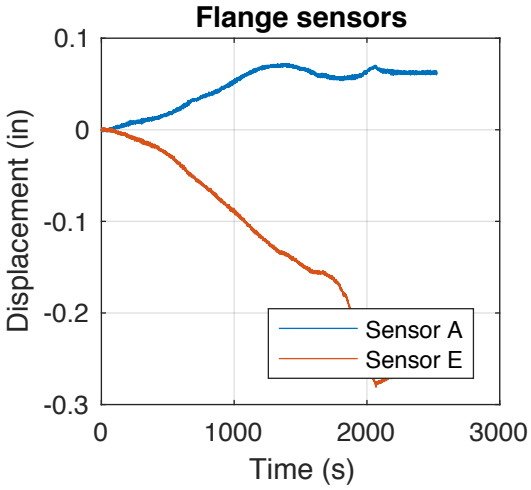


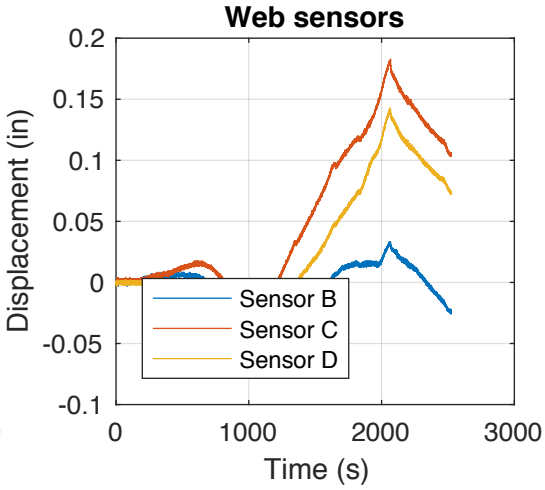


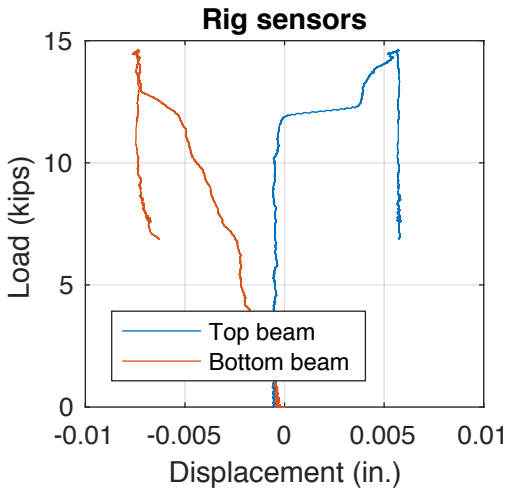


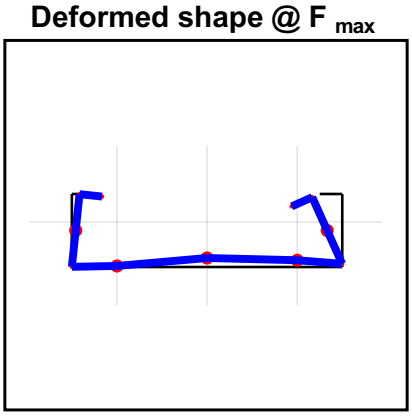

**Information**

Test Name: 600S16233O1

Stud: 600S162-33

Track: 600T125-33

1" Overhang

Capacity=11.4717 Kips

$\Delta$ at $F_{max}$ = 0.26531 in

K=119 kips/in

**Force-displacement**

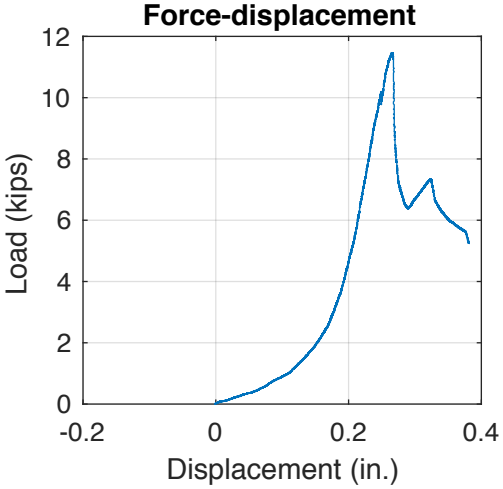


**Flange sensors**

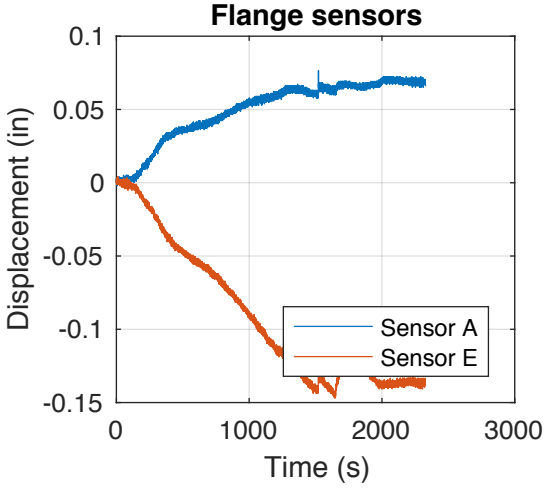


**Web sensors**

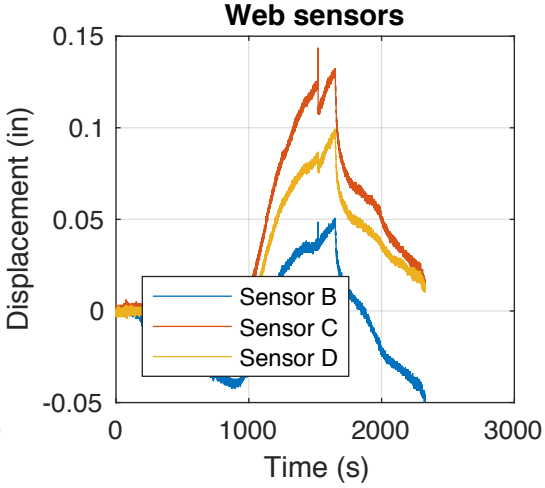


**Rig sensors**

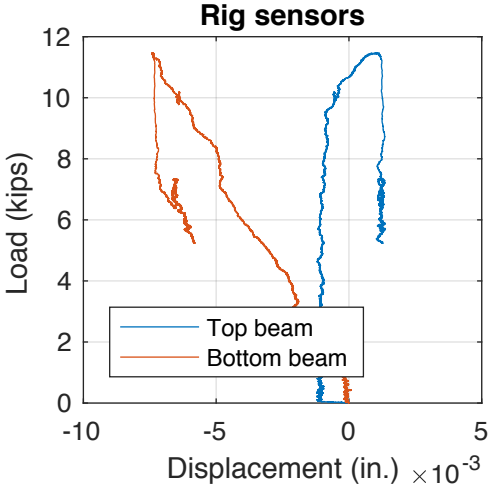


**Deformed shape @ $F_{max}$**

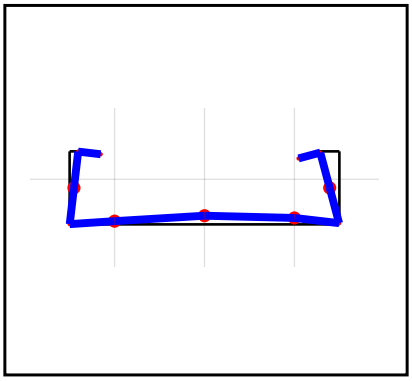

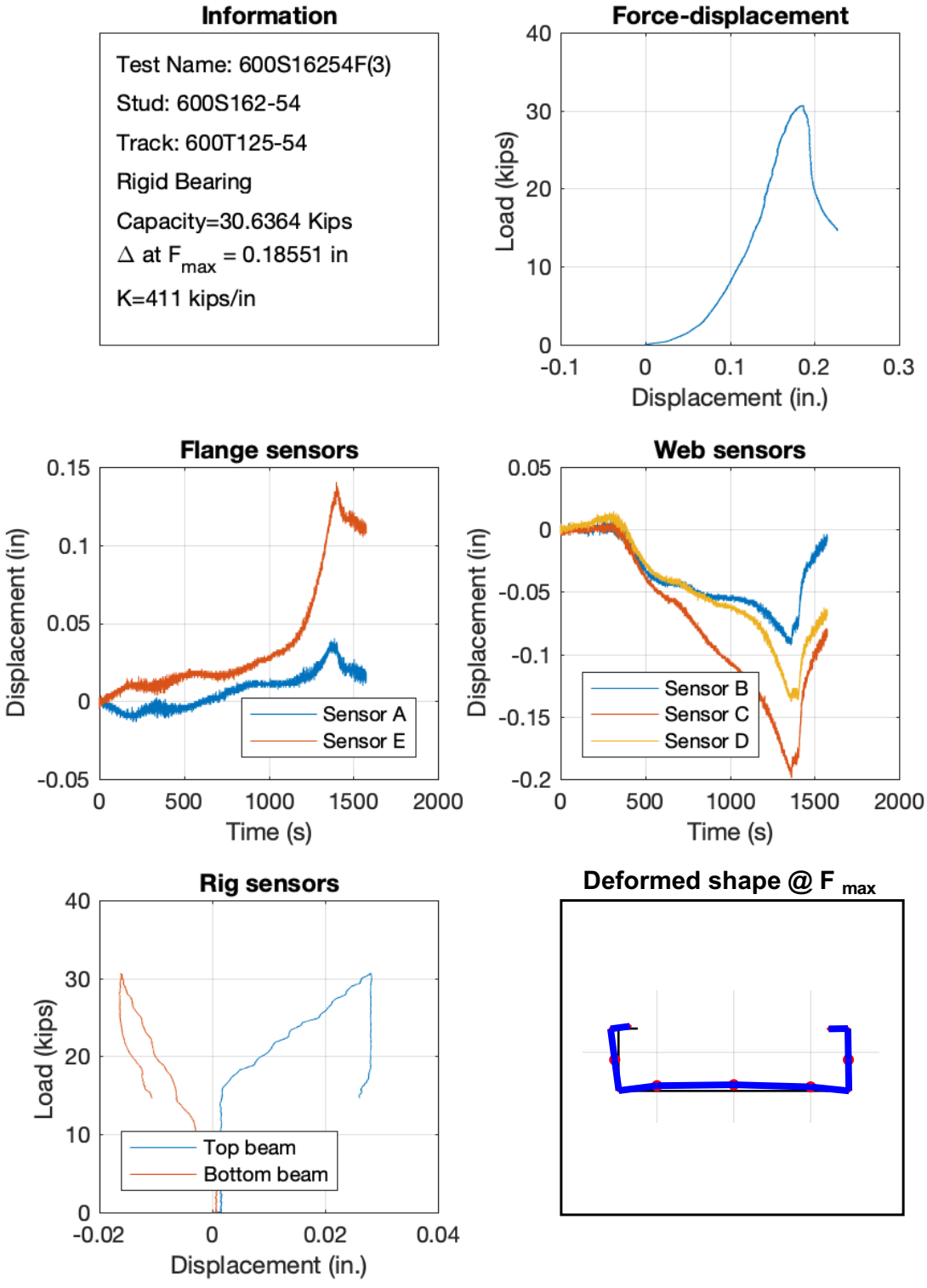
Information
Test Name: 600S16254F(3)
Stud: 600S162-54
Track: 600T125-54
Rigid Bearing
Capacity=30.6364 Kips
Δ at F max = 0.18551 in
K=411 kips/in
Force-displacement
Load (kips)
Displacement (in.)
Flange sensors
Displacement (in)
Time (s)
Sensor A
Sensor E
Web sensors
Displacement (in)
Time (s)
Sensor B
Sensor C
Sensor D
Rig sensors
Load (kips)
Displacement (in.)
Top beam
Bottom beam
Deformed shape @ F max

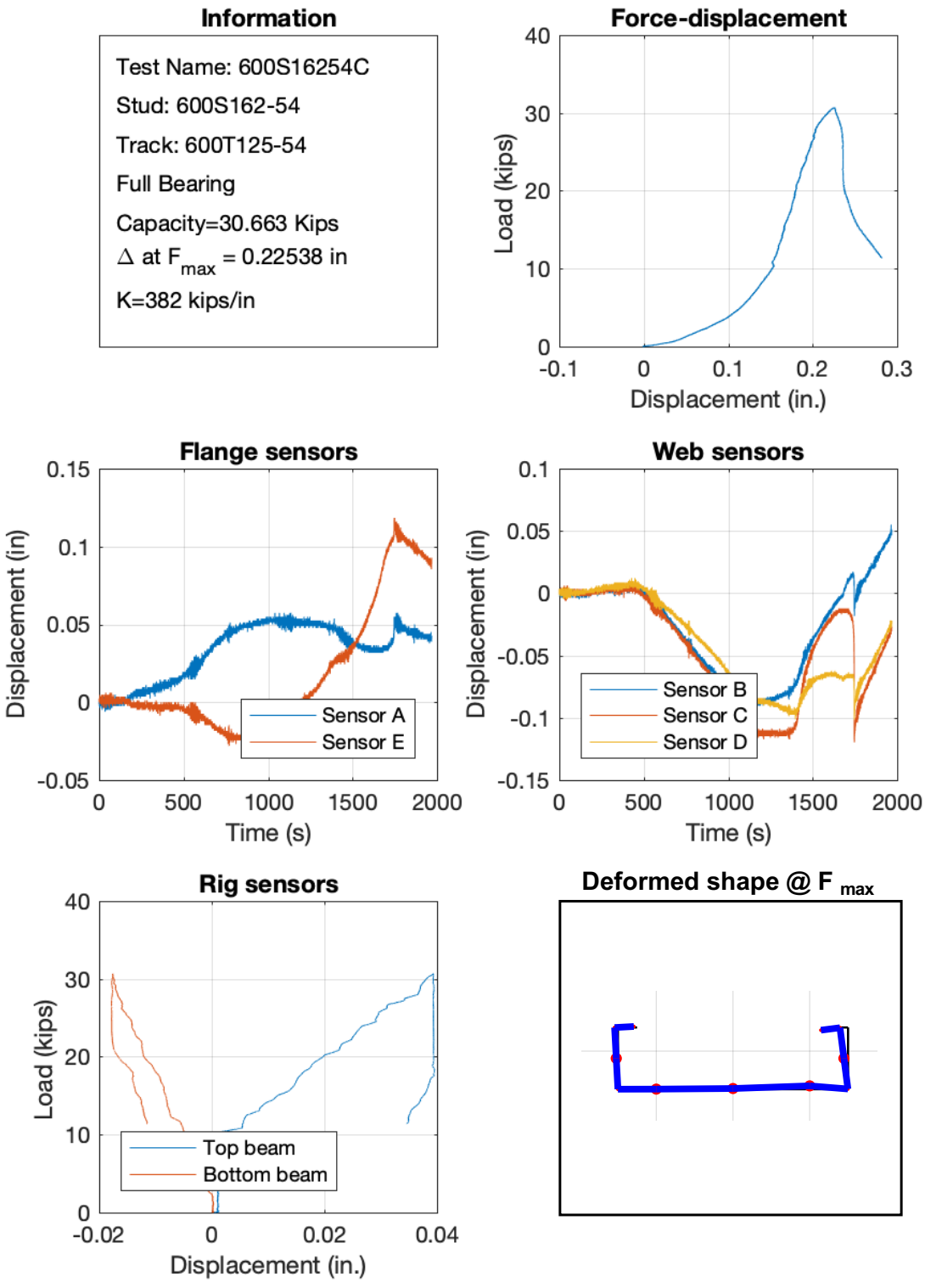
Information
Test Name: 600S16254C
Stud: 600S162-54
Track: 600T125-54
Full Bearing
Capacity=30.663 Kips
Δ at F max = 0.22538 in
K=382 kips/in
Force-displacement
Load (kips)
Displacement (in.)
Flange sensors
Displacement (in)
Time (s)
Sensor A
Sensor E
Web sensors
Displacement (in)
Time (s)
Sensor B
Sensor C
Sensor D
Rig sensors
Load (kips)
Displacement (in.)
Top beam
Bottom beam
Deformed shape @ F max

**Information**

Test Name: 600S16254E1

Stud: 600S162-54

Track: 600T125-54

1" to the edge

Capacity=27.6675 Kips

$\Delta$ at $F_{max}$ = 0.27813 in

K=249 kips/in

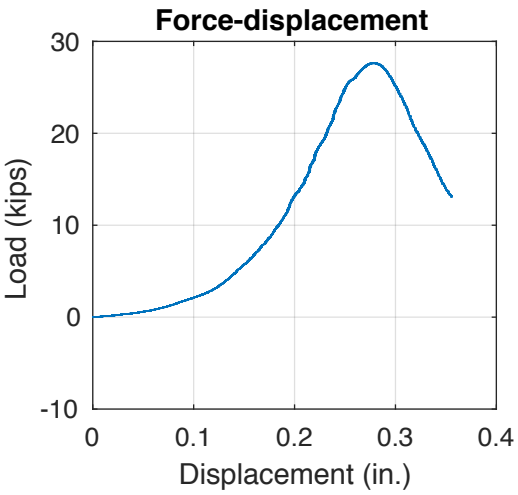


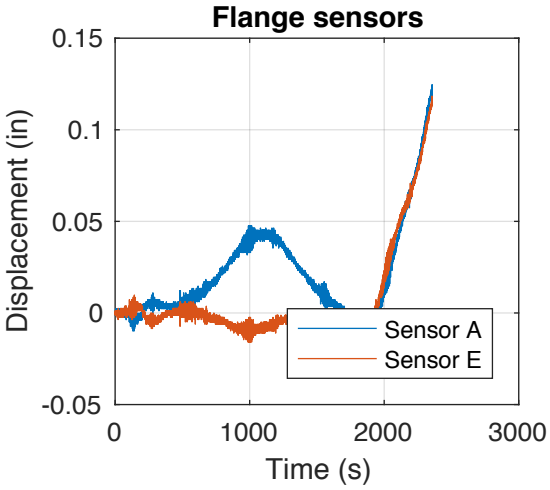


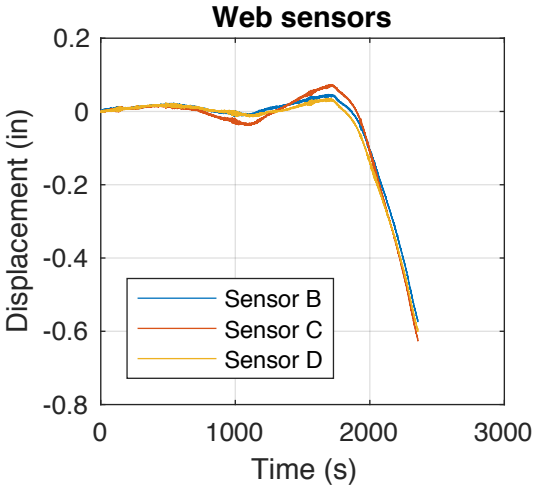


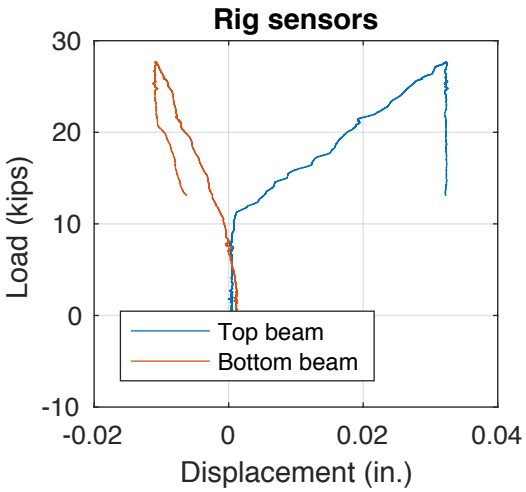


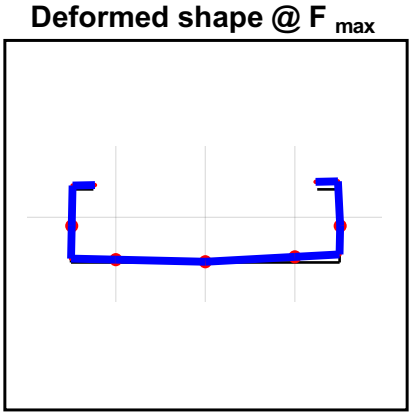

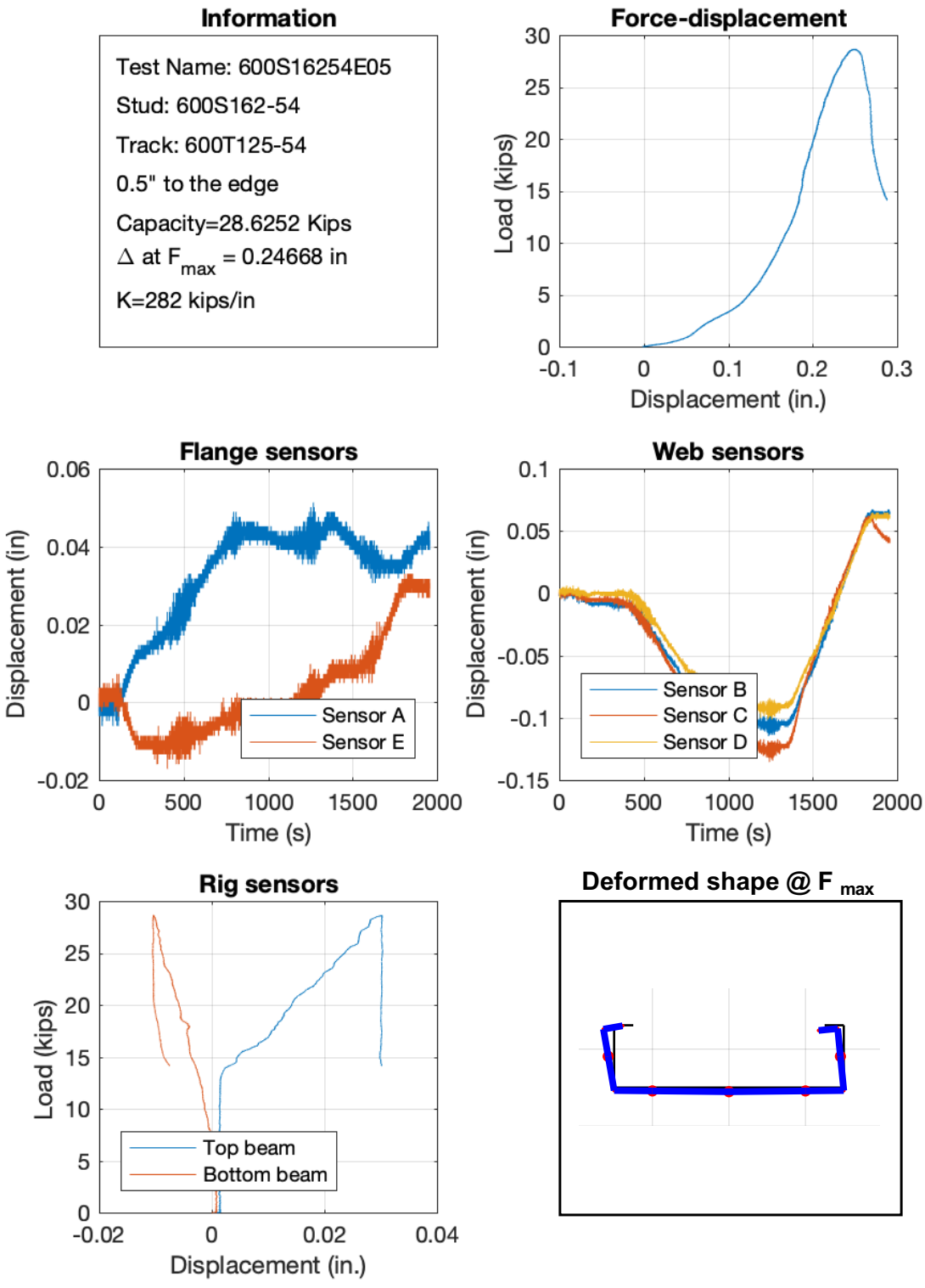
Information
Test Name: 600S16254E05
Stud: 600S162-54
Track: 600T125-54
0.5" to the edge
Capacity=28.6252 Kips
Δ at F max = 0.24668 in
K=282 kips/in
Force-displacement
Load (kips)
Displacement (in.)
Flange sensors
Displacement (in)
Time (s)
Sensor A
Sensor E
Web sensors
Displacement (in)
Time (s)
Sensor B
Sensor C
Sensor D
Rig sensors
Load (kips)
Displacement (in.)
Top beam
Bottom beam
Deformed shape @ F max

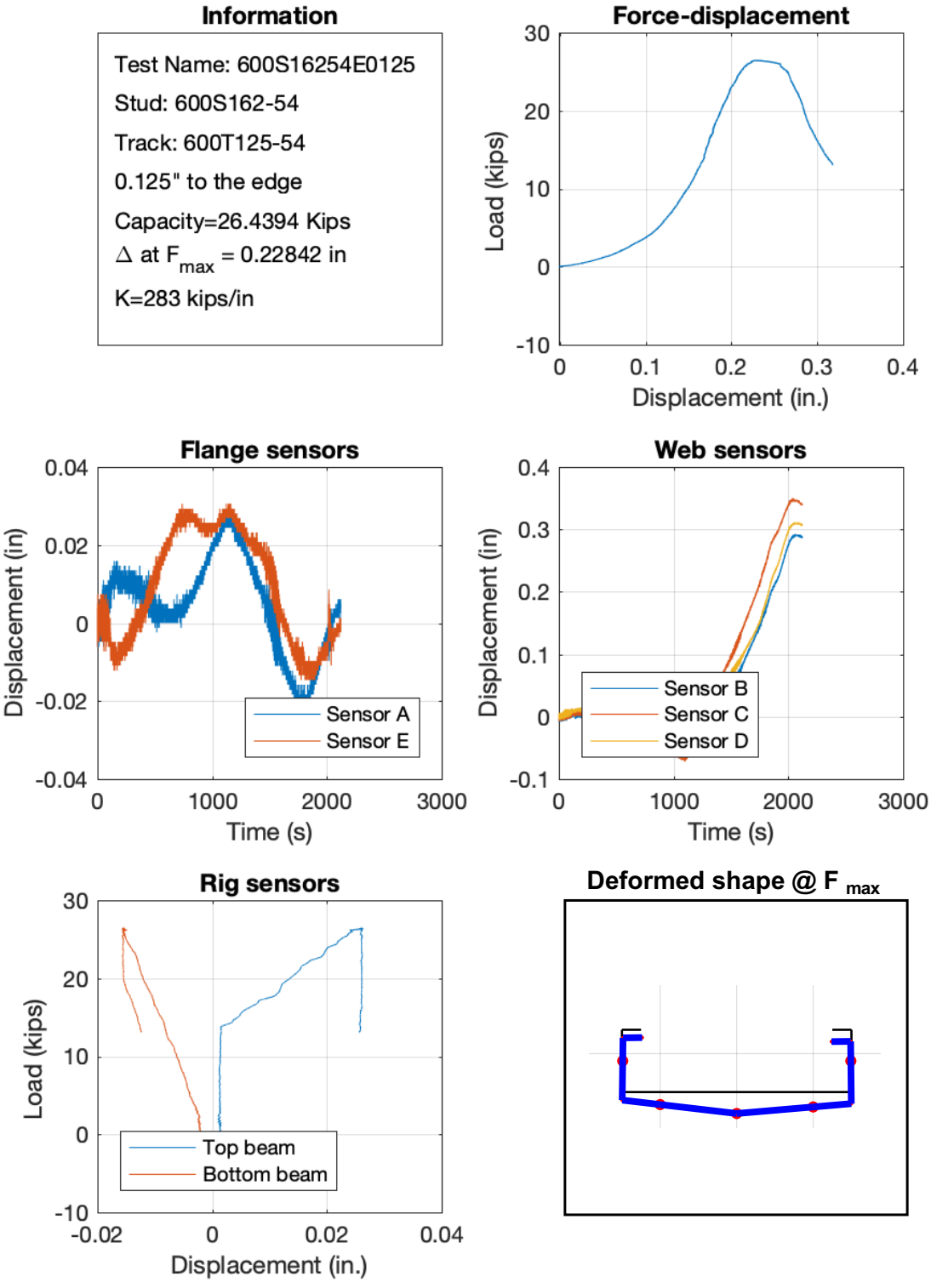
Information
Test Name: 600S16254E0125
Stud: 600S162-54
Track: 600T125-54
0.125" to the edge
Capacity=26.4394 Kips
Δ at F max = 0.22842 in
K=283 kips/in
Force-displacement
Load (kips)
Displacement (in.)
Flange sensors
Displacement (in)
Time (s)
Sensor A
Sensor E
Web sensors
Displacement (in)
Time (s)
Sensor B
Sensor C
Sensor D
Rig sensors
Load (kips)
Displacement (in.)
Top beam
Bottom beam
Deformed shape @ F max

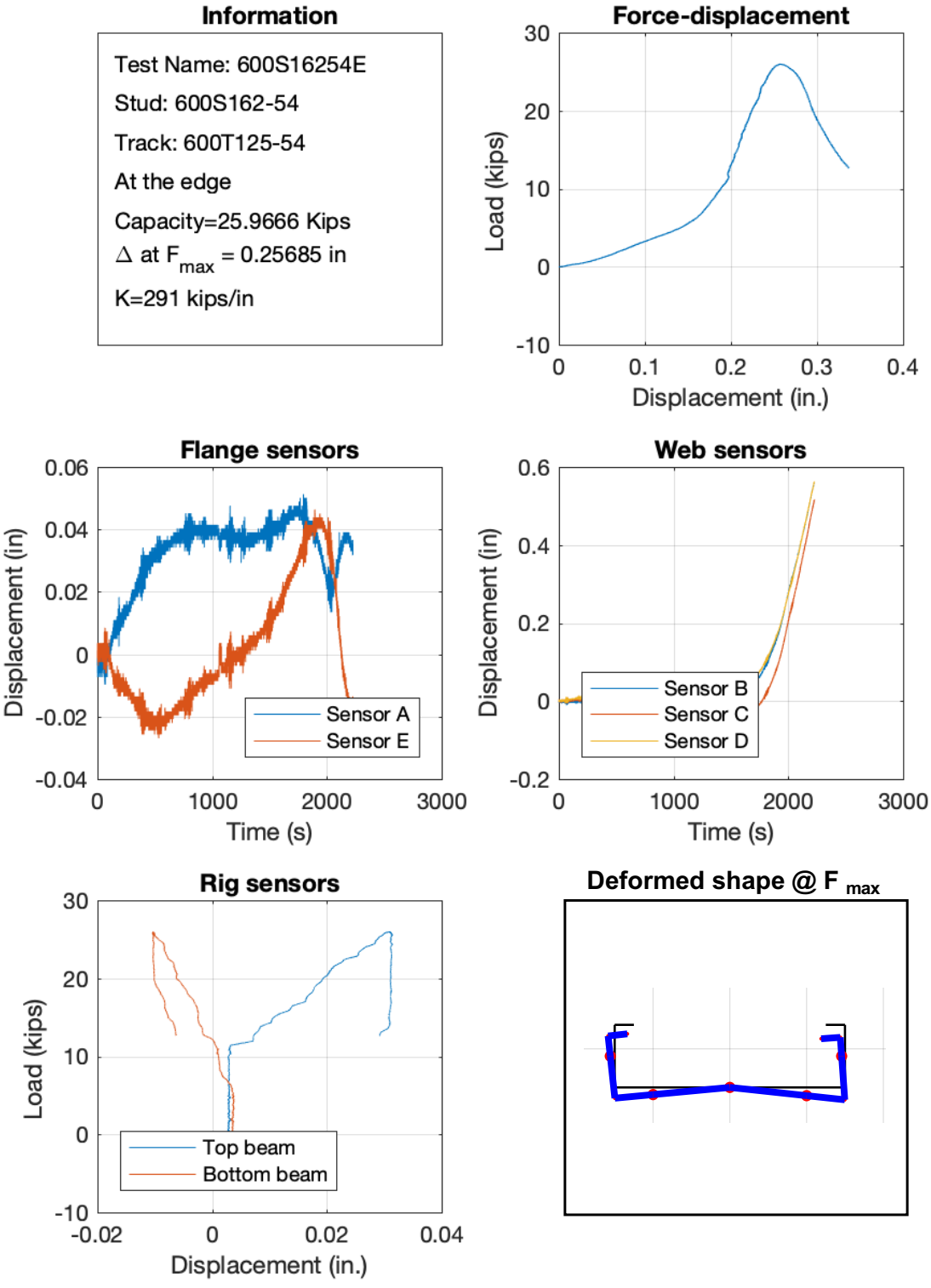
Information
Test Name: 600S16254E
Stud: 600S162-54
Track: 600T125-54
At the edge
Capacity=25.9666 Kips
Δ at F max = 0.25685 in
K=291 kips/in
Force-displacement
Load (kips)
Displacement (in.)
Flange sensors
Displacement (in)
Time (s)
Sensor A
Sensor E
Web sensors
Displacement (in)
Time (s)
Sensor B
Sensor C
Sensor D
Rig sensors
Load (kips)
Displacement (in.)
Top beam
Bottom beam
Deformed shape @ F max

**Information**

Test Name: 600S16254O05

Stud: 600S162-54

Track: 600T125-54

0.5" Overhang

Capacity=24.1711 Kips

$\Delta$ at $F_{max}$ = 0.23447 in

K=226 kips/in

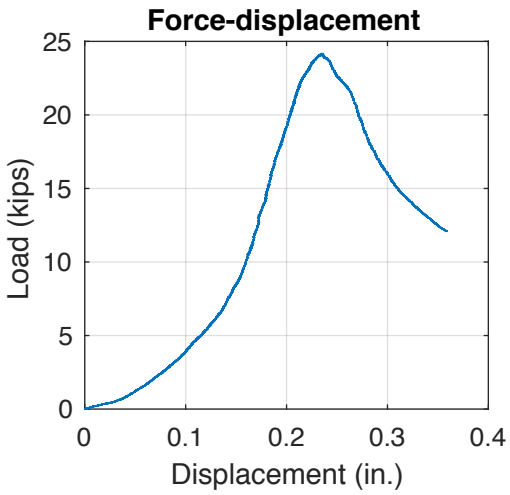


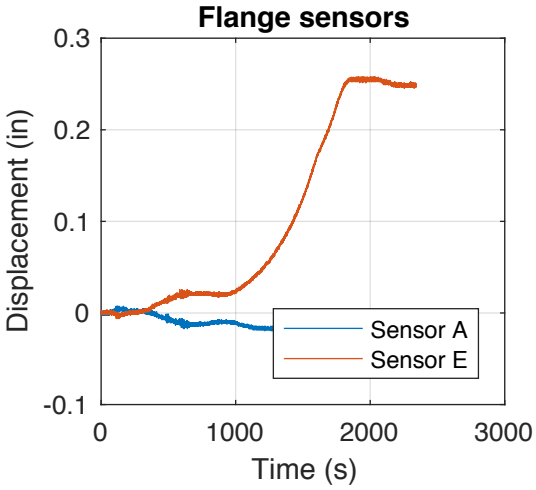


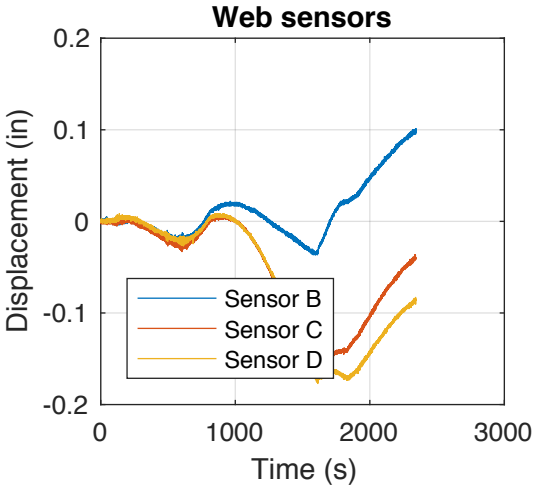


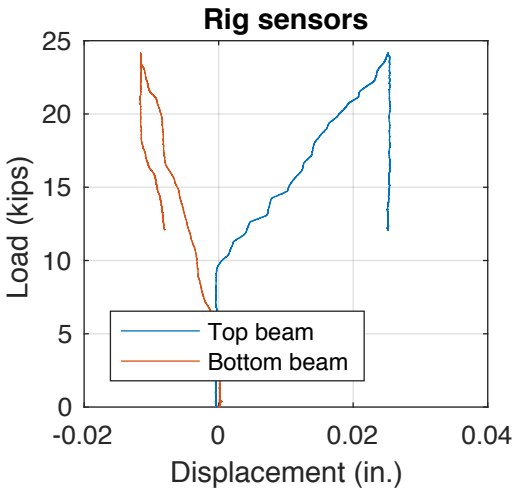


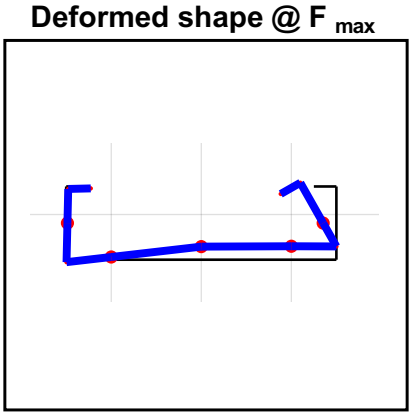

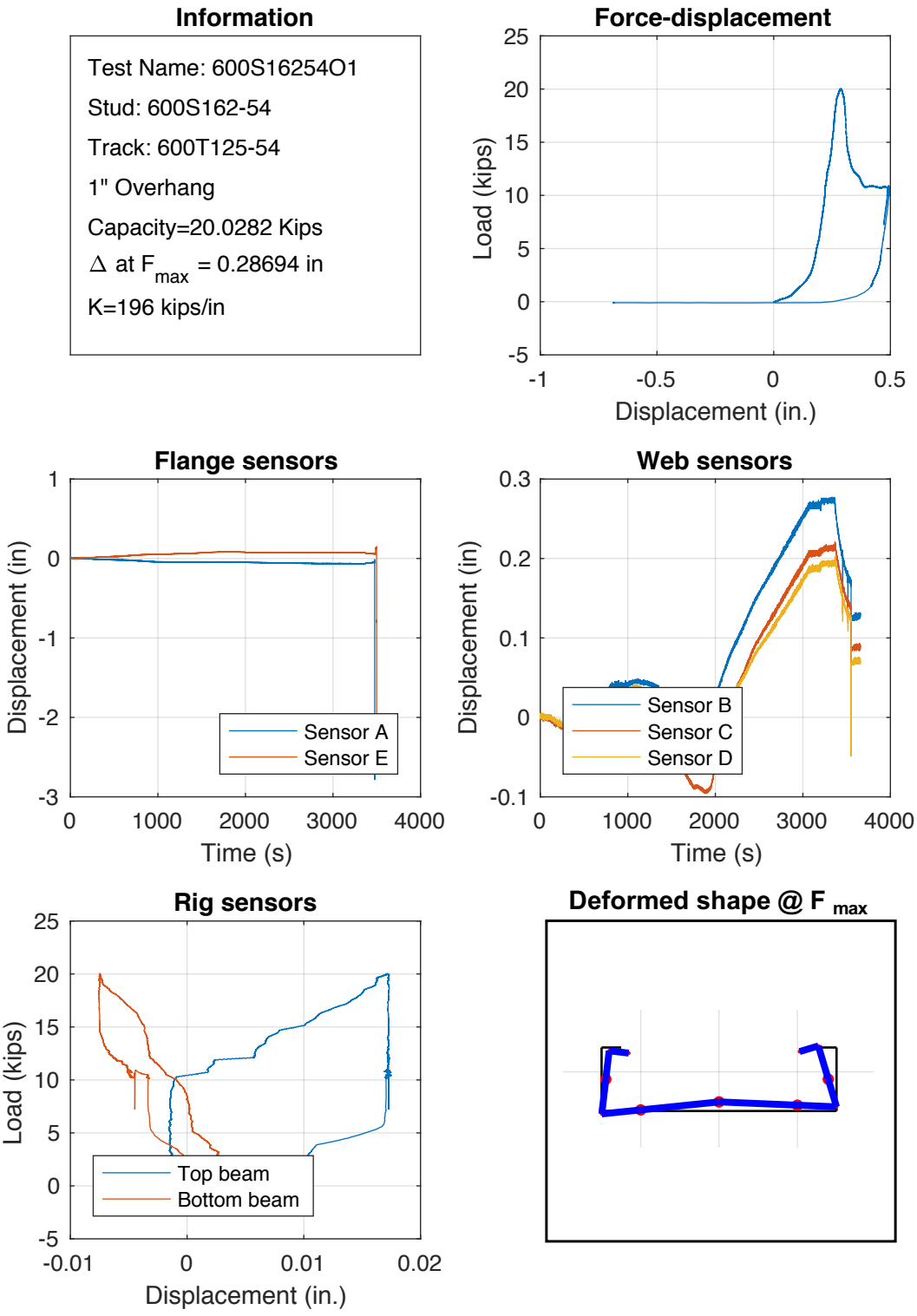
Information
Test Name: 600S16254O1
Stud: 600S162-54
Track: 600T125-54
1" Overhang
Capacity=20.0282 Kips
Δ at F max = 0.28694 in
K=196 kips/in
Force-displacement
Load (kips)
Displacement (in.)
Flange sensors
Displacement (in)
Time (s)
Sensor A
Sensor E
Web sensors
Displacement (in)
Time (s)
Sensor B
Sensor C
Sensor D
Rig sensors
Load (kips)
Displacement (in.)
Top beam
Bottom beam
Deformed shape @ F max

**Information**

Test Name: 600S16297F

Stud: 600S162-97

Track: 600T125-97

Rigid Bearing

Capacity=73.6892 Kips

$\Delta$ at $F_{max}$ = 0.1937 in

K=1288 kips/in

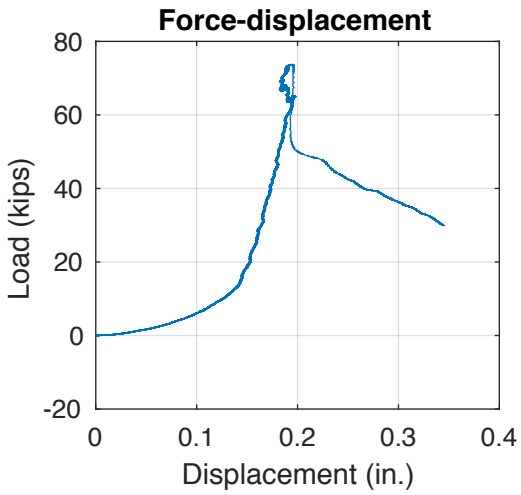


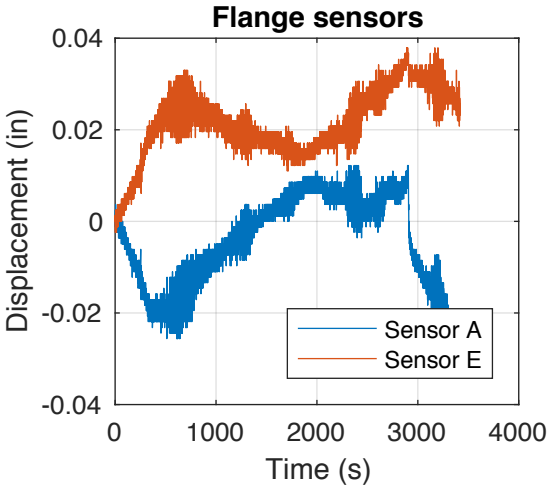


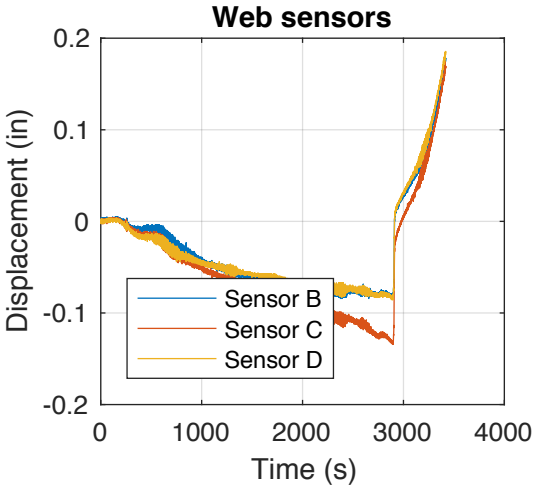


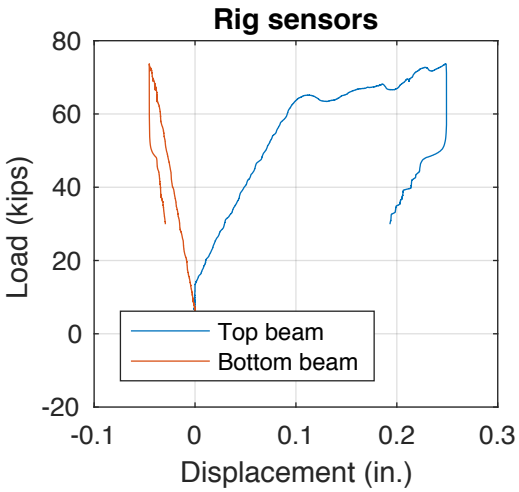


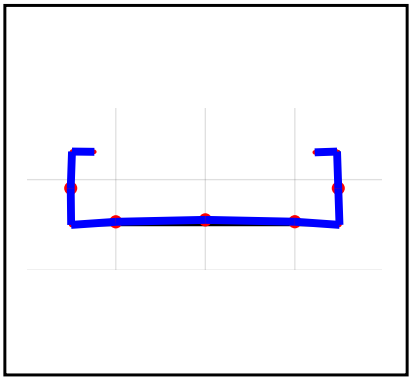

**Information**

Test Name: 600S16297C

Stud: 600S162-97

Track: 600T125-97

Full Bearing

Capacity=72.0695 Kips

$\Delta$ at $F_{max}$ = 0.33493 in

K=635 kips/in

**Force-displacement**

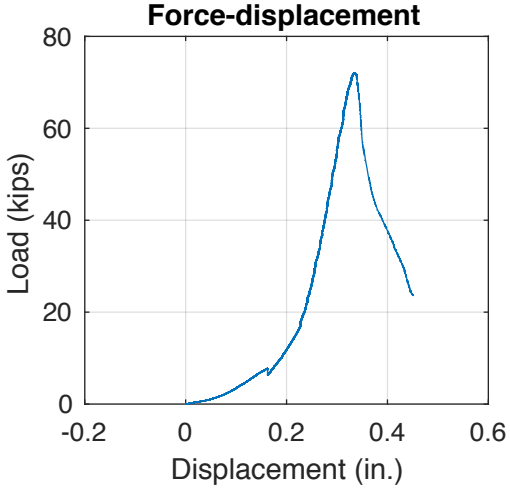


**Flange sensors**

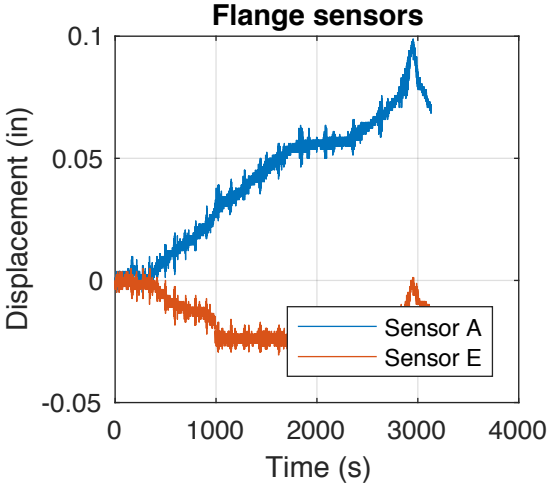


**Web sensors**

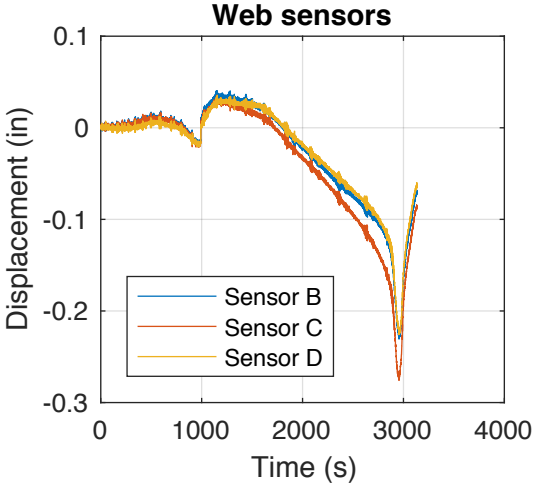


**Rig sensors**

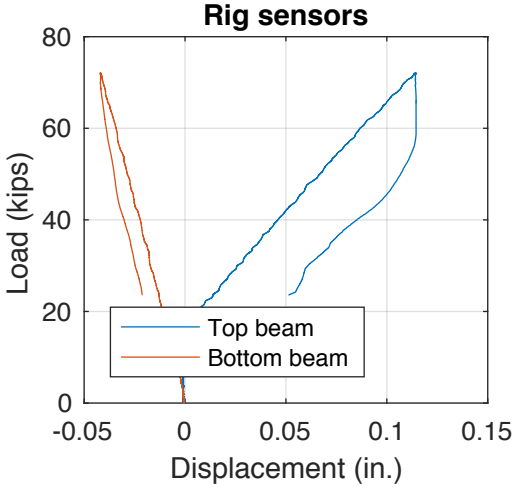


**Deformed shape @ $F_{max}$**

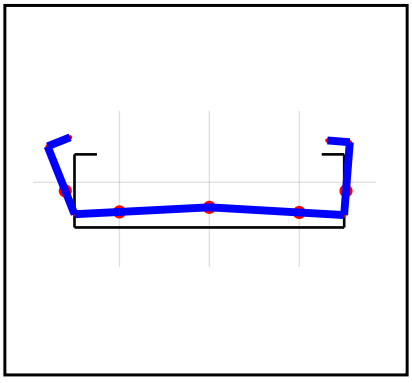

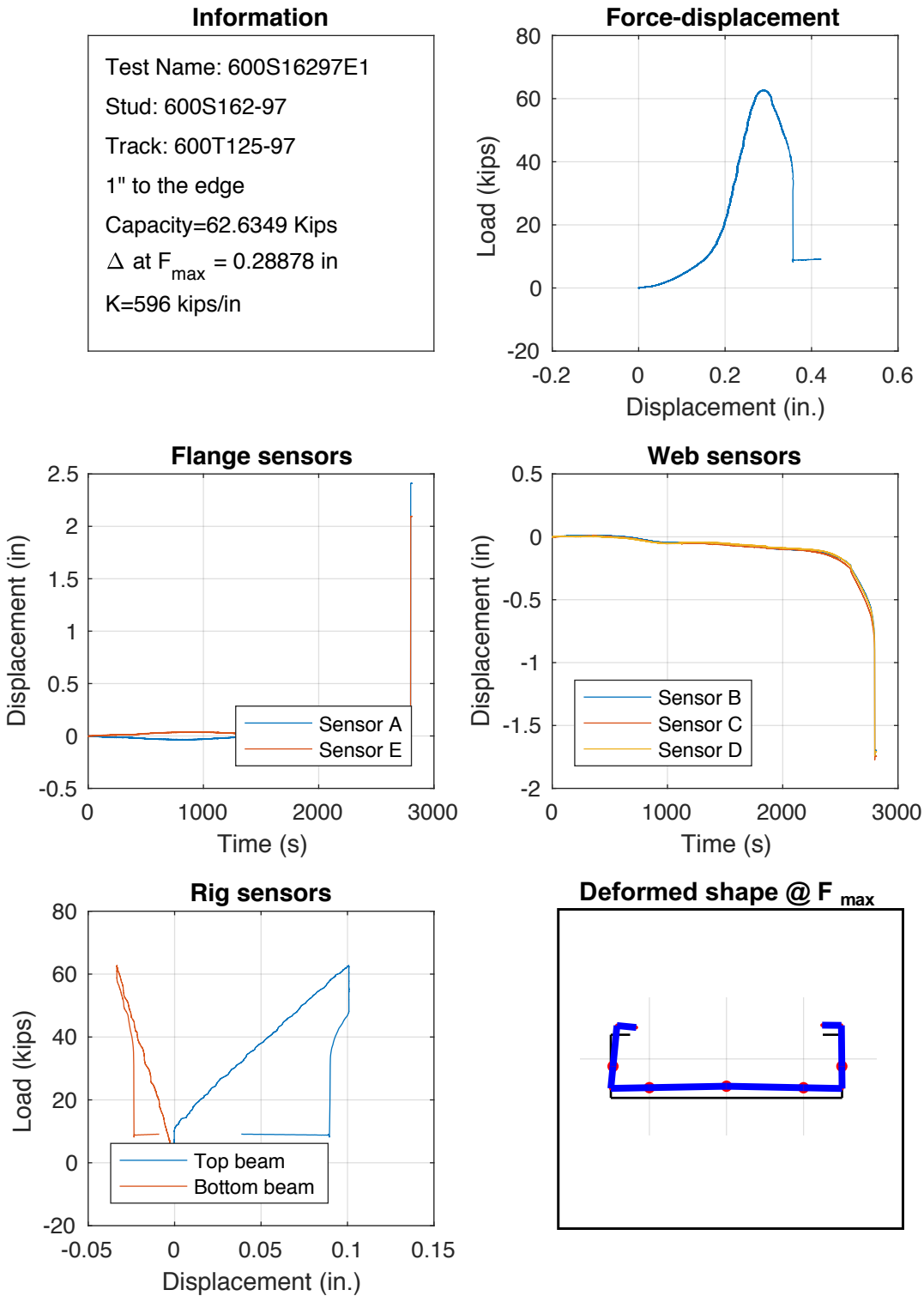
Information
Test Name: 600S16297E1
Stud: 600S162-97
Track: 600T125-97
1" to the edge
Capacity=62.6349 Kips
Δ at F max = 0.28878 in
K=596 kips/in
Force-displacement
Load (kips)
Displacement (in.)
Flange sensors
Displacement (in)
Time (s)
Sensor A
Sensor E
Web sensors
Displacement (in)
Time (s)
Sensor B
Sensor C
Sensor D
Rig sensors
Load (kips)
Displacement (in.)
Top beam
Bottom beam
Deformed shape @ F max

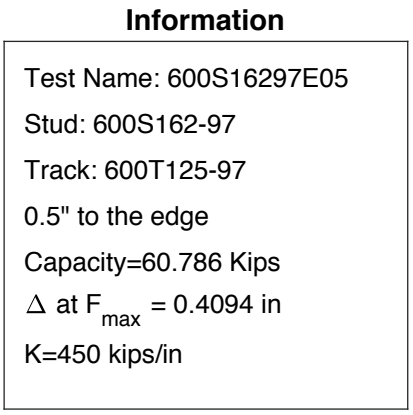
Information
Test Name: 600S16297E05
Stud: 600S162-97
Track: 600T125-97
0.5" to the edge
Capacity=60.786 Kips
Δ at F max = 0.4094 in
K=450 kips/in

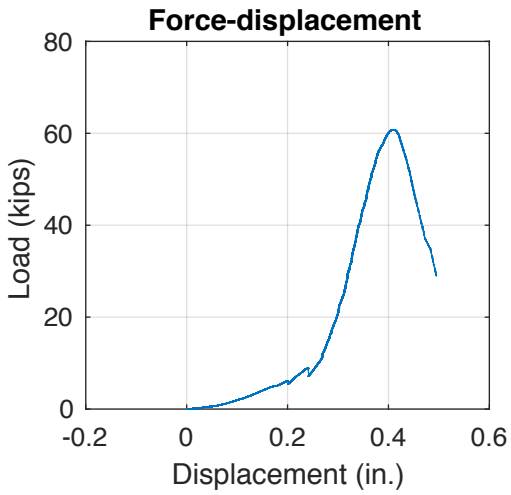
Force-displacement
Load (kips)
Displacement (in.)
80
60
40
20
0
-0.2
0
0.2
0.4
0.6

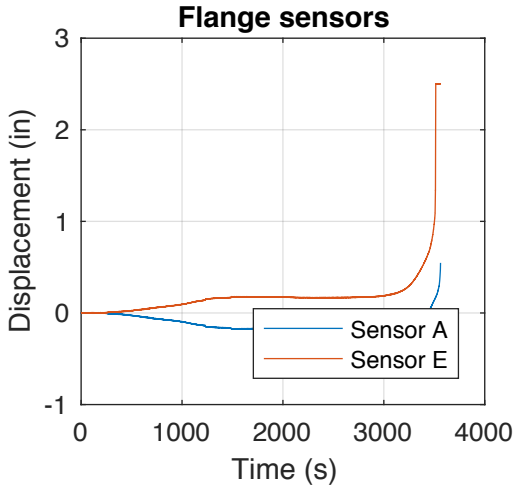
Flange sensors
Displacement (in)
Time (s)
Sensor A
Sensor E
3
2
1
0
-1
0
1000
2000
3000
4000

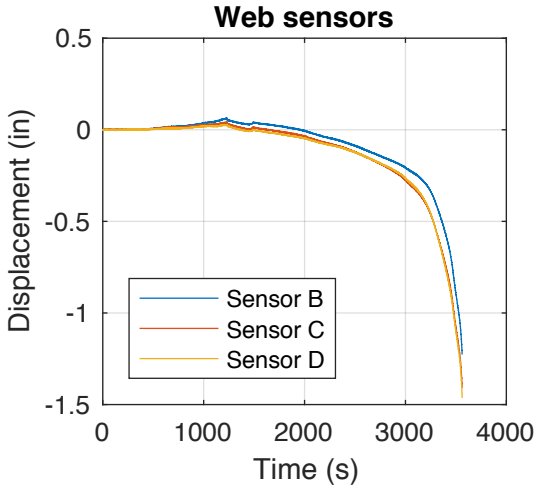
Web sensors
Displacement (in)
Time (s)
Sensor B
Sensor C
Sensor D
0.5
0
-0.5
-1
-1.5
0
1000
2000
3000
4000

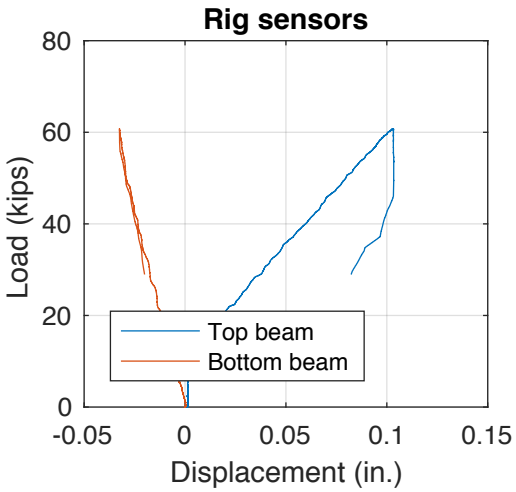
Rig sensors
Load (kips)
Displacement (in.)
Top beam
Bottom beam
80
60
40
20
0
-0.05
0
0.05
0.1
0.15

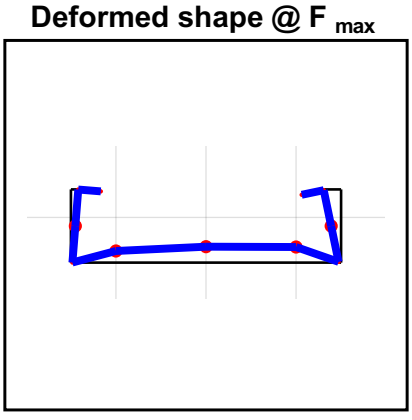
Deformed shape @ F max

**Information**

Test Name: 600S16297E0125

Stud: 600S162-97

Track: 600T125-97

0.125" to the edge

Capacity=51.4204 Kips

$\Delta$ at $F_{max}$ = 0.33853 in

K=473 kips/in

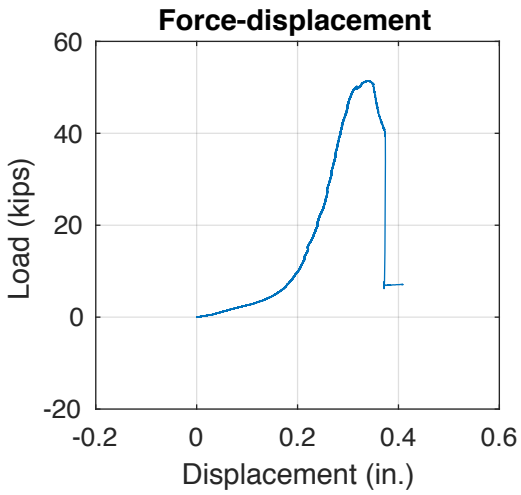


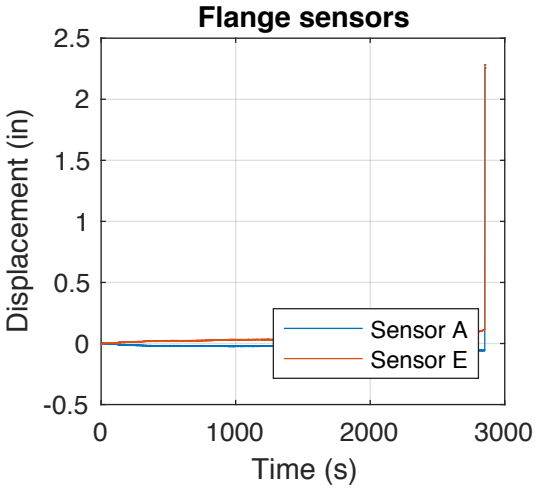


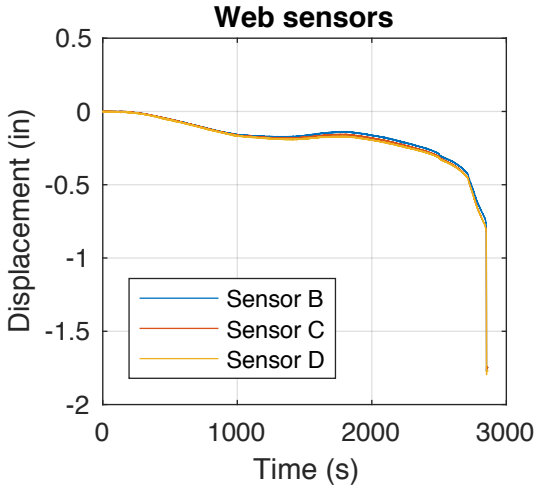


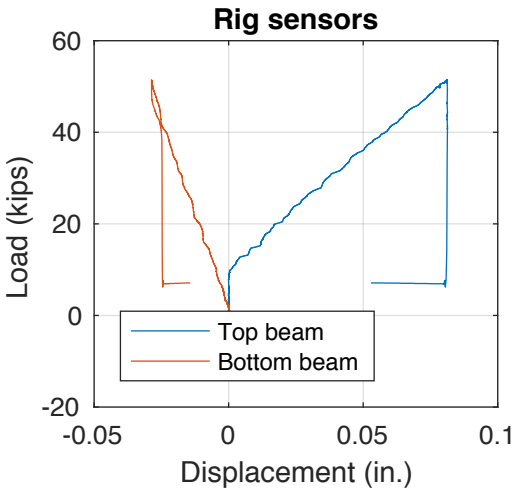


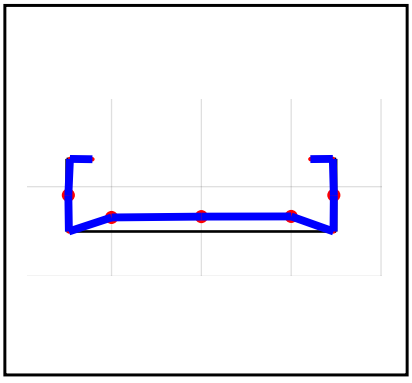

**Information**

Test Name: 600S16297E

Stud: 600S162-97

Track: 600T125-97

At the edge

Capacity=55.7654 Kips

$\Delta$ at $F_{max}$ = 0.31973 in

K=678 kips/in

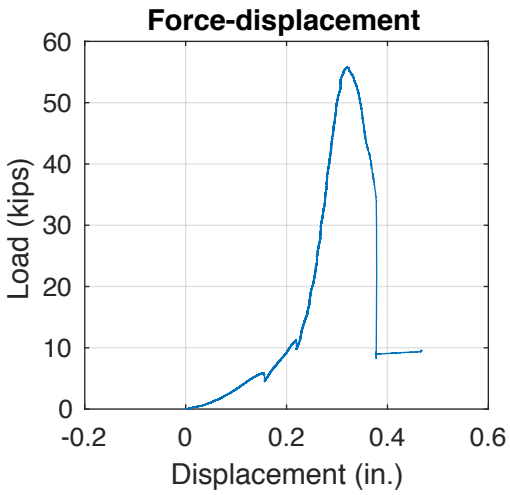


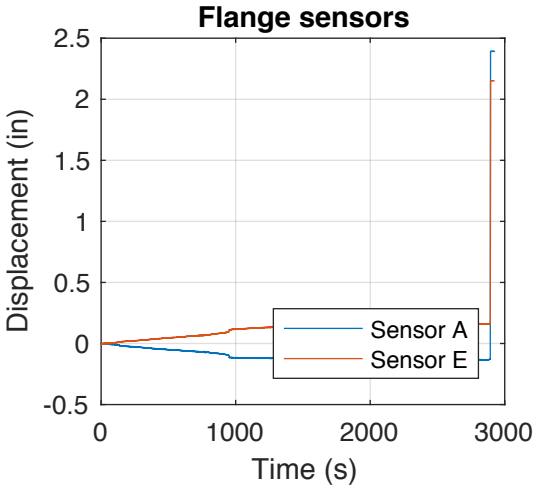


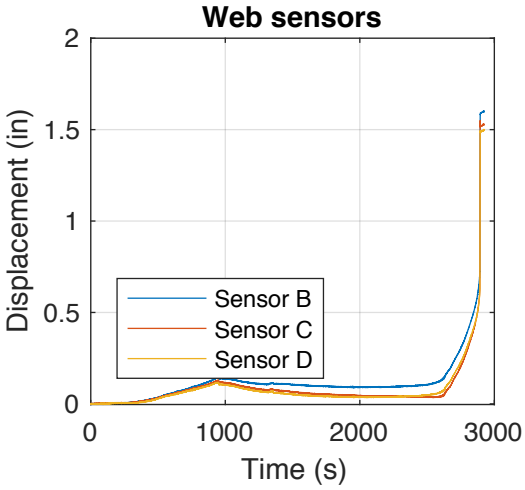


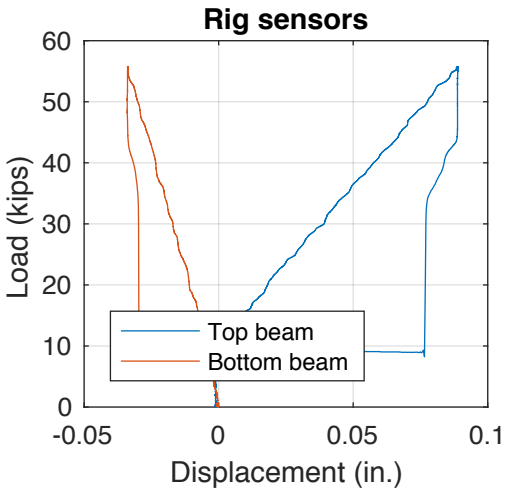


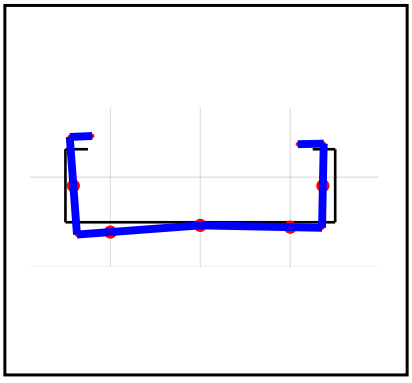

**Information**

Test Name: 600S16297O05

Stud: 600S162-97

Track: 600T125-97

0.5" Overhang

Capacity=50.3944 Kips

$\Delta$ at $F_{max}$ = 0.3562 in

K=387 kips/in

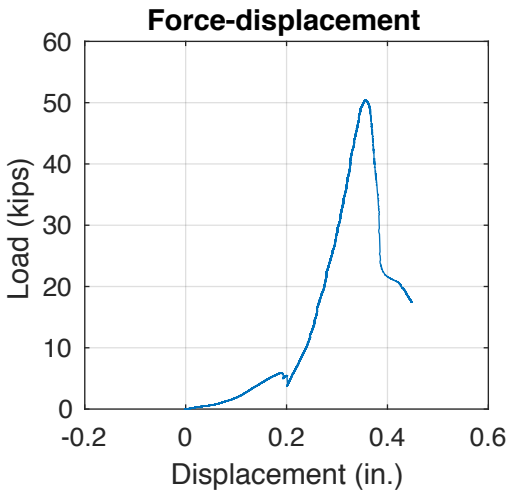


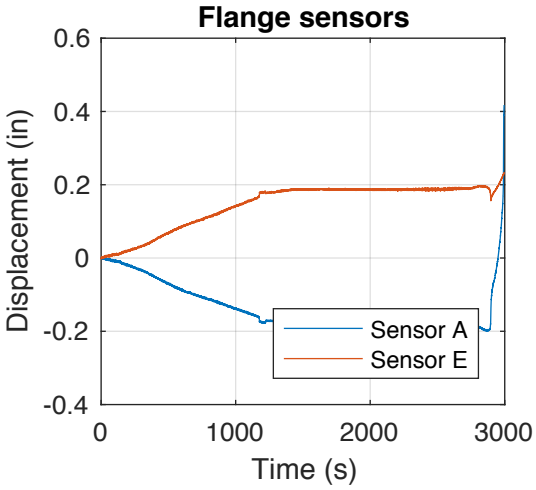


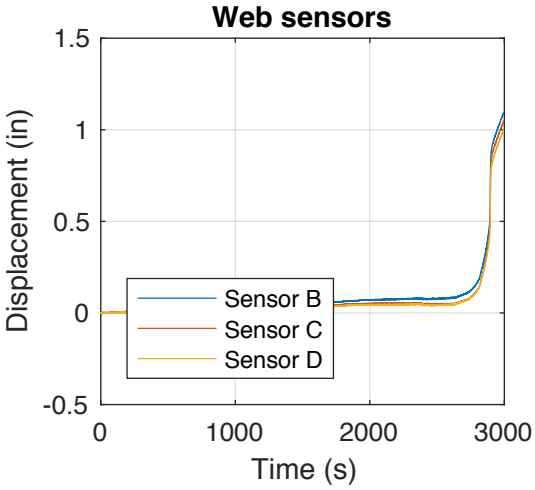


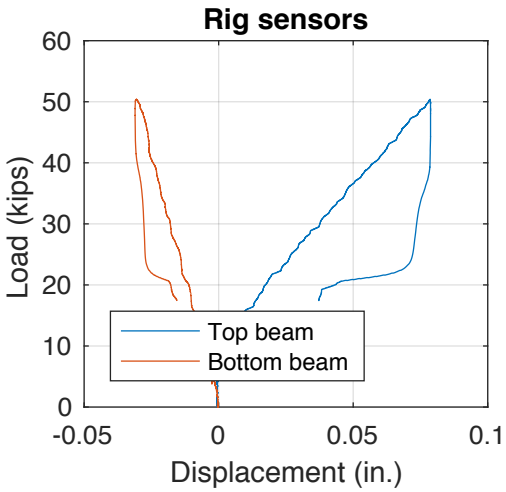


**Deformed shape @ $F_{max}$**

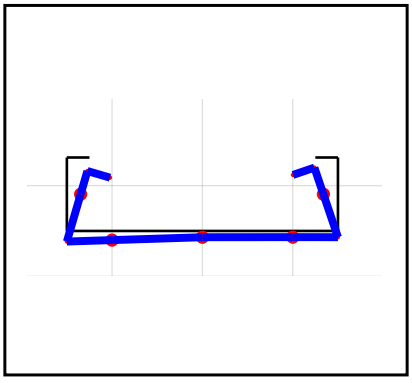

**Information**

Test Name: 600S16297O1

Stud: 600S162-97

Track: 600T125-97

1" Overhang

Capacity=43.9886 Kips

$\Delta$ at $F_{max}$ = 0.36837 in

K=356 kips/in

**Force-displacement**

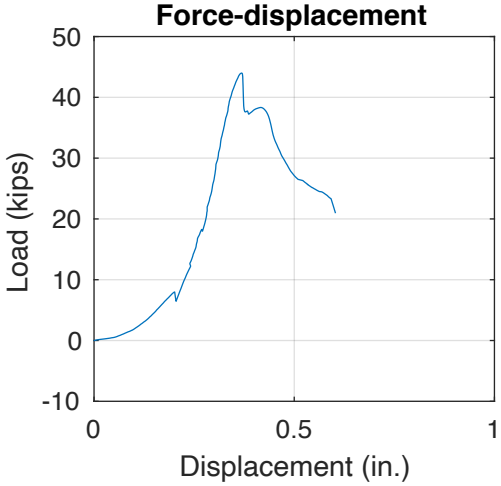


**Flange sensors**

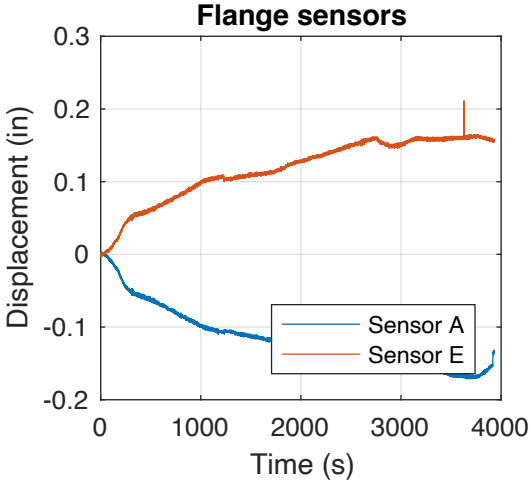


**Web sensors**

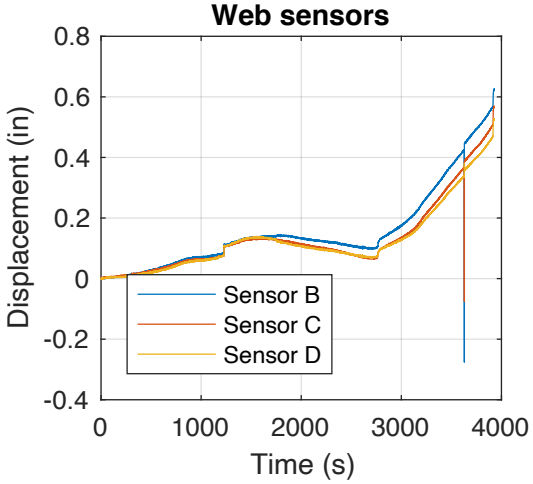


**Rig sensors**

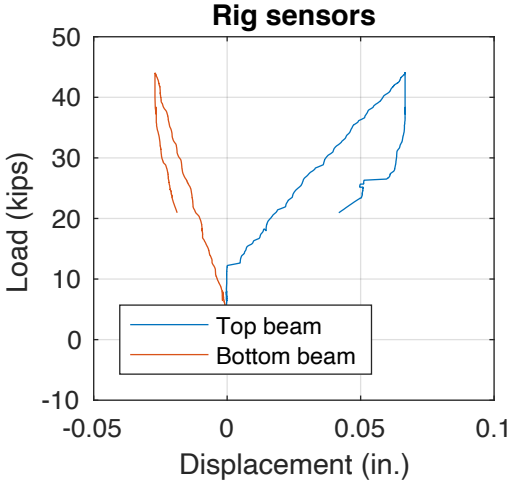


**Deformed shape @ $F_{max}$**

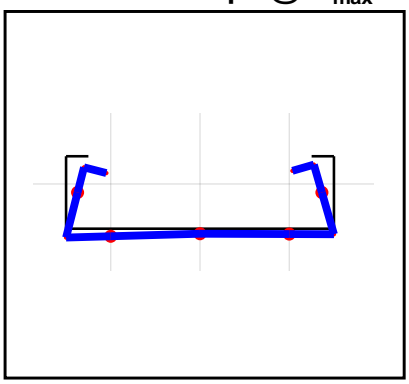

**Stress vs. strain relations from tensile tests on coupon cut from different thickness**

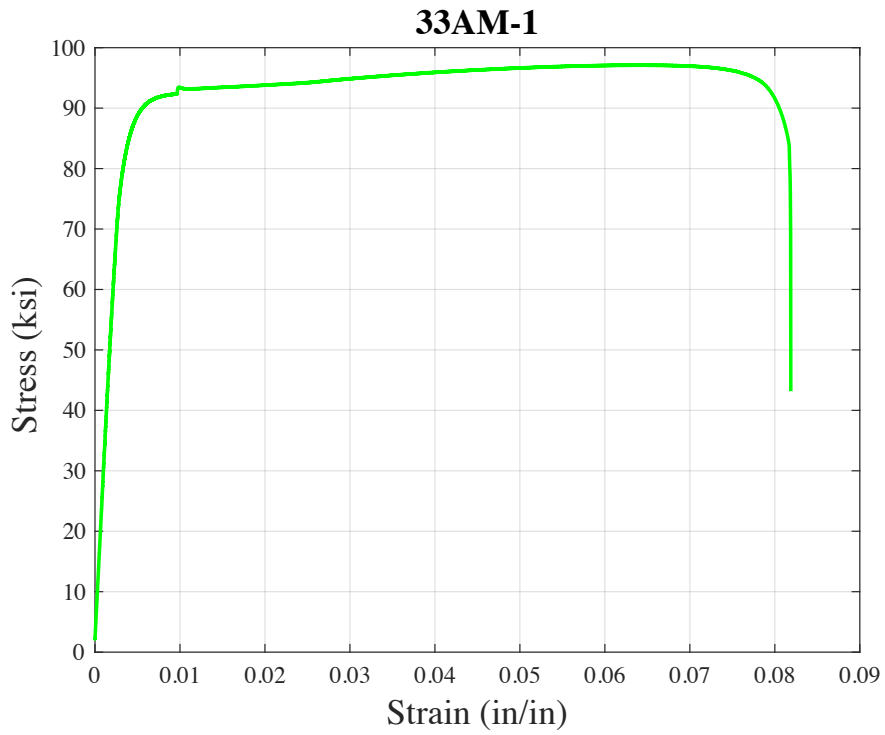

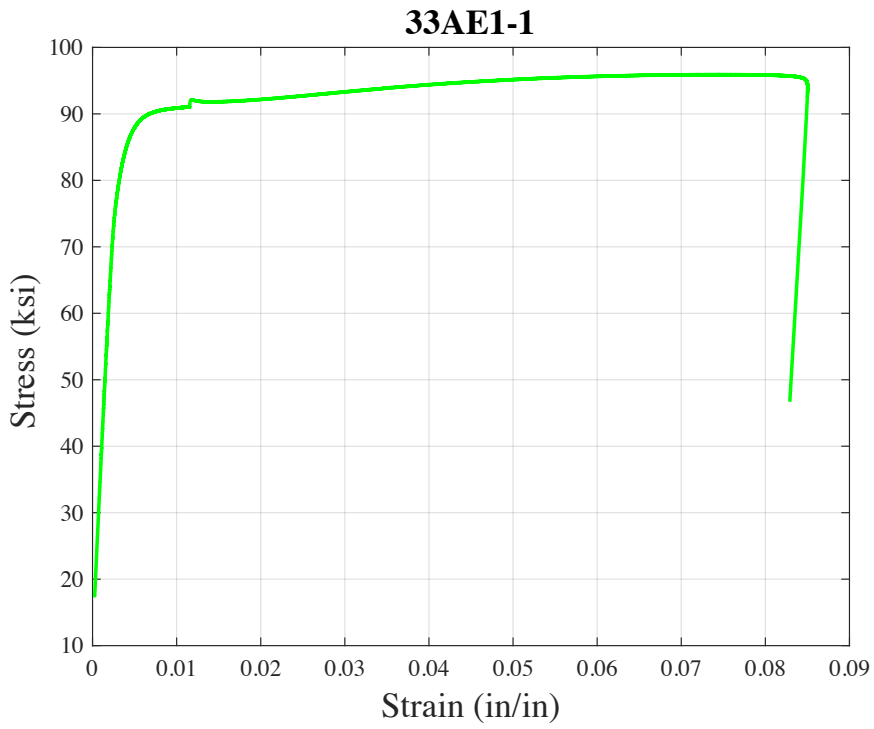
33AE1-1
Stress (ksi)
Strain (in/in)
100
90
80
70
60
50
40
30
20
10
0
0.01
0.02
0.03
0.04
0.05
0.06
0.07
0.08
0.09

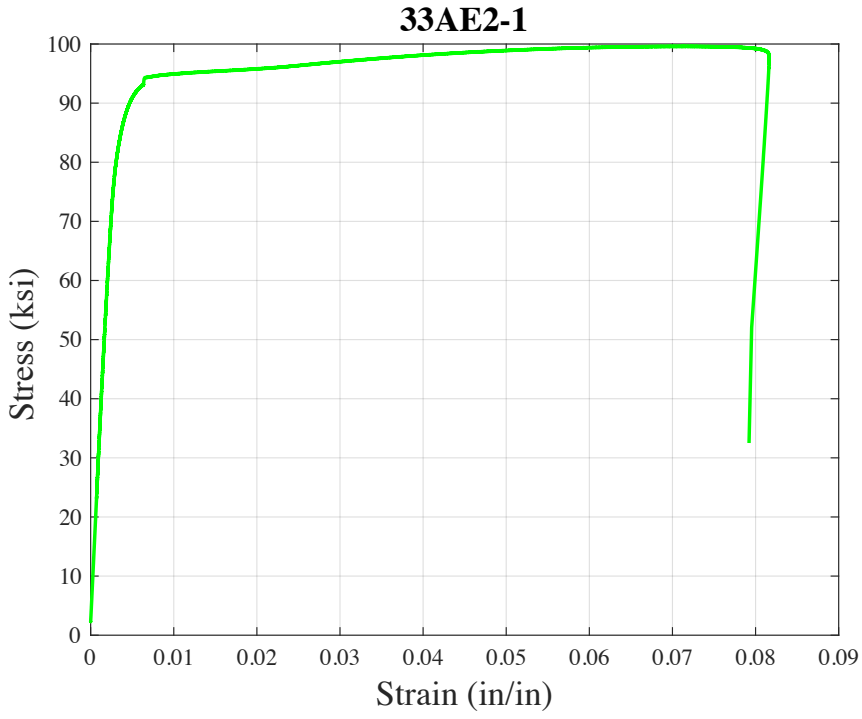
33AE2-1
Stress (ksi)
Strain (in/in)
100
90
80
70
60
50
40
30
20
10
0
0.01
0.02
0.03
0.04
0.05
0.06
0.07
0.08
0.09

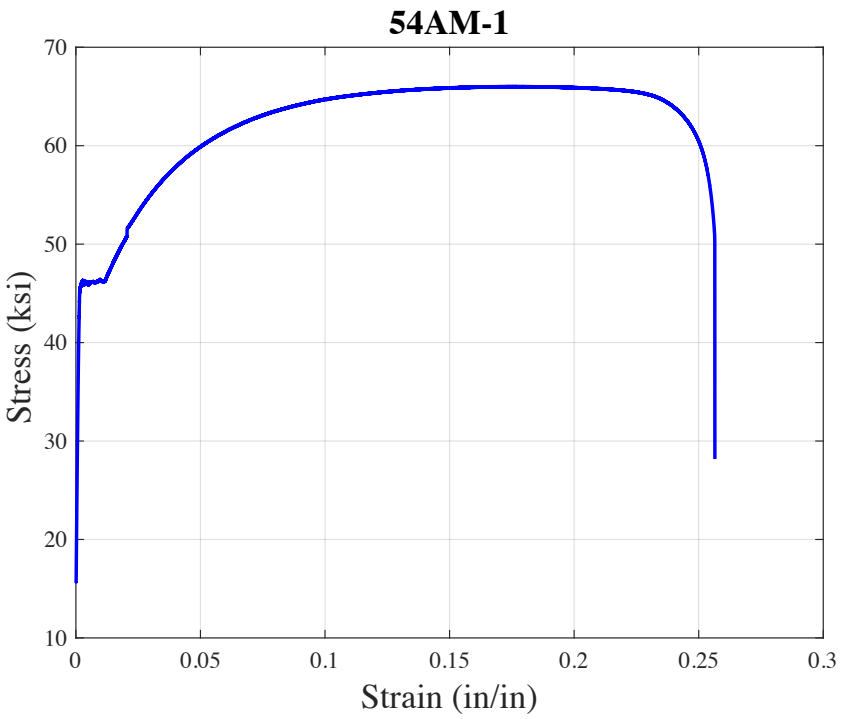
54AM-1
Stress (ksi)
Strain (in/in)
70
60
50
40
30
20
10
0
0.05
0.1
0.15
0.2
0.25
0.3

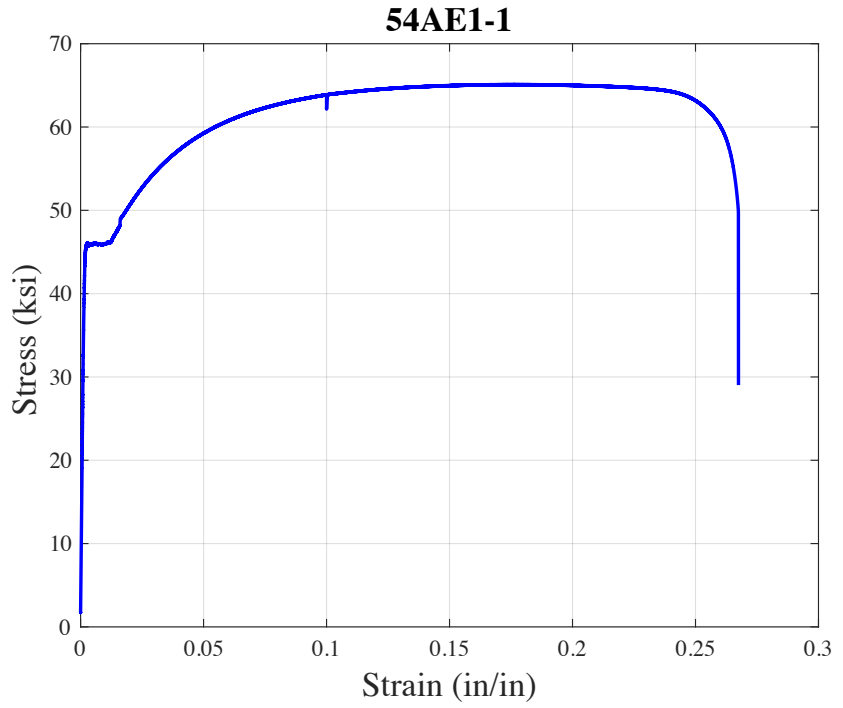
54AE1-1
Stress (ksi)
Strain (in/in)
70
60
50
40
30
20
10
0
0.05
0.1
0.15
0.2
0.25
0.3

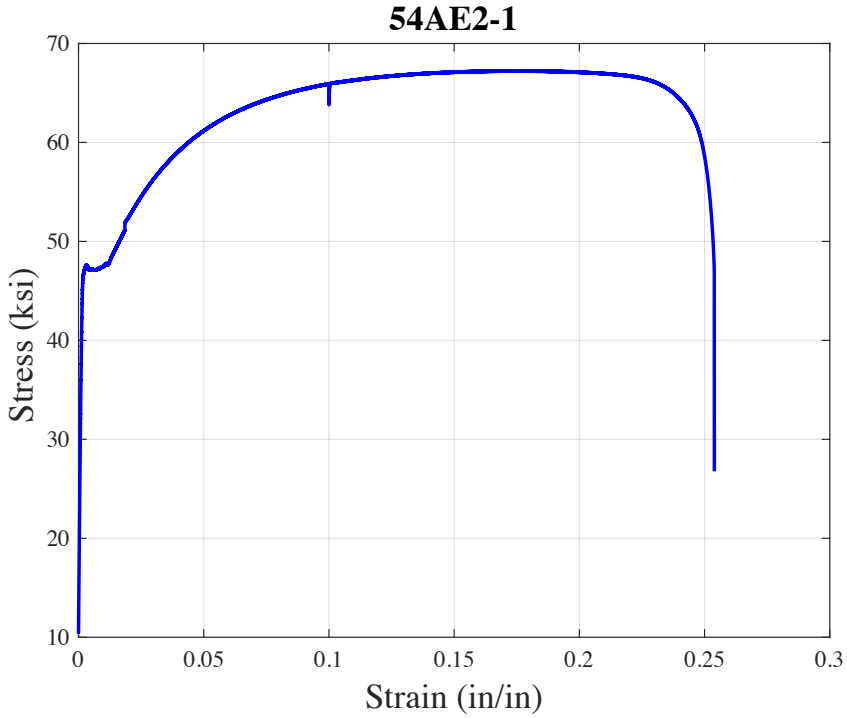
54AE2-1
Stress (ksi)
Strain (in/in)
70
60
50
40
30
20
10
0
0.05
0.1
0.15
0.2
0.25
0.3

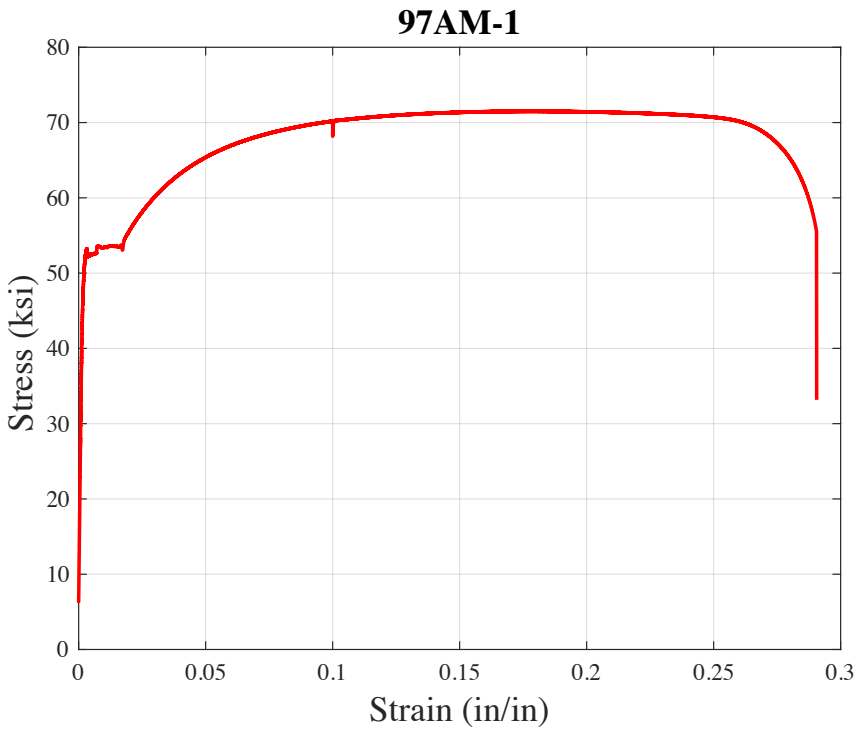
97AM-1
Stress (ksi)
Strain (in/in)
0
10
20
30
40
50
60
70
80
0
0.05
0.1
0.15
0.2
0.25
0.3

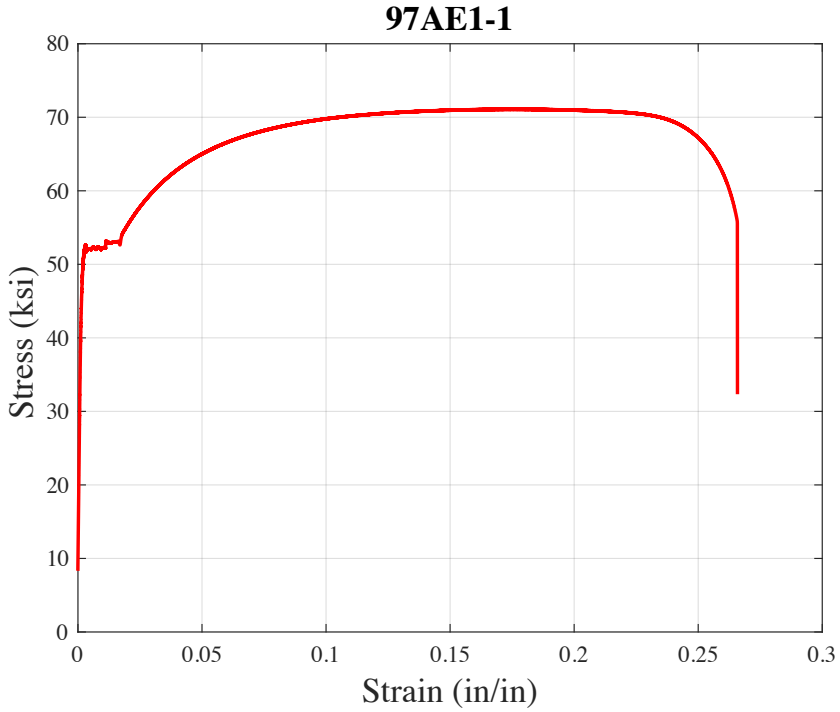
97AE1-1
Stress (ksi)
Strain (in/in)
0
10
20
30
40
50
60
70
80
0
0.05
0.1
0.15
0.2
0.25
0.3

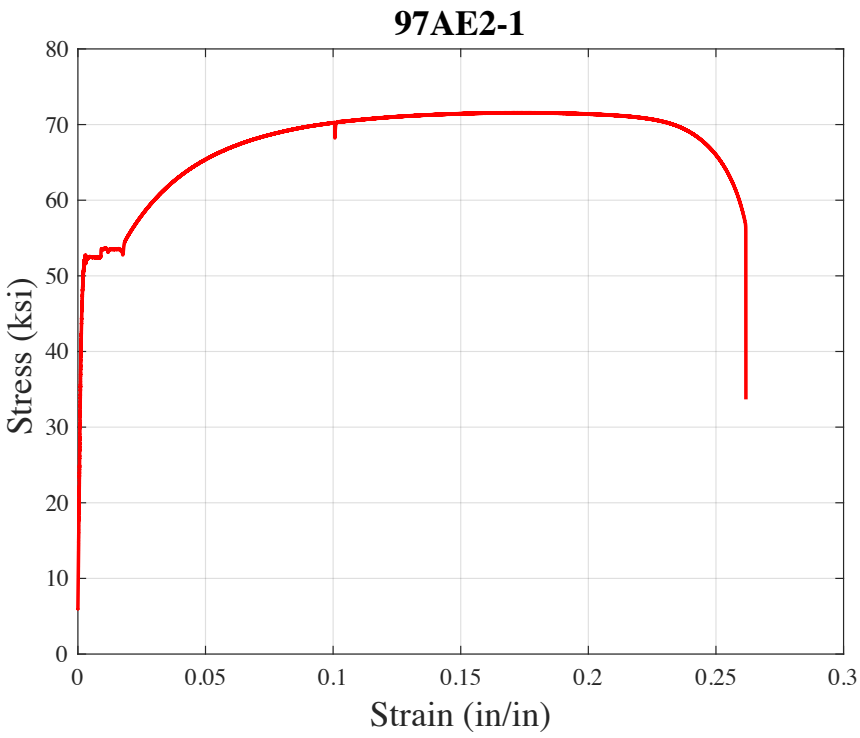
97AE2-1
Stress (ksi)
Strain (in/in)
0
10
20
30
40
50
60
70
80
0
0.05
0.1
0.15
0.2
0.25
0.3

# Appendix B

## Computational modeling program results

| Section | Bearing condition | Peak load (FEM) | | |
|---|---|---|---|---|
| | | Buckling mode | | |
| | | Local | Distortional | Global |
| | | *kips* | | |
| 362S137-33 | F | 10.00 | 10.18 | 8.28 |
| | 5" | 9.96 | 9.77 | 8.27 |
| | 2" | 9.97 | 9.50 | 8.26 |
| | 1" | 10.00 | 9.60 | 8.25 |
| | 0.75" | 9.89 | 10.00 | 8.22 |
| | 0.5" | 10.00 | 9.60 | 8.20 |
| | 0.25" | 9.96 | 9.70 | 8.15 |
| | 0.125" | 9.88 | 9.60 | 8.13 |
| | E | 9.44 | 9.40 | 8.07 |
| | O 0.25 | 7.07 | 7.02 | 6.00 |
| | O 0.5 | 6.44 | 6.90 | 5.55 |
| | O 1 | 5.98 | 6.05 | 4.32 |
| 362S137-43 | F | 14.93 | 14.52 | 12.59 |
| | 5" | 14.78 | 14.51 | 12.58 |
| | 2" | 14.76 | 14.51 | 12.51 |
| | 1" | 14.93 | 14.40 | 12.48 |
| | 0.75" | 14.63 | 14.31 | 12.39 |
| | 0.5" | 14.99 | 14.20 | 12.26 |
| | 0.25" | 14.66 | 14.48 | 12.19 |
| | 0.125" | 14.42 | 14.04 | 12.05 |
| | E | 13.92 | 13.49 | 11.65 |
| | O 0.25 | 13.07 | 10.50 | 9.29 |
| | O 0.5 | 10.15 | 10.41 | 8.51 |
| | O 1 | 9.31 | 8.32 | 7.36 |
| 362S137-54 | F | 27.29 | 25.31 | 23.47 |
| | 5" | 27.25 | 25.16 | 23.45 |
| | 2" | 27.26 | 25.17 | 23.42 |
| | 1" | 27.24 | 25.22 | 23.39 |
| | 0.75" | 25.87 | 24.53 | 23.18 |
| | 0.5" | 27.45 | 25.31 | 22.81 |

| | | | | |
|---|---|---|---|---|
| | 0.25" | 26.87 | 25.08 | 22.69 |
| | 0.125" | 25.75 | 24.42 | 21.92 |
| | E | 24.03 | 23.28 | 20.55 |
| | O 0.25 | 20.16 | 17.52 | 15.75 |
| | O 0.5 | 18.22 | 16.95 | 13.59 |
| | O 1 | 16.42 | 15.13 | 12.28 |
| 362S137-68 | F | 36.25 | 35.06 | 35.26 |
| | 5" | 36.20 | 34.97 | 35.15 |
| | 2" | 36.19 | 34.95 | 35.06 |
| | 1" | 35.57 | 34.54 | 34.33 |
| | 0.75" | 35.10 | 33.74 | 33.83 |
| | 0.5" | 34.83 | 35.39 | 33.46 |
| | 0.25" | 34.60 | 34.80 | 33.21 |
| | 0.125" | 34.46 | 33.72 | 32.93 |
| | E | 33.10 | 32.37 | 31.79 |
| | O 0.25 | 28.68 | 27.20 | 26.10 |
| | O 0.5 | 26.10 | 24.07 | 23.00 |
| | O 1 | 22.84 | 21.27 | 21.00 |
| 362S162-33 | F | 10.80 | 10.82 | 9.48 |
| | 5" | 10.72 | 10.61 | 9.46 |
| | 2" | 10.70 | 10.15 | 9.43 |
| | 1" | 10.88 | 9.54 | 9.42 |
| | 0.75" | 10.64 | 9.54 | 9.37 |
| | 0.5" | 10.78 | 10.17 | 9.48 |
| | 0.25" | 10.78 | 10.12 | 9.42 |
| | 0.125" | 10.57 | 9.80 | 9.30 |
| | E | 8.59 | 9.19 | 9.00 |
| | O 0.25 | 7.67 | 7.58 | 6.86 |
| | O 0.5 | 6.74 | 6.67 | 6.24 |
| | O 1 | 5.95 | 6.44 | 5.26 |
| 362S162-43 | F | 16.11 | 15.30 | 14.39 |
| | 5" | 16.00 | 15.19 | 14.37 |
| | 2" | 15.85 | 15.10 | 14.38 |
| | 1" | 15.60 | 15.07 | 14.35 |
| | 0.75" | 15.55 | 14.72 | 14.29 |
| | 0.5" | 15.50 | 15.13 | 14.19 |
| | 0.25" | 14.20 | 14.99 | 14.07 |
| | 0.125" | 15.04 | 14.95 | 13.96 |

| | | | | |
|---|---|---|---|---|
| | E | 14.74 | 14.55 | 13.16 |
| | O 0.25 | 12.21 | 11.75 | 10.20 |
| | O 0.5 | 10.51 | 9.82 | 9.72 |
| | O 1 | 9.42 | 8.68 | 8.12 |
| 362S162-54 | F | 30.67 | 29.12 | 27.07 |
| | 5" | 30.26 | 28.96 | 27.05 |
| | 2" | 30.00 | 28.77 | 27.00 |
| | 1" | 29.50 | 28.67 | 26.91 |
| | 0.75" | 28.46 | 28.63 | 26.83 |
| | 0.5" | 28.31 | 28.56 | 26.66 |
| | 0.25" | 27.93 | 28.43 | 26.54 |
| | 0.125" | 27.03 | 28.18 | 26.08 |
| | E | 25.97 | 27.27 | 24.34 |
| | O 0.25 | 22.00 | 16.69 | 20.26 |
| | O 0.5 | 20.08 | | 18.35 |
| | O 1 | 17.97 | | 16.00 |
| 362S162-68 | F | 41.52 | 40.32 | 39.70 |
| | 5" | 41.48 | 40.09 | 39.49 |
| | 2" | 41.54 | 40.01 | 39.27 |
| | 1" | 41.13 | 39.45 | 38.50 |
| | 0.75" | 40.06 | 39.19 | 37.76 |
| | 0.5" | 39.88 | 39.00 | 37.57 |
| | 0.25" | 39.15 | 38.84 | 37.05 |
| | 0.125" | 38.60 | 38.56 | 37.00 |
| | E | 37.03 | 35.25 | 35.91 |
| | O 0.25 | 32.13 | 28.07 | 29.58 |
| | O 0.5 | 28.55 | 25.93 | 26.43 |
| | O 1 | 25.58 | 23.67 | 22.87 |
| 362S200-33 | F | 13.25 | 12.52 | 10.95 |
| | 5" | 13.20 | 12.49 | 10.92 |
| | 2" | 13.10 | 12.33 | 10.76 |
| | 1" | 13.01 | 11.96 | 10.73 |
| | 0.75" | 12.90 | 11.41 | 10.65 |
| | 0.5" | 12.80 | 11.24 | 10.56 |
| | 0.25" | 12.78 | 11.00 | 10.46 |
| | 0.125" | 12.68 | 10.80 | 10.32 |
| | E | 11.81 | 10.68 | 10.09 |
| | O 0.25 | 9.65 | 8.43 | 7.23 |

| | | | | |
|---|---|---|---|---|
| | O 0.5 | 6.85 | 6.13 | 6.88 |
| | O 1 | 6.18 | 5.47 | 5.70 |
| 362S200-43 | F | 18.09 | 16.52 | 16.64 |
| | 5" | 17.97 | 16.42 | 16.61 |
| | 2" | 17.68 | 16.38 | 16.49 |
| | 1" | 17.60 | 16.37 | 16.46 |
| | 0.75" | 17.50 | 16.21 | 16.29 |
| | 0.5" | 17.40 | 16.13 | 16.19 |
| | 0.25" | 17.30 | 16.09 | 16.00 |
| | 0.125" | 17.18 | 16.06 | 15.73 |
| | E | 16.31 | 15.31 | 14.76 |
| | O 0.25 | 13.29 | 12.54 | 12.22 |
| | O 0.5 | 11.51 | 10.68 | 10.98 |
| | O 1 | 10.80 | 9.08 | 8.91 |
| 362S200-54 | F | 35.99 | 32.60 | 23.80 |
| | 5" | 35.62 | 32.60 | 23.87 |
| | 2" | 35.61 | 32.19 | 23.55 |
| | 1" | 34.54 | 32.15 | 23.43 |
| | 0.75" | 34.05 | 32.06 | 23.30 |
| | 0.5" | 33.60 | 32.00 | 23.12 |
| | 0.25" | 33.35 | 31.91 | 23.05 |
| | 0.125" | 33.07 | 31.24 | 22.81 |
| | E | 30.36 | 27.49 | 21.33 |
| | O 0.25 | 25.37 | 22.88 | 18.13 |
| | O 0.5 | 22.57 | 19.57 | 16.01 |
| | O 1 | 20.83 | 16.42 | 13.18 |
| 362S200-68 | F | 48.39 | 46.26 | 44.77 |
| | 5" | 48.20 | 46.25 | 44.08 |
| | 2" | 48.19 | 45.84 | 44.00 |
| | 1" | 47.09 | 45.51 | 43.41 |
| | 0.75" | 46.47 | 46.11 | 42.45 |
| | 0.5" | 46.20 | 43.38 | 41.70 |
| | 0.25" | 45.31 | 45.77 | 40.82 |
| | 0.125" | 43.14 | 43.34 | 39.91 |
| | E | 41.80 | 40.87 | 38.70 |
| | O 0.25 | 36.03 | 31.51 | 30.30 |
| | O 0.5 | 32.30 | 26.47 | 28.95 |
| | O 1 | 29.04 | 25.39 | 25.90 |

| | | | | |
|---|---|---|---|---|
| 400S137-33 | F | 13.07 | 12.61 | 8.67 |
| | 5" | | 12.60 | 8.64 |
| | 2" | | 12.58 | 8.65 |
| | 1" | 12.83 | 12.55 | 8.63 |
| | 0.75" | 12.79 | 12.51 | 8.61 |
| | 0.5" | 12.96 | 12.32 | 8.56 |
| | 0.25" | | 12.21 | 8.47 |
| | 0.125" | | 12.06 | 8.31 |
| | E | | 11.38 | 8.23 |
| | O 0.25 | | 9.19 | 6.17 |
| | O 0.5 | | 7.66 | 5.64 |
| | O 1 | | 6.55 | 4.10 |
| 400S137-43 | F | 14.75 | 13.89 | 12.98 |
| | 5" | 14.70 | 13.85 | 12.98 |
| | 2" | 14.63 | 13.75 | 12.91 |
| | 1" | 14.54 | 13.65 | 12.81 |
| | 0.75" | 14.56 | 13.59 | 12.76 |
| | 0.5" | 14.70 | 13.79 | 12.66 |
| | 0.25" | | 13.67 | 12.52 |
| | 0.125" | | 13.51 | 12.31 |
| | E | | 12.31 | 11.87 |
| | O 0.25 | | 10.16 | 9.58 |
| | O 0.5 | | 8.37 | 8.70 |
| | O 1 | | 7.26 | 7.35 |
| 400S137-54 | F | 27.74 | 27.45 | 24.43 |
| | 5" | | 27.23 | 24.38 |
| | 2" | | 27.11 | 24.09 |
| | 1" | | 26.85 | 23.85 |
| | 0.75" | 27.00 | | 23.72 |
| | 0.5" | 26.98 | 26.87 | 23.60 |
| | 0.25" | 26.75 | 26.30 | 23.47 |
| | 0.125" | 25.93 | 25.32 | 23.25 |
| | E | 23.96 | 23.60 | 21.79 |
| | O 0.25 | | | 18.33 |
| | O 0.5 | | | 15.40 |
| | O 1 | | | 12.22 |
| 400S137-68 | F | 37.38 | 36.38 | 34.59 |
| | 5" | 37.14 | 36.31 | 34.48 |

| | | | | |
|---|---|---|---|---|
| | 2" | 36.87 | 36.13 | 34.39 |
| | 1" | 36.44 | 35.74 | 34. 29 |
| | 0.75" | 36.20 | 35.66 | 34.17 |
| | 0.5" | 36.18 | 35.57 | 34.04 |
| | 0.25" | 36.00 | 35.23 | 33.81 |
| | 0.125" | 35.11 | 34.70 | 33.19 |
| | E | 33.10 | 32.46 | 31.01 |
| | O 0.25 | 29.20 | 29.00 | 26.51 |
| | O 0.5 | 27.20 | 25.70 | 23.90 |
| | O 1 | 23.05 | 21.42 | 20.50 |
| 400S162-33 | F | 13.20 | 12.16 | 9.63 |
| | 5" | 12.94 | 12.08 | 9.61 |
| | 2" | 12.89 | 12.24 | 9.57 |
| | 1" | | 12.02 | 9.53 |
| | 0.75" | 12.76 | 12.21 | 9.50 |
| | 0.5" | 12.87 | 12.08 | 9.46 |
| | 0.25" | 11.91 | 10.91 | 9.40 |
| | 0.125" | 13.00 | 12.16 | 9.31 |
| | E | 10.73 | 10.00 | 8.90 |
| | O 0.25 | | 7.73 | 6.85 |
| | O 0.5 | | 6.15 | 6.26 |
| | O 1 | | 5.15 | 5.27 |
| 400S162-43 | F | 17.44 | 16.37 | 14.29 |
| | 5" | 17.39 | 15.68 | 14.28 |
| | 2" | 17.25 | 15.58 | 14.15 |
| | 1" | 17.09 | 15.52 | 13.89 |
| | 0.75" | 17.03 | 15.38 | 13.87 |
| | 0.5" | 16.79 | 15.30 | 13.83 |
| | 0.25" | 16.66 | 15.15 | 13.75 |
| | 0.125" | 16.21 | 15.08 | 13.61 |
| | E | 15.27 | 14.45 | 13.00 |
| | O 0.25 | 14.47 | 11.28 | 10.77 |
| | O 0.5 | 11.02 | 9.52 | 9.78 |
| | O 1 | 9.71 | 7.94 | 8.11 |
| 400S162-54 | F | 31.44 | 29.44 | 26.96 |
| | 5" | 31.40 | 29.35 | 26.74 |
| | 2" | 31.30 | 29.10 | 26.73 |
| | 1" | 30.20 | 28.92 | 26.57 |

| | | | | |
|---|---|---|---|---|
| | 0.75" | 29.79 | 28.86 | 26.36 |
| | 0.5" | 29.73 | 28.76 | 26.10 |
| | 0.25" | 29.69 | 28.26 | 25.88 |
| | 0.125" | 29.15 | 27.78 | 25.58 |
| | E | 26.75 | 26.83 | 24.03 |
| | O 0.25 | 23.26 | 21.19 | 20.36 |
| | O 0.5 | 21.81 | 18.80 | 18.01 |
| | O 1 | 18.49 | 15.66 | 16.07 |
| 400S162-68 | F | 42.68 | 41.61 | 38.41 |
| | 5" | 42.55 | 41.57 | 38.25 |
| | 2" | 42.33 | 41.40 | 38.16 |
| | 1" | 41.16 | 41.39 | 38.00 |
| | 0.75" | 40.88 | 41.00 | 37.78 |
| | 0.5" | 40.56 | 40.70 | 37.67 |
| | 0.25" | 39.40 | 39.59 | 37.51 |
| | 0.125" | 39.16 | 38.95 | 36.79 |
| | E | 37.24 | 36.60 | 34.27 |
| | O 0.25 | 32.13 | 28.83 | 29.60 |
| | O 0.5 | 29.46 | 25.54 | 26.66 |
| | O 1 | 25.56 | 22.41 | 23.00 |
| 400S200-33 | F | 13.03 | 12.53 | 10.83 |
| | 5" | 13.00 | | 10.83 |
| | 2" | 12.97 | | 10.80 |
| | 1" | 12.91 | | 10.79 |
| | 0.75" | 12.85 | 12.39 | 10.75 |
| | 0.5" | 12.73 | 12.14 | 10.70 |
| | 0.25" | 12.64 | | 10.65 |
| | 0.125" | 12.54 | | 10.41 |
| | E | 11.51 | 10.90 | 9.99 |
| | O 0.25 | 10.30 | 7.84 | 7.28 |
| | O 0.5 | 10.00 | 7.37 | 6.91 |
| | O 1 | 7.42 | 5.74 | 5.73 |
| 400S200-43 | F | 18.82 | 16.31 | 16.27 |
| | 5" | 18.60 | 16.29 | 16.15 |
| | 2" | 18.00 | 16.29 | 16.07 |
| | 1" | 17.70 | 16.28 | 16.01 |
| | 0.75" | 17.62 | 16.25 | 15.96 |
| | 0.5" | 17.00 | 16.24 | 15.89 |

| | | | | |
|---|---|---|---|---|
| | 0.25" | 17.54 | 14.13 | 15.74 |
| | 0.125" | 17.06 | 16.02 | 15.57 |
| | E | 15.94 | 14.20 | 14.43 |
| | O 0.25 | 13.20 | 12.58 | 12.21 |
| | O 0.5 | | | 10.91 |
| | O 1 | | | 8.86 |
| 400S200-54 | F | 34.69 | 37.24 | 30.61 |
| | 5" | 34.51 | 36.94 | 30.18 |
| | 2" | 34.37 | 35.95 | 29.83 |
| | 1" | 34.30 | 34.26 | 29.37 |
| | 0.75" | 34.23 | 33.60 | 28.97 |
| | 0.5" | 34.18 | 33.20 | 28.52 |
| | 0.25" | 33.71 | 32.81 | 28.05 |
| | 0.125" | 32.83 | 32.66 | 27.44 |
| | E | 31.97 | 32.25 | 26.85 |
| | O 0.25 | 25.96 | 22.35 | 22.95 |
| | O 0.5 | 23.60 | 19.18 | 20.95 |
| | O 1 | 19.22 | 16.77 | 17.77 |
| 400S200-68 | F | 50.04 | 47.11 | 43.34 |
| | 5" | 49.33 | 47.06 | 43.43 |
| | 2" | 49.25 | 46.26 | 43.16 |
| | 1" | 48.54 | 46.04 | 42.77 |
| | 0.75" | 47.72 | 46.02 | 42.70 |
| | 0.5" | 47.51 | 45.53 | 42.61 |
| | 0.25" | 47.30 | 45.05 | 42.11 |
| | 0.125" | 45.76 | 43.78 | 41.53 |
| | E | 43.60 | 39.48 | 38.36 |
| | O 0.25 | 35.27 | 33.80 | 33.19 |
| | O 0.5 | 32.18 | 29.50 | 30.15 |
| | O 1 | 29.45 | 24.83 | 25.89 |
| 550S162-33 | F | 10.49 | 10.53 | 9.60 |
| | 5" | 10.49 | 10.53 | 9.58 |
| | 2" | 10.49 | 10.50 | 9.64 |
| | 1" | 10.49 | 10.43 | 9.56 |
| | 0.75" | 10.40 | 10.38 | 9.51 |
| | 0.5" | 10.35 | 10.34 | 9.51 |
| | 0.25" | 10.31 | 10.30 | 9.64 |
| | 0.125" | 10.20 | 10.28 | 9.58 |

| | | | | |
|---|---|---|---|---|
| | E | 9.88 | 9.52 | 9.21 |
| | O 0.25 | 9.32 | 6.98 | 7.07 |
| | O 0.5 | 8.20 | 6.28 | 6.13 |
| | O 1 | 6.74 | 5.27 | 5.38 |
| 550S162-43 | F | 16.46 | 15.81 | 14.30 |
| | 5" | 16.44 | 15.68 | 14.22 |
| | 2" | 16.28 | 15.56 | 14.21 |
| | 1" | 16.12 | 15.41 | 14.18 |
| | 0.75" | 15.97 | 15.30 | 14.14 |
| | 0.5" | 15.82 | 15.17 | 14.11 |
| | 0.25" | 15.73 | 15.06 | 14.07 |
| | 0.125" | 15.54 | 14.60 | 14.02 |
| | E | 14.93 | 13.67 | 13.35 |
| | O 0.25 | 12.13 | 10.93 | 10.75 |
| | O 0.5 | 10.84 | 9.27 | 9.86 |
| | O 1 | 8.31 | 8.04 | 8.23 |
| 550S162-54 | F | 32.17 | 29.40 | 26.60 |
| | 5" | 32.15 | 29.08 | 26.48 |
| | 2" | 32.13 | 29.15 | 26.41 |
| | 1" | 31.50 | 28.81 | 26.39 |
| | 0.75" | 30.43 | 27.79 | 26.32 |
| | 0.5" | 29.81 | 27.50 | 26.21 |
| | 0.25" | 29.60 | 27.13 | 26.13 |
| | 0.125" | 29.28 | 26.33 | 25.76 |
| | E | 27.82 | 24.91 | 24.55 |
| | O 0.25 | 23.40 | 22.00 | 20.81 |
| | O 0.5 | 21.00 | 19.77 | 19.06 |
| | O 1 | 19.27 | 17.18 | 16.54 |
| 550S162-68 | F | 42.70 | 41.80 | 37.68 |
| | 5" | 42.63 | 41.60 | 37.66 |
| | 2" | 42.45 | 41.23 | 37.62 |
| | 1" | 42.35 | 40.91 | 37.54 |
| | 0.75" | 41.96 | 40.50 | 37.41 |
| | 0.5" | 41.50 | 40.18 | 37.31 |
| | 0.25" | 40.89 | 39.50 | 37.19 |
| | 0.125" | 39.83 | 38.70 | 36.93 |
| | E | 37.78 | 36.17 | 34.93 |
| | O 0.25 | 32.63 | 30.50 | 30.35 |

| | | | | |
|---|---|---|---|---|
| | O 0.5 | 29.46 | 26.77 | 27.43 |
| | O 1 | 26.88 | 23.26 | 23.99 |
| 600S137-33 | F | 10.45 | 9.66 | 8.93 |
| | 5" | 10.31 | 9.62 | 8.91 |
| | 2" | 10.17 | 9.75 | 8.91 |
| | 1" | 10.08 | 9.58 | 8.87 |
| | 0.75" | 9.93 | 9.56 | 8.84 |
| | 0.5" | 9.54 | 9.49 | 8.81 |
| | 0.25" | 9.25 | 9.24 | 8.76 |
| | 0.125" | 9.17 | 9.18 | 8.70 |
| | E | 9.04 | 8.93 | 8.51 |
| | O 0.25 | 7.34 | 6.61 | 6.33 |
| | O 0.5 | 6.45 | 5.61 | 5.81 |
| | O 1 | 5.98 | 5.09 | 4.47 |
| 600S137-43 | F | 15.30 | 14.19 | 13.09 |
| | 5" | 15.27 | 14.09 | 13.13 |
| | 2" | 15.19 | 14.00 | 13.10 |
| | 1" | 14.83 | 13.96 | 13.03 |
| | 0.75" | 14.54 | 13.88 | 12.70 |
| | 0.5" | 14.44 | 13.66 | 13.11 |
| | 0.25" | 14.23 | 13.41 | 13.08 |
| | 0.125" | 14.00 | 13.06 | 13.04 |
| | E | 13.63 | 12.45 | 12.15 |
| | O 0.25 | 12.73 | 10.33 | 9.84 |
| | O 0.5 | 9.88 | 8.57 | 8.93 |
| | O 1 | 8.28 | 7.71 | 7.62 |
| 600S137-54 | F | 28.40 | 27.54 | 24.46 |
| | 5" | 28.37 | 27.29 | 24.45 |
| | 2" | 28.26 | 26.59 | 24.42 |
| | 1" | 27.40 | 25.44 | 24.35 |
| | 0.75" | 26.67 | 24.92 | 23.29 |
| | 0.5" | 26.50 | 24.63 | 24.25 |
| | 0.25" | 26.32 | 24.23 | 24.16 |
| | 0.125" | 26.13 | 23.81 | 24.06 |
| | E | 25.43 | 22.88 | 22.44 |
| | O 0.25 | 20.75 | 19.17 | 18.57 |
| | O 0.5 | 20.02 | 16.96 | 17.13 |
| | O 1 | 17.21 | 15.11 | 14.94 |

| | | | | |
|---|---|---|---|---|
| 600S137-68 | F | 38.34 | 36.80 | 33.60 |
| | 5" | 38.28 | 36.73 | 33.56 |
| | 2" | 38.27 | 36.71 | 33.55 |
| | 1" | 37.70 | 36.04 | 33.41 |
| | 0.75" | 36.10 | 35.24 | 33.31 |
| | 0.5" | 35.80 | 35.03 | 33.00 |
| | 0.25" | 35.40 | 34.71 | 32.85 |
| | 0.125" | 35.02 | 34.23 | 32.63 |
| | E | 34.12 | 33.14 | 31.72 |
| | O 0.25 | 29.32 | 28.06 | 27.51 |
| | O 0.5 | 26.78 | 25.02 | 25.13 |
| | O 1 | 24.11 | 22.24 | 21.88 |
| 600S137-97 | F | 63.51 | 61.55 | 58.63 |
| | 5" | 63.22 | 61.42 | 58.54 |
| | 2" | 61.90 | 61.48 | 58.41 |
| | 1" | 61.59 | 60.13 | 58.27 |
| | 0.75" | 61.30 | 59.96 | 58.04 |
| | 0.5" | 61.08 | 59.69 | 57.88 |
| | 0.25" | 60.57 | 59.36 | 57.55 |
| | 0.125" | 59.97 | 58.89 | 57.33 |
| | E | 58.80 | 57.98 | 56.31 |
| | O 0.25 | 52.78 | 51.51 | 49.72 |
| | O 0.5 | 48.82 | 47.14 | 44.37 |
| | O 1 | 43.41 | 41.81 | 38.32 |
| 600S162-33 | F | 12.57 | 10.81 | 9.69 |
| | 5" | 12.55 | 10.53 | 9.71 |
| | 2" | 11.97 | 10.46 | 9.68 |
| | 1" | 11.61 | 10.40 | 9.62 |
| | 0.75" | 12.50 | 10.37 | 9.62 |
| | 0.5" | 11.51 | 10.22 | 9.57 |
| | 0.25" | 11.80 | 10.02 | 9.51 |
| | 0.125" | 12.06 | 9.78 | 9.40 |
| | E | 10.13 | 9.43 | 9.20 |
| | O 0.25 | 8.29 | 7.36 | 7.13 |
| | O 0.5 | 7.99 | 5.96 | 6.40 |
| | O 1 | 7.08 | 5.25 | 5.46 |
| 600S162-43 | F | 17.50 | 15.73 | 14.49 |
| | 5" | 17.47 | 15.60 | 14.42 |

| | | | | |
|---|---|---|---|---|
| | 2" | 17.42 | 15.43 | 14.25 |
| | 1" | 17.35 | 15.36 | 14.20 |
| | 0.75" | 17.28 | 15.28 | 14.13 |
| | 0.5" | 17.05 | 15.13 | 14.15 |
| | 0.25" | 16.91 | 14.92 | |
| | 0.125" | 16.03 | 14.64 | |
| | E | 14.24 | 13.69 | |
| | O 0.25 | 12.51 | 11.11 | |
| | O 0.5 | 11.85 | 9.39 | |
| | O 1 | 10.48 | 8.20 | |
| 600S162-54 | F | 32.14 | 30.10 | 26.95 |
| | 5" | 32.00 | 30.09 | 26.92 |
| | 2" | 31.86 | 29.70 | 26.91 |
| | 1" | 31.79 | 28.81 | 26.84 |
| | 0.75" | 30.70 | 27.93 | 26.78 |
| | 0.5" | 29.80 | 27.63 | 26.76 |
| | 0.25" | 29.50 | 27.23 | 26.75 |
| | 0.125" | 28.75 | 26.73 | 26.65 |
| | E | 27.66 | 25.70 | 24.62 |
| | O 0.25 | 23.17 | 20.72 | 20.79 |
| | O 0.5 | 21.32 | 18.85 | 19.22 |
| | O 1 | 18.94 | 16.31 | 16.61 |
| 600S162-68 | F | 43.05 | 41.82 | 26.95 |
| | 5" | 42.90 | 41.50 | 26.92 |
| | 2" | 42.00 | 40.90 | 26.91 |
| | 1" | 41.79 | 40.30 | 26.84 |
| | 0.75" | 39.34 | 39.40 | 26.78 |
| | 0.5" | 39.19 | 38.80 | 26.76 |
| | 0.25" | 38.99 | 38.30 | 26.75 |
| | 0.125" | 38.74 | 37.70 | 26.65 |
| | E | 38.13 | 36.90 | 24.62 |
| | O 0.25 | 32.59 | 30.48 | 20.79 |
| | O 0.5 | 29.90 | 27.60 | 19.22 |
| | O 1 | 27.19 | 24.00 | 16.61 |
| 600S162-97 | F | 69.79 | 67.85 | 37.51 |
| | 5" | 69.81 | 67.82 | 37.53 |
| | 2" | 69.19 | 67.82 | 37.56 |
| | 1" | 67.54 | 66.04 | 36.84 |

| | | | | |
|---|---|---|---|---|
| | 0.75" | 66.63 | 65.80 | 36.16 |
| | 0.5" | 66.43 | 65.64 | 37.19 |
| | 0.25" | 66.03 | 65.34 | 37.26 |
| | 0.125" | 65.50 | 64.74 | 37.27 |
| | E | 64.86 | 63.96 | 35.10 |
| | O 0.25 | 57.12 | 54.98 | 30.60 |
| | O 0.5 | 52.71 | 49.41 | 27.72 |
| | O 1 | 47.30 | 43.70 | 24.28 |
| 600S200-33 | F | 13.71 | 12.29 | 11.36 |
| | 5" | 13.68 | 12.20 | 11.22 |
| | 2" | 13.58 | 12.05 | 11.15 |
| | 1" | 13.35 | 11.58 | 10.78 |
| | 0.75" | 13.29 | 11.56 | 10.77 |
| | 0.5" | 13.27 | 11.41 | 10.72 |
| | 0.25" | 12.97 | 11.66 | 10.65 |
| | 0.125" | 12.52 | 11.31 | 10.52 |
| | E | 11.55 | 10.37 | 10.22 |
| | O 0.25 | 9.00 | 7.50 | 7.63 |
| | O 0.5 | 8.50 | 6.96 | 7.17 |
| | O 1 | 7.03 | 5.67 | 5.88 |
| 600S200-43 | F | 19.56 | 18.13 | 16.52 |
| | 5" | 19.47 | 17.93 | 16.31 |
| | 2" | 19.17 | 17.63 | 16.29 |
| | 1" | 18.80 | 17.47 | 16.22 |
| | 0.75" | 18.42 | 17.27 | 16.18 |
| | 0.5" | 18.22 | 16.97 | 16.90 |
| | 0.25" | 17.97 | 16.72 | 15.99 |
| | 0.125" | 17.60 | 16.22 | 15.80 |
| | E | 16.74 | 14.90 | 14.62 |
| | O 0.25 | 13.88 | 12.01 | 12.32 |
| | O 0.5 | 13.20 | 11.03 | 10.98 |
| | O 1 | 11.18 | 8.97 | 9.09 |
| 600S200-54 | F | 39.96 | 33.63 | 30.22 |
| | 5" | 39.80 | 33.60 | 30.21 |
| | 2" | 38.43 | 32.91 | 30.21 |
| | 1" | 38.19 | 32.20 | 29.16 |
| | 0.75" | 35.58 | 31.55 | 28.71 |
| | 0.5" | 33.75 | 31.14 | 28.54 |

| | | | | |
|---|---|---|---|---|
| | 0.25" | 33.14 | 30.73 | 28.29 |
| | 0.125" | 31.86 | 30.16 | 27.98 |
| | E | 30.81 | 29.07 | 26.69 |
| | O 0.25 | 26.03 | 22.95 | 23.81 |
| | O 0.5 | 23.95 | 20.60 | 20.71 |
| | O 1 | 21.42 | 17.72 | 15.62 |
| 600S200-68 | F | 49.51 | 46.94 | 41.24 |
| | 5" | 49.07 | 46.62 | 41.00 |
| | 2" | 48.40 | 47.67 | 40.70 |
| | 1" | 47.37 | 46.02 | 40.12 |
| | 0.75" | 46.80 | 45.75 | 39.79 |
| | 0.5" | 46.36 | 45.25 | 39.63 |
| | 0.25" | 45.65 | 44.55 | 39.42 |
| | 0.125" | 44.30 | 43.55 | 39.15 |
| | E | 43.47 | 41.23 | 38.84 |
| | O 0.25 | 35.70 | 33.93 | 34.07 |
| | O 0.5 | 33.74 | 30.44 | 31.18 |
| | O 1 | 27.60 | 26.17 | 26.79 |
| 600S200-97 | F | 79.28 | 76.32 | 72.29 |
| | 5" | 78.50 | 76.10 | 71.95 |
| | 2" | 77.10 | 75.05 | 71.90 |
| | 1" | 76.13 | 74.33 | 71.74 |
| | 0.75" | 76.80 | 74.00 | 71.57 |
| | 0.5" | 75.55 | 73.89 | 71.36 |
| | 0.25" | 74.84 | 73.41 | 71.07 |
| | 0.125" | 73.70 | 72.78 | 70.81 |
| | E | 72.46 | 71.67 | 69.54 |
| | O 0.25 | 63.36 | 60.25 | 59.29 |
| | O 0.5 | 57.82 | 53.86 | 56.08 |
| | O 1 | 52.08 | 46.72 | 46.94 |
| 600S250-43 | F | 22.18 | 20.19 | 17.95 |
| | 5" | 22.07 | 20.08 | 17.95 |
| | 2" | 22.08 | 19.73 | 17.93 |
| | 1" | 21.22 | 19.55 | 17.85 |
| | 0.75" | 20.55 | 19.21 | 17.75 |
| | 0.5" | 19.85 | 18.72 | 17.63 |
| | 0.25" | 19.00 | 17.99 | 17.49 |
| | 0.125" | 18.15 | 16.92 | 17.21 |

| | | | | |
|---|---|---|---|---|
| | E | 17.69 | 15.63 | 15.85 |
| | O 0.25 | 15.11 | 12.27 | 12.99 |
| | O 0.5 | 14.39 | 11.13 | 11.38 |
| | O 1 | 12.75 | 9.23 | 9.49 |
| 600S250-54 | F | 41.91 | 41.58 | 34.28 |
| | 5" | 41.40 | 41.63 | 34.23 |
| | 2" | 39.60 | 37.81 | 34.12 |
| | 1" | 38.31 | 35.79 | 33.64 |
| | 0.75" | 38.00 | 35.35 | 33.42 |
| | 0.5" | 37.26 | 34.01 | 33.35 |
| | 0.25" | 36.12 | 32.59 | 33.07 |
| | 0.125" | 34.90 | 31.00 | 32.78 |
| | E | 33.91 | 29.81 | 29.48 |
| | O 0.25 | 32.41 | 23.46 | 24.71 |
| | O 0.5 | 26.80 | 21.15 | 22.11 |
| | O 1 | 24.84 | 18.39 | 18.96 |
| 600S250-68 | F | 55.05 | 52.11 | 46.06 |
| | 5" | 54.91 | 51.87 | 46.34 |
| | 2" | 54.86 | 50.11 | 46.68 |
| | 1" | 53.94 | 49.28 | 44.88 |
| | 0.75" | 52.70 | 48.27 | 44.01 |
| | 0.5" | 51.31 | 47.36 | 45.84 |
| | 0.25" | 49.89 | 46.06 | |
| | 0.125" | 48.18 | 44.00 | |
| | E | 46.13 | 43.69 | |
| | O 0.25 | 40.86 | 35.42 | |
| | O 0.5 | 37.72 | 31.68 | |
| | O 1 | 34.17 | 27.45 | |
| 600S250-97 | F | 89.00 | 84.60 | |
| | 5" | 88.96 | 83.50 | |
| | 2" | 86.78 | 82.96 | |
| | 1" | 85.40 | 81.80 | |
| | 0.75" | 84.96 | 81.60 | |
| | 0.5" | 83.90 | 81.55 | |
| | 0.25" | 83.10 | 80.69 | |
| | 0.125" | 81.60 | 79.39 | |
| | E | 79.04 | 78.25 | |
| | O 0.25 | 68.52 | 64.04 | |

| | | | | |
|---|---|---|---|---|
| | O 0.5 | 62.26 | 57.66 | |
| | O 1 | 56.62 | 49.41 | |
| 800S137-33 | F | 13.57 | 13.20 | 8.93 |
| | 5" | 13.54 | 13.10 | 8.94 |
| | 2" | 13.20 | 13.00 | 8.95 |
| | 1" | 13.00 | 12.96 | 8.92 |
| | 0.75" | 12.80 | 12.88 | 8.92 |
| | 0.5" | 12.60 | 12.75 | 8.93 |
| | 0.25" | 12.41 | 12.58 | 8.94 |
| | 0.125" | 12.34 | 12.27 | 8.91 |
| | E | 11.64 | 11.39 | 8.54 |
| | O 0.25 | 9.69 | 9.15 | 6.49 |
| | O 0.5 | 9.12 | 7.40 | 5.87 |
| | O 1 | 8.16 | 7.06 | 4.98 |
| 800S137-43 | F | 14.59 | 14.28 | 13.22 |
| | 5" | 14.46 | 14.16 | 13.21 |
| | 2" | 14.31 | 14.03 | 13.17 |
| | 1" | 14.21 | 13.80 | 13.15 |
| | 0.75" | 14.13 | 13.71 | 13.11 |
| | 0.5" | 14.02 | 13.64 | 13.08 |
| | 0.25" | 13.88 | 13.47 | 13.02 |
| | 0.125" | 13.61 | 13.21 | 12.91 |
| | E | 13.06 | 12.60 | 12.17 |
| | O 0.25 | 10.57 | 10.23 | 10.00 |
| | O 0.5 | 10.17 | 9.50 | 9.06 |
| | O 1 | 8.98 | 7.94 | 7.77 |
| 800S137-54 | F | 27.98 | 26.91 | 24.48 |
| | 5" | 27.94 | 26.90 | 24.44 |
| | 2" | 27.54 | 26.79 | 24.42 |
| | 1" | 27.32 | 26.74 | 24.37 |
| | 0.75" | 26.95 | 26.36 | 24.33 |
| | 0.5" | 26.72 | 25.95 | 24.29 |
| | 0.25" | 26.14 | 25.24 | 24.28 |
| | 0.125" | 25.13 | 24.31 | 24.04 |
| | E | 24.05 | 23.08 | 22.51 |
| | O 0.25 | 20.60 | 19.37 | 19.07 |
| | O 0.5 | 18.97 | 17.88 | 17.59 |
| | O 1 | 17.32 | 15.82 | 14.89 |

| | | | | |
|---|---|---|---|---|
| 800S137-68 | F | 39.32 | 37.98 | 34.18 |
| | 5" | 39.28 | 37.93 | 34.10 |
| | 2" | 39.11 | 37.87 | 33.98 |
| | 1" | 38.71 | 37.82 | 33.87 |
| | 0.75" | 38.44 | 37.11 | 33.65 |
| | 0.5" | 38.41 | 36.87 | 33.51 |
| | 0.25" | 37.73 | 36.23 | 33.42 |
| | 0.125" | 36.60 | 35.25 | 33.02 |
| | E | 34.82 | 33.53 | 31.65 |
| | O 0.25 | 30.43 | 29.00 | 28.28 |
| | O 0.5 | 27.92 | 26.64 | |
| | O 1 | 25.30 | 23.73 | |
| 800S137-97 | F | 64.47 | 61.58 | 57.16 |
| | 5" | 64.39 | 61.49 | 57.11 |
| | 2" | 64.32 | 61.21 | 57.03 |
| | 1" | 64.18 | 61.07 | 56.93 |
| | 0.75" | 63.83 | 60.69 | 56.80 |
| | 0.5" | 63.16 | 60.38 | 56.66 |
| | 0.25" | 62.41 | 59.90 | 56.48 |
| | 0.125" | 61.33 | 59.37 | 56.27 |
| | E | 59.97 | 58.64 | 55.24 |
| | O 0.25 | 53.75 | 51.97 | 50.35 |
| | O 0.5 | 49.62 | 47.44 | 46.03 |
| | O 1 | 44.90 | 42.69 | 40.45 |
| 800S162-33 | F | 11.06 | 10.59 | 9.67 |
| | 5" | 11.03 | 10.56 | 9.65 |
| | 2" | 10.94 | 10.58 | 9.61 |
| | 1" | 10.92 | 10.50 | 9.56 |
| | 0.75" | 10.88 | 10.41 | 9.51 |
| | 0.5" | 10.63 | 10.35 | 9.48 |
| | 0.25" | 10.65 | 10.23 | 9.42 |
| | 0.125" | 10.55 | 10.02 | 9.37 |
| | E | 10.32 | 9.37 | 9.26 |
| | O 0.25 | 9.17 | 7.01 | 7.19 |
| | O 0.5 | 8.33 | 6.52 | 6.32 |
| | O 1 | 6.79 | 5.51 | 5.45 |
| 800S162-43 | F | 16.79 | 15.91 | 14.56 |
| | 5" | 16.78 | 15.70 | 14.54 |

| | | | | |
|---|---|---|---|---|
| | 2" | 16.72 | 14.96 | 14.52 |
| | 1" | 16.71 | 14.94 | 14.49 |
| | 0.75" | 16.57 | 14.60 | 14.41 |
| | 0.5" | 16.47 | 14.56 | 14.36 |
| | 0.25" | 16.11 | 14.43 | 14.29 |
| | 0.125" | 15.72 | 14.29 | 14.17 |
| | E | 14.43 | 13.95 | 13.45 |
| | O 0.25 | 12.21 | 11.01 | 11.40 |
| | O 0.5 | 11.26 | 10.20 | 10.01 |
| | O 1 | 9.93 | 8.67 | 8.53 |
| 800S162-54 | F | 31.66 | 30.45 | 27.21 |
| | 5" | 31.60 | 30.36 | 27.18 |
| | 2" | 31.50 | 30.24 | 27.14 |
| | 1" | 31.06 | 30.25 | 27.13 |
| | 0.75" | 30.68 | 29.28 | 27.1 |
| | 0.5" | 29.91 | 28.68 | 26.85 |
| | 0.25" | 29.11 | 28.07 | 26.57 |
| | 0.125" | 28.05 | 27.43 | 26.23 |
| | E | 26.85 | 25.89 | 24.77 |
| | O 0.25 | 23.33 | 21.36 | 21.34 |
| | O 0.5 | 21.34 | 19.39 | 19.41 |
| | O 1 | 19.00 | 16.65 | 16.66 |
| 800S162-68 | F | 44.18 | 41.31 | 38.28 |
| | 5" | 44.09 | 41.27 | 38.23 |
| | 2" | 43.91 | 41.15 | 38.19 |
| | 1" | 43.76 | 41.09 | 38.14 |
| | 0.75" | 42.82 | 40.31 | 38.1 |
| | 0.5" | 42.69 | 40.25 | 38.05 |
| | 0.25" | 42.02 | 39.51 | 33.91 |
| | 0.125" | 41.19 | 38.58 | 37.79 |
| | E | 37.99 | 36.14 | 35.01 |
| | O 0.25 | 33.26 | 31.00 | 31.1 |
| | O 0.5 | 30.50 | 28.12 | 28.02 |
| | O 1 | 27.72 | 24.88 | 24.59 |
| 800S162-97 | F | 41.31 | 68.13 | 62.55 |
| | 5" | 41.27 | 68.05 | 62.53 |
| | 2" | 41.15 | 67.93 | 62.43 |
| | 1" | 41.09 | 66.99 | 62.35 |

| | | | | |
|---|---|---|---|---|
| | 0.75" | 40.31 | 66.73 | 62.27 |
| | 0.5" | 40.25 | 66.53 | 62.15 |
| | 0.25" | 39.51 | 65.81 | 62.03 |
| | 0.125" | 38.58 | 65.90 | 61.81 |
| | E | 36.14 | 63.41 | 60.66 |
| | O 0.25 | 31.00 | 56.31 | 54.69 |
| | O 0.5 | 28.12 | 50.68 | 49.89 |
| | O 1 | 24.88 | 45.12 | 44.02 |
| 800S200-33 | F | 13.79 | 11.91 | 10.89 |
| | 5" | 13.75 | 11.79 | 10.83 |
| | 2" | 13.68 | 11.77 | 10.77 |
| | 1" | 12.75 | 11.76 | 10.75 |
| | 0.75" | 12.61 | 11.55 | 10.71 |
| | 0.5" | 12.57 | 11.43 | 10.66 |
| | 0.25" | 12.31 | 11.21 | 10.59 |
| | 0.125" | 12.19 | 11.03 | 10.50 |
| | E | 11.35 | 10.36 | 10.14 |
| | O 0.25 | 9.59 | 7.66 | 7.55 |
| | O 0.5 | 9.03 | 7.11 | 6.77 |
| | O 1 | 7.09 | 5.77 | 5.83 |
| 800S200-43 | F | 19.59 | 18.00 | 16.21 |
| | 5" | 19.58 | 17.95 | 16.2 |
| | 2" | 19.55 | 17.94 | 16.17 |
| | 1" | 19.50 | 17.92 | 16.11 |
| | 0.75" | 18.94 | 17.83 | 16.04 |
| | 0.5" | 18.70 | 17.74 | 15.99 |
| | 0.25" | 18.33 | 17.73 | 15.90 |
| | 0.125" | 17.72 | 16.62 | 15.80 |
| | E | 16.69 | 15.13 | 14.63 |
| | O 0.25 | 14.27 | 12.05 | 12.62 |
| | O 0.5 | 10.20 | 11.13 | 11.09 |
| | O 1 | 9.95 | 9.16 | 9.22 |
| 800S200-54 | F | 36.82 | 33.98 | 30.25 |
| | 5" | 36.70 | 33.94 | 30.21 |
| | 2" | 36.56 | 33.84 | 30.17 |
| | 1" | 36.31 | 32.95 | 30.11 |
| | 0.75" | 35.23 | 32.01 | 30.04 |
| | 0.5" | 34.67 | 31.93 | 29.99 |

| | | | | |
|---|---|---|---|---|
| | 0.25" | 33.71 | 31.22 | 29.73 |
| | 0.125" | 32.12 | 30.51 | 29.54 |
| | E | 30.91 | 28.47 | 27.42 |
| | O 0.25 | 26.09 | 23.30 | 23.25 |
| | O 0.5 | 24.16 | 21.12 | 21.39 |
| | O 1 | 21.70 | 18.13 | 18.1 |
| 800S200-68 | F | 48.93 | 47.64 | 42.26 |
| | 5" | 48.85 | 47.54 | 42.2 |
| | 2" | 49.81 | 47.34 | 42.18 |
| | 1" | 49.80 | 46.77 | 42.17 |
| | 0.75" | 48.81 | 46.46 | 42.07 |
| | 0.5" | 48.43 | 46.36 | 41.96 |
| | 0.25" | 47.66 | 46.07 | 41.83 |
| | 0.125" | 46.20 | 45.91 | 41.68 |
| | E | 43.20 | 41.75 | 38.76 |
| | O 0.25 | 37.34 | 34.50 | 34.88 |
| | O 0.5 | 34.11 | 31.05 | 31.23 |
| | O 1 | 31.32 | 26.68 | 27.023 |
| 800S200-97 | F | 80.50 | 76.94 | 71.32 |
| | 5" | 80.48 | 76.92 | 71.28 |
| | 2" | 80.43 | 76.40 | 70.84 |
| | 1" | 80.36 | 76.38 | 70.48 |
| | 0.75" | 77.31 | 74.40 | 70.08 |
| | 0.5" | 77.12 | 74.22 | 69.65 |
| | 0.25" | 76.33 | 73.66 | 69.18 |
| | 0.125" | 75.11 | 72.83 | 68.67 |
| | E | 72.35 | 70.53 | 67.34 |
| | O 0.25 | 65.11 | 61.89 | 60.65 |
| | O 0.5 | 59.00 | 55.57 | 55.02 |
| | O 1 | 53.26 | 48.75 | 48.45 |
| 800S250-43 | F | 21.87 | 20.35 | 18.2 |
| | 5" | 21.84 | 20.30 | 18.18 |
| | 2" | 21.24 | 20.29 | 18.13 |
| | 1" | 20.91 | 20.20 | 18.015 |
| | 0.75" | 20.41 | 20.11 | 17.86 |
| | 0.5" | 20.04 | 19.66 | 17.65 |
| | 0.25" | 19.66 | 19.18 | 17.44 |
| | 0.125" | 19.11 | 18.44 | 17.14 |

| | | | | |
|---|---|---|---|---|
| | E | 17.73 | 16.19 | 15.66 |
| | O 0.25 | 15.34 | 12.38 | 14.98 |
| | O 0.5 | 14.46 | 11.33 | 13.28 |
| | O 1 | 12.86 | 9.47 | 9.49 |
| 800S250-54 | F | 42.37 | 38.48 | 34.70 |
| | 5" | 42.33 | 38.35 | 34.59 |
| | 2" | 41.74 | 38.01 | 34.26 |
| | 1" | 41.23 | 37.78 | 34.07 |
| | 0.75" | 40.47 | 37.68 | 33.97 |
| | 0.5" | 39.25 | 37.55 | 33.84 |
| | 0.25" | 38.17 | 36.56 | 33.63 |
| | 0.125" | 37.43 | 35.21 | 32.94 |
| | E | 33.06 | 30.16 | 29.83 |
| | O 0.25 | 29.02 | 23.94 | 24.41 |
| | O 0.5 | 27.15 | 21.73 | 22.20 |
| | O 1 | 25.15 | 18.84 | 18.61 |
| 800S250-68 | F | 55.42 | 53.38 | 47.01 |
| | 5" | 55.21 | 53.04 | 46.83 |
| | 2" | 54.97 | 52.83 | 46.68 |
| | 1" | 54.76 | 52.36 | 46.55 |
| | 0.75" | 53.79 | 51.49 | 46.41 |
| | 0.5" | 52.54 | 51.20 | 46.23 |
| | 0.25" | 51.66 | 50.03 | 45.98 |
| | 0.125" | 50.32 | 48.78 | 45.67 |
| | E | 48.10 | 43.96 | 41.40 |
| | O 0.25 | 40.26 | 35.93 | 36.61 |
| | O 0.5 | 38.54 | 32.44 | 32.10 |
| | O 1 | 35.38 | 28.04 | 28.2 |
| 800S250-97 | F | 89.92 | 86.41 | 78.26 |
| | 5" | 89.72 | 86.31 | 78.19 |
| | 2" | 89.62 | 86.18 | 78.055 |
| | 1" | 89.10 | 85.95 | 77.77 |
| | 0.75" | 87.88 | 84.74 | 77.46 |
| | 0.5" | 85.69 | 83.27 | 77.09 |
| | 0.25" | 83.91 | 81.87 | 76.65 |
| | 0.125" | 82.03 | 79.41 | 76.09 |
| | E | 78.89 | 74.65 | 72.70 |
| | O 0.25 | 70.06 | 66.01 | 64.72 |

| | | | | |
|---|---|---|---|---|
| | O 0.5 | 63.60 | 58.98 | 58.61 |
| | O 1 | 57.83 | 51.85 | 51.74 |

## Brack lab test frame at UMass Amherst

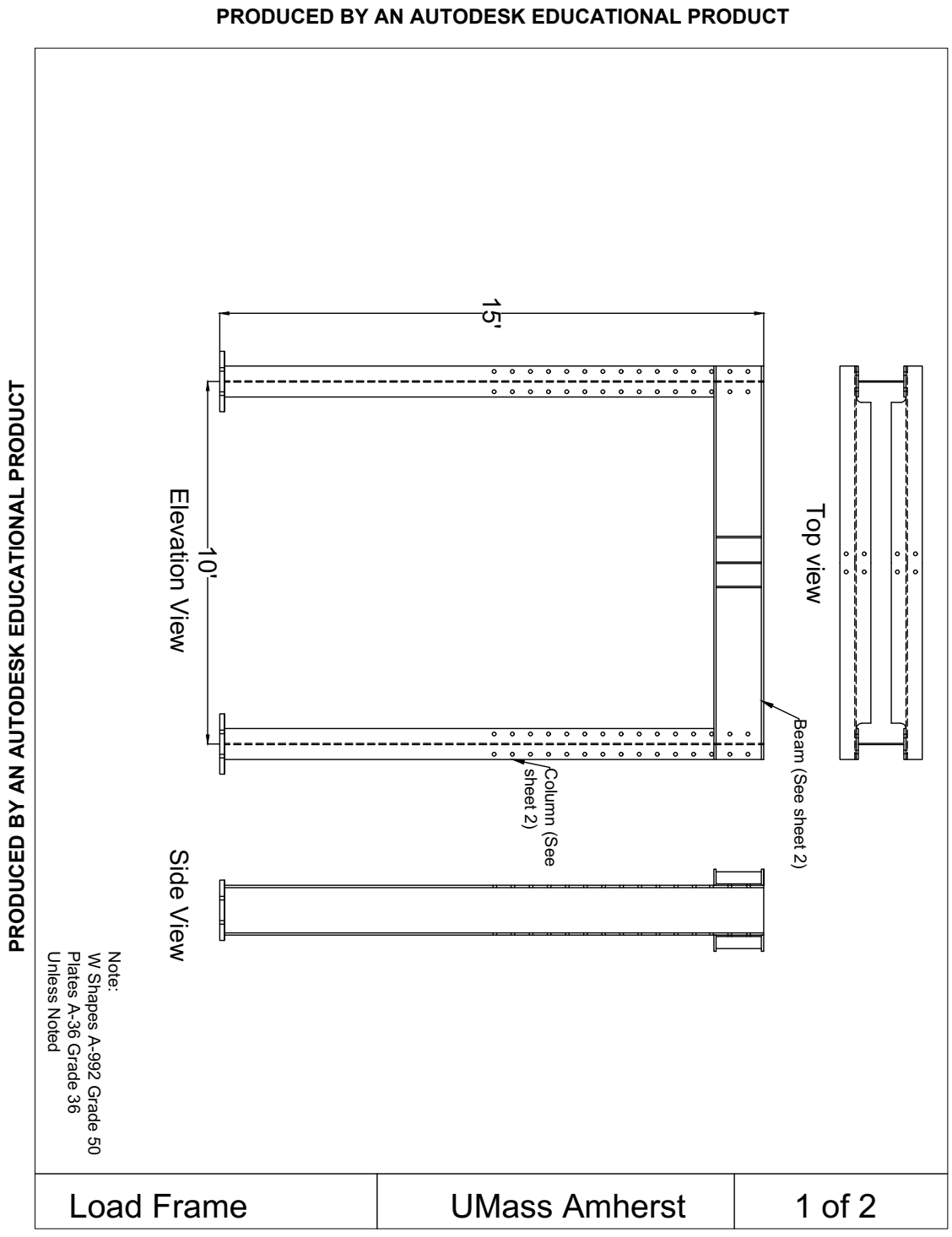

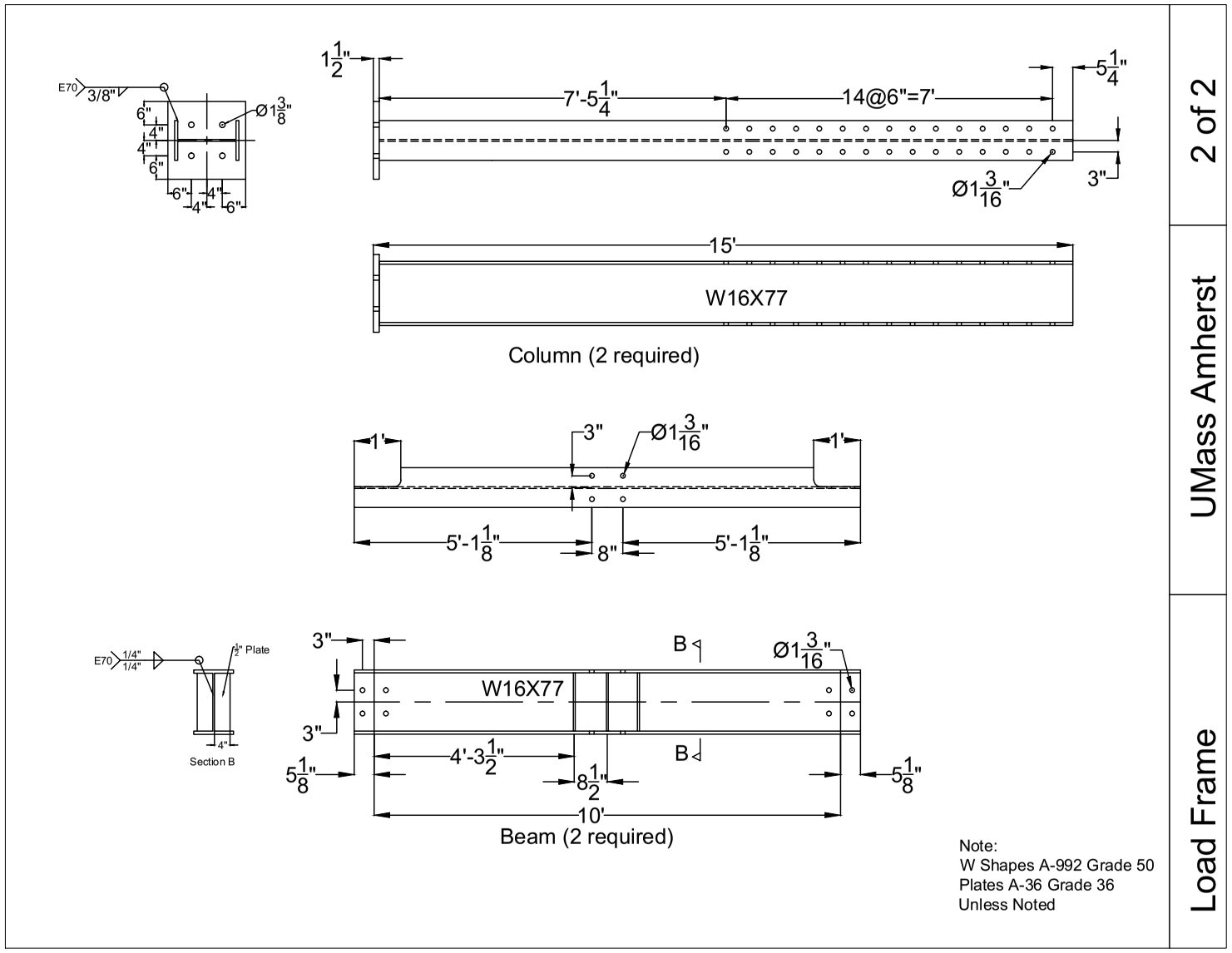


PRODUCED BY AN AUTODESK EDUCATIONAL PRODUCT

PRODUCED BY AN AUTODESK EDUCATIONAL PRODUCT

PRODUCED BY AN AUTODESK EDUCATIONAL PRODUCT

## Python script

```
nn=1+1 #Number of models
sleep_time=0
for ii in range(1,nn):
    from abaqus import *
    from abaqusConstants import *
    import regionToolset
    mdb.Model(name='Model-1', modelType=STANDARD_EXPLICIT)
    session.viewports['Viewport: 1'].setValues(displayedObject=None)
    mdb.models.changeKey(fromName='Model-1', toName=str(ii))
    beamModel = mdb.models[str(ii)]

    BC=[8.00,5.00,2.00,1.00,0.75,0.50,0.25,0.125,0.00,-0.25,-0.50,-1.00]

    #STUD
    studH=8.00
    studW=2.50
    studLip=0.625
    studt=0.0451
    studL=96.00
```

```
cc=0.386  #the distance between the web and the centroid of the stud

#

##Track

trackt=studt

trackH=studH+trackt

trackW=1.25

trackL=24.00

#

Fy=50.00

##Slab

slabL=34.00

slabW=22.00

slabH=6.00

#

## Edge distance

el=BC[ii-1]

#

##Span length

sl=12.00

#

##Screws info.
```

dd=3.00 #distance of the pins to the edge of the track for fastening that to the concrete slab

#

##Mesh size

Mslab=1.00

Mstud=0.200

Mtrack=0.400  #0.2500

Mrebar=0.50

#

##Step info

StabMag=0.0002

adapDamp=0.05

initial_inc=0.00001

min_inc=1e-15

max_inc=0.01

max_num_inc=120

tol_contact=0.00 #it defines how much the contact area in flange of stud is larger than the flange length of track

##

if el >= 0:

 oo=trackH/2

```
 slab_screw=slabW-(trackH/2+el+trackt/2)
else:
 oo=2+(-1*el)-trackt/2
 slab_screw=slabW-2

########################
#if BC==0.75 or 0.5 or 0.25 or 0.125:
 #oo=trackH/2 +0.25
 #slab_screw=slabW-(trackH/2+el+trackt/2)-0.25
########################
from abaqus import *
from abaqusConstants import *
import section
import regionToolset
import displayGroupMdbToolset as dgm
import part
import material
import assembly
import step
import interaction
import load
```

```
import mesh

import optimization

import job

import sketch

import visualization

import xyPlot

import displayGroupOdbToolset as dgo

import connectorBehavior

s = mdb.models[str(ii)].ConstrainedSketch(name='__profile__',

sheetSize=200.0)

g, v, d, c = s.geometry, s.vertices, s.dimensions, s.constraints

s.setPrimaryObject(option=STANDALONE)

#Stud corner cordinates

#1

s.Line(point1=(0.0, 0.0), point2=(0.0, studH-studt))

#2

s.Line(point1=(0.0, studH-studt), point2=(studW-studt, studH-studt))

#3

s.Line(point1=(studW-studt, studH-studt), point2=(studW-studt,  studH-studt-
studLip+studt/2))

#4
```

```
        s.Line(point1=(0.0, 0.0), point2=(studW-studt, 0.0))
        #5
        s.Line(point1=(studW-studt, 0.0), point2=(studW-studt, studLip-studt/2))
        s.unsetPrimaryObject()
        del mdb.models[str(ii)].sketches['__profile__']
        s1 = mdb.models[str(ii)].ConstrainedSketch(name='__profile__',
        sheetSize=200.0)
        g, v, d, c = s1.geometry, s1.vertices, s1.dimensions, s1.constraints
        s1.setPrimaryObject(option=STANDALONE)
        #1
        s1.Line(point1=(0.0, 0.0), point2=(0.0, studH-studt))
        #2
        s1.Line(point1=(0.0, studH-studt), point2=(studW-studt, studH-studt))
        #3
        s1.Line(point1=(studW-studt, studH-studt), point2=(studW-studt, studH-studt-
studLip+studt/2))
        #4
        s1.Line(point1=(0.0, 0.0), point2=(studW-studt, 0.0))
        #5
        s1.Line(point1=(studW-studt, 0.0), point2=(studW-studt, studLip+studt/2))
        p = mdb.models[str(ii)].Part(name='Stud', dimensionality=THREE_D,
```

```
type=DEFORMABLE_BODY)
p = mdb.models[str(ii)].parts['Stud']
#stud Length
p.BaseShellExtrude(sketch=s1, depth=studL)
s1.unsetPrimaryObject()
p = mdb.models[str(ii)].parts['Stud']
del mdb.models[str(ii)].sketches['__profile__']
#Track corner cordinates
s = mdb.models[str(ii)].ConstrainedSketch(name='__profile__',
sheetSize=200.0)
g, v, d, c = s.geometry, s.vertices, s.dimensions, s.constraints
s.setPrimaryObject(option=STANDALONE)
#1
s.Line(point1=(0.0, 0.0), point2=(0.0, trackH))
#2
s.Line(point1=(0.0, trackH), point2=(trackW-trackt/2, trackH))
#3
s.Line(point1=(0.0, 0.0), point2=(trackW-trackt/2, 0.0))
p = mdb.models[str(ii)].Part(name='Track', dimensionality=THREE_D,
type=DEFORMABLE_BODY)
p = mdb.models[str(ii)].parts['Track']
```

```
#Track Length
p.BaseShellExtrude(sketch=s, depth=trackL)
s.unsetPrimaryObject()
p = mdb.models[str(ii)].parts['Track']
del mdb.models[str(ii)].sketches['__profile__']
#slab
s = mdb.models[str(ii)].ConstrainedSketch(name='__profile__',
sheetSize=200.0)
g, v, d, c = s.geometry, s.vertices, s.dimensions, s.constraints
s.setPrimaryObject(option=STANDALONE)
#s.rectangle(point1=(0.0, 0.0), point2=(0.0, slabH))
#1
s.Line(point1=(0.0, 0.0), point2=(0.0, slabH))
#2
s.Line(point1=(0.0, slabH), point2=(slabW, slabH))
#3
s.Line(point1=(slabW, slabH), point2=(slabW, 0.0))
#4
s.Line(point1=(slabW, 0.0), point2=(0.0, 0.0))
p = mdb.models[str(ii)].Part(name='Slab', dimensionality=THREE_D,
type=DEFORMABLE_BODY)
```

```
p = mdb.models[str(ii)].parts['Slab']
p.BaseSolidExtrude(sketch=s, depth=slabL)
s.unsetPrimaryObject()
p = mdb.models[str(ii)].parts['Slab']
del mdb.models[str(ii)].sketches['__profile__']
#Rebars
s1 = mdb.models[str(ii)].ConstrainedSketch(name='__profile__',
sheetSize=200.0)
g, v, d, c = s1.geometry, s1.vertices, s1.dimensions, s1.constraints
s1.setPrimaryObject(option=STANDALONE)
#Rebar32
s1.Line(point1=(0.0, 0.0), point2=(slabL-2, 0.0))
p = mdb.models[str(ii)].Part(name='Rebar32', dimensionality=THREE_D,
type=DEFORMABLE_BODY)
p = mdb.models[str(ii)].parts['Rebar32']
p.BaseWire(sketch=s1)
s1.unsetPrimaryObject()
p = mdb.models[str(ii)].parts['Rebar32']
del mdb.models[str(ii)].sketches['__profile__']
s = mdb.models[str(ii)].ConstrainedSketch(name='__profile__',
sheetSize=200.0)
```

```
g, v, d, c = s.geometry, s.vertices, s.dimensions, s.constraints
s.setPrimaryObject(option=STANDALONE)
#Rebar20
s.Line(point1=(0.0, 0.0), point2=(slabW-2, 0.0))
p = mdb.models[str(ii)].Part(name='Rebar20', dimensionality=THREE_D,
type=DEFORMABLE_BODY)
p = mdb.models[str(ii)].parts['Rebar20']
p.BaseWire(sketch=s)
s.unsetPrimaryObject()
p = mdb.models[str(ii)].parts['Rebar20']
del mdb.models[str(ii)].sketches['__profile__']
#Material
mdb.models[str(ii)].Material(name='CFS')
mdb.models[str(ii)].materials['CFS'].Density(table=((0.00029, ), ))
mdb.models[str(ii)].materials['CFS'].Elastic(table=((29500, 0.3), ))
mdb.models[str(ii)].materials['CFS'].Plastic(table=((Fy, 0.0), ))
mdb.models[str(ii)].Material(name='Concrete')
mdb.models[str(ii)].materials['Concrete'].Density(table=((8.3912e-05, ), ))
mdb.models[str(ii)].materials['Concrete'].Elastic(table=((4593.8, 0.18), ))
mdb.models[str(ii)].materials['Concrete'].ConcreteDamagedPlasticity(table=((
30.0, 0.1, 1.16, 0.667, 1e-05), ))
```

```
        mdb.models[str(ii)].materials['Concrete'].concreteDamagedPlasticity.ConcreteCo
mpressionHardening(

        table=((1.924, 0.0), (2.53357018, 0.0003), (3.313890324, 0.0006), (

        3.931043077, 0.0009), (4.385028439, 0.0012), (4.675846411, 0.0015), (

        4.803496991, 0.0018), (4.767980181, 0.0021), (4.56929598, 0.0024), (

        4.207444388, 0.0027), (3.682425405, 0.003), (2.994239031, 0.0033), (

        2.142885266, 0.0036), (1.12836411, 0.0039)))

        mdb.models[str(ii)].materials['Concrete'].concreteDamagedPlasticity.ConcreteTen
sionStiffening(

        table=((0.341, 0.0), (0.1137, 0.0011), (0.0, 0.0049)))

        mdb.models[str(ii)].Material(name='Rebar')

        mdb.models[str(ii)].materials['Rebar'].Density(table=((0.00029, ), ))

        mdb.models[str(ii)].materials['Rebar'].Elastic(table=((29000.0, 0.3), ))

        mdb.models[str(ii)].materials['Rebar'].Plastic(table=((36.0, 0.0), (36.0,

        0.1723)))

        #Sections

        #Stud

        mdb.models[str(ii)].HomogeneousShellSection(name='stud', preIntegrate=OFF,

        material='CFS', thicknessType=UNIFORM, thickness=studt,

        thicknessField='', idealization=NO_IDEALIZATION,

        poissonDefinition=DEFAULT, thicknessModulus=None,
temperature=GRADIENT,
```

```
        useDensity=OFF, integrationRule=SIMPSON, numIntPts=5)
        #Track
        mdb.models[str(ii)].HomogeneousShellSection(name='track', preIntegrate=OFF,
        material='CFS', thicknessType=UNIFORM, thickness=trackt,
        thicknessField='', idealization=NO_IDEALIZATION,
        poissonDefinition=DEFAULT, thicknessModulus=None,
temperature=GRADIENT,
        useDensity=OFF, integrationRule=SIMPSON, numIntPts=5)
        #Slab
        mdb.models[str(ii)].HomogeneousSolidSection(name='slab', material='Concrete',
        thickness=None)
        #Rebar
        mdb.models[str(ii)].TrussSection(name='rebar', material='Rebar', area=0.0398)
        #ASSEMBLY
        #Bottom Track
        a = mdb.models[str(ii)].rootAssembly
        a = mdb.models[str(ii)].rootAssembly
        a.DatumCsysByDefault(CARTESIAN)
        p = mdb.models[str(ii)].parts['Track']
        a.Instance(name='Track-1', part=p, dependent=ON)
        a = mdb.models[str(ii)].rootAssembly
```

```
        a.rotate(instanceList=('Track-1', ), axisPoint=(0.0, trackH/2, trackL),
        axisDirection=(0.0, 0.0, -1*trackL), angle=-90.0)
        session.viewports['Viewport: 1'].view.setValues(nearPlane=39.7394,
        farPlane=70.5513, width=40.7489, height=21.7761, viewOffsetX=4.52815,
        viewOffsetY=0.0720845)
        a = mdb.models[str(ii)].rootAssembly
        a.translate(instanceList=('Track-1', ), vector=(0.0, -1*trackH/2, -1*trackL/2))
        a = mdb.models[str(ii)].rootAssembly
        a.translate(instanceList=('Track-1', ), vector=(slabW/2-el-trackH/2-trackt/2, 0.0,
0.0))
        #1st Stud
        a = mdb.models[str(ii)].rootAssembly
        p = mdb.models[str(ii)].parts['Stud']
        a.Instance(name='Stud-1', part=p, dependent=ON)
        a = mdb.models[str(ii)].rootAssembly
        a.rotate(instanceList=('Stud-1', ), axisPoint=(0.0, 0.0, 0.0), axisDirection=(
        0.0, 0.0, studL), angle=90.0)
        a = mdb.models[str(ii)].rootAssembly
        a.rotate(instanceList=('Stud-1', ), axisPoint=(0.0, 0.0, 0.0), axisDirection=(
        -1*studL-studt, 0.0, 0.0), angle=-90.0)
        a = mdb.models[str(ii)].rootAssembly
```

```
        a.translate(instanceList=('Stud-1', ), vector=(slabW/2-el-trackH/2-
trackt/2+(studH-studt)/2, studL+trackt/2, 0.0))

        #Relocating the 1st stud from the center to its true location

        a = mdb.models[str(ii)].rootAssembly

        a.translate(instanceList=('Stud-1', ), vector=(0.0, 0.0, sl/2-cc))

        #2nd Stud

        a = mdb.models[str(ii)].rootAssembly

        p = mdb.models[str(ii)].parts['Stud']

        a.Instance(name='Stud-2', part=p, dependent=ON)

        a = mdb.models[str(ii)].rootAssembly

        a.rotate(instanceList=('Stud-2', ), axisPoint=(0.0, 0.0, 0.0), axisDirection=(

        0.0, 0.0, studL), angle=90.0)

        a = mdb.models[str(ii)].rootAssembly

        a.rotate(instanceList=('Stud-2', ), axisPoint=(0.0, 0.0, 0.0), axisDirection=(

        -1*studL-studt, 0.0, 0.0), angle=-90.0)

        a = mdb.models[str(ii)].rootAssembly

        a.translate(instanceList=('Stud-2', ), vector=(slabW/2-el-trackH/2-
trackt/2+(studH-studt)/2, studL+trackt/2, 0.0))

        #Relocating the 2nd stud from the center to its true location

        a = mdb.models[str(ii)].rootAssembly

        a.translate(instanceList=('Stud-2', ), vector=(0.0, 0.0, -(sl/2+cc)))

        #Top track
```

```
        a = mdb.models[str(ii)].rootAssembly

        p = mdb.models[str(ii)].parts['Track']

        a.Instance(name='Track-2', part=p, dependent=ON)

        a = mdb.models[str(ii)].rootAssembly

        a.rotate(instanceList=('Track-2', ), axisPoint=(0.0, trackH/2, trackL),

        axisDirection=(0.0, 0.0, -1*trackL), angle=-90.0)

        a = mdb.models[str(ii)].rootAssembly

        a.translate(instanceList=('Track-2', ), vector=(0.0, -1*trackH/2, -1*trackL/2))

        a = mdb.models[str(ii)].rootAssembly

        a.translate(instanceList=('Track-2', ), vector=(slabW/2-el-trackH/2-trackt/2, 0.0,
0.0))

        #rotating the track

        a = mdb.models[str(ii)].rootAssembly

        a.rotate(instanceList=('Track-2', ), axisPoint=(slabW/2-el-trackH/2-trackt/2, 0.0,
trackL/2),

        axisDirection=(0.0, 0.0, -1*trackL), angle=180.0)

        a = mdb.models[str(ii)].rootAssembly

        a.translate(instanceList=('Track-2', ), vector=(0.0, studL+trackt, 0.0))

        #Concrete Slab

        a = mdb.models[str(ii)].rootAssembly

        p = mdb.models[str(ii)].parts['Slab']

        a.Instance(name='Slab-1', part=p, dependent=ON)
```

```
a = mdb.models[str(ii)].rootAssembly

a.translate(instanceList=('Slab-1', ), vector=(-1*slabW/2, -(slabH+trackt/2), -
1*slabL/2))

#Mesh

#Rebar 30

a = mdb.models[str(ii)].rootAssembly

p = mdb.models[str(ii)].parts['Rebar32']

a.Instance(name='Rebar32-1', part=p, dependent=ON)

a = mdb.models[str(ii)].rootAssembly

a.rotate(instanceList=('Rebar32-1', ), axisPoint=(11.0, -6.027, 17.0),

axisDirection=(0.0, 6.0, 0.0), angle=90.0)

a = mdb.models[str(ii)].rootAssembly

a.LinearInstancePattern(instanceList=('Rebar32-1', ), direction1=(1.0, 0.0,

0.0), direction2=(0.0, 1.0, 0.0), number1=4, number2=1, spacing1=6.0,

spacing2=1.0)

a = mdb.models[str(ii)].rootAssembly

a.LinearInstancePattern(instanceList=('Rebar32-1-lin-2-1', 'Rebar32-1-lin-3-1',

'Rebar32-1', 'Rebar32-1-lin-4-1'), direction1=(1.0, 0.0, 0.0),

direction2=(0.0, 1.0, 0.0), number1=1, number2=2, spacing1=18.0,

spacing2=4.048)

a = mdb.models[str(ii)].rootAssembly
```

```
a.translate(instanceList=('Rebar32-1', 'Rebar32-1-lin-2-1',
'Rebar32-1-lin-2-1-lin-1-2', 'Rebar32-1-lin-1-2',
'Rebar32-1-lin-3-1-lin-1-2', 'Rebar32-1-lin-3-1', 'Rebar32-1-lin-4-1',
'Rebar32-1-lin-4-1-lin-1-2'), vector=(-3.0, -4.938, -12.0))
#Rebar20
a1 = mdb.models[str(ii)].rootAssembly
p = mdb.models[str(ii)].parts['Rebar20']
a1.Instance(name='Rebar20-1', part=p, dependent=ON)
p = a1.instances['Rebar20-1']
p.translate(vector=(13.0, 0.0, 0.0))
a1 = mdb.models[str(ii)].rootAssembly
a1.LinearInstancePattern(instanceList=('Rebar20-1', ), direction1=(1.0, 0.0,
0.0), direction2=(0.0, 1.0, 0.0), number1=1, number2=6, spacing1=20.0,
spacing2=6.0)
a1 = mdb.models[str(ii)].rootAssembly
a1.rotate(instanceList=('Rebar20-1', 'Rebar20-1-lin-1-2', 'Rebar20-1-lin-1-3',
'Rebar20-1-lin-1-4', 'Rebar20-1-lin-1-5', 'Rebar20-1-lin-1-6'),
axisPoint=(-11.0, -6.027, 17.0), axisDirection=(22.0, 0.0, 0.0),
angle=90.0)
a1 = mdb.models[str(ii)].rootAssembly
a1.LinearInstancePattern(instanceList=('Rebar20-1', 'Rebar20-1-lin-1-2',
```

'Rebar20-1-lin-1-3', 'Rebar20-1-lin-1-4', 'Rebar20-1-lin-1-5',

'Rebar20-1-lin-1-6'), direction1=(1.0, 0.0, 0.0), direction2=(0.0, 1.0,

0.0), number1=1, number2=2, spacing1=20.0, spacing2=4.04)

a1 = mdb.models[str(ii)].rootAssembly

a1.translate(instanceList=('Rebar20-1-lin-1-2-1', 'Rebar20-1',

'Rebar20-1-lin-1-2-lin-1-2', 'Rebar20-1-lin-1-2', 'Rebar20-1-lin-1-3',

'Rebar20-1-lin-1-4', 'Rebar20-1-lin-1-5', 'Rebar20-1-lin-1-6',

'Rebar20-1-lin-1-4-lin-1-2', 'Rebar20-1-lin-1-6-lin-1-2',

'Rebar20-1-lin-1-3-lin-1-2', 'Rebar20-1-lin-1-5-lin-1-2'), vector=(

-23.0, -16.137, -38.027))

#Merging rebars

a = mdb.models[str(ii)].rootAssembly

a.InstanceFromBooleanMerge(name='Mesh', instances=(a.instances['Rebar32-1'],

a.instances['Rebar32-1-lin-2-1'], a.instances['Rebar32-1-lin-3-1'],

a.instances['Rebar32-1-lin-4-1'],

a.instances['Rebar32-1-lin-2-1-lin-1-2'],

a.instances['Rebar32-1-lin-3-1-lin-1-2'],

a.instances['Rebar32-1-lin-1-2'],

a.instances['Rebar32-1-lin-4-1-lin-1-2'], a.instances['Rebar20-1'],

a.instances['Rebar20-1-lin-1-2'], a.instances['Rebar20-1-lin-1-3'],

a.instances['Rebar20-1-lin-1-4'], a.instances['Rebar20-1-lin-1-5'],

```
a.instances['Rebar20-1-lin-1-6'], a.instances['Rebar20-1-lin-1-2-1'],
a.instances['Rebar20-1-lin-1-2-lin-1-2'],
a.instances['Rebar20-1-lin-1-4-lin-1-2'],
a.instances['Rebar20-1-lin-1-6-lin-1-2'],
a.instances['Rebar20-1-lin-1-3-lin-1-2'],
a.instances['Rebar20-1-lin-1-5-lin-1-2'], ),
originalInstances=SUPPRESS, domain=GEOMETRY)
#Creating partitions for track web
#creating 3 datum points
p = mdb.models[str(ii)].parts['Track']
session.viewports['Viewport: 1'].setValues(displayedObject=p)
p = mdb.models[str(ii)].parts['Track']
p.DatumPointByCoordinate(coords=(0.0, oo, dd))
p = mdb.models[str(ii)].parts['Track']
p.DatumPointByCoordinate(coords=(0.0, oo, 12.0))
p = mdb.models[str(ii)].parts['Track']
p.DatumPointByCoordinate(coords=(0.0, oo, trackL-dd))
p = mdb.models[str(ii)].parts['Track']
#Creating partitions
#
f, e, d = p.faces, p.edges, p.datums
```

```
t = p.MakeSketchTransform(sketchPlane=f[1], sketchUpEdge=e[4],
sketchPlaneSide=SIDE1, origin=(0.0, oo, trackL/2))
s = mdb.models[str(ii)].ConstrainedSketch(name='__profile__', sheetSize=49.5,
gridSpacing=1.23, transform=t)
g, v, d1, c = s.geometry, s.vertices, s.dimensions, s.constraints
s.setPrimaryObject(option=SUPERIMPOSE)
p = mdb.models[str(ii)].parts['Track']
p.projectReferencesOntoSketch(sketch=s, filter=COPLANAR_EDGES)
s.Line(point1=(-1*trackL/2, 0.0), point2=(-1*(trackL/2-dd), 0.0))
p = mdb.models[str(ii)].parts['Track']
f = p.faces
pickedFaces = f.getSequenceFromMask(mask=('[#2 ]', ), )
e1, d2 = p.edges, p.datums
p.PartitionFaceBySketch(sketchUpEdge=e1[4], faces=pickedFaces, sketch=s)
s.unsetPrimaryObject()
del mdb.models[str(ii)].sketches['__profile__']
#
p = mdb.models[str(ii)].parts['Track']
f, e, d = p.faces, p.edges, p.datums
t = p.MakeSketchTransform(sketchPlane=f[1], sketchUpEdge=e[4],
sketchPlaneSide=SIDE1, origin=(0.0, oo, trackL/2))
```

```
s = mdb.models[str(ii)].ConstrainedSketch(name='__profile__', sheetSize=49.5,
gridSpacing=1.23, transform=t)
g, v, d1, c = s.geometry, s.vertices, s.dimensions, s.constraints
s.setPrimaryObject(option=SUPERIMPOSE)
p = mdb.models[str(ii)].parts['Track']
p.projectReferencesOntoSketch(sketch=s, filter=COPLANAR_EDGES)
s.Line(point1=(-1*(trackL/2-dd), 0.0), point2=(0.0, 0.0))
s.HorizontalConstraint(entity=g[11], addUndoState=False)
s.Line(point1=(0.0, 0.0), point2=(trackL/2-dd, 0.0))
s.Line(point1=(trackL/2-dd, 0.0), point2=(trackL/2, 0.0))
p = mdb.models[str(ii)].parts['Track']
f = p.faces
pickedFaces = f.getSequenceFromMask(mask=('[#2 ]', ), )
e1, d2 = p.edges, p.datums
p.PartitionFaceBySketch(sketchUpEdge=e1[4], faces=pickedFaces, sketch=s)
s.unsetPrimaryObject()
del mdb.models[str(ii)].sketches['__profile__']
#Defining the location of the screws for the tracks
#1
p = mdb.models[str(ii)].parts['Track']
```

```
        p.DatumPointByCoordinate(coords=((trackW-(trackt/2))/2, 0, (trackL/2-
(sl/2+cc)+(studW-studt)/2)))

        #2

        p = mdb.models[str(ii)].parts['Track']

        p.DatumPointByCoordinate(coords=((trackW-(trackt/2))/2, 0, (trackL/2-
(sl/2+cc)+(studW-studt)/2)+sl))

        #3

        p = mdb.models[str(ii)].parts['Track']

        p.DatumPointByCoordinate(coords=((trackW-(trackt/2))/2, trackH, (trackL/2-
(sl/2+cc)+(studW-studt)/2)))

        #4

        p = mdb.models[str(ii)].parts['Track']

        p.DatumPointByCoordinate(coords=((trackW-(trackt/2))/2, trackH, (trackL/2-
(sl/2+cc)+(studW-studt)/2)+sl))

        #Defining the location of the screws for the studs

        #1

        p = mdb.models[str(ii)].parts['Stud']

        p = mdb.models[str(ii)].parts['Stud']

        p.DatumPointByCoordinate(coords=((studW-studt)/2, 0.0, (trackW-(trackt/2))/2-
trackt/2))

        #2

        p = mdb.models[str(ii)].parts['Stud']

        p.DatumPointByCoordinate(coords=((studW-studt)/2, 0.0, studL-((trackW-
(trackt/2))/2-trackt/2)))
```

```
        #3

        p = mdb.models[str(ii)].parts['Stud']

        p.DatumPointByCoordinate(coords=((studW-studt)/2, studH-studt/2, (trackW-
(trackt/2))/2-trackt/2))

        #4

        p = mdb.models[str(ii)].parts['Stud']

        p.DatumPointByCoordinate(coords=((studW-studt)/2, studH-studt/2, studL-
((trackW-(trackt/2))/2-trackt/2)))

        #Creating partition in the flanges of tracks

        #1

        p = mdb.models[str(ii)].parts['Track']

        p = mdb.models[str(ii)].parts['Track']

        f, e, d = p.faces, p.edges, p.datums

        t = p.MakeSketchTransform(sketchPlane=f[3], sketchUpEdge=e[13],

        sketchPlaneSide=SIDE1, origin=(0, 0.0, 0))

        s = mdb.models[str(ii)].ConstrainedSketch(name='__profile__',

        sheetSize=48.44, gridSpacing=1.21, transform=t)

        g, v, d1, c = s.geometry, s.vertices, s.dimensions, s.constraints

        s.setPrimaryObject(option=SUPERIMPOSE)

        p = mdb.models[str(ii)].parts['Track']

        p.projectReferencesOntoSketch(sketch=s, filter=COPLANAR_EDGES)
```

```
        s.Line(point1=((trackL/2-(sl/2+cc)+(studW-studt)/2), (trackW-(trackt/2))/2),
point2=((trackL/2-(sl/2+cc)+(studW-studt)/2), (trackW-(trackt/2))))

        s.Line(point1=((trackL/2-(sl/2+cc)+(studW-studt)/2), (trackW-(trackt/2))/2),
point2=((trackL/2-(sl/2+cc)+(studW-studt)/2), 0))

        s.Line(point1=(sl+(trackL/2-(sl/2+cc)+(studW-studt)/2), (trackW-(trackt/2))/2),
point2=(sl+(trackL/2-(sl/2+cc)+(studW-studt)/2), (trackW-(trackt/2))))

        s.Line(point1=(sl+(trackL/2-(sl/2+cc)+(studW-studt)/2), (trackW-(trackt/2))/2),
point2=(sl+(trackL/2-(sl/2+cc)+(studW-studt)/2), 0))

        p = mdb.models[str(ii)].parts['Track']

        f = p.faces

        pickedFaces = f.getSequenceFromMask(mask=('[#8 ]', ), )

        e1, d2 = p.edges, p.datums

        p.PartitionFaceBySketch(sketchUpEdge=e1[13], faces=pickedFaces, sketch=s)

        s.unsetPrimaryObject()

        del mdb.models[str(ii)].sketches['__profile__']

        #

        p = mdb.models[str(ii)].parts['Track']

        f, e, d = p.faces, p.edges, p.datums

        t = p.MakeSketchTransform(sketchPlane=f[3], sketchUpEdge=e[16],

        sketchPlaneSide=SIDE1, origin=(0, trackH, 0))

        s = mdb.models[str(ii)].ConstrainedSketch(name='__profile__',

        sheetSize=49.56, gridSpacing=1.23, transform=t)

        g, v, d1, c = s.geometry, s.vertices, s.dimensions, s.constraints
```

```
        s.setPrimaryObject(option=SUPERIMPOSE)

        p = mdb.models[str(ii)].parts['Track']

        p.projectReferencesOntoSketch(sketch=s, filter=COPLANAR_EDGES)

        s.Line(point1=((trackL/2-(sl/2+cc)+(studW-studt)/2), -(trackW-(trackt/2))/2),
point2=((trackL/2-(sl/2+cc)+(studW-studt)/2), -(trackW-(trackt/2))))

        s.Line(point1=((trackL/2-(sl/2+cc)+(studW-studt)/2), -(trackW-(trackt/2))/2),
point2=((trackL/2-(sl/2+cc)+(studW-studt)/2), 0))

        s.Line(point1=(sl+(trackL/2-(sl/2+cc)+(studW-studt)/2), -(trackW-(trackt/2))/2),
point2=(sl+(trackL/2-(sl/2+cc)+(studW-studt)/2), -(trackW-(trackt/2))))

        s.Line(point1=(sl+(trackL/2-(sl/2+cc)+(studW-studt)/2), -(trackW-(trackt/2))/2),
point2=(sl+(trackL/2-(sl/2+cc)+(studW-studt)/2), 0))

        p = mdb.models[str(ii)].parts['Track']

        f = p.faces

        pickedFaces = f.getSequenceFromMask(mask=('[#8 ]', ), )

        e1, d2 = p.edges, p.datums

        p.PartitionFaceBySketch(sketchUpEdge=e1[16], faces=pickedFaces, sketch=s)

        s.unsetPrimaryObject()

        del mdb.models[str(ii)].sketches['__profile__']

        #Creating partition in the flanges of studs

        #

        p = mdb.models[str(ii)].parts['Stud']

        f, e, d = p.faces, p.edges, p.datums

        t = p.MakeSketchTransform(sketchPlane=f[3], sketchUpEdge=e[10],
```

```
        sketchPlaneSide=SIDE1, origin=(0, 0.0, 0))

        s = mdb.models[str(ii)].ConstrainedSketch(name='__profile__', sheetSize=24.2,

        gridSpacing=0.6, transform=t)

        g, v, d1, c = s.geometry, s.vertices, s.dimensions, s.constraints

        s.setPrimaryObject(option=SUPERIMPOSE)

        p = mdb.models[str(ii)].parts['Stud']

        p.projectReferencesOntoSketch(sketch=s, filter=COPLANAR_EDGES)

        s.Line(point1=((trackW-(trackt/2))/2-trackt/2, (studW-studt)/2), point2=(studL-
((trackW-(trackt/2))/2-trackt/2), (studW-studt)/2))

        p = mdb.models[str(ii)].parts['Stud']

        f = p.faces

        pickedFaces = f.getSequenceFromMask(mask=('[#8 ]', ), )

        e1, d2 = p.edges, p.datums

        p.PartitionFaceBySketch(sketchUpEdge=e1[10], faces=pickedFaces, sketch=s)

        s.unsetPrimaryObject()

        del mdb.models[str(ii)].sketches['__profile__']

        #

        p = mdb.models[str(ii)].parts['Track']

        p = mdb.models[str(ii)].parts['Stud']

        p = mdb.models[str(ii)].parts['Stud']

        f, e, d = p.faces, p.edges, p.datums
```

```
        t = p.MakeSketchTransform(sketchPlane=f[1], sketchUpEdge=e[4],
        sketchPlaneSide=SIDE1, origin=(0, studH-studt, 0))
        s = mdb.models[str(ii)].ConstrainedSketch(name='__profile__',
        sheetSize=26.96, gridSpacing=0.67, transform=t)
        g, v, d1, c = s.geometry, s.vertices, s.dimensions, s.constraints
        s.setPrimaryObject(option=SUPERIMPOSE)
        p = mdb.models[str(ii)].parts['Stud']
        p.projectReferencesOntoSketch(sketch=s, filter=COPLANAR_EDGES)
        s.Line(point1=(((trackW-(trackt/2))/2-trackt/2), -(studW-studt)/2),
point2=((studL-((trackW-(trackt/2))/2-trackt/2)), -(studW-studt)/2))
        p = mdb.models[str(ii)].parts['Stud']
        f = p.faces
        pickedFaces = f.getSequenceFromMask(mask=('[#2 ]', ), )
        e1, d2 = p.edges, p.datums
        p.PartitionFaceBySketch(sketchUpEdge=e1[4], faces=pickedFaces, sketch=s)
        s.unsetPrimaryObject()
        del mdb.models[str(ii)].sketches['__profile__']
        ###################Creating datumn plane for TRACK
        p1 = mdb.models[str(ii)].parts['Track']
        session.viewports['Viewport: 1'].setValues(displayedObject=p1)
        p = mdb.models[str(ii)].parts['Track']
```

```
        p.DatumPlaneByPrincipalPlane(principalPlane=XYPLANE, offset=(trackL/2-
sl/2-cc-0.1))



        p1 = mdb.models[str(ii)].parts['Track']

        p = mdb.models[str(ii)].parts['Track']

        p.DatumPlaneByPrincipalPlane(principalPlane=XYPLANE, offset=(trackL/2-
sl/2-cc+studW+0.1))



        p1 = mdb.models[str(ii)].parts['Track']

        p = mdb.models[str(ii)].parts['Track']

        p.DatumPlaneByPrincipalPlane(principalPlane=XYPLANE,
offset=(trackL/2+sl/2-cc-0.1))



        p1 = mdb.models[str(ii)].parts['Track']

        p = mdb.models[str(ii)].parts['Track']

        p.DatumPlaneByPrincipalPlane(principalPlane=XYPLANE,
offset=(trackL/2+sl/2-cc+studW+0.1))



        ######################Creating Partition based on the datumn plane

        p = mdb.models[str(ii)].parts['Track']

        f = p.faces

        pickedRegions = f.getSequenceFromMask(mask=('[#28 ]', ), )

        p.deleteMesh(regions=pickedRegions)
```

```
p = mdb.models[str(ii)].parts['Track']
f = p.faces
pickedFaces = f.getSequenceFromMask(mask=('[#82 ]', ), )
d1 = p.datums
p.PartitionFaceByDatumPlane(datumPlane=d1[13], faces=pickedFaces)
p = mdb.models[str(ii)].parts['Track']
f = p.faces
pickedRegions = f.getSequenceFromMask(mask=('[#14 ]', ), )
p.deleteMesh(regions=pickedRegions)
p = mdb.models[str(ii)].parts['Track']
f = p.faces
pickedFaces = f.getSequenceFromMask(mask=('[#a0 ]', ), )
d = p.datums
p.PartitionFaceByDatumPlane(datumPlane=d[14], faces=pickedFaces)
p = mdb.models[str(ii)].parts['Track']
f = p.faces
pickedFaces = f.getSequenceFromMask(mask=('[#280 ]', ), )
d1 = p.datums
p.PartitionFaceByDatumPlane(datumPlane=d1[15], faces=pickedFaces)
p = mdb.models[str(ii)].parts['Track']
f = p.faces
```

```
        pickedFaces = f.getSequenceFromMask(mask=('[#140 ]', ), )

        d = p.datums

        p.PartitionFaceByDatumPlane(datumPlane=d[16], faces=pickedFaces)

        ###################

        ######################Creating datumn plane for STUD

        p = mdb.models[str(ii)].parts['Stud']

        p.DatumPlaneByPrincipalPlane(principalPlane=XYPLANE,
offset=trackW+tol_contact)

        p = mdb.models[str(ii)].parts['Stud']

        p.DatumPlaneByPrincipalPlane(principalPlane=XYPLANE, offset=studL-
trackW-tol_contact)

        ######################Creating Partition based on datumn plane for STUD

        p = mdb.models[str(ii)].parts['Stud']

        f = p.faces

        pickedFaces = f.getSequenceFromMask(mask=('[#a ]', ), )

        d1 = p.datums

        p.PartitionFaceByDatumPlane(datumPlane=d1[9], faces=pickedFaces)

        p = mdb.models[str(ii)].parts['Stud']

        f = p.faces

        pickedFaces = f.getSequenceFromMask(mask=('[#3 ]', ), )

        d = p.datums

        p.PartitionFaceByDatumPlane(datumPlane=d[8], faces=pickedFaces)
```

```
        #Defining the location of the screws for the slab

        p = mdb.models[str(ii)].parts['Slab']

        p = mdb.models[str(ii)].parts['Slab']

        p.DatumPointByCoordinate(coords=(slab_screw, slabH, dd+(slabL-trackL)/2))

        p.DatumPointByCoordinate(coords=(slab_screw, slabH, slabL/2))

        p.DatumPointByCoordinate(coords=(slab_screw, slabH, slabL-(dd+(slabL-
trackL)/2)))



        #Creating partition in the slab

        p = mdb.models[str(ii)].parts['Slab']

        f1, e, d = p.faces, p.edges, p.datums

        t = p.MakeSketchTransform(sketchPlane=f1[1], sketchUpEdge=e[6],

        sketchPlaneSide=SIDE1, origin=(0, 6.0, 0))

        s1 = mdb.models[str(ii)].ConstrainedSketch(name='__profile__',

        sheetSize=81.87, gridSpacing=2.04, transform=t)

        g, v, d1, c = s1.geometry, s1.vertices, s1.dimensions, s1.constraints

        s1.setPrimaryObject(option=SUPERIMPOSE)

        p = mdb.models[str(ii)].parts['Slab']

        p.projectReferencesOntoSketch(sketch=s1, filter=COPLANAR_EDGES)

        s1.Line(point1=(dd+(slabL-trackL)/2, slab_screw), point2=(slabL/2, slab_screw))
```

```
        s1.Line(point1=(slabL/2,  slab_screw), point2=(slabL-(dd+(slabL-trackL)/2),
slab_screw))

        p = mdb.models[str(ii)].parts['Slab']

        f = p.faces

        pickedFaces = f.getSequenceFromMask(mask=('[#2 ]', ), )

        e1, d2 = p.edges, p.datums

        p.PartitionFaceBySketch(sketchUpEdge=e1[6], faces=pickedFaces, sketch=s1)

        s1.unsetPrimaryObject()

        del mdb.models[str(ii)].sketches['__profile__']

        #Assigning the sections

        #Slab

        p = mdb.models[str(ii)].parts['Slab']

        c = p.cells

        cells = c.getSequenceFromMask(mask=('[#1 ]', ), )

        region = regionToolset.Region(cells=cells)

        p = mdb.models[str(ii)].parts['Slab']

        p.SectionAssignment(region=region, sectionName='slab', offset=0.0,

        offsetType=MIDDLE_SURFACE, offsetField='',

        thicknessAssignment=FROM_SECTION)

        #Stud

        p = mdb.models[str(ii)].parts['Stud']
```

```
p = mdb.models[str(ii)].parts['Stud']
f = p.faces
faces = f.getSequenceFromMask(mask=('[#7ff ]', ), )
region = regionToolset.Region(faces=faces)
p = mdb.models[str(ii)].parts['Stud']
p.SectionAssignment(region=region, sectionName='stud', offset=0.0,
offsetType=MIDDLE_SURFACE, offsetField='',
thicknessAssignment=FROM_SECTION)
#track
p = mdb.models[str(ii)].parts['Track']
p = mdb.models[str(ii)].parts['Track']
f = p.faces
faces = f.getSequenceFromMask(mask=('[#ffff ]', ), )
region = regionToolset.Region(faces=faces)
p = mdb.models[str(ii)].parts['Track']
p.SectionAssignment(region=region, sectionName='track', offset=0.0,
offsetType=MIDDLE_SURFACE, offsetField='',
thicknessAssignment=FROM_SECTION)
#Rebars
p = mdb.models[str(ii)].parts['Rebar20']
p = mdb.models[str(ii)].parts['Rebar20']
```

```
e = p.edges
edges = e.getSequenceFromMask(mask=('[#1 ]', ), )
region = regionToolset.Region(edges=edges)
p = mdb.models[str(ii)].parts['Rebar20']
p.SectionAssignment(region=region, sectionName='rebar', offset=0.0,
offsetType=MIDDLE_SURFACE, offsetField='',
thicknessAssignment=FROM_SECTION)
p = mdb.models[str(ii)].parts['Rebar32']
p = mdb.models[str(ii)].parts['Rebar32']
e = p.edges
edges = e.getSequenceFromMask(mask=('[#1 ]', ), )
region = regionToolset.Region(edges=edges)
p = mdb.models[str(ii)].parts['Rebar32']
p.SectionAssignment(region=region, sectionName='rebar', offset=0.0,
offsetType=MIDDLE_SURFACE, offsetField='',
thicknessAssignment=FROM_SECTION)
#MESH
p = mdb.models[str(ii)].parts['Mesh']
session.viewports['Viewport: 1'].setValues(displayedObject=p)
p = mdb.models[str(ii)].parts['Mesh']
e = p.edges
```

```
edges = e.getSequenceFromMask(mask=('[#fffff ]', ), )
region = regionToolset.Region(edges=edges)
p = mdb.models[str(ii)].parts['Mesh']
p.SectionAssignment(region=region, sectionName='rebar', offset=0.0,
offsetType=MIDDLE_SURFACE, offsetField='',
thicknessAssignment=FROM_SECTION)
#Slab
p = mdb.models[str(ii)].parts['Slab']
p.seedPart(size=Mslab, deviationFactor=0.1, minSizeFactor=0.1)
p = mdb.models[str(ii)].parts['Slab']
p.generateMesh()
#Stud
p = mdb.models[str(ii)].parts['Stud']
p.seedPart(size=Mstud, deviationFactor=0.1, minSizeFactor=0.1)
p = mdb.models[str(ii)].parts['Stud']
p.generateMesh()
#Track
p = mdb.models[str(ii)].parts['Track']
p.seedPart(size=Mtrack, deviationFactor=0.1, minSizeFactor=0.1)
p = mdb.models[str(ii)].parts['Track']
p.generateMesh()
```

```
#Rebar
p = mdb.models[str(ii)].parts['Mesh']
p.seedPart(size=Mrebar, deviationFactor=0.1, minSizeFactor=0.1)
p = mdb.models[str(ii)].parts['Mesh']
p.generateMesh()
elemType1 = mesh.ElemType(elemCode=T3D2, elemLibrary=STANDARD)
p = mdb.models[str(ii)].parts['Mesh']
e = p.edges
edges = e.getSequenceFromMask(mask=('[#fffff ]', ), )
pickedRegions =(edges, )
p.setElementType(regions=pickedRegions, elemTypes=(elemType1, ))
p = mdb.models[str(ii)].parts['Mesh']
p.seedPart(size=Mrebar, deviationFactor=0.1, minSizeFactor=0.1)
p = mdb.models[str(ii)].parts['Mesh']
p.generateMesh()
#Constraints
#screws
#
a = mdb.models[str(ii)].rootAssembly
v1 = a.instances['Track-1'].vertices
verts1 = v1.getSequenceFromMask(mask=('[#100 ]', ), )
```

```
region1=regionToolset.Region(vertices=verts1)
a = mdb.models[str(ii)].rootAssembly
v1 = a.instances['Stud-1'].vertices
verts1 = v1.getSequenceFromMask(mask=('[#2000000 ]', ), )
region2=regionToolset.Region(vertices=verts1)
mdb.models[str(ii)].MultipointConstraint(name='Constraint-1',
controlPoint=region1, surface=region2, mpcType=PIN_MPC,
userMode=DOF_MODE_MPC, userType=0, csys=None)
#
a = mdb.models[str(ii)].rootAssembly
a.regenerate()
a = mdb.models[str(ii)].rootAssembly
session.viewports['Viewport: 1'].setValues(displayedObject=a)
session.viewports['Viewport: 1'].assemblyDisplay.setValues(interactions=ON,
constraints=ON, connectors=ON, engineeringFeatures=ON)
a = mdb.models[str(ii)].rootAssembly
v1 = a.instances['Track-1'].vertices
verts1 = v1.getSequenceFromMask(mask=('[#80000 ]', ), )
region1=regionToolset.Region(vertices=verts1)
a = mdb.models[str(ii)].rootAssembly
v1 = a.instances['Stud-2'].vertices
```

```
verts1 = v1.getSequenceFromMask(mask=('[#2000000 ]', ), )
region2=regionToolset.Region(vertices=verts1)
mdb.models[str(ii)].MultipointConstraint(name='Constraint-2',
controlPoint=region1, surface=region2, mpcType=PIN_MPC,
userMode=DOF_MODE_MPC, userType=0, csys=None)
session.viewports['Viewport: 1'].assemblyDisplay.setValues(visibleInstances=(
'Mesh-1', 'Rebar20-1', 'Rebar20-1-lin-1-2', 'Rebar20-1-lin-1-2-1',
'Rebar20-1-lin-1-2-lin-1-2', 'Rebar20-1-lin-1-3',
'Rebar20-1-lin-1-3-lin-1-2', 'Rebar20-1-lin-1-4',
'Rebar20-1-lin-1-4-lin-1-2', 'Rebar20-1-lin-1-5',
'Rebar20-1-lin-1-5-lin-1-2', 'Rebar20-1-lin-1-6',
'Rebar20-1-lin-1-6-lin-1-2', 'Rebar32-1', 'Rebar32-1-lin-1-2',
'Rebar32-1-lin-2-1', 'Rebar32-1-lin-2-1-lin-1-2', 'Rebar32-1-lin-3-1',
'Rebar32-1-lin-3-1-lin-1-2', 'Rebar32-1-lin-4-1',
'Rebar32-1-lin-4-1-lin-1-2', 'Slab-1', 'Stud-1', 'Stud-2', 'Track-1',
'Track-2'))
a = mdb.models[str(ii)].rootAssembly
v1 = a.instances['Track-2'].vertices
verts1 = v1.getSequenceFromMask(mask=('[#8 ]', ), )
region1=regionToolset.Region(vertices=verts1)
a = mdb.models[str(ii)].rootAssembly
```

```
v1 = a.instances['Stud-1'].vertices
verts1 = v1.getSequenceFromMask(mask=('[#2000 ]', ), )
region2=regionToolset.Region(vertices=verts1)
mdb.models[str(ii)].MultipointConstraint(name='Constraint-3',
controlPoint=region1, surface=region2, mpcType=PIN_MPC,
userMode=DOF_MODE_MPC, userType=0, csys=None)
a = mdb.models[str(ii)].rootAssembly
v1 = a.instances['Track-2'].vertices
verts1 = v1.getSequenceFromMask(mask=('[#400000 ]', ), )
region1=regionToolset.Region(vertices=verts1)
a = mdb.models[str(ii)].rootAssembly
v1 = a.instances['Stud-2'].vertices
verts1 = v1.getSequenceFromMask(mask=('[#2000 ]', ), )
region2=regionToolset.Region(vertices=verts1)
mdb.models[str(ii)].MultipointConstraint(name='Constraint-4',
controlPoint=region1, surface=region2, mpcType=PIN_MPC,
userMode=DOF_MODE_MPC, userType=0, csys=None)
#
a = mdb.models[str(ii)].rootAssembly
v1 = a.instances['Track-1'].vertices
verts1 = v1.getSequenceFromMask(mask=('[#400000]', ), )
```

```
region1=regionToolset.Region(vertices=verts1)
a = mdb.models[str(ii)].rootAssembly
v1 = a.instances['Stud-2'].vertices
verts1 = v1.getSequenceFromMask(mask=('[#400000 ]', ), )
region2=regionToolset.Region(vertices=verts1)
mdb.models[str(ii)].MultipointConstraint(name='Constraint-5',
controlPoint=region1, surface=region2, mpcType=PIN_MPC,
userMode=DOF_MODE_MPC, userType=0, csys=None)
a = mdb.models[str(ii)].rootAssembly
v1 = a.instances['Track-1'].vertices
verts1 = v1.getSequenceFromMask(mask=('[#8 ]', ), )
region1=regionToolset.Region(vertices=verts1)
a = mdb.models[str(ii)].rootAssembly
v1 = a.instances['Stud-1'].vertices
verts1 = v1.getSequenceFromMask(mask=('[#400000 ]', ), )
region2=regionToolset.Region(vertices=verts1)
mdb.models[str(ii)].MultipointConstraint(name='Constraint-6',
controlPoint=region1, surface=region2, mpcType=PIN_MPC,
userMode=DOF_MODE_MPC, userType=0, csys=None)
a = mdb.models[str(ii)].rootAssembly
v1 = a.instances['Track-2'].vertices
```

```
verts1 = v1.getSequenceFromMask(mask=('[#80000 ]', ), )
region1=regionToolset.Region(vertices=verts1)
a = mdb.models[str(ii)].rootAssembly
v1 = a.instances['Stud-2'].vertices
verts1 = v1.getSequenceFromMask(mask=('[#20 ]', ), )
region2=regionToolset.Region(vertices=verts1)
mdb.models[str(ii)].MultipointConstraint(name='Constraint-7',
controlPoint=region1, surface=region2, mpcType=PIN_MPC,
userMode=DOF_MODE_MPC, userType=0, csys=None)
a = mdb.models[str(ii)].rootAssembly
v1 = a.instances['Track-2'].vertices
verts1 = v1.getSequenceFromMask(mask=('[#100 ]', ), )
region1=regionToolset.Region(vertices=verts1)
a = mdb.models[str(ii)].rootAssembly
v1 = a.instances['Stud-1'].vertices
verts1 = v1.getSequenceFromMask(mask=('[#20 ]', ), )
region2=regionToolset.Region(vertices=verts1)
mdb.models[str(ii)].MultipointConstraint(name='Constraint-8',
controlPoint=region1, surface=region2, mpcType=PIN_MPC,
userMode=DOF_MODE_MPC, userType=0, csys=None)
```

```
#Pins for attaching the bottom track to the slab
a = mdb.models[str(ii)].rootAssembly
v1 = a.instances['Slab-1'].vertices
verts1 = v1.getSequenceFromMask(mask=('[#20 ]', ), )
region1=regionToolset.Region(vertices=verts1)
a = mdb.models[str(ii)].rootAssembly
v1 = a.instances['Track-1'].vertices
verts1 = v1.getSequenceFromMask(mask=('[#0 #40 ]', ), )
region2=regionToolset.Region(vertices=verts1)
mdb.models[str(ii)].MultipointConstraint(name='Constraint-9',
controlPoint=region1, surface=region2, mpcType=PIN_MPC,
userMode=DOF_MODE_MPC, userType=0, csys=None)
a = mdb.models[str(ii)].rootAssembly
v1 = a.instances['Slab-1'].vertices
verts1 = v1.getSequenceFromMask(mask=('[#10 ]', ), )
region1=regionToolset.Region(vertices=verts1)
a = mdb.models[str(ii)].rootAssembly
v1 = a.instances['Track-1'].vertices
verts1 = v1.getSequenceFromMask(mask=('[#0 #20 ]', ), )
region2=regionToolset.Region(vertices=verts1)
mdb.models[str(ii)].MultipointConstraint(name='Constraint-10',
```

```
controlPoint=region1, surface=region2, mpcType=PIN_MPC,
userMode=DOF_MODE_MPC, userType=0, csys=None)
a = mdb.models[str(ii)].rootAssembly
v1 = a.instances['Slab-1'].vertices
verts1 = v1.getSequenceFromMask(mask=('[#40 ]', ), )
region1=regionToolset.Region(vertices=verts1)
a = mdb.models[str(ii)].rootAssembly
v1 = a.instances['Track-1'].vertices
verts1 = v1.getSequenceFromMask(mask=('[#0 #10 ]', ), )
region2=regionToolset.Region(vertices=verts1)
mdb.models[str(ii)].MultipointConstraint(name='Constraint-11',
controlPoint=region1, surface=region2, mpcType=PIN_MPC,
userMode=DOF_MODE_MPC, userType=0, csys=None)
#session.viewports['Viewport: 1'].view.setValues(session.views['Iso'])
#Constraints between the stud ends and top track
session.viewports['Viewport: 1'].view.setValues(nearPlane=73.8963,
farPlane=119.637, width=19.1644, height=9.75038, viewOffsetX=4.43841,
viewOffsetY=2.77781)
session.viewports['Viewport: 1'].view.setValues(nearPlane=74.5343,
farPlane=119.017, width=16.3862, height=8.33689, viewOffsetX=3.57565,
viewOffsetY=2.78628)
```

```
a = mdb.models[str(ii)].rootAssembly
s1 = a.instances['Track-2'].faces
side1Faces1 = s1.getSequenceFromMask(mask=('[#5000 ]', ), )
region1=regionToolset.Region(side1Faces=side1Faces1)
a = mdb.models[str(ii)].rootAssembly
e1 = a.instances['Stud-1'].edges
edges1 = e1.getSequenceFromMask(mask=('[#81010080 #20 ]', ), )
e2 = a.instances['Stud-2'].edges
edges2 = e2.getSequenceFromMask(mask=('[#81010080 #20 ]', ), )
region2=regionToolset.Region(edges=edges1+edges2)
mdb.models[str(ii)].Tie(name='Constraint-12', master=region1, slave=region2,
positionToleranceMethod=COMPUTED, adjust=ON, tieRotations=OFF,
thickness=ON)
#Defining a reference point at bottom of the slab
a = mdb.models[str(ii)].rootAssembly
a.ReferencePoint(point=(0.0, -(slabH+trackt/2), 0.0))
#Define set for bottom of the slab and Ref point
##Ref point
a = mdb.models[str(ii)].rootAssembly
r1 = a.referencePoints
refPoints1=(r1[78], )
```

```
a.Set(referencePoints=refPoints1, name='RefPoint')
##slab
a = mdb.models[str(ii)].rootAssembly
f1 = a.instances['Slab-1'].faces
faces1 = f1.getSequenceFromMask(mask=('[#8 ]', ), )
a.Set(faces=faces1, name='BottSlab')
##Equation constraint
mdb.models[str(ii)].Equation(name='Constraint-13', terms=((-1.0, 'BottSlab',
2), (1.0, 'RefPoint', 2)))
#Embedded region
a = mdb.models[str(ii)].rootAssembly
e1 = a.instances['Mesh-1'].edges
edges1 = e1.getSequenceFromMask(mask=('[#fffff ]', ), )
region1=regionToolset.Region(edges=edges1)
a = mdb.models[str(ii)].rootAssembly
c1 = a.instances['Slab-1'].cells
cells1 = c1.getSequenceFromMask(mask=('[#1 ]', ), )
region2=regionToolset.Region(cells=cells1)
mdb.models[str(ii)].EmbeddedRegion(name='Constraint-14',
embeddedRegion=region1, hostRegion=region2,
weightFactorTolerance=1e-06, absoluteTolerance=0.0,
```

```
fractionalTolerance=0.05, toleranceMethod=BOTH)
#CONTACTS
##Defining interaction properties
mdb.models[str(ii)].ContactProperty('steel to steel')
mdb.models[str(ii)].interactionProperties['steel to steel'].TangentialBehavior(
formulation=PENALTY, directionality=ISOTROPIC, slipRateDependency=OFF,
pressureDependency=OFF, temperatureDependency=OFF, dependencies=0,
table=((0.000, ), ), shearStressLimit=None,
maximumElasticSlip=FRACTION, fraction=0.005, elasticSlipStiffness=None)
mdb.models[str(ii)].interactionProperties['steel to steel'].NormalBehavior(
pressureOverclosure=HARD, allowSeparation=ON,
constraintEnforcementMethod=DEFAULT)
#
mdb.models[str(ii)].ContactProperty('steel to concrete')
mdb.models[str(ii)].interactionProperties['steel to concrete'].TangentialBehavior(
formulation=FRICTIONLESS)
mdb.models[str(ii)].interactionProperties['steel to concrete'].NormalBehavior(
pressureOverclosure=HARD, allowSeparation=ON,
constraintEnforcementMethod=DEFAULT)
#Interactions
##studs flanges to tracks flanges
```

```
#For defining the contacts, copy commands from 4.py script
a = mdb.models[str(ii)].rootAssembly
s1 = a.instances['Track-1'].faces
side1Faces1 = s1.getSequenceFromMask(mask=('[#21 ]', ), )
region1=regionToolset.Region(side1Faces=side1Faces1)
a = mdb.models[str(ii)].rootAssembly
s1 = a.instances['Stud-1'].faces
side2Faces1 = s1.getSequenceFromMask(mask=('[#2 ]', ), )
region2=regionToolset.Region(side2Faces=side2Faces1)
mdb.models[str(ii)].SurfaceToSurfaceContactStd(name='Int-1',
createStepName='Initial', master=region1, slave=region2,
sliding=FINITE, thickness=ON, interactionProperty='steel to steel',
adjustMethod=NONE, initialClearance=OMIT, datumAxis=None,
clearanceRegion=None)
a = mdb.models[str(ii)].rootAssembly
s1 = a.instances['Track-1'].faces
side1Faces1 = s1.getSequenceFromMask(mask=('[#22 ]', ), )
region1=regionToolset.Region(side1Faces=side1Faces1)
a = mdb.models[str(ii)].rootAssembly
s1 = a.instances['Stud-2'].faces
side2Faces1 = s1.getSequenceFromMask(mask=('[#2 ]', ), )
```

```
region2=regionToolset.Region(side2Faces=side2Faces1)
mdb.models[str(ii)].SurfaceToSurfaceContactStd(name='Int-2',
createStepName='Initial', master=region1, slave=region2,
sliding=FINITE, thickness=ON, interactionProperty='steel to steel',
adjustMethod=NONE, initialClearance=OMIT, datumAxis=None,
clearanceRegion=None)
a = mdb.models[str(ii)].rootAssembly
s1 = a.instances['Track-1'].faces
side1Faces1 = s1.getSequenceFromMask(mask=('[#c ]', ), )
region1=regionToolset.Region(side1Faces=side1Faces1)
a = mdb.models[str(ii)].rootAssembly
s1 = a.instances['Stud-1'].faces
side2Faces1 = s1.getSequenceFromMask(mask=('[#8 ]', ), )
region2=regionToolset.Region(side2Faces=side2Faces1)
mdb.models[str(ii)].SurfaceToSurfaceContactStd(name='Int-3',
createStepName='Initial', master=region1, slave=region2,
sliding=FINITE, thickness=ON, interactionProperty='steel to steel',
adjustMethod=NONE, initialClearance=OMIT, datumAxis=None,
clearanceRegion=None)
a = mdb.models[str(ii)].rootAssembly
s1 = a.instances['Track-1'].faces
```

```
side1Faces1 = s1.getSequenceFromMask(mask=('[#88 ]', ), )
region1=regionToolset.Region(side1Faces=side1Faces1)
a = mdb.models[str(ii)].rootAssembly
s1 = a.instances['Stud-2'].faces
side2Faces1 = s1.getSequenceFromMask(mask=('[#8 ]', ), )
region2=regionToolset.Region(side2Faces=side2Faces1)
mdb.models[str(ii)].SurfaceToSurfaceContactStd(name='Int-4',
createStepName='Initial', master=region1, slave=region2,
sliding=FINITE, thickness=ON, interactionProperty='steel to steel',
adjustMethod=NONE, initialClearance=OMIT, datumAxis=None,
clearanceRegion=None)
a = mdb.models[str(ii)].rootAssembly
s1 = a.instances['Track-2'].faces
side1Faces1 = s1.getSequenceFromMask(mask=('[#c ]', ), )
region1=regionToolset.Region(side1Faces=side1Faces1)
a = mdb.models[str(ii)].rootAssembly
s1 = a.instances['Stud-1'].faces
side2Faces1 = s1.getSequenceFromMask(mask=('[#2 ]', ), )
region2=regionToolset.Region(side2Faces=side2Faces1)
mdb.models[str(ii)].SurfaceToSurfaceContactStd(name='Int-5',
createStepName='Initial', master=region1, slave=region2,
```

```
sliding=FINITE, thickness=ON, interactionProperty='steel to steel',
adjustMethod=NONE, initialClearance=OMIT, datumAxis=None,
clearanceRegion=None)
a = mdb.models[str(ii)].rootAssembly
s1 = a.instances['Track-2'].faces
side1Faces1 = s1.getSequenceFromMask(mask=('[#88 ]', ), )
region1=regionToolset.Region(side1Faces=side1Faces1)
a = mdb.models[str(ii)].rootAssembly
s1 = a.instances['Stud-2'].faces
side2Faces1 = s1.getSequenceFromMask(mask=('[#2 ]', ), )
region2=regionToolset.Region(side2Faces=side2Faces1)
mdb.models[str(ii)].SurfaceToSurfaceContactStd(name='Int-6',
createStepName='Initial', master=region1, slave=region2,
sliding=FINITE, thickness=ON, interactionProperty='steel to steel',
adjustMethod=NONE, initialClearance=OMIT, datumAxis=None,
clearanceRegion=None)
a = mdb.models[str(ii)].rootAssembly
s1 = a.instances['Track-2'].faces
side1Faces1 = s1.getSequenceFromMask(mask=('[#21 ]', ), )
region1=regionToolset.Region(side1Faces=side1Faces1)
a = mdb.models[str(ii)].rootAssembly
```

```
s1 = a.instances['Stud-1'].faces
side2Faces1 = s1.getSequenceFromMask(mask=('[#8 ]', ), )
region2=regionToolset.Region(side2Faces=side2Faces1)
mdb.models[str(ii)].SurfaceToSurfaceContactStd(name='Int-7',
createStepName='Initial', master=region1, slave=region2,
sliding=FINITE, thickness=ON, interactionProperty='steel to steel',
adjustMethod=NONE, initialClearance=OMIT, datumAxis=None,
clearanceRegion=None)
a = mdb.models[str(ii)].rootAssembly
s1 = a.instances['Track-2'].faces
side1Faces1 = s1.getSequenceFromMask(mask=('[#22 ]', ), )
region1=regionToolset.Region(side1Faces=side1Faces1)
a = mdb.models[str(ii)].rootAssembly
s1 = a.instances['Stud-2'].faces
side2Faces1 = s1.getSequenceFromMask(mask=('[#8 ]', ), )
region2=regionToolset.Region(side2Faces=side2Faces1)
mdb.models[str(ii)].SurfaceToSurfaceContactStd(name='Int-8',
createStepName='Initial', master=region1, slave=region2,
sliding=FINITE, thickness=ON, interactionProperty='steel to steel',
adjustMethod=NONE, initialClearance=OMIT, datumAxis=None,
clearanceRegion=None)
```

```
##Studs ends to the botoom track web
a = mdb.models[str(ii)].rootAssembly
s1 = a.instances['Track-1'].faces
side1Faces1 = s1.getSequenceFromMask(mask=('[#5000 ]', ), )
region1=regionToolset.Region(side1Faces=side1Faces1)
a = mdb.models[str(ii)].rootAssembly
e1 = a.instances['Stud-1'].edges
edges1 = e1.getSequenceFromMask(mask=('[#24400000 #9]', ), )
region2=regionToolset.Region(edges=edges1)
mdb.models[str(ii)].SurfaceToSurfaceContactStd(name='Int-9',
createStepName='Initial', master=region1, slave=region2, sliding=SMALL,
enforcement=NODE_TO_SURFACE, thickness=ON,
interactionProperty='steel to steel', surfaceSmoothing=NONE,
adjustMethod=NONE, smooth=0.2, initialClearance=OMIT, datumAxis=None,
clearanceRegion=None)
a = mdb.models[str(ii)].rootAssembly
s1 = a.instances['Track-1'].faces
side1Faces1 = s1.getSequenceFromMask(mask=('[#5000 ]', ), )
region1=regionToolset.Region(side1Faces=side1Faces1)
a = mdb.models[str(ii)].rootAssembly
e1 = a.instances['Stud-2'].edges
```

```
edges1 = e1.getSequenceFromMask(mask=('[#24400000 #9 ]', ), )
region2=regionToolset.Region(edges=edges1)
mdb.models[str(ii)].SurfaceToSurfaceContactStd(name='Int-10',
createStepName='Initial', master=region1, slave=region2, sliding=SMALL,
enforcement=NODE_TO_SURFACE, thickness=ON,
interactionProperty='steel to steel', surfaceSmoothing=NONE,
adjustMethod=NONE, smooth=0.2, initialClearance=OMIT, datumAxis=None,
clearanceRegion=None)
##Bottom track web to the slab
a = mdb.models[str(ii)].rootAssembly
s1 = a.instances['Slab-1'].faces
side1Faces1 = s1.getSequenceFromMask(mask=('[#2 ]', ), )
region1=regionToolset.Region(side1Faces=side1Faces1)
a = mdb.models[str(ii)].rootAssembly
s1 = a.instances['Track-1'].faces
side2Faces1 = s1.getSequenceFromMask(mask=('[#5000 ]', ), )
region2=regionToolset.Region(side2Faces=side2Faces1)
mdb.models[str(ii)].SurfaceToSurfaceContactStd(name='Int-11',
createStepName='Initial', master=region1, slave=region2,
sliding=FINITE, thickness=ON, interactionProperty='steel to concrete',
adjustMethod=NONE, initialClearance=OMIT, datumAxis=None,
```

```
clearanceRegion=None)
#######Flange to flange contacts!
a = mdb.models[str(ii)].rootAssembly
s1 = a.instances['Track-1'].faces
side1Faces1 = s1.getSequenceFromMask(mask=('[#802 ]', ), )
region1=regionToolset.Region(side1Faces=side1Faces1)
a = mdb.models[str(ii)].rootAssembly
s1 = a.instances['Stud-1'].faces
side2Faces1 = s1.getSequenceFromMask(mask=('[#200 ]', ), )
region2=regionToolset.Region(side2Faces=side2Faces1)
mdb.models[str(ii)].SurfaceToSurfaceContactStd(name='Int-12',
createStepName='Initial', master=region1, slave=region2,
sliding=FINITE, thickness=ON, interactionProperty='steel to steel',
adjustMethod=NONE, initialClearance=OMIT, datumAxis=None,
clearanceRegion=None)

a = mdb.models[str(ii)].rootAssembly
s1 = a.instances['Track-1'].faces
side1Faces1 = s1.getSequenceFromMask(mask=('[#8010 ]', ), )
region1=regionToolset.Region(side1Faces=side1Faces1)
a = mdb.models[str(ii)].rootAssembly
```

```
s1 = a.instances['Stud-2'].faces
side2Faces1 = s1.getSequenceFromMask(mask=('[#200 ]', ), )
region2=regionToolset.Region(side2Faces=side2Faces1)
mdb.models[str(ii)].SurfaceToSurfaceContactStd(name='Int-13',
createStepName='Initial', master=region1, slave=region2,
sliding=FINITE, thickness=ON, interactionProperty='steel to steel',
adjustMethod=NONE, initialClearance=OMIT, datumAxis=None,
clearanceRegion=None)

a = mdb.models[str(ii)].rootAssembly
s1 = a.instances['Track-2'].faces
side1Faces1 = s1.getSequenceFromMask(mask=('[#2001 ]', ), )
region1=regionToolset.Region(side1Faces=side1Faces1)
a = mdb.models[str(ii)].rootAssembly
s1 = a.instances['Stud-1'].faces
side2Faces1 = s1.getSequenceFromMask(mask=('[#8 ]', ), )
region2=regionToolset.Region(side2Faces=side2Faces1)
mdb.models[str(ii)].SurfaceToSurfaceContactStd(name='Int-14',
createStepName='Initial', master=region1, slave=region2,
sliding=FINITE, thickness=ON, interactionProperty='steel to steel',
adjustMethod=NONE, initialClearance=OMIT, datumAxis=None,
```

```
clearanceRegion=None)


a = mdb.models[str(ii)].rootAssembly
s1 = a.instances['Track-2'].faces
side1Faces1 = s1.getSequenceFromMask(mask=('[#220 ]', ), )
region1=regionToolset.Region(side1Faces=side1Faces1)
a = mdb.models[str(ii)].rootAssembly
s1 = a.instances['Stud-2'].faces
side2Faces1 = s1.getSequenceFromMask(mask=('[#8 ]', ), )
region2=regionToolset.Region(side2Faces=side2Faces1)
mdb.models[str(ii)].SurfaceToSurfaceContactStd(name='Int-15',
createStepName='Initial', master=region1, slave=region2,
sliding=FINITE, thickness=ON, interactionProperty='steel to steel',
adjustMethod=NONE, initialClearance=OMIT, datumAxis=None,
clearanceRegion=None)


a = mdb.models[str(ii)].rootAssembly
s1 = a.instances['Track-1'].faces
side1Faces1 = s1.getSequenceFromMask(mask=('[#220 ]', ), )
region1=regionToolset.Region(side1Faces=side1Faces1)
```

```
a = mdb.models[str(ii)].rootAssembly
s1 = a.instances['Stud-2'].faces
side2Faces1 = s1.getSequenceFromMask(mask=('[#80 ]', ), )
region2=regionToolset.Region(side2Faces=side2Faces1)
mdb.models[str(ii)].SurfaceToSurfaceContactStd(name='Int-16',
createStepName='Initial', master=region1, slave=region2,
sliding=FINITE, thickness=ON, interactionProperty='steel to steel',
adjustMethod=NONE, initialClearance=OMIT, datumAxis=None,
clearanceRegion=None)

a = mdb.models[str(ii)].rootAssembly
s1 = a.instances['Track-1'].faces
side1Faces1 = s1.getSequenceFromMask(mask=('[#2001 ]', ), )
region1=regionToolset.Region(side1Faces=side1Faces1)
a = mdb.models[str(ii)].rootAssembly
s1 = a.instances['Stud-1'].faces
side2Faces1 = s1.getSequenceFromMask(mask=('[#80 ]', ), )
region2=regionToolset.Region(side2Faces=side2Faces1)
mdb.models[str(ii)].SurfaceToSurfaceContactStd(name='Int-17',
createStepName='Initial', master=region1, slave=region2,
sliding=FINITE, thickness=ON, interactionProperty='steel to steel',
```

```
adjustMethod=NONE, initialClearance=OMIT, datumAxis=None,
clearanceRegion=None)

a = mdb.models[str(ii)].rootAssembly
s1 = a.instances['Track-2'].faces
side1Faces1 = s1.getSequenceFromMask(mask=('[#8010 ]', ), )
region1=regionToolset.Region(side1Faces=side1Faces1)
a = mdb.models[str(ii)].rootAssembly
s1 = a.instances['Stud-2'].faces
side2Faces1 = s1.getSequenceFromMask(mask=('[#2 ]', ), )
region2=regionToolset.Region(side2Faces=side2Faces1)
mdb.models[str(ii)].SurfaceToSurfaceContactStd(name='Int-18',
createStepName='Initial', master=region1, slave=region2,
sliding=FINITE, thickness=ON, interactionProperty='steel to steel',
adjustMethod=NONE, initialClearance=OMIT, datumAxis=None,
clearanceRegion=None)

a = mdb.models[str(ii)].rootAssembly
s1 = a.instances['Track-2'].faces
side1Faces1 = s1.getSequenceFromMask(mask=('[#802 ]', ), )
region1=regionToolset.Region(side1Faces=side1Faces1)
```

```
    a = mdb.models[str(ii)].rootAssembly
    s1 = a.instances['Stud-1'].faces
    side2Faces1 = s1.getSequenceFromMask(mask=('[#2 ]', ), )
    region2=regionToolset.Region(side2Faces=side2Faces1)
    mdb.models[str(ii)].SurfaceToSurfaceContactStd(name='Int-19',
    createStepName='Initial', master=region1, slave=region2,
    sliding=FINITE, thickness=ON, interactionProperty='steel to steel',
    adjustMethod=NONE, initialClearance=OMIT, datumAxis=None,
    clearanceRegion=None)
####################################

    #Defining STEP
    session.viewports['Viewport: 1'].assemblyDisplay.setValues(interactions=OFF,
    constraints=OFF, connectors=OFF, engineeringFeatures=OFF,
    adaptiveMeshConstraints=ON)
    mdb.models[str(ii)].StaticStep(name='Step-1', previous='Initial',
    maxNumInc=max_num_inc, stabilizationMagnitude=StabMag,
    stabilizationMethod=DISSIPATED_ENERGY_FRACTION,
    continueDampingFactors=False, adaptiveDampingRatio=adapDamp,
    initialInc=initial_inc, minInc=min_inc, maxInc=max_inc, nlgeom=ON)
    session.viewports['Viewport: 1'].assemblyDisplay.setValues(step='Step-1')
```

```
        ###################### Quasi static
        session.viewports['Viewport: 1'].assemblyDisplay.setValues(step='Step-1')
        session.viewports['Viewport: 1'].assemblyDisplay.setValues(
        adaptiveMeshConstraints=ON)
        mdb.models[str(ii)].ImplicitDynamicsStep(name='Step-1', previous='Initial',
        maintainAttributes=True, maxNumInc=max_num_inc,
application=QUASI_STATIC,
        initialInc=initial_inc, minInc=min_inc, nohaf=OFF, amplitude=RAMP,
        alpha=DEFAULT, initialConditions=OFF, nlgeom=ON)
        mdb.models[str(ii)].steps['Step-1'].setValues(maxInc=max_inc)

        #session.viewports['Viewport: 1'].assemblyDisplay.setValues(
        #adaptiveMeshConstraints=ON)
        #mdb.models['1'].steps['Step-1'].setValues(maxInc=DEFAULT)

        #BOUNDARY CONDITIONS
        session.viewports['Viewport: 1'].assemblyDisplay.setValues(loads=ON, bcs=ON,
        predefinedFields=ON, connectors=ON, adaptiveMeshConstraints=OFF)
        a = mdb.models[str(ii)].rootAssembly
        f1 = a.instances['Track-2'].faces
        faces1 = f1.getSequenceFromMask(mask=('[#5000 ]', ), )
```

```
region = regionToolset.Region(faces=faces1)
mdb.models[str(ii)].DisplacementBC(name='BC-1', createStepName='Step-1',
region=region, u1=0.0, u2=-0.3, u3=0.0, ur1=UNSET, ur2=UNSET,
ur3=UNSET, amplitude=UNSET, fixed=OFF, distributionType=UNIFORM,
fieldName='', localCsys=None)
a = mdb.models[str(ii)].rootAssembly
f1 = a.instances['Slab-1'].faces
faces1 = f1.getSequenceFromMask(mask=('[#8 ]', ), )
region = regionToolset.Region(faces=faces1)
mdb.models[str(ii)].DisplacementBC(name='BC-2', createStepName='Step-1',
region=region, u1=0.0, u2=UNSET, u3=0.0, ur1=UNSET, ur2=UNSET,
ur3=UNSET, amplitude=UNSET, fixed=OFF, distributionType=UNIFORM,
fieldName='', localCsys=None)
a = mdb.models[str(ii)].rootAssembly
r1 = a.referencePoints
refPoints1=(r1[78], )
region = regionToolset.Region(referencePoints=refPoints1)
mdb.models[str(ii)].DisplacementBC(name='BC-3', createStepName='Step-1',
region=region, u1=UNSET, u2=0.0, u3=UNSET, ur1=UNSET, ur2=UNSET,
ur3=UNSET, amplitude=UNSET, fixed=OFF, distributionType=UNIFORM,
fieldName='', localCsys=None)
```

```
##
session.viewports['Viewport: 1'].view.setValues(session.views['Iso'])
##
#Supressing some of the constraint
#mdb.models[str(ii)].constraints['Constraint-1'].suppress()
#mdb.models[str(ii)].constraints['Constraint-2'].suppress()
#mdb.models[str(ii)].constraints['Constraint-3'].suppress()
#mdb.models[str(ii)].constraints['Constraint-4'].suppress()
#mdb.models[str(ii)].constraints['Constraint-5'].suppress()
#mdb.models[str(ii)].constraints['Constraint-6'].suppress()
#mdb.models[str(ii)].constraints['Constraint-7'].suppress()
#mdb.models[str(ii)].constraints['Constraint-8'].suppress()
#mdb.models[str(ii)].constraints['Constraint-14'].suppress()
##
#Supressing Mesh
#a = mdb.models[str(ii)].rootAssembly
#session.viewports['Viewport: 1'].setValues(displayedObject=a)
#a = mdb.models[str(ii)].rootAssembly
#a.features['Mesh-1'].suppress()
##
##Supressing flanges contact
```

```
        mdb.models[str(ii)].interactions['Int-1'].suppress()

        mdb.models[str(ii)].interactions['Int-2'].suppress()

        mdb.models[str(ii)].interactions['Int-3'].suppress()

        mdb.models[str(ii)].interactions['Int-4'].suppress()

        mdb.models[str(ii)].interactions['Int-5'].suppress()

        mdb.models[str(ii)].interactions['Int-6'].suppress()

        mdb.models[str(ii)].interactions['Int-7'].suppress()

        mdb.models[str(ii)].interactions['Int-8'].suppress()

        #Defining attachment points

        a = mdb.models[str(ii)].rootAssembly

        d1 = a.instances['Track-1'].datums

        d2 = a.instances['Track-2'].datums

        v1 = a.instances['Track-1'].vertices

        a.AttachmentPoints(name='Attachment Points-1', points=(d1[8], d1[7], d2[9],
d2[10], d1[9], d2[7], d1[10], d2[8]),

        setName='Attachment Points-1-Set-1')

        ##

        #CONNECTORS

        #a = mdb.models[str(ii)].rootAssembly

        #region=a.sets['Attachment Points-1-Set-1']

        #datum = mdb.models[str(ii)].rootAssembly.datums[1]
```

```
    #mdb.models[str(ii)].rootAssembly.engineeringFeatures.PointFastener(
    #name='Fasteners-1', region=region, localCsys=datum,
    #physicalRadius=0.01, connectionType=BEAM_MPC, adjustOrientation=OFF,
    #influenceRadius=0.01)
    #
    #Creating JOB
    mdb.Job(name=str(ii), model=str(ii), description='', type=ANALYSIS,
    atTime=None, waitMinutes=0, waitHours=0, queue=None, memory=90,
    memoryUnits=PERCENTAGE, getMemoryFromAnalysis=True,
    explicitPrecision=SINGLE, nodalOutputPrecision=SINGLE, echoPrint=OFF,
    modelPrint=OFF, contactPrint=OFF, historyPrint=OFF, userSubroutine='',
    scratch='', resultsFormat=ODB, multiprocessingMode=DEFAULT, numCpus=4,
    numDomains=4, numGPUs=0)

#SUBMIT
import time
for ii in range(1,nn):
    session.viewports['Viewport: 1'].setValues(displayedObject=None)
    a = mdb.models[str(ii)].rootAssembly
    session.viewports['Viewport: 1'].setValues(displayedObject=a)
```

```
        session.viewports['Viewport: 1'].assemblyDisplay.setValues(loads=OFF,
bcs=OFF,

        predefinedFields=OFF, connectors=OFF, optimizationTasks=OFF,

        geometricRestrictions=OFF, stopConditions=OFF)

        mdb.jobs[str(ii)].submit(consistencyChecking=OFF)

        time.sleep(sleep_time)


    #SAVING RESULT

    for ii in range (1,nn):


        a = mdb.models[str(ii)].rootAssembly

        session.viewports['Viewport: 1'].setValues(displayedObject=a)


        #import os.path #defining the name of files

        #save_path='E:/Parametric Study II/'

        #Name_of_file=str(ii)

        #CompleteName=os.path.join(save_path,Name_of_file+".odb")

        CompleteName='E:/Parametric Study II/26/'+str(ii)+'.odb'


        o3 = session.openOdb(name=CompleteName)

        session.viewports['Viewport: 1'].setValues(displayedObject=o3)
```

```
        a = mdb.models[str(ii)].rootAssembly

        session.viewports['Viewport: 1'].setValues(displayedObject=a)

        session.mdbData.summary()

        odb = session.odbs[CompleteName]

        xyList = xyPlot.xyDataListFromField(odb=odb, outputPosition=NODAL,
variable=((

        'RF', NODAL, ((COMPONENT, 'RF2'), )), ), nodeSets=('REFPOINT', ))

        xyp = session.xyPlots['XYPlot-1']

        chartName = xyp.charts.keys()[0]

        chart = xyp.charts[chartName]

        curveList = session.curveSet(xyData=xyList)

        chart.setValues(curvesToPlot=curveList)

        session.viewports['Viewport: 1'].setValues(displayedObject=xyp)

        x0 = session.xyDataObjects['_RF:RF2 PI: ASSEMBLY N: 1']

        session.writeXYReport(fileName=str(ii)+".rpt", xyData=(x0, ))

        del session.xyDataObjects['_RF:RF2 PI: ASSEMBLY N: 1']
```

# References

[1] R. Brockenbrough, F. Merrit, “Structural steel designer's handbook”, 3rd ed., McGraw-Hill education, New York, NY, 1999.

[2] AISI S100, North America Specification for the Design of Cold- Formed Steel Structures, American Iron and Steel Institute, Washington, D.C., 2016.

[3] AISI S240, North America Standard for Cold-Formed Steel Structural Framing, American Iron and Steel Institute, Washington, D.C., 2015.

[4] T.H. Miller, T. Pekoz, “Behavior of cold-formed steel wall stud assemblies,” Journal of structural engineering, vol. 119, no. 2, pp. 641–651, 1993.

[5] Y. Telue, M. Mahendran, “Behavior of cold-formed steel wall frames lined with plasterboard,” Journal of Constructional Steel Research, vol. 57, pp. 435–452, 2001.

[6] R.A. Laboube, P.F. Findlay, “Wall Stud-to-Track Gap: Experimental Investigation,” Journal of Architectural Engineering, vol. 13, no. 2, pp. 105–110, 2007.

[7] J. Wang, Y.S. Tian, and T. J. Lu, “The role of frame members and sheathing in partition wall panels subjected to compression,” Journal of thin-walled structures, vol. 43, pp. 983–1002, 2005.

[8] L.C.M. Vieira, Y. Shifferaw, and B. W. Schafer, “Experiments on sheathed cold- formed steel studs in compression,” Journal of Constructional Steel Research, vol. 67, no. 10, pp. 1554–1566, 2011.

[9] K.D. Peterman, B. W. Schafer, “Sheathed cold-formed steed studs under axial and lateral load,” Journal of Constructional Steel Research, vol. 140, no. 10, pp. 1–12, 2014.

[10] D.C. Fratamico, S. Torabian, K.J.R. Rasmussen, and B.W. Schafer, “Experimental studies on the composite action in wood-sheathed and screw-fastened built-up cold-formed steel columns,” Proc. of the Annual Stability Conference, Structural Stability Council, Orlando, FL., 2016.

[11] D. Polyzois, S. Fox, “Bearing of Steel Studs on Concrete,” Newsletter for the Light Gauge Steel Engineering Association (now the Cold-Formed Steel Engineering Institute), 2011.

[12] S. Bae, A. Belarbi, and R. A. LaBoube, “Bearing Strength of Slabs on Grade Supporting a Cold-Formed Steel Wall in Low-Rise Building,” Journal of Architectural Engineering, vol. 12, no. 1, pp. 24–32, 2006.

[13] ACI Committee 318. Building Code Requirements for Structural Concrete (ACI 318-05) and Commentary (ACI 318R-05). Farmington Hills, Mich.: American Concrete Institute, 2005.

[14] B.W. Schafer, S. Ádány, “Buckling analysis of cold-formed steel members using CUFSM: conventional and constrained finite strip method.” Proc. of 18th International Specialty Conference on Cold-Formed Steel Structures, Orlando, FL, 2006.

[15] Z. Li, B.W. Schafer, “Buckling analysis of cold-formed steel members with general boundary conditions using CUFSM: conventional and constrained finite strip methods.” Proc. of International Specially Conference on Cold-Formed Steel Structures, St. Louis, Missouri, 2010.

[16] ABAQUS, ABAQUS standard version 6.14-4, Dassault Systems Simulia Corp.

[17] AISI S220, North America Standard for Cold-Formed Steel Framing - Nonstructural Members, American Iron and Steel Institute, Washington, D.C., 2015.

[18] ACI Committee 318. Building Code Requirements for Structural Concrete (ACI 318-14) and Commentary (ACI 318R-05). Farmington Hills, Mich.: American Concrete Institute, 2014.

[19] "Hilti product tech guide supplement, X-U and X-P fasteners".

[20] ASTM C31/C31M-18b, Standard Practice for Making and Curing Concrete Test Specimens in the Field, ASTM International, West Conshohocken, PA, 2018, www.astm.org.

[21] ASTM C143/C143M-15a, Standard Test Method for Slump of Hydraulic-Cement Concrete, ASTM International, West Conshohocken, PA, 2015, www.astm.org.

[22] ASTM E8/E8M-16a, Standard Test Methods for Tension Testing of Metallic Materials, ASTM International, West Conshohocken, PA, 2016, www.astm.org.

[23] A. Joorabchian, Z. Li, and K.D. Peterman, "Steel stud assemblies bearing on concrete slabs (Phase 1)," American Iron and Steel Institute (AISI), 2019.

[24] J. P. Papangelis, G. J. Hancock, "Computer analysis of this-walled structural members," Computers and Structures, vol. 56, no. I, 1995.

[25] A. Joorabchian, K.D. Peterman, "Using Photogrammetry-Based Imperfection

Measurement Tools to Determine the Impact of Corner Radii Imperfection on Cold-Formed Steel Member Strength," Proc. of the Annual Stability Conference, Structural Stability Research Council, Baltimore, Maryland, 2018.

[26] A. Joorabchian, Z. Li, and K.D. Peterman, "Experimental and numerical investigation of fixed-height cold-formed steel wall assemblies bearing on concrete slabs" Journal of thin-walled structures, 2020 <submitted>.

[27] A. Joorabchian, Z. Li, and K.D. Peterman, "The Impact of Bearing Conditions on the Stability Behavior of Cold- Formed Steel Stud Assemblies," Proc. of the Annual Stability Conference, Structural Stability Research Council, St. Louis, Missouri-Rolla, 2019.

[28] A. Joorabchian, Z. Li, and K.D. Peterman, "The Impact of Bearing Conditions on the Behavior of Cold- Formed Steel Stud Assemblies," Proc. of International Specially Conference on Cold-Formed Steel Structures, St. Louis, Missouri, 2018.

[29] E. Hognestad, "A study of Combined Bending and Axial Load in Reinforced Concrete Members," Bulletin Series No. 399, Engineering Experiment Station, Urbana, USA: University of Illinois, 1951.

[30] A.S. Genikomsou and M.A. Polak, "Finite element analysis of punching shear of concrete slabs using damaged plasticity model in ABAQUS," Journal of Engineering Structures, vol. 98, pp. 38–48, 2015.

[31] Comité Euro-international du Béton, CEB-FIB-model Code 1990: Design code. London: Thomas Telford, 1993.

[32] B.W. Schafer, T. Peköz, "Computational modeling of cold-formed steel: characterizing geometric imperfections and residual stresses," Journal of Constructional Steel Research, vol. 47, no. 3, pp. 193–210, 1998.

[33] F. Liao, H. Wu, R. Wang, and T. Zhou, “Compression test and analysis of multi- limbs built-up cold-formed steel stub columns,” Journal of Constructional Steel Research, vol. 128, pp. 405–415, 2017.

[34] C.D. Moen and B.W. Schafer, “Experiments on cold-formed steel columns with holes,” Journal of Thin-Walled Structures, vol. 46, pp. 1164–1182, 2008.

[35] J.B.P. Lim and D.A. Nethercot, “Ultimate strength of bolted moment-connections between cold-formed steel members,” Journal of Thin-Walled Structures, vol. 41, pp. 1019–1039, 2003.

[36] Z. Li and B.W. Schafer, “Application of the finite strip method in cold-formed steel member design,” Journal of Construction Steel Research, vol. 66, no. 8–9, pp. 971–980, 2010.

[37] Z. Beregszászi and S. Ádány, “Application of the constrained finite strip method for the buckling design of cold-formed steel columns and beams via the direct strength method,” Computer and Structures, vol. 89, no. 2011, pp. 2020–2027, 2011.

[38] S. Torabian and B.W. Schafer, “Development of a New Beam-Column Design Method for Cold- Formed Steel Lipped Channel Members,” Proceeding of the 22nd international specially conference on Cold-formed steel structure, St. Louis, Missouri, 20